University of Alberta

Beta Dosimetry of Micrometastases During Targeted Liposomal Intraperitoneal Radionuclide Therapy

by

Alasdair Syme ©

A thesis submitted to the Faculty of Graduate Studies and Research in partial
fulfillment of the requirements for the degree of Doctor of Philosophy

in

Medical Physics

Department of Physics

Edmonton, Alberta

Fall 2004

Library and
Archives Canada

Published Heritage
Branch

395 Wellington Street
Ottawa ON K1A 0N4
Canada

Bibliothèque et
Archives Canada

Direction du
Patrimoine de l'édition

395, rue Wellington
Ottawa ON K1A 0N4
Canada

Your file Votre référence
ISBN: 0-612-96025-0
Our file Notre référence
ISBN: 0-612-96025-0

The author has granted a non-exclusive license allowing the Library and Archives Canada to reproduce, loan, distribute or sell copies of this thesis in microform, paper or electronic formats.

The author retains ownership of the copyright in this thesis. Neither the thesis nor substantial extracts from it may be printed or otherwise reproduced without the author's permission.

L'auteur a accordé une licence non exclusive permettant à la Bibliothèque et Archives Canada de reproduire, prêter, distribuer ou vendre des copies de cette thèse sous la forme de microfiche/film, de reproduction sur papier ou sur format électronique.

L'auteur conserve la propriété du droit d'auteur qui protège cette thèse. Ni la thèse ni des extraits substantiels de celle-ci ne doivent être imprimés ou aturement reproduits sans son autorisation.

In compliance with the Canadian Privacy Act some supporting forms may have been removed from this thesis.

While these forms may be included in the document page count, their removal does not represent any loss of content from the thesis.

Conformément à la loi canadienne sur la protection de la vie privée, quelques formulaires secondaires ont été enlevés de cette thèse.

Bien que ces formulaires aient inclus dans la pagination, il n'y aura aucun contenu manquant.

Canadä

Acknowledgement

I would like to thank my supervisors, Dr. Steve McQuarrie and Dr. B. Gino Fallone, for their support and guidance during my tenure as a graduate student at the University of Alberta. This thesis benefited greatly from their insights, both scientific and editorial, and I am truly grateful for their efforts. I would also like to thank Dr. Terence Riauka for our numerous conversations about dosimetry. They were always illuminating and entertaining.

Over the last five years I have had the pleasure of working with a number of people from the Faculty of Pharmacy who have helped me with my various experimental efforts. In particular, I would like to thank Dr. Jerry Miller, Dr. Mavanur Suresh and Dr. John Mercer for their assistance and advice. In addition, I would like to thank Dr. John Duke from the University of Alberta SLOWPOKE nuclear reactor facility for his time, effort, interminable patience and good humour, as well the extended use of his various laboratory supplies.

Outside of the research world, I have been extremely lucky to have the love and support of my parents Colin and Morag and my sisters Alison and Catriona. I cannot adequately express my gratitude, but thank-you. Finally, I would like to thank Ellen Crawford for her love and support. She was there for me throughout as my better half and my best friend. She made my time as a graduate student truly memorable and happy.

Table of Contents

Chapter 1 .... **1**

Thesis Overview **1**

References 4

Chapter 2 .... **5**

Ovarian Cancer: Pathology, Prognosis, Treatment **5**

2.1 General Information 5

2.2 Treatment 12

2.3 Intraperitoneal Radionuclide Therapy 13

References 24

Chapter 3 .... **29**

Beta Dosimetry **29**

3.1 Electron Interactions With Matter 30

3.2 Dose Point Kernels And Their Applications 33

3.3 Microdosimetry 37

References 43

Chapter 4 .... **46**

Liposome-Mediated Targeted Intraperitoneal Radionuclide Therapy **46**

4.1 Liposomes 46

4.2 Liposome Preparation 51

4.3 Liposome Purification 52

4.4 Therapy Design 53

4.5 Evidence of Successful Therapeutic Design 61

  4.5.1 Targeting of Liposomes to Ovarian Cancer Cells 61

4.5.1.1 Materials and Methods 61
4.5.1.2 Results 62
4.5.2 Radiolabeling of Liposomes 65
4.5.2.1 Materials and Methods 65
4.5.2.2 Labeling Mixture 65
4.5.2.3 Results 66

4.6 Conclusion 75

References 76

Chapter 5 78

Dose-Rate Profiles In Microscopic Spherical Tumours 78

5.1 Introduction 78

5.2 Radioactive Bath 82

5.3 Surface-Bound Radioactivity 85

5.4 Results 87
5.4.1 Radioactive Bath 87
5.4.2 Surface-Bound Radioactivity 90

5.5 Discussion 93

5.6 Conclusion 97

References 98

Appendix 1: Dose-Rate Profiles (Radioactive Bath) 101

Appendix 2: Dose-rate Profiles (Surface-bound radioactivity) 104

Chapter 6 109

Dosimetric Model For Liposomal Radionuclide Therapy Of Micrometastases In The Peritoneal Cavity 109

6.1 Introduction 109

6.2 Model Development 111

6.3 Dose Calculations 113

6.4 Tumour Control Probability 115

6.5 Results 117
    6.5.1 Binding Kinetics 117
    6.5.2 Tumour Control Probabilities 119

6.6 Discussion 137

6.7 Conclusion 140

References 141

Chapter 7 144

Microdosimetry of Single Cells During Intraperitoneal Radionuclide Therapy 144

7.1 Introduction 144

7.2 Monte Carlo Simulations 147
    7.2.1 Surface-Bound Radioactivity 148
    7.2.2 Free Radioactivity 151

7.3 Results 153

7.4 Discussion 182

7.5 Conclusion 186

References 187

Chapter 8 190

Concluding Remarks and Future Directions 190

Bibliography 195

List of Tables

Table 2.1: FIGO Staging System For Ovarian Cancer

Table 2.2: Survival-Rate Of Epithelial Ovarian Cancers

Table 2.3: Physical properties of alpha and beta emitting radionuclides of potential use in radionuclide therapy

Table 5.1: Physical Properties of Radionuclides

Table A1: Non-Targeted Dose-Rate Profile: Tumour Radius = 0.001cm

Table A2: Non-Targeted Dose-Rate Profile: Tumour Radius = 0.005cm

Table A3: Non-Targeted Dose-Rate Profile: Tumour Radius = 0.01cm

Table A4: Non-Targeted Dose-Rate Profile: Tumour Radius = 0.05cm

Table A5: Non-Targeted Dose-Rate Profile: Tumour Radius = 0.1cm

Table A6: Dose-Rate Profile From Surface-Bound Activity: Tumour Radius = 0.001cm

Table A7: Dose-Rate Profile From Surface-Bound Activity: Tumour Radius = 0.005cm

Table A8: Dose-Rate Profile From Surface-Bound Activity: Tumour Radius = 0.01cm

Table A9: Dose-Rate Profile From Surface-Bound Activity: Tumour Radius = 0.05cm

Table A10: Dose-Rate Profile From Surface-Bound Activity: Tumour Radius = 0.1cm

Table 7.1: Sampling frequency for "monoenergetic" single event spectra

Table 7.2: Frequency mean specific energy per event, $\bar{z}_f$, and their standard deviations for both surface-bound radioactivity and free radioactivity in the peritoneal fluid. As the energy of the beta emitter increases, the value of $\bar{z}_f$ decreases.

Table 7.3: Comparison of EGSnrc with the OREC and PENELOPE Monte Carlo systems. Values of $\bar{z}_f$ were calculated for a sphere with a radius of 5 μm. Agreement between EGSnrc and OREC is very good at 1000 keV but shows a 7.3% discrepancy at 100 keV. PENELOPE also shows reasonable agreement with EGSnrc.

Table 7.4: Radionuclide-specific p values

List of Figures

Figure 2.1: Diagram of the female reproductive system. Figure taken from an update to the FDA Publication No. (FDA) 94-1215 found at http://www.fda.gov/fdac/reprints/ots_mens.html.

Figure 3.1: Collisional, radiative and total stopping powers of water for electrons up to 100 MeV. In the energy range of interest for radionuclide therapies (< 2.5 MeV) the total stopping power is almost entirely collisional.

Figure 4.1: Illustration of size exclusion chromatography. Large particles such as liposomes (represented by circles) cannot enter the pores of the column's beads and pass through the column quickly. Small particles such as free radioactivity (shown as 'x') can enter the pores and have longer transit times due to their tortuous path through the column.

Figure 4.2: Hypothetical elution profile from a PD-10 size exclusion column. Typically there is good separation between the liposome peak and the exclusion peak corresponding to the unbound radioactivity

Figure 4.3: Schematic illustration of the construction of a bi-specific monoclonal antibody. In step 1, the intact MAb A is fragmented into two identical FAb fragments (FAb A) and a single Fc fragment. In step 2, the FAb fragments are covalently linked to the Fc region of a second MAb, B to form the bs-MAb.

Figure 4.4: Constituent molecules of liposome formulation used to carry radioactive Y-90 atoms to CA-125-expressing cancer cells. Figures used with permission from Avanti Polar Lipids.

Figure 4.5: Schematic diagram of the targeted delivery of radioactivity to the surface of an ovarian cancer cell that is expressing the antigen CA-125. The wavy lines extending out from the surface of the liposomes are long chain polyethylene glycol polymers. The bs-MAb molecules bind to both the cancer cell and the liposome to act as a tether between the two.

Figure 4.6: Confocal microscopy images of a pair of liposome-labeled OVCAR-3 cancer cells. Panel A is a phase contrast image of the cells. Panel B is the fluorescent signal from the cells.

Panel C shows the fluorescent signal superimposed on the phase contrast image. There appears to be significant labeling of the cells with liposomes.

Figure 4.7: Confocal microscopy images of an SKOV-3 cell. SKOV-3 cells do not express CA-125. Panel A is the phase contrast image of the cell. Panel B is the fluorescent signal from the cell. Panel C shows the fluorescent signal superimposed on the phase contrast image. There does not appear to be any labeling of this cell with liposomes.

Figure 4.8: Elution profile of a liposome-free Y-90 sample. The radioactivity peaks in fraction 10 which is where a small molecule such as Y-acetate would be expected to be eluted.

Figure 4.9: Elution profile of a sample with incomplete labeling of Y-90 to DTPA-liposomes. The radioactivity associated with the liposomes peaks in fraction 4 and can be clearly differentiated from the free radioactivity that peaks in fraction 10 as it did when no liposomes were used.

Figure 4.10: Elution profile of sample prepared by incubating 200 µL of liposomes (pH 6), 200µL of saline and 50 µL of Y-90 at room temperature for 3 hours. No free Yttrium tail is observed at fraction 10 suggesting that all of the radioactivity was labeled to the liposomes.

Figure 4.11: Labeling efficiency as a function of incubation time. After three hours of incubation at room temperature, the reaction mixture consisting of 10 µL of liposomes (pH 6), 10 µL of saline and 10 µL of Y-90 produced almost complete labeling of the liposomes.

Figure 4.12: Elution profiles of samples labeled with different concentrations of liposomes. Samples were prepared with the stock solution of liposomes as well as dilution factors of 10, 100 and 1000. Dilute samples show a peak broadening effect and shift to the right.

Figure 4.13: Elution profile of dilute liposomes labeled with Y-90. The dilute nature of the sample produced a broadening of the liposome peak, a phenomenon known to occur in size exclusion chromatography.

Figure 4.14: Elution profile produced when fraction 8 from figure 4.13 was passed down a second PD-10 column. The peak in this case appears in fraction 6 suggesting that the counts in the tail of

the peak in figure 4.13 are still primarily liposome counts. The fact that this profile extends beyond fraction 10 suggests that there could be an unbound Yttrium component present.

Figure 4.15: Stability profile of Y-90-labeled liposomes. Liposomes were kept at room temperature for 72 hours after labeling. Every 24 hours, an aliquot of liposomes was passed down a PD-10 column. The ratio of counts in the liposome peak to the total number of counts loaded on the column was used to determine the percentage of radioactivity still bound to the liposomes.

Figure 5.1: Interpolated dose point kernels for four radionuclides. Data from Cross et al. (1992) was interpolated using Matlab's piecewise cubic hermite interpolating polynomials (pchip)

Figure 5.2: Illustration of the calculation of dose-rate at a distance a from the center of a tumor submerged in a radioactive bath. Contributions from thin spherical shells are summed over all volumes capable of contributing to the dose at point a. R = tumor radius; R' = radius of spherical shell; r = distance from all source elements defined by angle θ to point at distance a.

Figure 5.3: Illustration of the calculation of dose-rate at a distance a from the center of a tumor with uniform activity distributed over its surface. All elements of surface area described by a particular value of θ will make an equal contribution to the dose-rate at point a because they are all located a distance r from that point. R = tumor radius.

Figure 5.4: Radial dose-rate profiles through tumors submerged in a bath of (a) Re-188 and (b) Cu-67. This is the type of dose distribution produced by a nontargeted therapy. For small tumors the profiles are virtually flat (especially for the high-energy beta emitter Re-188) with dose-rates approximately equal to the equilibrium dose-rates.

Figure 5.5: Dose-rate at the center of the tumor as a percentage of the equilibrium dose-rate. Charged particle equilibrium is preserved only for very small tumors with all nuclides; however, divergence from equilibrium is significantly quicker with low-energy beta emitters such as Cu-67 or I-131.

Figure 5.6: Radial dose-rate profiles through tumors with uniform surface distributions of (a) Re-188 and (b) Cu-67. The lower-energy beta emitter, Cu-67, produces significantly higher dose-rates than the high-energy bea emitter, Re-188, in smaller tumors (R = 10 μm, R = 50 μm). By the

time the tumor reaches a radius of 1 mm, however, the short range of the Cu-67 betas renders this nuclide ineffective whereas the Re-188 betas are still able to penetrate to the center of the tumor.

Figure 5.7: Dose-rate to the center of a tumor as a function of tumor radius for surface-bound Re-188 and Cu-67. The low-energy emitter Cu-67 produces higher dose-rates than the high-energy emitter Re-188 for very small tumors. Once the radius of the tumor exceeds approximately 0.025 cm, the high-energy emitter produces higher dose-rates.

Figure 6.1: Number of liposomes bound to the surface of a 0.05 cm radius tumour as a function of time. Four different parameter sets are shown to illustrate the importance of the binding kinetics in an intraperitoneal immunotherapy. The parameter sets used are: Set 1: $k_1 = 10^5$ $M^{-1}s^{-1}$, $k_2 = 10^{-5}$ s^{-1} and $k_3 = 0$. Set 2: $k_1 = 10^5$ $M^{-1}s^{-1}$, $k_2 = 10^{-5}$ s^{-1} and $k_3 = 8.022x10^{-6}$ s^{-1}. Set 3: $k_1 = 10^6$ $M^{-1}s^{-1}$, $k_2 = 10^{-4}$ s^{-1} and $k_3 = 1.6044x10^{-5}$ s^{-1}. Set 4: $k_1 = 10^5$ $M^{-1}s^{-1}$, $k_2 = 10^{-4}$ s^{-1} and $k_3 = 4.011x10^{-6}$ s^{-1}

Figure 6.2: Tumour Control Probability (TCP) as a function of time for a 0.05 cm radius tumour. The parameter sets used are: Set 1: $k_1 = 10^5$ $M^{-1}s^{-1}$, $k_2 = 10^{-5}$ s^{-1} and $k_3 = 0$. Set 2: $k_1 = 10^5$ $M^{-1}s^{-1}$, $k_2 = 10^{-5}$ s^{-1} and $k_3 = 8.022x10^{-6}$ s^{-1}. Set 3: $k_1 = 10^6$ $M^{-1}s^{-1}$, $k_2 = 10^{-4}$ s^{-1} and $k_3 = 1.6044x10^{-5}$ s^{-1}. Set 4: $k_1 = 10^5$ $M^{-1}s^{-1}$, $k_2 = 10^{-4}$ s^{-1} and $k_3 = 4.011x10^{-6}$ s^{-1}. The biological processes play an important role in determining how quickly a tumour will be killed. For these particular data sets, the biological elimination constant, k_3, appears to be the dominant factor since the TCP curves appear in order of increasing k_3 from left to right.

Figure 6.3: Surface plot of the time required to produce a TCP of 95% ($TTCP_{95}$) as a function of the binding rate constant, k_1, and antigen surface density, C_o, for a 0.05cm radius tumour. In part A), the injected activity is 37 GBq in 1 litre of fluid and in part B) it is 9 GBq in 1 litre of fluid. For both parts, $k_2 = 10^{-5}$ s^{-1} and $k_3 = 8.022x10^{-6}$ s^{-1}. As k1 and Co decrease, the surfaces eventually reach a plateau. The value of TTCP95 at the plateau is the same as it would be if a non-targeted approach were used (i.e. if there were no liposomes bound to the surface of the tumour).

Figure 6.4. $TTCP_{95}$ as a function of injected activity (IA) for a non-targeted approach. These curves assume that there is no radioactivity bound to the surface of the tumour so that the lethal effects of the treatment are mediated entirely by the radioactivity in solution. Any binding of radioactive material to the surface would boost the dose to the tumour and reduce $TTCP_{95}$ (as shown in Figure 6.3), however very weak or slow binding cannot increase TTCP_{95} beyond the values shown in this Figure. The values of TTCP_{95} in this figure would correspond to the plateau values of surface plots such as those shown in Figure 6.3.

Figure 6.5. Antigen density required to produce a 5% improvement in TTCP_{95} over that from a non-targeted approach for tumours of various radii: a) 0.005cm, b) 0.01cm, c) 0.05 cm and d) 0.1cm. This requirement is expressed as a function of both the dissociation rate constant, k_2, and the biological elimination constant, k_3. The value of k_1 was taken as 10^5 $M^{-1}s^{-1}$ and the injected activity was 18 GBq. The required antigen density increases as the value of k_2 increases and the value of k_3 decreases.

Figure 6.5 B. Antigen density required to produce a 5% improvement in TTCP_{95} over that from a non-targeted approach for tumour of radius 0.01cm. This requirement is expressed as a function of both the dissociation rate constant, k_2, and the biological elimination constant, k_3. The value of k_1 was taken as 10^5 $M^{-1}s^{-1}$ and the injected activity was 18 GBq. The required antigen density increases as the value of k_2 increases and the value of k_3 decreases.

Figure 6.5 C. Antigen density required to produce a 5% improvement in TTCP_{95} over that from a non-targeted approach for tumour of radius 0.05 cm. This requirement is expressed as a function of both the dissociation rate constant, k_2, and the biological elimination constant, k_3. The value of k_1 was taken as 10^5 $M^{-1}s^{-1}$ and the injected activity was 18 GBq. The required antigen density increases as the value of k_2 increases and the value of k_3 decreases.

Figure 6.5 D. Antigen density required to produce a 5% improvement in TTCP_{95} over that from a non-targeted approach for tumours of radius 0.1cm. This requirement is expressed as a function of both the dissociation rate constant, k_2, and the biological elimination constant, k_3. The value of k_1 was taken as 10^5 $M^{-1}s^{-1}$ and the injected activity was 18 GBq. The required antigen density increases as the value of k_2 increases and the value of k_3 decreases.

Figure 6.6: The percent of the total dose contributed by the surface-bound radioactivity is shown as a function of both the time of the treatment and the depth within the tumour, r, for Cu-67. In panel A, the parameter values are: $k_1 = 10^5$ and $k_3 = 0$. In panel B, the values are: $k_1 = 10^5$ and $k_3 = 1.6 \times 10^{-5}$. In panel C, the parameter values are: $k_1 = 10^6$ and $k_3 = 0$. In panel D, the values are: $k_1 = 10^6$ and $k_3 = 1.6 \times 10^{-5}$. The injected activity was 1.85 GBq and the values of k_2 and C_o were 10^{-5} and 10^8 respectively.

Figure 6.6 B: The percent of the total dose contributed by the surface-bound radioactivity as a function of both the time of the treatment and the depth within the tumour, r, for Cu-67. Parameter values are: $k_1 = 10^5$ and $k_3 = 1.6 \times 10^{-5}$. The injected activity was 1.85 GBq and the values of k_2 and C_o are 10^{-5} and 10^8 respectively.

Figure 6.6 C: The percent of the total dose contributed by the surface-bound radioactivity as a function of both the time of the treatment and the depth within the tumour, r, for Cu-67. Parameter values are: $k_1 = 10^6$ and $k_3 = 0$. The injected activity was 1.85 GBq and the values of k_2 and C_o are 10^{-5} and 10^8 respectively.

Figure 6.6 D: The percent of the total dose contributed by the surface-bound radioactivity as a function of both the time of the treatment and the depth within the tumour, r, for Cu-67. Parameter values are: $k_1 = 10^6$ and $k_3 = 1.6 \times 10^{-5}$. The injected activity was 1.85 GBq and the values of k_2 and C_o are 10^{-5} and 10^8 respectively.

Figure 6.7: The percent of the total dose contributed by the surface-bound radioactivity is shown as a function of both the time of the treatment and the depth within the tumour, r, for Y-90. In panel A, the parameter values are: $k_1 = 10^5$ and $k_3 = 0$. In panel B, the values are: $k_1 = 10^5$ and $k_3 = 1.6 \times 10^{-5}$. In panel C, the parameter values are: $k_1 = 10^6$ and $k_3 = 0$. In panel D, the values are: $k_1 = 10^6$ and $k_3 = 1.6 \times 10^{-5}$. The injected activity was 1.85 GBq and the values of k_2 and C_o were 10^{-5} and 10^8 respectively.

Figure 6.7 B: The percent of the total dose contributed by the surface-bound radioactivity as a function of both the time of the treatment and the depth within the tumour, r, for Y-90. Parameter values are: $k_1 = 10^5$ and $k_3 = 1.6 \times 10^{-5}$. The injected activity was 1.85 GBq and the values of k_2 and C_o are 10^{-5} and 10^8 respectively.

Figure 6.7 C: The percent of the total dose contributed by the surface-bound radioactivity as a function of both the time of the treatment and the depth within the tumour, r, for Y-90. Parameter values are: $k_1 = 10^6$ and $k_3 = 0$. The injected activity was 1.85 GBq and the values of k_2 and C_o are 10^{-5} and 10^8 respectively.

Figure 6.7 D: The percent of the total dose contributed by the surface-bound radioactivity as a function of both the time of the treatment and the depth within the tumour, r, for Y-90. Parameter

values are: $k_1 = 10^6$ and $k_3 = 1.6 \times 10^{-5}$. The injected activity was 1.85 GBq and the values of k_2 and C_o are 10^{-5} and 10^8 respectively.

Figure 7.1: Beta spectra of the radionuclides used in this work. I(E) denotes the relative intensity of beta emissions of energy E. Spectra have not been normalized.

Figure 7.2: CSDA spectra for the radionuclides used in this work. C(E) denotes the relative intensity of electrons of energy E at any point in the medium.

Figure 7.3: Single event spectra for surface-bound low energy electrons. Below 50 keV the spectra show a peak at a value of z corresponding to the initial energy of the electrons. At these energies the spectra change rapidly with energy.

Figure 7.4: Single event spectra for low energy electrons in the free radioactivity source geometry.

Figure 7.5: Single event spectra for surface-bound high energy electrons. The spectra change much more slowly at these energies. The peaks appear noisy due to the 50 eV bins used to score energy deposition.

Figure 7.6: Single event spectra for high energy electrons in the free radioactivity source geometry. The peaks are shifted to higher values of z relative to the surface bound geometry due to larger mean path lengths through the target.

Figure 7.7: Illustration of a sample path length through a spherical target volume from a radionuclide bound to the surface of the target.

Figure 7.8: Illustration of weighting system used to calculate radionuclide single event spectra. Monoenergetic single event spectra were calculated at all energies E_{si}. The spectrum at E_{si} is used to represent all electron spectra between energies E_i and E_{i+1}.

Figure 7.9: Radionuclide single event spectra for surface bound radioactivity. Lower energy emitters have a larger frequency mean specific energy per event, $\bar{z}_f$, than high energy emitters due to the more pronounced high z tail.

Figure 7.10: Radionuclide single event spectra for free radioactivity. The value of $\bar{z}_f$ in this geometry is larger than the corresponding value for the surface-bound radioactivity for each radionuclide because of the longer mean path length through the target for this source geometry.

Figure 7.11: Single event spectra for surface-bound 50 keV electrons with cutoff energies of 10 keV and 20 keV. The higher cutoff energy results in an increased number of events that deposit the entire electron energy in the target volume.

Figure 7.12: Peak area as a function of cutoff energy for surface-bound 50 keV electrons. The curve has not completely leveled off at a cutoff energy of 10 keV suggesting that EGSnrc is slightly overestimating the number of events in the 1.9 mGy peak shown in Figure 10.

Figure 7.13: Single event spectra for surface-bound 20 keV electrons with cutoff energies of 10 keV and 15 keV. The higher cutoff energy results in an increased number of events that deposit the entire electron energy in the target volume

Figure 7.14: Peak area as a function of cutoff energy for surface-bound 20 keV electrons. The effects of the cutoff energy are more pronounced at lower electron energies. As the cutoff energy decreases to 10 keV, the area of the 0.75 mGy peak is still decreasing, suggesting that the cutoff energy of 10 keV results in an overestimate of the true peak size.

Figure 7.15: Energy-dependent probability that an electron emitted from the surface of a cell will undergo at least one hard interaction in the cell volume.

Figure 7.16: Specific energy distributions, $f_n(z)$, for Y-90. The mean value of the distributions is given by $n\bar{z}_1$. The x-axis is on a logarithmic scale and has been normalized to the expectation value of $f_1(z)$. The y-axis has been scaled by this normalized energy.

Figure 7.17: Relative spread of specific energy distributions, $f_n(z)$, as a function of n. The relative spread decreases rapidly with increasing n at low n but is decreasing slowly at n = 100.

Figure 7.18: Weighted event spectra for Lu-177. Spectra are shown for N = 1 – 10, 20, 50 and100. N is the number of radioactive atoms per carrier. As N increases, the spectra shift to higher values of $z/\langle z_1 \rangle$ and the relative spread decreases. The spectra are scaled such that the expectation value of $z/\langle z_1 \rangle$ for N = 1 is 1.

Figure 7.19: Weighted event spectra for Cu-67.

Figure 7.20: Weighted event spectra for Re-186.

Figure 7.21: Weighted event spectra for Re-188.

Figure 7.22: Weighted event spectra for Y-90.

Figure 7.23: Mean values of f(z,N) for different radionuclides. The lower energy emitters (Lu-177, Cu-67) clearly deposit significantly more energy per carrier than the high energy emitters (Re-188, Y-90).

List of Abbreviations

BCA	Bifunctional Chelating Agent
Bq	Becquerel
Bs-MAb	Bispecific Monoclonal Antibody
Chol	Cholesterol
Ci	Curie
CSDA	Continuous Slowing Down Approximation
Da	Dalton
DMPE-DTPA	1,2-Dimyristoyl-*sn*-Glycero-3-Phosphoethanolamine-N-
DTPA	
DOTA	tetraazacyclododecane tetraacetic acid
DPK	Dose Point Kernel
DSPC	1,2-Distearoyl-*sn*-Glycero-3-Phosphocholine (DSPC
DSPE-PEG-Biotin	1,2-Distearoyl-*sn*-Glycero-3-Phosphoethanolamine-N-[Biotinyl(Polyethylene Glycol)2000] (Ammonium Salt) (DSPE-PEG-Biotin)
DTPA	Diethylene-triamine-pentaacetate
FAb	Antibody Fragment
FIGO	International Federation of Gynecology and Obstetrics
HAMA	Human Anti-Mouse Antibody
i.p.	Intraperitoneal
i.v.	Intravenous
keV	Kilo Electron Volt
MAb	Monoclonal Antibody
MAC	macrocyclic azacarboxylates
MPS	Mononuclear Phagocyte System
LET	Linear Energy Transfer
MBq	Mega Becquerel
mCi	Milli Curie
MeV	Mega Eelctron Volt
PBS	Phosphate-Buffered Saline
PEG	Polyethylene Glycol
PPV	Positive Predictive Value
RBE	Relative Biological Effectiveness
SEC	Size Exclusion Chromatography
TCP	Tumour Control Probability
$TTCP_{95}$	Time required to produce a TCP of 95

Chapter 1

Thesis Overview

The treatment of late stage ovarian cancer presents an unmet clinical need for women around the world. Ovarian cancer remains one of the deadliest cancers because it is often not diagnosed until the disease has metastasized, making it much more difficult to treat effectively. The work presented in this thesis focuses on the development of a novel variation on the theme of intraperitoneal radionuclide therapy for the treatment of primary or recurrent late stage ovarian cancer. The therapy uses radiolabeled liposomes and bispecific antibodies to target the delivery of radioactivity to cancer cells in the peritoneal cavity. Liposomes were chosen as the delivery vehicle because of their potential to carry significantly more radioactivity per carrier than conventional targeting moieties such as monoclonal antibodies. The experimental component of this work involved the development of a liposome formulation that could be labeled with radioactivity and the demonstration that radioactivity could be selectively delivered to cancer cells that express the ovarian cancer antigen CA-125. Theoretical models were developed to investigate the radiation dosimetry of micrometastases suspended in the peritoneal fluid during this type of therapy.

An introduction to the subject of ovarian cancer is presented in chapter 2. Various topics are surveyed, including ovarian anatomy, disease pathology and staging, prognosis and treatment. Particular attention is paid to the subject of intraperitoneal radionuclide therapy. Within this context there is a discussion of radionuclides of potential use for this type of therapy, their properties and their application in small clinical trials.

Chapter 3 introduces the concepts of the physical interactions of electrons with matter. The development of dose point kernels for beta-emitting radionuclides is illustrated for the simplified case of "straight ahead" electron trajectories using the Continuous Slowing Down Approximation (CSDA) to describe the rate of energy loss by the electron. The chapter also introduces the subject of microdosimetry. The quantity specific energy is described along with some of its associated distributions. Electron dosimetry, both macro and micro, is a subject about which many books have been written. Consequently, the scope of this chapter is limited to those particular areas of dosimetry that are applied in subsequent thesis chapters.

The details of the therapeutic design are presented in chapter 4. The concepts of the liposome and the bispecific antibody are introduced. The goal of the experimental work presented in this chapter was to produce a liposome formulation that could be labeled with radioactivity and used in conjunction with bispecific antibodies to selectively bind to ovarian cancer cells that express the antigen CA-125 on their surfaces. The chapter details the labeling procedures used to bind atoms of Y-90 to the surface of liposomes and the purification procedure used to separate free Y-90 from Y-90 bound to the liposomes. In addition, selected images are presented from the confocal microscopy work performed to visualize the selective targeting of liposomes to cells expressing CA-125.

Dosimetry calculations in the remaining chapters of the thesis are presented in the context of this intraperitoneal radionuclide therapy. In chapter 5, the dose-rate profiles through micrometastases of various sizes are presented for six different radionuclides of potential use in radionuclide therapy (Cu-67, I-131, Re-186, P-32, Re-188, Y-90). Profiles are presented for two source geometries: radioactivity uniformly distributed on the surface of the micrometastases and a large radioactive bath in which the micrometastases are submerged. The work presented in this chapter was published in 2003 (Syme *et al.* 2003a)

Chapter 6 expands on the dosimetry model of chapter 5 to include dynamic processes that will affect the integrated dose to micrometastases in the peritoneal cavity. In particular, a simple tumour control probability model is developed that incorporates the effects of biological processes such as liposome-CA-125 binding kinetics, antigen shedding and the escape of radioactivity from the peritoneal cavity during treatment. A system of differential equations is used to describe the behaviour of the population of liposomes over the course of the treatment and the dose-rate profiles calculated in chapter 5 are used to calculate integrated tumour dose and time-dependent tumour control probabilities. The majority of the work presented in chapter 6 was published in 2003 (Syme *et al.* 2003b)

The dosimetry of single cells is given special consideration in chapter 7. A microdosimetric approach is taken to study the patterns of energy deposition in a small target volume by beta emitters. Monoenergetic single event spectra for electrons are shown for a number of electron energies for both of the source geometries mentioned previously. Radionuclide single event spectra produced from the monoenergetic spectra are presented for five different radionuclides (Lu-177, Cu-67, Re-186, Re-188, Y-90). A significant portion of the work presented in chapter 7 was published in 2004. (Syme *et al.* 2004)

A summary of the work presented in the thesis is given in chapter 8. Concluding remarks about the field of research and future directions for this particular project are outlined.

References

Syme A M, Kirkby C, Riauka T A, Fallone B G and McQuarrie S A. 2004 Monte Carlo investigation of single cell beta dosimetry for intraperitoneal radionuclide therapy. *Phys. Med. Biol.* **49** 1959 – 1972.

Syme A M, McQuarrie S A and Fallone B G. 2003a Beta Dose-Rate Distributions In Microscopic Spherical Tumours For Intraperitoneal Radioimmunotherapy. *Int. J. Radiat. Oncol. Biol. Phys.* **56** 1495 – 1506.

Syme A M, McQuarrie S A, Middleton J W and Fallone BG. 2003b Dosimetric Model For Intraperitoneal Targeted Liposomal Radioimmunotherapy Of Ovarian Cancer Micrometastases. *Phys. Med. Biol.* **48** 1305 – 1320.

Chapter 2

Ovarian Cancer: Pathology, Prognosis, Treatment

The information presented in this section is a general overview of the subject of ovarian cancer. This includes a brief summary of aspects of the disease such as epidemiology, pathology, treatment and prognosis. Of the treatment modalities, intraperitoneal radionuclide therapy is given special consideration because the majority of the work presented in subsequent chapters is based on a variation this theme.

2.1 General Information

The ovaries are two nodular organs located one on either side of the uterus with respect to the lateral wall of the pelvis (Gray, 2000) (see Figure 2.1). They are approximately 4 cm in length, 2 cm in width and 0.8 cm in thickness. In premenopausal women they have a flattened ovoid form with deep crevices.

They become sclerotic, atrophied and smooth after menopause (del Regato *et al.* 1985). There is an extensive network of lymphatics that surrounds the graafian follicles within the ovaries and the collecting trunks extend upwards to the lower pole of the kidney and eventually terminate in the lumboaortic lymph nodes (del Regato *et al.* 1985). The ovaries are the production sites for the ova and play an important role in sexual development as part of the endocrine system. These organs produce the sex hormones estrogen, progesterone and testosterone.

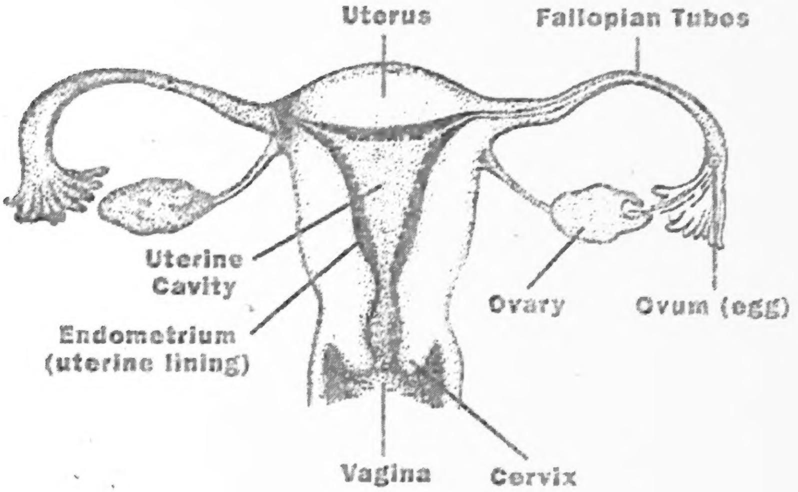

Figure 2.1: Diagram of the female reproductive system. Figure taken from an update to the FDA Publication No. (FDA) 94-1215 found at http://www.fda.gov/fdac/reprints/ots_mens.html.

Ovarian cancer accounts for 4 – 5% of all cancers in women in the United States (Whitehouse *et al.* 2003, Berek *et al.* 1993) and 6% of all cancer deaths in women. In the year 2004, the National Cancer Institute of Canada (2004) expects 2300 new cases of ovarian cancer and 1550 deaths in Canada. In terms of malignancies of the female genital tract, ovarian cancer accounts for 25% of the cancers and 50% of the deaths, making it the deadliest of the gynecologic malignancies (Berek *et al.* 1993). As with many cancers, ovarian cancer is most prevalent amongst the elderly. Approximately 85 – 90% of ovarian cancers are found in postmenopausal women. The median age for epithelial ovarian cancer is between 60 and 65 years and less than 1% of these cancers are found in women less than 30 years of age (Berek *et al.* 1993).

Causes of ovarian cancer have not been definitively identified. However, there is evidence to support certain theories. For example, it has been hypothesized that the ovaries could be exposed to carcinogens that have entered the peritoneal cavity through the lower genital canal and spread through the uterus and the fallopian tubes (Berek *et al.* 1997). This claim is supported by studies that link asbestos-contaminated talc, used in douche and contraceptive products, with the development of epithelial tumours (Cramer *et al.*, 1982). The majority of cases of ovarian cancer appear to be sporadic. Only 3 – 4% of all cases occur in individuals with a family history of the disease. Risk factors that result in predisposition to ovarian cancer include: early menarche and late menopause, high fat diet, Caucasian descent and nulliparity. Women who have taken the estrogen-progesterone oral contraceptive for as little as one year demonstrate a lower incidence of ovarian cancer than women who have not taken the preparation at all. Geographic location is also an important factor. The incidence of ovarian cancer in western countries such as the United States and Great Britain is 3 to 7 times higher than it is in Japan (Berek *et al.* 1993)).

Ovarian cancer, while localized to the ovaries, is typically difficult to diagnose. In such cases, the disease tends to be either asymptomatic or present non-specific symptoms that result from the enlarging of the ovaries. These symptoms can include abdominal distension, pressure and other gastrointestinal discomforts (Berek *et al.* 1997). Observation of tumours is often possible using transvaginal or transabdominal ultrasonography. The use of radiographic techniques such as abdominal x-rays, computed tomography and magnetic resonance imaging is not necessary for the diagnosis of ovarian cancer, however, in cases where ascites are present but a pelvic mass is not, these techniques can be used to exclude tumours from other primary sites (Berek *et al.* 1993).

There is currently no single, reliable screening tool available for early stage ovarian cancer. Urban *et al.* (2003) suggest that a cost-effective, efficacious program would be difficult to construct. Desirable characteristics of such a program would include a sensitivity (true positive fraction) of at least 80% and a nearly perfect specificity (true negative fraction). The requirement for near perfect specificity is to minimize the number of unnecessary exploratory surgeries. The positive predictive value (PPV) of a screening test describes the probability that the disease is present if the test is positive. A PPV of 10% would result in a maximum of 10 surgeries for every cancer found. To achieve this PPV with a sensitivity of 80%, the specificity must be 99.6% (Urban *et al.* 2003).

Studies have investigated the potential of a blood test to measure the serum content of a high molecular weight glycoprotein called CA-125 that is found in 97% of patients with late stage ovarian cancer (Berek *et al.* 2003). This protein is often expressed on the surface of ovarian cancer cells and then shed from the surface into the bloodstream. There have been extensive efforts to characterize the structure of this protein, however this process is not yet complete (Whitehouse *et al.* 2003). Definitive identification of the protein's function has also proved elusive. It has been demonstrated that the shedding of CA-125 from the cell is dependent on the phosphorylation status of the protein and that the protein has a calcium-dependent autoproteolytic activity (Whitehouse *et al.* 2003, O'Brien *et al.* 1998). Elevated CA-125 levels correlate very well with late stage ovarian cancer and have proven to be of good predictive value for recurrent disease progression and prognosis, however, questions about its value as a screening tool remain (Perkins *et al.* 2003). One study found the test to have a reasonable sensitivity of 50% for stage I tumours and 90% in stage II. The problems with the test arise in its specificity. Ovarian cancer is not the only condition that results in elevated levels of CA-125. Benign disorders including ovarian cysts, endometriosis and pelvic inflammatory disease can result in elevated CA-125 levels as can the first trimester of pregnancy. Furthermore, CA-125 levels have been shown to vary during the menstrual cycle. Finally, not all ovarian tumours express the antigen CA-125. One study found the CA-125 blood test to have a PPV of 3.43% (del Regato *et al.* 1985). Anderiesz *et al.* (2003) suggest that annual CA-125 measurements in conjunction with transvaginal ultrasound would be prudent for women at higher risk for ovarian cancer because this combination of modalities provides the highest specificity and positive predictive value.

A second standard screening technique is transvaginal ultrasound. In a review of existing screening data, Karlan (1997) remarked that sensitivities approaching 100% were possible, but the technique was limited by insufficient specificities. Improvements in specificities are being realized with the use of colour Doppler imaging (Karlan, 1997). A study by Tailor *et al.* (2003) found an overall ultrasound sensitivity of 92% with a specificity of 97.8%. Furthermore, they demonstrated that ultrasound requisition based on threshold levels of serum CA-125 can lead to a reduced detection rate for early stage cancers.

Definitive diagnosis of ovarian cancer is made by surgical exploration (Urban *et al.* 2003). After careful examination of the pelvic region, the surfaces of the peritoneal cavity and associated lymphatics, staging of the disease is determined using the system developed by the International Federation of Gynecology and Obstetrics (FIGO) (Heintz *et al.*, 2001). Table 2.1 contains the details of this system. Essentially, Stage I tumours are limited to the ovaries, Stage II describes tumours involving one or both ovaries with pelvic extension, Stage III involves the ovaries with peritoneal implants and/or certain lymph nodes and Stage IV involves the ovaries and distant metastasis. Typically, ovarian tumours metastasize as a result of the exfoliation of cells from the primary tumour into the peritoneal fluid. The cells can then implant on the surfaces of the peritoneal cavity and develop into secondary tumours. Cytologic studies of peritoneal ascitic fluids reveals the presence of single cells as well as clusters containing hundreds of cells (Wong *et al.* 2002, Yanoh *et al.* 1999). Lymphatic dissemination is also a common route of spread. Although only 5 – 10% of Stage I and Stage II tumours involve the retroperitoneal nodes, that number increases to between 42% and 78% for Stage III tumours. Less common are metastases involving the blood, bone and central nervous system. Typically these routes involve long term survivors of primary ovarian tumours (Berek *et al.* 1993).

Table 2.1: FIGO Staging System For Ovarian Cancer*

Stage I	Growth limited to the ovaries
Ia	Growth limited to one ovary; no ascites present containing malignant cells. No tumour on the external surface; capsule intact.
Ib	Growth limited to both ovaries; no ascites present containing malignant cells. No tumour on the external surfaces; capsules intact
Ic	Tumour either Stage Ia or Ib, but with tumour on surface of one or both ovaries, or with capsule ruptured, or with ascites present containing malignant cells, or with positive peritoneal washings
Stage II	Growth involving one or both ovaries with pelvic extension
IIa	Extension and/or metastases to the uterus and/or tubes
IIb	Extension to other pelvic tissues
IIc	Tumour either Stage IIa or IIb, but with tumour on surface of one or both ovaries; or with capsule(s) ruptured; or with ascites present containing malignant cells or with positive peritoneal washings

Stage III	Tumour involving one or both ovaries with histologically confirmed peritoneal implants outside the pelvis and/or positive retroperitoneal or inguinal nodes. Superficial liver metastases equals Stage III. Tumour is limited to the true pelvis, but with histologically proven malignant extension to small bowel or Omentum
IIIa	Tumour grossly limited to the true pelvis, with negative nodes, but with histologically confirmed microscopic seeding of abdominal peritoneal surfaces, or histologically proven extension to small bowel or mesentery
IIIb	Tumour of one or both ovaries with histologically confirmed implants, peritoneal metastasis of abdominal peritoneal surfaces, none exceeding 2 cm in diameter; nodes are negative
IIIc	Peritoneal metastasis beyond the pelvis > 2 cm in diameter and/or positive retroperitoneal or inguinal nodes
Stage IV	Growth involving one or both ovaries with distant metastases. If pleural effusion is present, there must be positive cytology to allot a case to Stage IV. Parenchymal liver metastasis equals Stage IV

* Taken from Heintz *et al.* (2001)

The prognosis for ovarian cancer patients varies significantly depending on the type of cancer and stage at which it is diagnosed. In all cases, early diagnosis increases the chances of survival, however many cases are not diagnosed until the cancer has progressed to Stage III or IV. Table 2.2 details an observed five year survival for four of the most common ovarian cancers (del Regato *et al.* 1985). More general survival statistics give five year survival rates of 90, 70 and 20% for tumours detected in stage I, II and III/IV respectively (Whitehouse *et al.* 2003).

2.2 Treatment

The first step in a treatment protocol for an ovarian cancer patient is surgery. For Stage Ia and Ib patients with low grade tumours, this will usually involve an abdominal hysterectomy and bilateral salpingo-oophorectomy. If only one ovary is involved and the patient is still in her childbearing years, the uterus and second ovary can be preserved. No additional treatment is usually necessary in this group. Additional therapy is generally prescribed for all other tumours (del Regato *et al.* 1985). Chemotherapy is the most common form of treatment in these cases. A protocol might involve platinum agents such as cisplatin and carboplatin, the tubulin-stabilizing agent paclitaxel or a combination of drugs. A summary of the findings of several large clinical trials presented by Trimble *et al.* (2003) suggested that carboplatin/paclitaxel was as effective as cisplatin/paclitaxel. The authors recommended that carboplatin/paclitaxel should be the standard in future clinical trials against which novel therapeutics or drug combinations should be tested.

Table 2.2: Survival-Rate Of Epithelial Ovarian Cancers

	5-Year Survival (%)		
Type	**Stage I**	**Stage II**	**Stage III/IV**
Serous	70	39	6
Mucinous	84	68	17
Endometrioid	73	79	28
Solid	58	24	2

External beam radiotherapy is a second treatment modality, though its application is limited. It is not generally appropriate for patients with late stage and large-volume residual disease, but it has been shown to be curative in some patients with early stage or minimal residual disease (MacGibbon *et al.* 1999). The treatment is designed to cover the entire peritoneal cavity. Dose to the upper abdomen is usually limited to 2500 to 2800 cGy in 100 to 120 cGy daily fractions. The limit is a compromise between the need to treat microscopic disease and complications arising in healthy liver tissue. The pelvic region is given a boost in 180 to 220 cGy fractions to a total of 4500 to 5000 cGy (Berek *et al.* 1997).

Chemotherapy can often result in tumour regression but experience has shown that it is usually temporary. Initial response rates of 60 – 80% have been reported (MacGibbon *et al.* 1999) in cisplatin-based combination treatment regimens, however, 40 – 60% of these patients will experience recurrent disease (MacGibbon *et al.* 1999). Investigations involving combinations radio and chemotherapy have not yet produced a treatment program with significant efficacy enhancement (del Regato *et al.* 1985). There is no standard treatment for recurrent ovarian cancer (Baker, 2003). Patients might undergo further radiotherapy, chemotherapy or a combination of the two. Another option is enrollment in a clinical trial of a novel therapeutic agent.

2.3 Intraperitoneal Radionuclide Therapy

Intraperitoneal (i.p.) radionuclide therapy is a treatment modality that involves the administration of an unsealed radioactive source into the peritoneal cavity for the purpose of treating malignant disease. The targets of i.p. radionuclide therapy are two-fold: single cells and clusters of cells that are floating in the peritoneal fluid and seeded tumour nodules that are found on the surfaces of the peritoneal cavity. This type of therapy was practiced for palliative purposes as early as 1945 (Croll *et al.* 1979). Radioactive gold (Au-198) colloid was used to treat malignant effusions in the peritoneal cavity. This radionuclide produced some successful results but also resulted in a number of serious complications and deaths (Kolstad *et al.* 1977). These were attributed to factors such as the short physical half-life of the radionuclide and the high energy (412 keV) gamma ray emitted in 5% of Au-198 decays (Rosenshein 1983). Investigators were subsequently drawn to P-32 for its high energy ($E_{\beta max} = 1.71$ MeV) beta emission and lack of gamma emissions (Rosenshein 1983). In a study comparing cisplatin chemotherapy with i.p. radionuclide therapy and whole-abdomen external beam irradiation, Vergote *et al.* (1992a) observed similar survival rates in all groups. They concluded that cisplatin was a more appropriate choice for therapy because the P-32 produced a higher incidence of bowel complications. A recent study by Young *et al.* (2003) confirmed these findings. There was no statistically significant difference in survival rates between patients receiving the chemotherapy compared to those receiving i.p. P-32. They did observe a difference in the ten year cumulative recurrence rates. Patients with stage I cancer had recurrence rates of 28% and 35% with chemotherapy and i.p. P-32 respectively. In addition, problems with radioactivity distribution within the peritoneal cavity and small bowel perforation in the i.p. P-32 group led Young *et al.* to conclude that chemotherapy was a more attractive treatment option. Today, research into i.p. administration of radioactivity for the treatment of ovarian cancer continues to evolve; aspiring to the goal of lethality for tumour tissue with minimal consequences for the surrounding healthy tissue. Efforts to spare healthy tissue have resulted in developments such as more appropriate radionuclide selection, improved retention of radioactivity in the cavity and greater tumour targeting selectivity.

A typical i.p. treatment protocol might involve a peritoneal lavage to drain as much fluid as possible from the cavity prior to the administration of the radioactive sample. Next a small volume of a very high specific activity solution would be injected into the cavity along with a large volume (on the order of 1 litre) of a sterile, aqueous solution such as saline. The purpose of the saline is to maximize the uniformity of the source distribution within the peritoneal cavity (Buijs *et al.*, 1998, Alvarez *et al.*, 1997, Kolstad *et al.*, 1977). Today, with improved surgical procedures, i.p. radionuclide therapy has the potential to expand its role from palliative treatment to life-prolonging and, in certain circumstances, curative therapy.

A number of beta-emitting radionuclides have been identified as promising candidates for this type of therapy, and alpha emitters are also under investigation (Bakri *et al.* 1984, Vergote *et al.* 1992b, Vergote *et al.* 1992c, Bloomer *et al.* 1984, Alvarez *et al.* 1997, Rotmensch *et al.* 1997, Buijs *et al.* 1998). Some of these radionuclides and their physical properties are presented in Table 2.3. Selection of an appropriate radionuclide is dependent on a number of factors. These include the physical half life of the radionuclide, the stability of the pharmaceutical preparation *in-vivo*, the type and energy of the particle emissions, the biodistribution kinetics of the radioactivity *in-vivo* and the tumour pathology. In addition to selecting a suitable radionuclide, it is also advantageous to find a preparation that will remain localized in the peritoneal cavity. Studies have shown that antibodies and colloids tend to escape the cavity, resulting in significant uptake in other tissues (Vergote *et al.* 1992b, Alvarez *et al.* 1997, Buijs *et al.* 1998, Srivastava *et al.* 2001). To combat this problem, investigators have turned to larger carriers such as microspheres. Biodistribution studies have verified that these preparations have less chance of escaping the peritoneal cavity (Vergotte *et al.* 1992b).

Table 2.3: Physical properties of alpha and beta emitting radionuclides of potential use in radionuclide therapy

Radionuclide	**Half-Life (hours)**	**Emission Type**	**Energy* (MeV)**	**Branching Ratio (%)**
Bi-212	1.01	α	6.09	9.8
		α	6.05	25.1
		β	0.832	55.5
		β	0.532	4.4
		β	0.229	1.4
		β	0.191	1.9
Pb-212	10.64	β	0.173	11.8
		β	0.095	82.5
		β	0.042	5.2
		γ	0.239	43.3
Bi-213	0.76	α	5.869	1.9
		β	0.492	65.9
		β	0.320	31.0
		γ	0.441	26.1
At-211	7.21	α	5.87	41.8
Lu-177	159.53	β	0.149	79.4
		β	0.112	9.0
		β	0.048	11.6
		γ	0.208	10.4
		γ	0.113	6.2
Cu-67	61.83	β	0.189	20.0
		β	0.154	22.0
		β	0.121	57.0
		β	0.051	1.1
		γ	0.185	48.7
I-131	192.5	β	0.283	0.5
		β	0.192	89.9
		β	0.097	7.3
		β	0.087	0.7
		β	0.069	2.1
		γ	0.637	7.2
		γ	0.365	81.7
		γ	0.284	6.1
Re-186	89.24	β	0.359	71.0
		β	0.306	21.5
		γ	0.137	9.5
P-32	342.31	β	0.695	100

Re-188	16.98	β	0.795	70.0
		β	0.729	26.3
		β	0.528	1.8
		γ	0.155	15.6
Y-90	64.10	β	0.934	100

Information in this table was taken from the website of the National Nuclear Data Center (NNDC); Brookhaven National Laboratory (http://www.nndc.bnl.gov/mird/).

* beta energies are given as the average energy of a particular beta group.

Alpha-emitters are interesting candidates for radionuclide therapy. The particles emitted by these radionuclides tend to have energies in the range of 4 – 8 MeV and they will deposit all of their energy within approximately 50 – 100 μm of their point of origin (Imam 2001). The linear energy transfer (LET) of these particles is on the order of 100 keV/μm (McDevitt *et al.* 1998). This is significantly larger than the LET of a high energy beta emitter such as Y-90, whose mean LET is approximately 0.2 keV/μm (McDevitt *et al.* 1998). The correspondingly large relative biological effectiveness (RBE) of alpha particles has resulted in extensive efforts to find a suitable alpha emitter for a radionuclide therapy. To date, few radionuclides have met appropriate selection criteria. Bismuth-213 has been used in humans (McDevitt *et al.* 1999) and two potential candidates for future clinical use are Bi-212 and At-211. The short physical half-lives of Bi-212 and Bi-213 might render these radionuclides incompatible with some intravenous (i.v.) administration applications since the time required to achieve therapeutic quantities of the agent in solid tumour tissue would result in significant decay of the radionuclide (Mattes 2002). One possible solution to this problem involves labeling the pharmaceutical compound with Pb-212, the parent of Bi-212. This radionuclide has a physical half-life of 10.6 hours which is more commensurate with antibody uptake kinetics and would serve as an "*in-vivo*" generator of the therapeutic alpha emitter Bi-212. In an i.p. therapy, the short physical half-life is less of an issue because the radionuclide is immediately localized to the same compartment as the tumour tissue requiring treatment.

Astatine-211 must be produced using a particle accelerator which, in conjunction with its short half-life, suggests that its use as a therapeutic agent could be limited to special situations.

Some alpha-emitters are the parents in decay chains that emit numerous other alpha particles. Bismuth-213 is an example of such a radionuclide. In addition to the therapeutic alpha emitted in 1.9% of decays (see table 2.3), other alpha and beta particles are emitted as various daughter and granddaughter radionuclides also decay. This can be problematic for several reasons. The energies associated with the alpha decay process are much greater than the energy stored in chemical bonds. This can result in the detachment of the daughter radionuclide from its pharmaceutical carrier. Such a separation might also result if the chemical properties of the daughter are incompatible with the carrier. The free radioactivity can then diffuse into the circulatory system which can in turn result in significant bone marrow dose as many alpha-emitting radionuclides are bone-seeking, heavy elements.

In terms of an i.p. radionuclide therapy, alpha-emitters appear to be useful tools, particularly for single cells and small clusters of cells in the peritoneal fluid. Unfortunately, many patients who are candidates for this type of therapy will also have macroscopic tumour nodules seeded on the walls of the peritoneal cavity due to incomplete surgical tumour debulking. Thus, even in the best of cases, an i.p. therapy might have to treat tumours that are orders of magnitude larger than the range of alpha particles. One of the major problems associated with radionuclide therapy is the heterogeneity of the radioactivity distribution within a tumour (Humm *et al.* 1990, Jain *et al.* 1988, Roberson *et al.* 1992). The short range of alpha particles in tissue suggests that regions of tumour without therapeutic quantities of radionuclide will survive the treatment and continue to proliferate. This problem would be exacerbated in an i.p. therapy because tumour penetration from the peritoneal cavity could be a very slow process, particularly for large molecular-weight carriers such as liposomes.

Recent *in-vivo* studies on i.p. tumour-bearing animals are numerous and some studies have progressed to stage I and II clinical trials on humans. In humans, studies have been carried out with the following radionuclides: I-131, Y-90, Re-186, P-32 and Lu-177. Iodine-131 has been used extensively in radionuclide therapy research, however, it is not the ideal candidate for these types of therapies. Its use has been justified by its cheap cost and the abundance of literature available on labeling procedures (Srivastava *et al.* 2001). Iodine-131 emits numerous betas but its most abundant beta group has an endpoint energy of 606 keV and is emitted in 89.9% of decays. The energetic gamma rays emitted during I-131 decay are not therapeutically beneficial but do present a hazard to healthy tissue in the body. Furthermore, its 8 day half-life is perhaps longer than desirable for certain applications. Buijs *et al.* (1998) administered diagnostic quantities of I-131-labeled cMOv antibody to ovarian cancer patients for the purpose of predictive dosimetry for therapeutic quantities. Calculations were based on scintigraphic imaging, biopsy gamma counting and blood and urine analysis. They investigated both i.v. and i.p. administration. With dose estimates based on the MIRD formalism and the assumption of a maximum acceptable marrow dose of 2 Gy, the investigators concluded that therapeutic activities of I-131 should be injectable without normal tissue toxicity. Their calculations suggested that 4.1 GBq i.p. and 3.5 GBq i.v. could produce 18 Gy and 8 Gy respectively to a 1 g tumour in the peritoneal cavity.

Yttrium-90 is seen as an attractive candidate for radionuclide therapy because of its high energy beta emission ($E_{\beta max}$ = 2.23 MeV) and lack of gamma emissions. It has a half-life of 2.7 days. The high beta energy results in dose deposition at distances up to 11 mm from the source. This is seen as greatly beneficial in treating macroscopic disease where uniform activity distribution is not achieved. The lack of gamma emissions from Y-90 means that dose calculations must be based on bremsstrahlung imaging procedures which have much poorer resolution than gamma images. Maraveyas *et al.* (1994) examined the pharmacokinetics and toxicity of Y-90-labeled antibodies in 19 patients. Yttrium was bound to the antibodies via the chelating agent CITC-DTPA and injected activities ranged from 15 – 34 mCi. Approximately 30% of the injected activity was found in the blood 48 hours after injection and 18% of the injected activity was cumulatively excreted in the urine after 96 hours. In all patients, bone marrow toxicity was observed after 4 weeks as was recovery after treatment at 56 days. When the injected activities were scaled by the patients' body surface areas, a reasonably linear correlation was observed between the injected activity and the degree of bone marrow toxicity. This led to the conclusion that a maximum activity of 18 – 18.5 mCi / m^2 should be injected. The antibodies used in this experiment were mouse antibodies and all of the patients tested for a HAMA (human anti-mouse antibody) response were positive. All but one were also positive for an antibody response against the chelating agent. These data suggest that repetitive injection protocols for prolonged tumour growth delay would be difficult using this approach.

Rhenium-186 has a half-life of 3.8 days and has two primary beta emissions in its decay shceme. The first is a 1.07 MeV maximum energy beta in 71.0% of decays and the other is a 0.934 MeV maximum energy beta in 21.5% of decays. It also emits a 137 keV gamma ray in 9.5% of decays. This relatively low energy gamma emission facilitates activity distribution assessment via gamma camera imaging. Jacobs *et al.* (1993) conducted a dose escalation study involving murine monoclonal antibodies labeled with Re-186 in 17 women with persistent or recurrent ovarian cancer after platinum-based chemotherapy. Biodistribution measurements indicated that radioactivity instilled into the peritoneal cavity was cleared with a mean half-life of 48 hours. Serum activity levels peaked between 24 and 72 hours post administration and by the sixth day, an average of 56% of the injected activity was excreted in the urine. The study found severe myelosuppression in two patients receiving 150 mCi/m^2 but overall toxicity was deemed acceptable. Even at 150 mCi/m^2, marrow dose was calculated at 110 cGy and whole body dose was less than 200 cGy. Second look laparotamy revealed decreased tumour size in those patients who entered the trial with residual disease measuring less than 5 mm. All patients developed a HAMA response.

The other rhenium isotope of interest for radionuclide therapies is Re-188. This radionuclide has a half-life of 17 hours and has three principal beta emissions. The endpoint energies and branching ratios are 1.487, 1.965 and 2.12 MeV and 1.8, 26.3 and 70.0% respectively. To date, Re-188 has not found application in i.p. therapy, however it has been used in intravascular therapies to prevent restenosis (Hang *et al.* 2003) and in synovectomy procedures in animals (Wang *et al.* 2001). Investigators have developed procedures to label antibodies and microspheres with Re-188 so extension of its application to i.p. therapy will likely occur in the near future.

Phosphorus-32 emits beta particles with an endpoint energy of 1.708 MeV in 100% of decays. It has no gamma emissions. As mentioned previously, it has been used extensively in i.p. radionuclide therapies for the treatment of late stage ovarian cancer, primarily in colloid form. Phosphate colloids are small, insoluble particles that can plate out on peritoneal cavity wall surfaces (Croll *et al.* 1979).

Meredith *et al.* (1996) performed a phase I clinical trial in which 12 women were treated with Lu-177-labeled antibodies. Lu-177 has a half-life of 6.7 days and three principal beta groups. The endpoint energies are 498, 385 and 177 keV with intensities of 79.4, 9.0 and 11.6% respectively. Injected activities did not exceed 30 mCi/m^2 and at these activities, the maximum tolerated dose was not reached. Calculated marrow doses did not exceed 54 cGy. Post treatment follow up revealed that most of the patients with gross disease at the time of treatment had tumours that progressed though one saw a reduction in tumour volume of more than 50%. Three of four patients with microscopic disease at the time of treatment were disease free 18 months post treatment.

From these and other studies, two important conclusions can be reached regarding intraperitoneal radionuclide therapies. First, the escape of radioactivity from the peritoneal cavity renders marrow dose one of the primary dose limiting factors in these therapies. Secondly, the size and amount of residual disease at the time of administration is an extremely important prognostic factor.

Macey *et al.* (1999) analyzed the pharmacokinetic data from a study involving the i.p. administration of Lu-177-labeled antibodies. With the assumption that the kinetics of the antibodies were independent of the radionuclide bound to them, the investigators employed a model developed by Sgouros (1993) to determine the maximum injectable activity that would keep the marrow dose below 200 cGy. These activities were: 58 mCi I-131, 34 mCi Y-90, 70 mCi Re-186, 169 mCi Re-188, 106 mCi Lu-177 and 110 mCi Ho-166. The significantly larger activity of Re-188 was attributed to the radionuclide's short physical half-life (17 hours). The peak serum activity levels in the original Lu-177 data were observed two days after administration. With its short half-life, only 14% of the original Re-188 activity remains at the 48 hour mark.

The size and number of tumour nodules that remain at the time of administration of a radiopharmaceutical preparation is of critical importance in terms of prognosis. Invariably, clinical trials have found that macroscopic residual disease (greater than 2 cm) after surgical tumour debulking results in very poor survival, whereas significant improvement in reponse can be achieved when surgery is able to leave only minimal residual disease (Epenetos *et al.* 1987, Ward *et al.* 1988, Stewart *et al.* 1989).

References

Alvarez RD, Partridge EE, Khazaeli MB, Plott G, Austin M, Kilgore L, Russell CD, Liu T, Grizzle WE, Schlom J, LoBuglio AF and Meredith RF 1997 Intraperitoneal Radioimmunotherapy Of Ovarian Cancer With ^{177}Lu-CC49: A Phase I/II Study. *Gynecol. Oncol.* **65** 94-101.

Anderiesz C and Quinn M A. 2003 Screening for Ovarian Cancer. *Med. J. Australia.* **178** 655 – 656.

Baker V V. 2003 Salvage Therapy For Recurrent Epithelial Ovarian Cancer. *Hematol. Oncol. Clin. N.* **17** 977 – 988.

Bakri YN, Given FT 1984 Radioactivity In Blood And Urine Following Intraperitoneal Instillation Of Chromic Phosphate In Patients With And Without Ascites. *Am. J. Obstet. Gynecol.* **150** 184-188.

Berek J S, Dembo A and Ozols R F. 1993 Cancer Medicine, 3rd Edition (Holland, Frei, Bast *et al.* eds). Section XXXI-5, pp1659 – 1690. Lea & Febiger, Philadelphia.

Berek J S, Dorigo O, Schultes B and Nicodemus C. 2003 Specific Keynote: Immunological Therapy For Ovarian Cancer. *Gynecol. Oncol.* **88** S105 – S109.

Berek J S, Thomas G M and Ozols R F. 1997 Cancer Medicine, 4th Edition (Holland, Bast, Morton *et al.* eds). Chapter 133, pp 2289 – 2326. Williams and Wilkins, Baltimore.

Bloomer W D, McLaughlin W H, Lambrecht R M, Atcher R W, Mirzadeh S, Madara J L, Milius R A, Zalutsky M R, Adelstein S J and Wolf A P. 1984 ^{211}At Radiocolloid Therapy: Further Observations And Comparison With Radiocolloids Of ^{32}P, ^{165}Dy and ^{90}Y. *Int. J. Radiat. Oncol. Biol. Phys.* **10** 341 – 348.

Buijs WC, Tibben JG, Boerman OC, Molthoff CF, Massuger LF, Koenders EB, Schijf CP, Siegel JA and Corstens FH 1998 Dosimetric Analysis Of Chimeric Monoclonal Antibody cMOv18 IgG In Ovarian Carcinoma Patients After Intraperitoneal And Intravenous Administration. *Eur. J. Nucl. Med.* **25** 1552-1561.

Cramer D W, Welch E R, Scully R E and Wojciechowski C A. 1982 Ovarian Cancer and Talc: A Case Control Study. *Cancer* **50** 372 – 376.

Croll M N and Brady L W. 1979 Intracavitary Uses Of Colloids. *Semin. Nucl. Med.* **IX** 108 – 113.

del Regato J A, Spjut H J and Cox J D. 1985 Ackerman and del Regato's Cancer. Chapter 16, pp 749 – 776. The C. V. Mosby Company, St. Louis.

Epenetos A A, Munro A J, Stewart S, Rampling R, Lambert H E, McKenzie C G, Soutter P, Rahemtulla A, Hooker G, Sivolapenko G B, Snook D, Courtenay-Luck N, Dhokia B, Krausz T, Taylor-Papadimitriou J, Durbin H and Bodmer W F. 1987 Antibody-Guided Irradiation Of Advanced Ovarian Cancer With Intraperitoneally Administered Radiolabeled Monoclonal Antibodies. *J. Clin. Oncol.* **5** 1890 – 1899.

Gray H. 2000 *Anatomy of the Human Body.* Lea & Febiger, Philadelphia. Bartleby.com. www.bartleby.com/107/.

Hang C L, Fu M, Hsieh B B, Leung S W, Wu C J, Yip H K and Ting G. 2003 Intracoronary Beta-Irradiation With Liquid Rhenium-188: Results Of The Taiwan Radiation In Prevention Of Post-Pure Balloon Angioplasty Restenosis Study. *Chest.* **124** 1284 – 1293.

Heintz A P M, Odicino F, Maisonneuve P, Beller U, Benedet J L, Creasman W T, Ngan H Y S, Sideri M and Pecorelli S. 2001 Carcinoma of the Ovary. *J. Epidemiol. Biostat.* **6** 107 – 138.

Humm J L and Cobb L M. 1990 Nonuniformity Of Tumor Dose In Radioimmunotherapy. *J. Nucl. Med.* **31** 75 – 83.

Imam S. 2001 Advancements In Cancer Therapy With Alpha-Emitters: A Review. *Int. J. Radiat. Oncol. Biol. Phys.* **51** 271 – 278.

Jacobs A J, Fer M, Su F M, Breitz H, Thompson J, Goodgold H, Cain J, Heaps J and Weiden P. 1993 A Phase I Trial Of A Rhenium 186-Labeled Monoclonal Antibody Administered Intraperitoneally In Ovarian Carcinoma: Toxicity And Clinical Response. *Obstet. Gynecol.* **82** 586 – 593.

Jain R K and Baxter L T. 1988 Mechanisms Of Heterogeneous Distribution Of Monoclonal Antibodies And Other Macromolecules In Tumors: Significance Of Elevated Interstitial Pressure. *Cancer Res.* **48** 7022 – 7032.

Karlan B Y. 1997 The Status Of Ultrasound And Color Doppler Imaging For The Early Detection Of Ovarian Carcinoma. *Cancer Invest.* **15** 265 – 269.

Kolstad P, Davy M and Hoeg K. 1977 Individualized Treatment Of Ovarian Cancer. *Am. J. Obstet. Gynecol.* **128** 617 – 625.

Macey D J and Meredith R F. 1999 A Strategy To Reduce Red Marrow Dose For Intraperitoneal Radioimmunotherapy. *Clin. Cancer Res.* **5** 3044s – 3047s.

MacGibbon A, Bucci J, MacLeod C, Solomon J, Dalrymple C, Firth I and Carter J. 1999 Whole Abdominal Radiotherapy Following Second-Look Laparotomy For Ovarian Carcinoma. *Gynecol. Oncol.* **75** 62 – 67.

Maraveyas A, Snook D, Hird V, Kosmas C, Meares C, Lambert H and Epenetos A A. 1994 Pharmacokinetics And Toxicity Of An Yttrium-90-CITC-DTPA-HMFG1 Radioimmunoconjugate For Intraperitoneal Radioimmunotherapy Of Ovarian Cancer. *Cancer* **73** 1067 – 1075.

Mattes M J. 2002 Radionuclide-Antibody Conjugates For Single-Cell Cytotoxicity. *Cancer.* **94** 1215 – 1223.

McDevitt M, Sgouros G, Finn R D, Humm J L, Jurcic J G, Larson S M and Scheinberg D A. 1998 Radioimmunotherapy With Alph-Emitting Nuclides. *Eur. J. Nucl. Med.* **25** 1341 – 1351.

McDevitt M R, Finn R D, Ma D, Larson S M and Scheinberg D A. 1999 Preparation Of Alpha-Emitting 213-Bi-Labeled Antibody Constructs For Clinical Use. *J. Nucl. Med.* **40** 1722 – 1727.

Meredith R F, Partridge E E, Alvarez R D, Khazaeli M B, Plott G, Russell C D, Wheeler R H, Liu T, Grizzle W E, Schlom J and LoBuglio A F. 1996 Intraperitoneal Radioimmunotherapy Of Ovarian Cancer. *J. Nucl. Med.* **37** 1491 – 1496.

National Cancer Institute of Canada 2004 Canadian Cancer Statistics 2004. p. 18. Toronto.

O'Brien T J, Tanimoto H, Konishi I and Gee M. 1998 More Than 15 Years Of CA 125: What Is Known About The Antigen, Its Sturcture And Its Function. *Int. J. Biol. Markers.* **13** 188 – 195.

Perkins G L, Slater E D, Sanders G K and Prichard J G. 2003 Serum Tumor Markers. *Am. Fam. Physician.* **68** 1075 – 1082.

Roberson, P.L., Buchsbaum, D.J., Heidorn, D.B. and Ten Haken R K. 1992 Three-Dimensional Tumor Dosimetry For Radioimmunotherapy Using Serial Autoradiography. *Int. J. Radiat. Oncol. Biol. Phys.* **24** 329 – 334.

Rosenshein N B. 1983 Radioisotopes In The Treatment Of Ovarian Cancer. *Clin. Obstet. Gynecol.* **10** 279 – 295.

Rotmensch J, Whitlock J L, Schwartz J L, Hines J J, Reba R C and Harper P V. 1997 *In vitro* And *In vivo* Studies On The Development Of The α-Emitting Radionuclide Bismuth 212 For Intraperitoneal Use Against Microscopic Ovarian Carcinoma. *Am. J. Obstet. Gynecol.* **176** 833 – 840.

Sgouros G. 1993 Bone Marrow Dosimetry For Radioimmunotherapy: Theoretical Considerations. *J. Nucl. Med.* **34** 689 – 694.

Srivastava S and Dadachova E. 2001 Recent Advances in Radionuclide Therapy. *Semin. Nucl. Med.* **XXXI** 330-341.

Stewart J S W, Hird V, Snook D, Sullivan M, Hooker G, Courtenay-Luck N, Sivolapenko G, Griffiths M, Myers M J, Lambert H E, Munro A J and Epenetos A A. 1989 Intraperitoneal Radioimmunotherapy For Ovarian Cancer: Pharmacokinetics, Toxicity , And Efficacy Of I-131 Labeled Monoclonal Antibodies. *Int. J. Radiat. Oncol. Biol. Phys.* **16** 405 – 413.

Tailor A, Bourne T H, Campbell S, Okokon E, Dew T and Collins W P. 2003 Results From An Ultrasound-Based Familial Ovarian Cancer Screening Clinic: a 10-Year Observational Study. *Ultrasound Obst. Gyn.* **21** 378 – 385

Trimble E, Berry D, Gore M, Kavanagh J, Cohen C, Pecorelli S, Creasman W, Mason P and Heinz P. 2003 Discussion: Current Issues In The Design Of Ovarian Cancer Treatment Trials. *Gynecol. Oncol.* **88** S122 – S123.

Urban N, McIntosh M W, Andersen M R and Karlan B Y. 2003 Ovarian Cancer Screening. *Hematol. Oncol. Clin. N.* **17** 989 – 1005.

Vergote I, Larsen RH, De Vos L, Winderen M, Ellingsen T, Bjorgum J, Hoff P, Aas M, Trope C and Nustad K. 1992b Distribution Of Intraperintoneally Injected Microspheres Labeled With The Alpha-Emitter Astatine (211At) Compared With Phosphorus (32P) And Yttrium (90Y) Colloids In Mice. *Gynecol. Oncol.* **47** 358-65.

Vergote I, Larsen RH, De Vos L, Nesland JM, Bruland O, Bjorgum J, Alstad J, Trope C and Nustad K. 1992c Therapeutic Efficacy Of The α-Emitter ^{211}At Bound On Microspheres Compared With ^{90}Y and ^{32}P Colloids In A Murine Intraperitoneal Tumour Model. *Gynecol. Oncol.* **47** 366-72.

Vergote I B, Vergote-De Vos L N, Abeler V M, Aas M, Lindegaard M W, Kjorstad K E, and Trope C G. 1992a Randomized Trial Comparing Cisplatin With Radioactive Phosphorus Or Whole Abdomen Irradiation As Adjuvant Treatment In Ovarian Cancer. *Cancer.* **69** 741 – 749.

Wang S J, Lin W Y, Chen M N, Chen J T, Ho W L, Hsieh B T, Huang H, Shen L H, Ting G and Knapp FF Jr. 2001 Histologic Study Of Effects Of Radiation Synovectomy With Rhenium-188 Microsphere. *Nucl. Med. Biol.* **28** 727 – 732.

Ward B, Mather S, Shepherd J, Crowther M, Hawkins L, Britton K and Slevin M L. 1988 The Treatment Of Intraperitoneal Malignant Disease With Monoclonal Antibody Guided ^{131}I Radiotherapy. *Br. J. Cancer.* **58** 658 – 662.

Whitehouse C and Solomon E. 2003 Current Status Of The Molecular Characterization Of The Ovarian Cancer Antigen CA125 And Implications For Its Use In Clinical Screening. *Gynecol. Oncol.* **88** S152 – S157.

Wong N A, Broadbent M R, Paterson-Brown S and al-Nafussi A. 2002 Gastrointestinal Stromal Tumor in Ascitic Fluid. A Case Report. *Acta Cytol.* **46** 723 – 727.

Yanoh K, Takeshima N, Hirai Y, Minami A, Tsuzuku M, Toyoda N and Hasumi K. 1999 Morphologic Analyses Of Positive Peritoneal Cytology In Endometrial Carcinoma. *Acta Cytol.* **43** 814 – 819.

Young R C, Brady M F, Nieberg R K, Long H J, Mayer A R, Lentz S S, Hurteau J and Alberts D S. 2003 Adjuvant Treatment For Early Ovarian Cancer: A Randomized Phase III Trial Of Intraperitoneal 32P Or Intravenous Cyclophosphamide And Cisplatin – A Gynecologic Oncology Group Study. *J. Clin. Oncol.* **21** 4350 – 4355.

Chapter 3

Beta Dosimetry

The deposition of energy in a biological system has the potential to initiate change in that system. For example, sufficient energy in the form of heat has the ability to denature proteins. Ionizing radiation is an example of an energy source that is extremely efficient at initiating biological change. A whole body dose of 4Gy of x-rays would often be fatal to a 70 kg man, however this dose corresponds to the absorption of approximately 67 calories – roughly the same amount of energy absorbed as heat from a single sip of a hot cup of coffee (Hall, 1994). Compared to non-ionizing radiations, ionizing radiations carry significantly more energy per particle. These particles have enough energy to rupture a chemical bond which in turn has the potential to initiate chemical and biochemical chain reactions that can ultimately lead to biological change (Hall, 1994). It wasn't long after the discovery of x-rays that investigators realized that there were deleterious consequences associated with excessive exposure to this type of radiation. Radiation dosimetry is the branch of science that attempts to provide a quantitative relationship between measurements associated with a radiation field and the chemical, biochemical and biological changes that would be made by that radiation field (Turner, 1995). The goal of this chapter is introduce some of the important concepts of beta dosimetry both at the macroscopic and microscopic levels. Particular focus is given to those areas of dosimetry used in subsequent chapters in the thesis.

3.1 Electron Interactions With Matter

In the energy range of interest for radionuclide therapy (< 2.5 MeV), electrons interact with their surrounding medium in two primary ways that can be described as collisional and radiative. Collisional processes are those that result in ionizations and excitations of the medium's constituent atoms and radiative processes are those that result in the emission of photons (ICRU 1983). The total stopping power of the medium describes the rate at which an electron loses energy as it travels through that medium. It is given by the sum of the collisional and radiative stopping powers and is dependent on the energy of the electron and the properties of the medium:

$$\left(\frac{S}{\rho}\right)_{tot} = \left(\frac{S}{\rho}\right)_{col} + \left(\frac{S}{\rho}\right)_{rad} \tag{3.1}$$

In Equation 3.1, S is the stopping power of the medium which, when divided by the density of the medium, ρ, gives the mass stopping power in units of MeV•cm^2/g. The subscripts *tot, col* and *rad* refer to total, collisional and radiative respectively. Collisional processes generally involve the incident beta particle interacting with the electrons of the medium. Both particles involved in the collisional process have an equal rest mass and relativistic effects become important even at reasonably low energies. A derivation of the equation that describes the collisional stopping power is beyond the scope of this work but the equation is presented here to illustrate the important behaviours in the energy range of interest for radionuclide therapy.

$$\left(\frac{S}{\rho}\right)_{col} = 2\pi r_c^2 N_e \frac{\mu_o}{\beta^2}\left[\ln\frac{E^2(E+2\mu_o)}{2\mu_o I^2} + \frac{\frac{E^2}{8} - (2E+\mu_o)\mu_o \ln 2}{(E+\mu_o)^2} + 1 - \beta^2 - \delta\right] \tag{3.2}$$

In Eq (3.2), r_c is the classical electron radius, N_e is the number of electrons per gram, μ_o is the rest mass of the electron, β is the ratio of the speed of the electron to the speed of light, E is the energy of the electron, I is the mean excitation energy of the atoms of the medium and δ is a density correction takes into account the polarization of the medium due to the electric field (Johns *et al.* 1983). For energies below 100 keV, Eq (3.2) is dominated by the term in front of the square parentheses. In this region the stopping power is approximately inversely proportional to the energy of the electron. Above 100 keV, the value of β is roughly constant so changes in stopping power are brought about by the terms inside the parentheses. These are generally slowly increasing functions of energy (Johns *et al.* 1983). Figure 3.1 is a plot of the collisional, radiative and total stopping powers of water. The data for these curves were taken from the online physical reference data of the National Institute for Standards and Technology (http://physics.nist.gov/PhysRefData/). Clearly the stopping power increases rapidly with decreasing energy below approximately 500 keV.

Radiative processes occur when a charged particle is accelerated as a result of an electrostatic interaction with a nucleus. If the charged particle has a mass M and charge ze, the force experienced by the particle due to a nucleus of charge Ze at a distance r is given by:

$$F = \frac{kzZe^2}{r^2} \tag{3.3}$$

and the resultant acceleration is then:

$$a = \frac{kzZe^2}{r^2 M} \qquad (3.4)$$

The rate at which the particle radiates energy is proportional to the square of the acceleration (Johns *et al.* 1983). Two important observations can then be made. First, radiative processes are more important in high Z materials than low Z materials due to the Z^2 term in the numerator. Second, radiative energy loss is more pronounced for light particles such as electrons than it is for heavier particles such as protons due to the M^2 term in the denominator. An approximate expression to describe the radiative stopping power of a medium is given by:

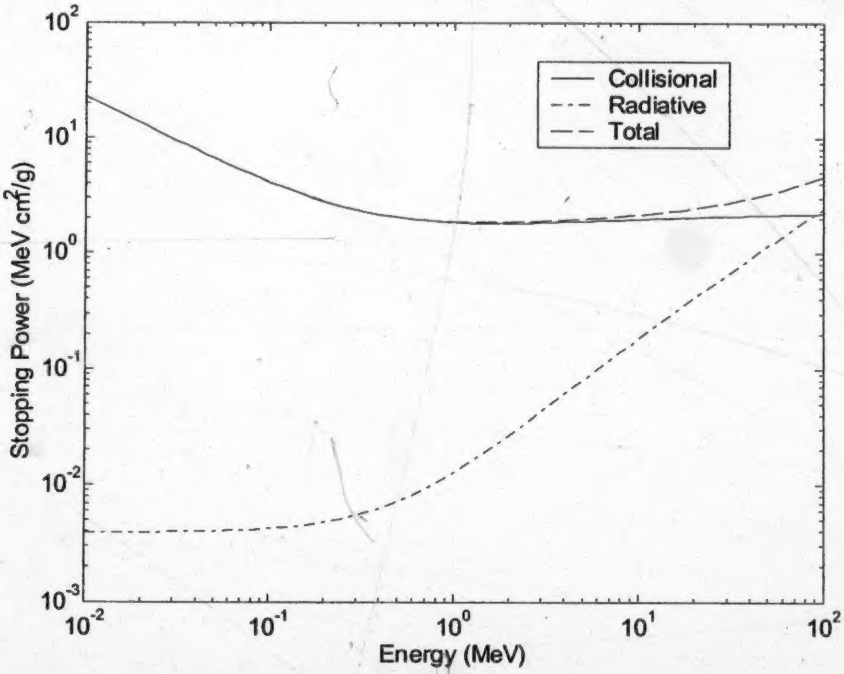

Figure 3.1: Collisional, radiative and total stopping powers of water for electrons up to 100 MeV. In the energy range of interest for radionuclide therapies (< 2.5 MeV) the total stopping power is almost entirely collisional.

$$\left(\frac{S}{\rho}\right)_{rad} = 4r_o^2 \frac{N_e ZE}{137}\left[\ln\frac{2(E+\mu_o)}{\mu_o} - \frac{1}{3}\right] \qquad (3.5)$$

From Figure 3.1, it is clear that radiative processes are not a particularly important form of energy loss for radionuclides whose mean beta energies are below 1 MeV. In fact, less than 1% of the energy of a 1 MeV electron will be lost due to radiative processes in water. The remainder of this discussion will focus on collisional processes due to their greater importance in terms of radionuclide therapy.

Within the realm of collisional processes, the principal processes of energy deposition are ionization and excitation. Ionization is a process that increases the number of ions in a closed system (Freeman, 1987). The ionized molecule is often left in an excited state that can de-excite by Auger electron emission, molecular dissociation, characteristic x-ray emission, etc (Paretzke, 1987). Excitation raises an orbital electron from one energy state to a higher energy state. In general, excitations are less important than ionizations in the energy range associated with radionuclide therapies. The ratio of ionizations to excitations between 1 keV and 100 keV is approximately 7 : 3 (Paretzke *et al.* 1978). Elastic collisions in which no energy is deposited are important at very low energies (below 200 eV) because they affect the spatial distribution of subsequent interactions (Paretzke, 1987).

3.2 Dose Point Kernels And Their Applications

Beta particles in the energy range of interest for radionuclide therapy typically deposit most of their energy within a few millimeters of their point of origin. For dosimetry calculations it is important to know how the spatial distribution of radioactivity corresponds to the absorbed dose distribution within the target volume. Beta Dose Point Kernels (DPKs) facilitate these calculations by providing the dose-rate as a function of distance from a point source of radioactivity (Cross *et al.*, 1992). When dealing with soft tissue tumours, an assumption of tissue uniformity (usually water equivalent) justifies a spatially independent DPK such that the dose distribution can be found by a convolution of the activity distribution with the DPK (Kwok *et al.*, 1985).

Early attempts at a DPK were made by Spencer (1955) in which a Continuous Slowing Down Approximation (CSDA) was applied to the transport of monoenergetic electrons. These were translated into radionuclide DPKs by averaging monoenergetic kernels over appropriate beta spectra (Cross 1967a, Berger 1971). These kernels underestimated the dose at large distances from the source because the CSDA neglects the stochastic nature of energy deposition and cannot account for the range straggling observed in experiments (Cross 1967b, 1969). To overcome the limitations of the CSDA, investigators applied Monte Carlo simulations to the problem. Berger (1973) produced a series of monoenergetic DPKs which were translated into radionuclide DPKs by Prestwich *et al.* (1989). Since then, important improvements in data pertaining to stopping powers and interaction cross sections have prompted the recalculation of the DPKs (Cross, 1992). To illustrate the concepts behind a DPK, a mathematical description from Prestwich *et al.* (1989) is shown in which the electron is assumed to move in a straight line and slow down according to the CSDA. In this case, an electron of initial energy E_o will have a range, r_o, given by:

$$r_o = \int_0^{E_o} \frac{dE}{S(E)} \tag{3.6}$$

Where S(E) is a stopping power function (not mass stopping power). At a distance r from an isotropically-emitting source in a medium of density ρ, the absorbed dose per transformation is:

$$D(r) = \frac{S(E(r))}{4\pi\rho r^2} \tag{3.7}$$

and the specific absorbed fraction (the fraction of the initial energy absorbed per unit mass) is:

$$\Phi(r, E_o) = \frac{S(E(r))}{4\pi\rho r^2 E_o} \tag{3.8}$$

This function is normalized such that:

$$\int_0^\infty 4\pi\rho r^2 \Phi(r, E_o) dr = 1 \tag{3.9}$$

The distance from the point source can be scaled by the CSDA range of the electron to produce the dimensionless quantity:

$$x = \frac{r}{r_o} \tag{3.10}$$

A scaled dose point kernel for monoenergetic electrons of energy E_o is defined as:

$$F(x, E_o) = 4\pi\rho r^2 r_o \Phi(r, E_o) \tag{3.11}$$

This function is also normalized such that its integral over all values of x is unity. Substituting Eq (3.8) gives:

$$F(x, E_o) = \frac{r_o S(E(x, r_o))}{E_o} = \frac{S(E(x, r_o))}{\langle S \rangle} \tag{3.12}$$

where:

$$\langle S \rangle = \frac{E_o}{r_o} \tag{3.13}$$

This quantity represents an average stopping power over the entire range of the electron.

A beta-emitting radionuclide may have several beta groups with different branching ratios (β) present in its decay scheme. The overall spectrum, n(E), observed from a radionuclide with N beta groups will be given by:

$$n(E) = \sum_{i=1}^{N} \beta_i n_i(E) \tag{3.14}$$

where $n_i(E)$ denotes the spectrum associated with the ith beta group. If the endpoint energy of the ith beta group is E_i, then its mean energy is:

$$\langle E_i \rangle = \int_0^{E_i} E n_i(E) dE \tag{3.15}$$

The specific absorbed fraction for this beta group is then:

$$\Phi_i(r) = \int_0^{E_i} \frac{E_o}{\langle E_i \rangle} n_i(E_o) \Phi(r, E_o) dE_o \tag{3.16}$$

Substituting from Eq (3.11):

$$4\pi\rho r^2 \Phi_i(r) = \int_0^{E_i} \frac{E_o}{r_o \langle E_i \rangle} n_i(E_o) F\left(\frac{r}{r_o}, E_o\right) dE_o \tag{3.17}$$

If the CSDA range of the maximum energy beta, E_i, is r_i, the dose point kernel can be scaled as:

$$F_i(x) = 4\pi\rho r^2 r_i \Phi_i(r) \tag{3.18}$$

When the contributions of all beta groups are considered, the specific absorbed fraction for a radionuclide is given by:

$$4\pi\rho r^2 \Phi_\beta(r) = \frac{\sum_{i=1}^{N} \beta_i \frac{\langle E_i \rangle}{r_i} F_i\left(\frac{r}{r_i}\right)}{\sum_{i=1}^{N} \beta_i \langle E_i \rangle} \tag{3.19}$$

A dose point kernel can be scaled by the CSDA range, r_N, of the highest energy beta emitted by the radionuclide:

$$F_\beta(x) = 4\pi\rho r^2 r_N \Phi_\beta(r) \tag{3.20}$$

When weighted over the entire beta spectrum, the dose can be expressed as a product of the specific absorbed fraction with the mean beta energy of each beta group:

$$r^2 D(r) = \frac{k \sum_{i=1}^{N} \beta_i \langle E_i \rangle F_\beta\left(\frac{r}{r_N}\right)}{r_N} \tag{3.21}$$

The constant k is used to convert the energy deposition per transformation from MeV cm^2 g^{-1} to mGy cm^2 MBq^{-1} h^{-1}. The numerical forms of D(r) for many radionuclides were published by Cross (1992). These dose point kernels were used for the work presented in subsequent chapters of this thesis.

3.3 Microdosimetry

The preceding discussion of electron dosimetry was framed in the context of macrodosimetry – the branch of dosimetry in which the stochastic nature of energy deposition is not of importance when assessing an absorbed dose. An absorbed dose in this case is a statistical average concerned only with the total amount of energy deposited in an object and the total mass of that object. This, by definition, forbids conclusions about the amount of energy actually deposited in an individual cell or subcellular component (Kellerer, 1985). Microdosimetry is the branch of radiation dosimetry that was developed to investigate the dosimetric consequences of the stochastic nature of energy deposition by ionizing radiation. As a general rule its application is most relevant when dealing with small target sites, densely ionizing radiations and low doses (Kellerer, 1985). Microdosimetry is frequently employed in the analysis of the biological effects of alpha-emitting radionuclides and bone marrow is a commonly studied tissue. Aurlien *et al.* (2002) used this technique to determine the relative biological effectiveness of At-211 compared to Co-60 in osteosarcoma cells and mononuclear bone marrow cells *in vitro*. By targeting the osteosarcoma cells with At-211-labeled antibodies they were able to more effectively kill the sarcoma cells relative to the mononuclear cells. They also found a relative biological effectiveness of 3.43 and 1.55 for the sarcoma cells and mononuclear cells respectively when the comparative endpoint was 37% survival. Austin *et al.* (1999) investigated the energy deposition patterns as a function of time for the bone-seeking alpha emitters Pu-239, Am-241 and U-233. Their analysis was able to show a trend in cumulative doses of Pu-239 > Am-241 > U-233 and this correlated with incidences of osteosarcoma observed in mice. Alpha dose to lung tissue is also of interest. Aubineau-Laniece et al. (2002) investigated the patterns of energy deposition on the inner surface of the lung airway for the purpose of modeling uniform and non-uniform contamination of the airways with radon progeny. In an attempt to make microdosimetry more clinically useful, Stinchcomb and Roeske (1999) combined the important information from microdosimetric distributions with the MIRD computational scheme. For three different source geometries, their technique provides the spread of specific energies and probabilities of any number of hits without requiring the calculation of multi-hit specific energy distributions.

A review of some of the key concepts in microdosimetry is presented below (Kellerer, 1985, Kellerer et al. 1975a, 1975b, 1975c, ICRU 1983).

When a particle of ionizing radiation travels through a medium it deposits energy in discrete energy transfer events. The magnitude of an individual energy transfer event, ε_i, is given by:

$$\varepsilon_i = T_b - \sum_i T_{a,i} + Q \qquad (3.22)$$

Where T_b is the kinetic energy of the particle prior to the interaction, $T_{a,i}$ are the kinetic energies of all ionizing particles (including the original particle if it is still an ionizing particle after the interaction) created during the interaction and Q denotes any change in the rest mass energy of a nucleus that results from the interaction. In terms of radionuclide therapies, only the first two terms in the equation are of practical importance as nuclear reactions are highly improbable. The energy imparted to a volume is defined as the sum of all energy transfers within that volume:

$$\varepsilon = \sum_i \varepsilon_i \qquad (3.23)$$

The microdosimetric analogue of absorbed dose is called specific energy, z, and is defined as the energy imparted divided by the mass, m, of the volume:

$$z = \frac{\varepsilon}{m} \tag{3.24}$$

Specific energy is a stochastic quantity and is typically described in terms of probability distributions. Consider a macroscopic volume that is comprised of a large number of microscopic sub-volumes. If the macroscopic volume receives an absorbed dose, D, the task of microdosimetry is to calculate the distribution of z that is produced in the sub-volumes. The function F(z,D) is used to denote the probability that a random variable, $\underline{z}$, is less than or equal to a specific energy, z, at an absorbed dose, D:

$$F(z,D) = P(\underline{z} \le z | D) \tag{3.25}$$

The derivative of this distribution with respect to z provides the probability density of z:

$$f(z,D) = dF(z,D)/dz \tag{3.26}$$

The quantity f(z,D)dz gives the probability that the specific energy has a value between z and z + dz. If the volume is a uniform body and is exposed to a uniform radiation field, then the expectation value of f(z,D) is equal to the absorbed dose, D:

$$\bar{z} = \int_0^\infty z f(z,D) dz = D \tag{3.27}$$

Implicit in this definition is that the distribution, f(z,D), has been normalized to unity.

A special distribution in microdosimetry is given to that which describes the energy deposited during a single event: the single event distribution, denoted by $f_1(z)$. An event is defined as the total energy deposited in a volume by particles that are statistically correlated (ICRU 36, 1983). The inclusion of 'statistically correlated' particles refers to secondary events such as delta rays and

Auger electrons. These particles are not necessarily the initial particle responsible for the primary radiation track but they result from the creation of the primary radiation track. The single event distribution is one of the most fundamental concepts in microdosimetry because many of the other concepts can be explained in terms of the single event distribution, including the dose-dependent distributions discussed above. The expectation value of the single event distribution is known as the frequency mean specific energy per event $\bar{z}_F$ (ICRU, 1983) and is given by:

$$\bar{z}_F = \int_0^\infty z f_1(z) dz \tag{3.28}$$

This quantity is related to the macroscopic absorbed dose by the mean number of events in a microscopic sub-volume, $\bar{\nu}$:

$$\bar{z}_F \bar{\nu} = D \tag{3.29}$$

The second moment of the single event distribution also plays an important role in microdosimetry and is defined by:

$$\overline{z_F^2} = \int_0^\infty z^2 f_1(z) dz \tag{3.30}$$

If the single event distribution is weighted by the specific energy, one obtains the dose distribution, $d_1(z)$. Appropriately normalized, this spectrum is given by:

$$d_1(z) = \frac{z f_1(z)}{\int z f_1(z) dz} \tag{3.31}$$

Which simplifies to:

$$d_1(z) = \frac{z}{\bar{z}_F} f_1(z) \tag{3.32}$$

The mean value of this distribution is known as the dose-mean specific energy per event and is given by:

$$\bar{z}_D = \int_0^\infty z d_1(z) dz \tag{3.33}$$

Which simplifies to:

$$\bar{z}_D = \frac{1}{\bar{z}_F}\int_0^\infty z^2 f_1(z)dz = \frac{\overline{z_F^2}}{\bar{z}_F} \tag{3.34}$$

The role of the single event distribution can be further expanded to examine the distribution of specific energies resulting from multiple events. If a target volume is crossed by two identical but statistically independent ionizing particles, each one will produce a distribution of specific energies given by $f_1(z)$. The distribution of specific energies observed by a target crossed by exactly 2 particles is then given by the convolution of the single event distribution with itself:

$$f_2(z) = \int_0^z f_1(x) f_1(z-x)dx \tag{3.35}$$

The spectrum for 3 events is found by convolving the spectrum for 2 events with the single event distribution and the generalized formula for a target crossed by n particles is given by:

$$f_n(z) = \int_0^z f_1(z) f_{n-1}(z-x)dx \tag{3.36}$$

When a macroscopic volume is exposed to a field of ionizing radiation, an event in a particular microscopic sub-volume is a rare event when compared to the total number of particles of ionizing radiation incident on the macroscopic volume. As such, the number of events observed in the sub-volumes is assumed to be distributed according to the Poisson distribution. This gives the probability, p(n), of observing n events when the mean number is $\bar{v}$ as:

$$p(n) = \frac{e^{\bar{v}}\bar{v}^n}{n!} \tag{3.37}$$

The mean number of events per sub-volume at an absorbed dose D is given in Eq (3.29). To calculate the distribution of specific energies observed by a sub-volume for a macroscopic dose, D, one must sum up all possible specific energy spectra, $f_n(z)$, after weighting them according to the probability of observing n events in the sub-volume:

$$f(z,D)=\sum_{n=0}^{\infty}\frac{e^{\bar{v}}\bar{v}^{n}}{n!}f_{n}(z) \tag{3.38}$$

The expectation value of this distribution is given by:

$$\bar{z}=\bar{v}\,\bar{z}_{F} \tag{3.39}$$

It is also of interest to determine the relative spread of this distribution with respect to its mean value. This quantity will be denoted by λ and is calculated with the standard deviation of the distribution in the following way:

$$\lambda=\frac{\sigma}{\bar{z}} \tag{3.40}$$

Where

$$\sigma^{2}=\overline{(z-\bar{z})^{2}}=\overline{z^{2}}-\bar{z}^{2} \tag{3.41}$$

And

$$\overline{z^{2}}=\sum_{n=0}^{\infty}\frac{e^{\bar{v}}\bar{v}^{n}}{n!}\int_{0}^{\infty}z^{2}f_{n}(z)dz=e^{\bar{v}}\sum_{n=1}^{\infty}\frac{\bar{v}^{n}}{n!}\overline{z_{n}^{2}} \tag{3.42}$$

With the knowledge of the single event distribution and the macroscopic absorbed dose, a tremendous amount of information about the patterns of energy deposition in small target volumes can be calculated. The focus of this section has been limited to those aspects of microdosimetry used in this thesis. Microdosimetry is now a sufficiently mature science that a large body of literature on the subject exists and yet it is still of current research interest.

References

Aubineau-Laniece I, Pihet P, Winkler R, Hofmann W and Charlton D E. 2002 Monte Carlo Code For Microdosimetry Of Inhaled Alpha Emitters. *Radiat. Protec. Dosim.* **99** 463 – 468.

Aurlien E, Larsen R H, Akabani G, Olsen D R, Zalutsky M R and Bruland O S. 2000 Exposure Of Human Osteosarcoma And Bone Marrow Cells To Tumour-Targeted Alpha-Particles And Gamma-Irradiation: Analysis Of Cell Survival And Microdosimetry. *Int. J. Radiat. Biol.* **76** 1129 – 1141.

Austin A L, Ellender M, Haines J W, Harrison J D and Lord B I. 1999 Temporal Change In Microdosimetry To Bone Marrow And Stromal Progenitor Cells From Alpha-Particle-Emitting Radionuclides Incorporated In Bone. *Radiat. Res.* **152(6 Suppl)** S38 – S42.

Berger M J. 1971 MIRD Pamphlet No. 7: Distribution Of Absorbed Dose Around A Point Beta Source Of Electrons And Beta Particles In Water And Other Media. Medical Internal Radiation Dose Committee. *J. Nucl. Med.* **12** 5S – 24S.

Berger M J. 1973 Improved Point Kernels For Electron And Beta Ray Dosimetry. *National Bureau Of Standards Report*: NBSIR-73-107.

Cross W G. 1967a Tables Of Beta Dose Distributions. *Atomic Energy of Canada Limited Publication*: AECL-2793.

Cross W G. 1967b The Distribution Of Absorbed Energy From A Point Beta Source. *Can. J. Phys.* **45** 2021 – 2040.

Cross W G. 1969 Distribution Of Absorbed Beta Energy in Solid Media. *Can J. Phys.* **47** 75 – 83.

Cross W G, Freedman N O and Wong P Y. 1992 Tables of Beta-Ray Dose Distributions in Water. *Atomic Energy of Canada Limited publication*: AECL-10521.

Freeman, G R. 1987 Ionization And Charge Separation In Irradiated Materials. Chapter 2 in Kinetics Of Non-Homogeneous Processes, A Practical Introduction For Chemists, Biologists, Physicists, and Materials Scientists (Freeman, G R. editor). John Wiley & Sons, New York.

Hall E J. 1994 Radiobiology For The Radiologist, 4th Edition. Lippincott, Philadelphia.

ICRU 1983 Microdosimetry. International Commission on Radiation Units and Measurements Report **36.** ICRU, Bethesda.

Johns H E and Cunningham J R. 1983 The Physics Of Radiology, 4th Edition. Charles C Thomas, Springfield.

Kellerer A M. 1985 Fundamentals Of Microdosimetry. Chapter 2 in The Dosimetry Of Ionizing Radiation, Volume 1 (Kase K R, Bjarngard B E and Attix F H. editors). Academic Press, Inc. Orlando. pp 77 – 162.

Kellerer A M and Chmelevsky D. 1975a Concepts Of Microdosimetry I. Quantities. *Rad. Environm. Biophys.* **12** 61 – 69.

Kellerer A M and Chmelevsky D. 1975b Concepts Of Microdosimetry II. Probability Distributions Of The Microdosimetric Variables. *Rad. Environm. Biophys.* **12** 205 – 216.

Kellerer A M and Chmelevsky D. 1975c Concepts Of Microdosimetry III. Mean Values Of The Microdosimetric Distributions. *Rad. Environm. Biophys.* **12** 321 – 335.

Kwok C, Prestwich W and Wilson B. 1985 Calculation Of Radiation Doses For Nonuniformly Distributed β and γ Radionuclides In Soft Tissue. *Med. Phys.* **12** 405 – 412.

Paretzke H G. 1987 Radiation Track Structure Theory. Chapter 3 in Kinetics Of Non-Homogeneous Processes, A Practical Introduction For Chemists, Biologists, Physicists, and Materials Scientists (Freeman, G R. editor). John Wiley & Sons, New York.

Paretzke H G and Berger M. 1978 Stopping Power And Energy Degradation For Electrons In Water Vapor. pp 749 - 758 in Sixth Symposium On Microdosimetry (Booz J and Ebert H G. editors), Report EUR 6064. Harwood Academic Publishers, London.

Prestwich W, Nunes J and Kwok C. 1989 Beta Dose Point Kernels for Radionuclides of Potential Use in Radioimmunotherapy. *J. Nucl. Med.* **30** 1036 – 1046.

Spencer L V. 1955 Theory Of Electron Penetration. *Phys. Rev.* **98** 1597 – 1615.

Stinchcomb T G and Roeske J C. 1999 Values Of "S", $<z_1>$ and $<z_1^2>$ For Dosimetry Using Alpha-Particle Emitters. *Med. Phys.* **26** 1960 – 1971.

Turner J E. 1995 Atoms, Radiation And Radiation Protection, 2nd Edition. John Wiley and Sons, New York.

Chapter 4

Liposome-Mediated Targeted Intraperitoneal Radionuclide Therapy

4.1 Liposomes

The term liposome refers to a synthetic structure composed of one or more membrane-like lipid bilayers arranged concentrically around a hollow interior, or “vacuole” which can serve as a storage compartment for active ingredients (Delrieu et al. 1999). The concept of the liposome is illustrated in Figure 4.1. The lipids forming the bilayers are typically of an amphiphilic nature with a polar headgroup and two hydrophobic hydrocarbon tails. When these lipids are exposed to an aqueous environment, they spontaneously form closed bilayers as a result of the hydrophilic interactions between the polar headgroups, the Van der Waals’ interactions between the hydrocarbon tails and the hydrophilic interactions of the headgroups with water (Frezard 1999). The hydrocarbon tails are usually fatty acids of varying lengths and degrees of saturation. Each double bond in the hydrocarbon puts a kink in the tail. The length and degree of saturation are two variables that are very important in defining certain membrane or liposome properties such as fluidity because they determine how densely the phospholipids can pack together.

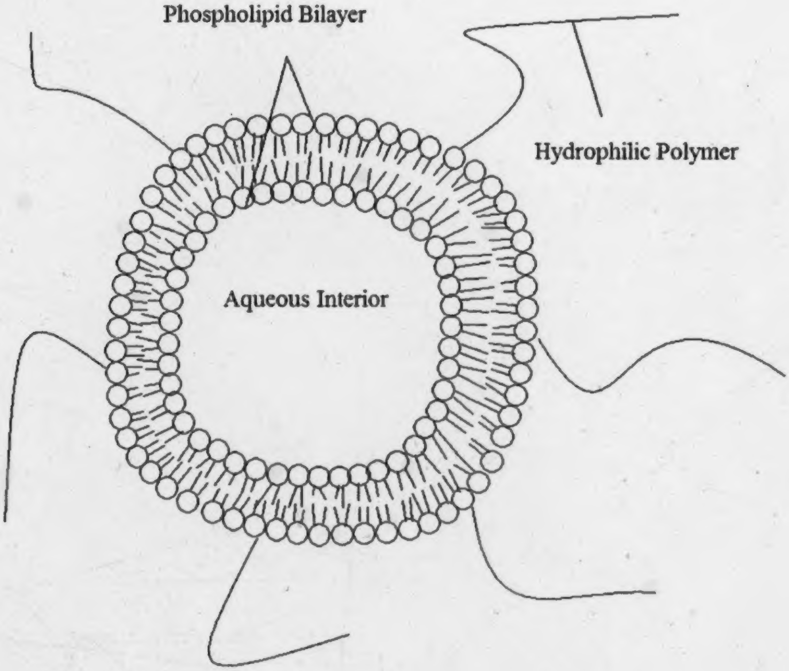

Figure 4.1: Schematic representation of a liposome. An aqueous interior is surrounded by a phospholipid bilayer. Hydrophilic polymers extending out from the surface create a hydration layer around the liposome.

Liposomes are valuable drug delivery vehicles because of the diversity of compounds that they can transport. Where the appropriate chemistry exists, hydrophilic molecules can be trapped in the interior volume of the liposome and hydrophobic molecules can be trapped in the space between the lipid bilayers filled with fatty acids. Molecules of intermediate solubility can be partitioned between both the fatty acid space and the interior/exterior of the liposome (Allen *et al.* 1998a). Quite often this chemistry is fairly complicated. For example, the intermediate solubility of certain molecules means that they will be quickly released from the liposome. This can be avoided in some instances (i.e. the anticancer drug doxorubicin) by manipulating the interior pH of the liposome or by forming molecular complexes of these molecules within the liposome resulting in greater retention.

The constitution of the liposome itself plays a significant role in determining its fate in the body. When classical liposomes were first developed in the early 1970s, there was immediate interest in their employment as drug carriers. This initial optimism was relatively short lived because it was quickly learned that liposomes injected intravenously are readily targeted for clearance by the mononuclear phagocyte system (MPS). Clearance of classical liposomes from the bloodstream is dependent on a number of factors including size, charge, phase transition, presence of cholesterol and dose (Allen *et al.* 1999). The effect of liposome size is such that the larger the diameter of the liposome, the greater the rate of their clearance from the vasculature. The rate of clearance is also increased for liposomes that carry a surface charge (positive or negative) over neutral liposomes. The phase transition temperature of the liposome is a property of a lipid membrane that is correlated with the tightness of the bilayer, with tighter bilayers having higher transition temperatures. For liposomes, higher transition temperatures result in decreased clearance. Cholesterol generally has the effect of tightening a phospholipid bilayer, thus increasing liposome circulation time. Variation of these parameters results in a range of circulation times for classical liposomes but in general they are too short to make the efficient drug carriers (Allen *et al.* 1999).

A classical liposome is one to which no stabilizing agents have been added. By contrast, a "Stealth" liposome is one that has been sterically stabilized. Stealth liposomes are stabilized by attaching hydrophilic polymers such as polyethylene glycol (PEG) or monosialylganglioside to the surface of the liposome with lipid anchors (Allen *et al.* 1989, Papahadjopoulos *et al.* 1991). The presence of PEG on the surface of the liposome creates a hydration layer around the liposome, essentially disguising it as a "bag of water". This has the effect of reducing the uptake of liposomes by the MPS because it interferes with the binding of plasma protein opsonins, which assist the MPS in this task (Lasic *et al.* 1995). Consequently, stealth liposomes have significantly increased circulation times relative to classical liposomes (Allen *et al.* 1998a). In addition, the decreased uptake by the MPS results in dose-independent pharmacokinetics, which means that a constant percentage of the injected dose is taken up by various tissues, regardless of the amount injected (Lasic *et al.* 1995, Papahadjopoulos *et al.* 1991). Clearance of Stealth liposomes is also independent of the phase of the liposome (i.e. whether the membrane is in a more fluid, liquid state or a more densely packed, crystalline state). There is, however, a dependence on both the molecular weight of the PEG molecules and their concentrations on the liposome surface. Increased circulation times are achieved in liposomes with PEG molecules with a molecular weight in the range of 1000 – 5000 Daltons (2000 Da considered optimum) at a concentration in the range of 3 – 10 mol% (5 – 7 mol% considered optimum) of phospholipid (Allen *et al.* 1998b).

Liposomes are attractive drug carriers for several reasons. They are capable of targeting a drug in a biologically inert manner to a desired location and they can significantly alter the pharmacokinetics of the drug relative to the free drug. These two factors are tremendously important in the treatment of diseases like cancer where the dose of an anticancer drug is severely limited by its toxic effects on healthy tissue.

Targeting of drug-carrying liposomes takes one of two forms: passive or active. Passive targeting takes advantage of one of the characteristics of the vasculature of solid tumours. As a tumour grows, so too grows its requirement for exchange of nutrients and metabolic end products. Cancer cells secrete angiogenic factors to stimulate the production of new capillary networks through cell locomotion and cell division (Vander *et al.* 1994). This newly synthesized vasculature is leaky relative to mature vasculature and therein lies the strategy of passive targeting. Liposomes cannot escape from mature vasculature but they can extravasate from new capillaries. Liposomes with sufficiently long circulation times will be selectively taken into the interstitium of tumours resulting in an increased tumour concentration of the drug relative to that achieved by the free drug (Allen *et al.* 1998a).

Active targeting is a strategy designed to deliver liposomes to locations with great specificity. The idea is to exploit the presence of molecules on the external cell membrane that are either exclusively expressed or over-expressed on the target cell relative to the normal cell. Once such a molecule has been identified, a ligand specific to this molecule is coupled to the liposome. There are a number of variations of this technique, each with distinct advantages and disadvantages. The specificity with which a liposome can be targeted to a cell can be enhanced with the attachment of whole monoclonal antibodies (MAb). Unfortunately MAb-labeled liposomes are also most likely to induce an immune response resulting in increased clearance from the blood stream (Allen *et al.* 1998b). The MAb can be coupled either directly to the surface of the liposome or to the terminus of the stabilizing agent (i.e. PEG). When the MAb is coupled to the surface, the immune response might be decreased, but the ability of the MAb to bind to its epitope is also decreased because of interference from the PEG polymers. Conversely, coupling the MAb to the PEG terminus improves MAb-epitope binding but it might also increase the immune response. One method for decreasing the immune response involves removing the region (called the Fc region) of the whole MAb that is recognized by the Fc receptor on phagocytic and effector immune cells (Allen *et al.* 1998b). Although the specificity for the epitope can be maintained, there is a loss of efficiency with which these antibody fragments will bind compared to the whole MAb.

One of the characteristics of cancer cells is an aggressive growth pattern and as such, malignant cells often over express receptors for growth factors. A third strategy for active targeting involves coupling the ligands for these growth factor receptors. Since healthy cells also express these molecules, the immune response will be decreased, but for the same reason, the specificity with which these liposomes can be targeted to cancer cells will also be decreased (Allen *et al.* 1998b).

4.2 Liposome Preparation

Liposomes can be prepared in a number of ways, however, only the method used for the experimental work in this research will be described here. Once the constituent molecules (lipids and cholesterol) have been selected and molar ratios determined, they are dissolved in an organic solvent such as chloroform. Certain lipids are not readily soluble in chloroform alone and are instead dissolved in a chloroform : methanol (1 : 0.03) mixture. The solution is placed in a round-bottom flask and the solvent is evaporated under vacuum using a rotovap machine. The lipid content remains on the surface of the flask as a thin film. The flask is left under vacuum for several hours to ensure complete removal of all solvents. The dry film is then resuspended in an aqueous medium. As the lipid film peels off the surface of the flask, it spontaneously forms liposomes.

These tend to be multilamellar liposomes in which a number of progressively smaller liposomes are enclosed by a larger outer liposome. Furthermore they tend to have a very inhomogeneous size distribution. These problems can both be overcome through an extrusion process. Multilamellar liposomes are passed through polycarbonate filters with uniform pore size under high pressure. The sheer force acting on the liposomes during this process results in unilamellar vesicles with a reasonably uniform size distribution. Filters are available that will produce liposomes with sizes that range from tens of to hundreds of nanometers in diameter.

Direct encapsulation of a therapeutic agent such as a chemotherapy drug or radioactivity in the aqueous interior of the liposomes is possible by resuspending the lipid film with an aqueous solution containing the agent. This approach is problematic when encapsulating radioactivity because the subsequent extrusion process involves significant sample handling time and requires the use of nitrogen gas at high pressure, creating a very serious radiation safety concern. For this research, a liposome formulation was developed that included a chelating agent coupled to one of the lipid components. This allowed the complete liposome sample preparation and purification to be a non-radioactive process. The labeling process was then a safe, efficient procedure in which the radioactive atoms were bound to the outer surface of the liposomes.

4.3 Liposome Purification

Liposome purification is generally accomplished using size exclusion chromatography (SEC). This technique involves passing a sample down a column that is filled with porous beads for the purpose of separating compounds based on their molecular weights. Sufficiently large particles, such as liposomes, will not enter the beads and will follow a shorter path through the column. Small particles, such as unencapsulated drug or unbound radioactivity will enter the pores of the beads and take a much more tortuous path through the column resulting in a much longer transit time. The principle of this technique is illustrated in Figure 4.2 and a hypothetical column elution profile is shown in Figure 4.3. The columns used for the experimental work in this research were PD-10 disposable columns from Amersham Biosciences. The bed consisted of 8.3 mL of Sephadex$^{\text{Tm}}$ G-25 beads and could handle sample volumes between 1.5 – 2.5 mL.

4.4 Therapy Design

The therapy design being investigated at the University of Alberta involves using liposomes to deliver radioactivity to tumour tissue in the peritoneal cavity (McQuarrie *et al.*, 2001, Xiao *et al.*, 2002). The targeting moiety is a synthetic construct called a bi-specific monoclonal antibody (bs-MAb). This molecule has a total of three binding regions. Two of the regions come from an intact MAb and are identical. They have been shown to target the ovarian cancer antigen CA-125. The third region comes from an antibody fragment (FAb) that has been covalently linked to the Fc region of the intact MAb. This fragment targets the molecule biotin. Figure 4.4 illustrates the synthesis of the bs-MAb. The function of the bs-MAb is to tether the radiolabeled, biotinilated liposomes to the surface of the CA-125-expressing cancer cells in the peritoneal cavity.

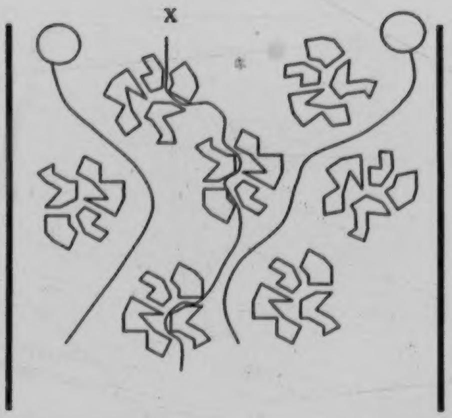

Figure 4.2: Illustration of size exclusion chromatography. Large particles such as liposomes (represented by circles) cannot enter the pores of the column's beads and pass through the column quickly. Small particles such as free radioactivity (shown as 'x') can enter the pores and have longer transit times due to their tortuous path through the column.

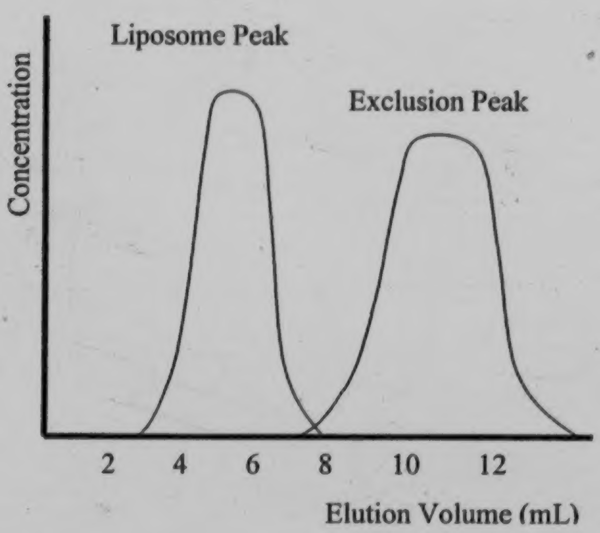

Figure 4.3: Hypothetical elution profile from a PD-10 size exclusion column. Typically there is good separation between the liposome peak and the exclusion peak corresponding to the unbound radioactivity

Liposomes for this therapy were designed with the following criteria in mind:

1. Liposomes must contain biotin to allow binding with the bs-MAb.
2. Liposomes must be able to carry significantly more radioactivity per particle than a radiolabeled MAb.

The compounds used in the formulation are as follows:

- 1,2-Distearoyl-*sn*-Glycero-3-Phosphocholine (DSPC)
- Cholesterol (Chol)
- 1,2-Distearoyl-*sn*-Glycero-3-Phosphoethanolamine-N-[Biotinyl(Polyethylene Glycol)2000] (Ammonium Salt) (DSPE-PEG-Biotin)
- 1,2-Dimyristoyl-*sn*-Glycero-3-Phosphoethanolamine-N-DTPA (DMPE-DTPA)

The components were added in the following molar ratios:
(DSPC : Chol : DSPE-PEG-Biotin : DMPE-DTPA) = (1 : 0.5 : 0.05 : 0.05).
Figure 4.5 shows the schematic structures of these molecules.

The last compound listed in the liposome formulation is DMPE-DTPA. This molecule serves as the chelating agent for the radioactive cargo. Diethylene-triamine-pentaacetate (DTPA) forms coordination complexes with multivalent metal ions; surrounding the ions to prevent the occurrence of chemical reactions that would otherwise take place. In the case of radionuclide therapy, DTPA is referred to as a bifunctional chelating agent (BCA) because it can be coupled to a targeting moiety such as an antibody or liposome to deliver the radioactive cargo to the tumour cells (Safavy *et al.* 2002). Initial oncologic diagnostic applications of DTPA involved the chelation of In-111 to image neuroendocrine tumours that express somatostatin receptors (Froidevaux *et al.* 2002). The same radionuclide was used for therapeutic purposes by Krenning *et al.* (1999). They observed a therapeutic benefit without major clinical side-effects in some end-stage neuroendocrine tumour patients. Thirty patients received repeated administrations up to a maximum cumulative activity of 74 GBq. Twenty-one patients received more than 20 GBq total activity and of these, 8 showed disease stabilization and 6 others showed tumour volume reductions. This chelating agent has also been shown to bind the therapeutic radionuclide yttrium-90 (Smith-Jones *et al.* 1998).

There are a number of different types of BCAs, including the macrocyclic azacarboxylates (MACs). These are cyclical structures such as 1,4,7,10-tetraazacyclododecane tetraacetic acid (DOTA) which have demonstrated excellent metal ion chelation properties and have been used in animal and human clinical trials (Froidevaux *et al.* 2000, Otte *et al.* 1999). The clinical trial by Otte *et al.* (1999) studied 29 patients with advanced somatostatin receptor-positive tumours with no other treatment options. Twenty-four of these patients received cumulative activities of less than 7400 MBq/m^2. Within this group, there were no cases of severe renal or haematological toxicity. Five patients received more than 7400 MBq/m^2 and all of them developed renal and/or haematological toxicity. Of the 29 patients, 20 demonstrated disease stabilization, 2 had a partial remission and 4 had a reduction of tumour mass of more than 50%. Three patients had tumour progression.

DTPA is an acyclic analogue of the MACs. The cyclical agents appear to produce more stable complexes with yttrium isotopes and have demonstrated better pharmacokinetic profiles in terms of tumour uptake and clearance rates (Kwekkeboom *et al.* 1999). Although these factors suggest that MACs would be a better choice for this therapy, a DOTA-derivatized lipid was not commercially available when this work was performed.

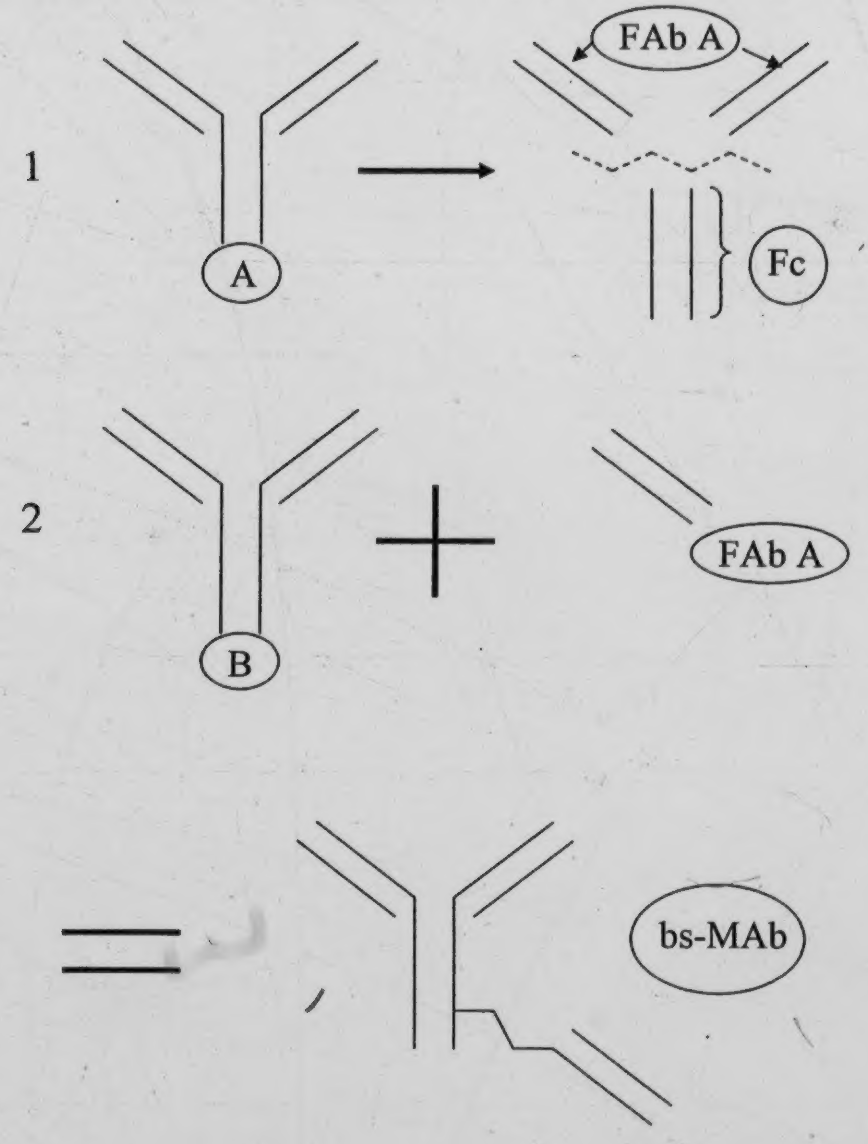

Figure 4.4: Schematic illustration of the construction of a bi-specific monoclonal antibody. In step 1, the intact MAb A is fragmented into two identical FAb fragments (FAb A) and a single Fc fragment. In step 2, the FAb fragments are covalently linked to the Fc region of a second MAb, B to form the bs-MAb.

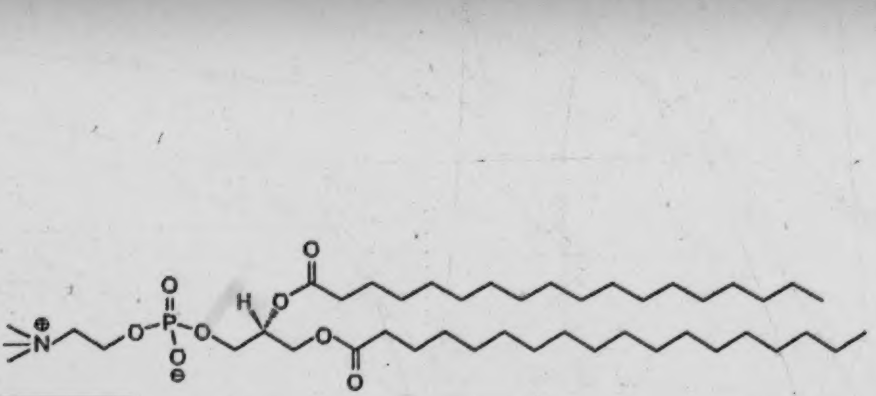

DSPC

©Avanti Polar Lipids

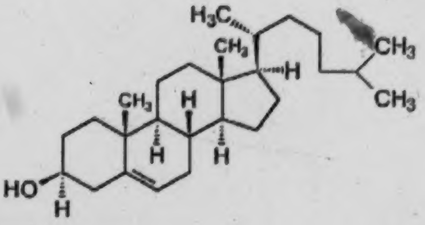

Cholesterol

©Avanti Polar Lipids

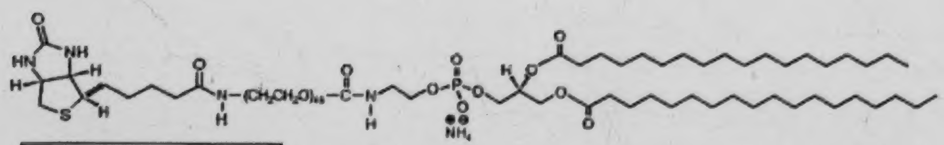

DSPE-PEG-Biotin

©Avanti Polar Lipids

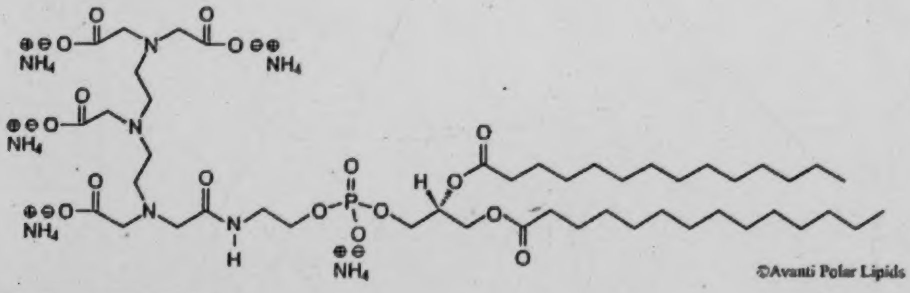

©Avanti Polar Lipids

DMPE-DTPA

Figure 4.5: Constituent molecules of liposome formulation used to carry radioactive Y-90 atoms to CA-125-expressing cancer cells. Figures used with permission from Avanti Polar Lipids.

The liposomes used in this work were approximately 150 nm in diameter. Alberts *et al.* (1994) state that there are 5 x 10^6 phospholipids / μm^2 in a lipid membrane. This suggests that 3.5 x 10^5 phospholipids would be required to form a liposome with a diameter of 150 nm. Half of these would be on the outer side of the membrane where radiolabeling would occur. If 5% of the phospholipids carry the chelating agent, the total number of potential binding sites per liposome can be estimated at more than 8 x 10^3. In the modeling work presented in later chapters, an assumption of 10^3 radioactive atoms per liposome is made in order to preserve this order of magnitude while recognizing the potential for less than 100% labeling efficiency. In general, only a few radioactive atoms can be bound to an antibody without deleterious consequences to its binding kinetics (van Gog *et al.* 1997) so the possibility of attaching 10^3 atoms per liposome is an exciting prospect for a targeted radionuclide therapy. Figure 4.6 is a schematic illustration of the targeting process used in this therapy.

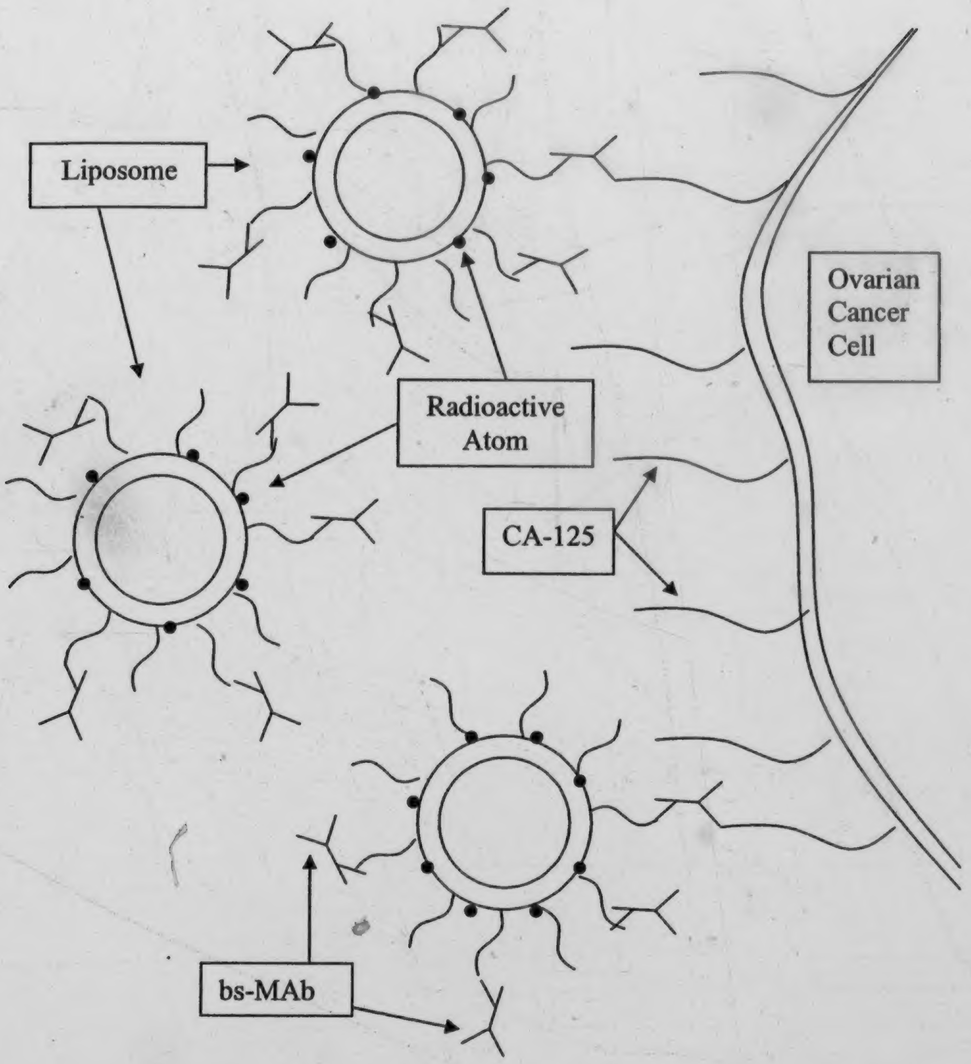
Liposome
Ovarian Cancer Cell
Radioactive Atom
CA-125
bs-MAb

Figure 4.6: Schematic diagram of the targeted delivery of radioactivity to the surface of an ovarian cancer cell that is expressing the antigen CA-125. The wavy lines extending out from the surface of the liposomes are long chain polyethylene glycol polymers with a terminal biotin molecule. The bs-MAb molecules bind to both the cancer cell and the liposome to act as a tether between the two.

4.5 Evidence of Successful Therapeutic Design

To validate this therapeutic design it was necessary to provide experimental evidence to clearly indicate that liposomes could be targeted to ovarian cancer cells expressing the antigen CA-125 and that liposomes could be labeled with radioactivity. There are a number of techniques that could be employed for the visualization of the targeting, however we chose to use confocal microscopy. Radiolabeling experiments were performed with Y-90.

4.5.1 Targeting of Liposomes to Ovarian Cancer Cells

4.5.1.1 Materials and Methods

The liposomes used for this experiment were slightly different than the therapeutic preparation. No radioactivity was used for the confocal experiments, so the DMPE-DTPA content of the liposomes was replaced by a new lipid called Lissamine™ rhodamine B 1,2-dihexadecanoyl-*sn*-glycero-3-phosphoethanolamine (rhodamine DHPE) from Molecular Probes. This lipid has the fluorescent probe rhodamine B coupled to its polar head group so that it is found on both the outer and inner surfaces of the liposomes, but not in the aqueous interior. Liposomes were prepared in the manner described in section 4.2. The resuspension medium was phosphate-buffered saline (PBS), pH 7.1. After extrusion, liposomes were purified from any free Rhodamine B using a PD-10 column to ensure that all of the fluorescent probe was attached to the liposomes. Liposomes were then incubated with the bs-MAb for a period of at least one hour.

Two different cell lines were used in the study. OVCAR-3 is a human ovarian cancer cell line that is known to express the antigen CA-125 and SKOV-3 is a human ovarian cancer cell line that does not express CA-125. Cells of these lines were grown on different microscope slides and prior to the confocal imaging, they were incubated with the liposome – bs-MAb prepration for approximately two hours. After this incubation, the microscope slides were washed three times with PBS to remove the unbound liposomes and the slides were imaged on a laser scanning confocal microscope (Zeiss LSM 510). This work was not intended to provide a quantitative measure of the binding kinetics of the liposomes. Instead it served only to show that the liposomes would bind to the surface of the OVCAR-3 cells and not the SKOV-3 cells.

4.5.1.2 Results

Figure 4.7 shows three views of an OVCAR-3 cell labeled with rhodamine liposomes. Panel A is the phase contrast image of the cell to provide a spatial reference. Panel B is the fluorescent signal taken from the same image area. In panel C, the fluorescent image from B has been superimposed on the light field image to visualize the spatial localization of the liposomes on the cell. Each red dot is interpreted to be an individual liposome that has successfully attached to the cell. Figure 4.8 shows the same series of images for an SKOV-3 cell. Clearly there is no fluorescent signal present, suggesting that the liposomes were not able to bind to these cells. This is important because it supports the claim that the fluorescent signal seen in Figure 4.7 results from the active targeting of the CA-125 on the surface of the OVCAR-3 cells. If the binding had resulted from another mechanism unrelated to the targeting moiety, it would likely have also been seen in the SKOV-3 images. These results were typical of the cells imaged from these slides. Time and resources prevented a more thorough investigation of the targeting using confocal microscopy.

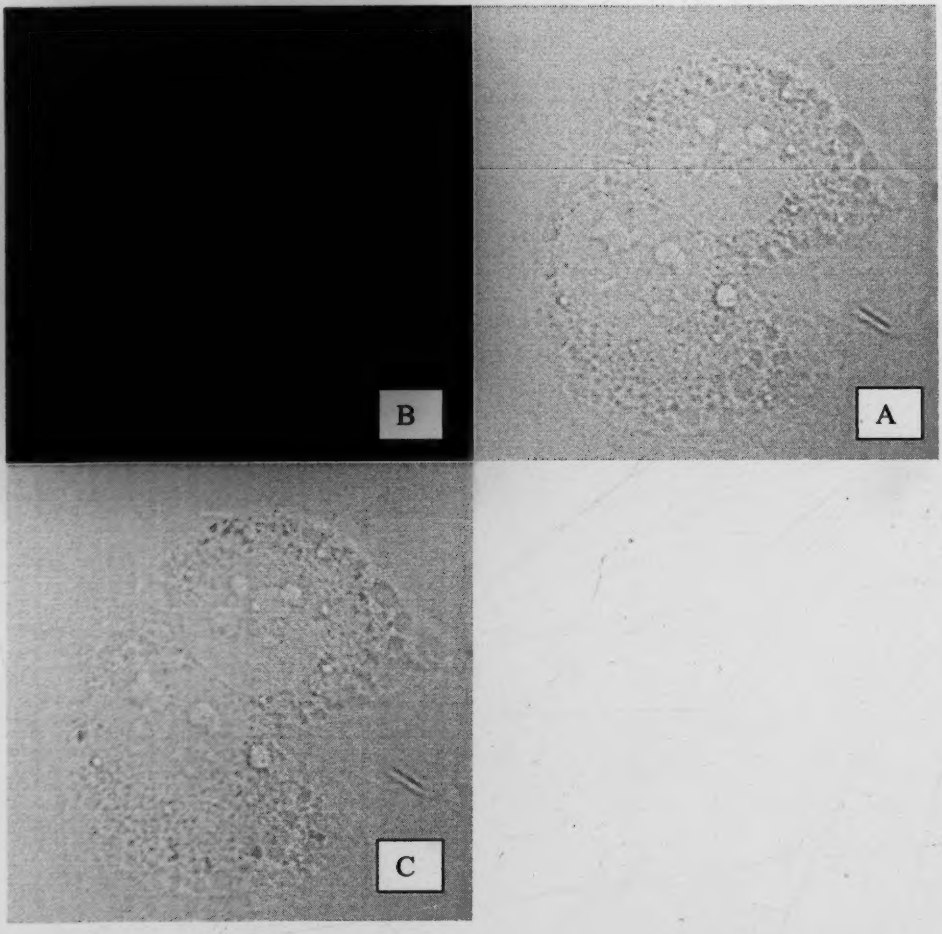

Figure 4.7: Confocal microscopy images of a pair of liposome-labeled OVCAR-3 cancer cells. Panel A is a phase contrast image of the cells. Panel B is the fluorescent signal from the cells. Panel C shows the fluorescent signal superimposed on the phase contrast image. There appears to be significant labeling of the cells with liposomes.

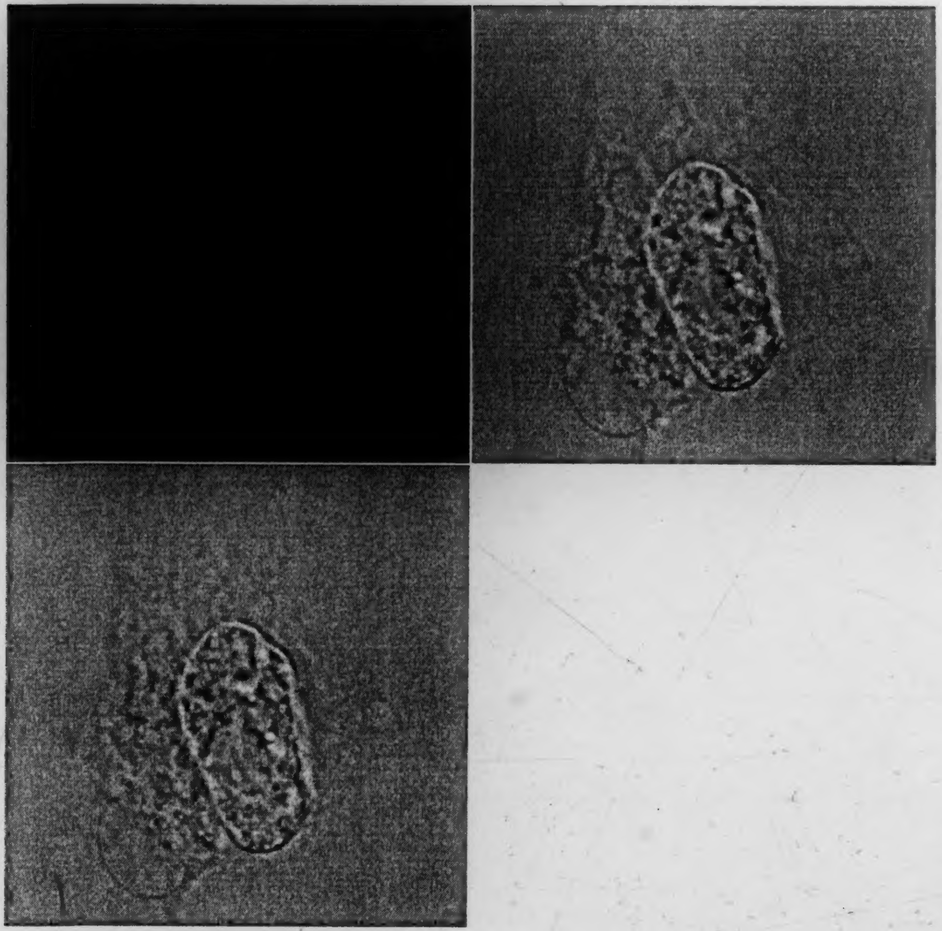

Figure 4.8: Confocal microscopy images of an SKOV-3 cell. SKOV-3 cells do not express CA-125. Panel A is the phase contrast image of the cell. Panel B is the fluorescent signal from the cell. Panel C shows the fluorescent signal superimposed on the phase contrast image. There does not appear to be any labeling of this cell with liposomes.

4.5.2 Radiolabeling of Liposomes

The radiolabeling experiments involved Y-90 which has been shown to bind to the chelating agent DTPA. The radiolabeling experiments investigated the effects of the labeling mixture, labeling time and liposome concentration on the labeling efficiency. A simple stability study of the labeled liposomes was also performed.

4.5.2.1 Materials and Methods

Liposomes were prepared in the manner described in section 4.2. The resuspension buffer was 1 M sodium acetate. Yttrium-90 was purchased as YCl_3 from Perkin Elmer.

4.5.2.2 Labeling Mixture

The ingredients chosen for the reaction mixture were based on the work of Pandey *et al.* (2002). Metallic yttrium is insoluble at neutral pH, so it is supplied in 0.05 M HCl. The sodium acetate in the liposome solution serves to convert the YCl into Y-acetate which will remain soluble at more physiological pHs. With four carboxylic acid groups available in the coordination complex of DMPE-DTPA, Y-acetate will donate the yttrium atom to the DTPA compound because it will reside in a lower energy state and will therefore be more stable. Isotonic saline solution was also used in the reaction mixture. Unless otherwise stated, the activity of Y-90 used in each experiment was low; on the order of 1 – 20 μCi per preparation.

4.5.2.3 Results

Evidence of labeling was taken from the elution profiles of PD-10 size exclusion chromatography columns. If only partial labeling were achieved, it would be necessary to differentiate between Y-90 bound to the liposomes and free Y-90. To test this, a sample was prepared in which 200 μL Na-acetate (pH 4), 500 μL saline and 50 μL Y-90 (approximately 5 μCi) were mixed for two minutes and then passed down a PD-10 column. No liposomes were used in this experiment. The eluent was collected in 1 mL fractions and then taken for bremsstrahlung counting in a gamma counter. Figure 4.9 shows the elution profile of this sample.

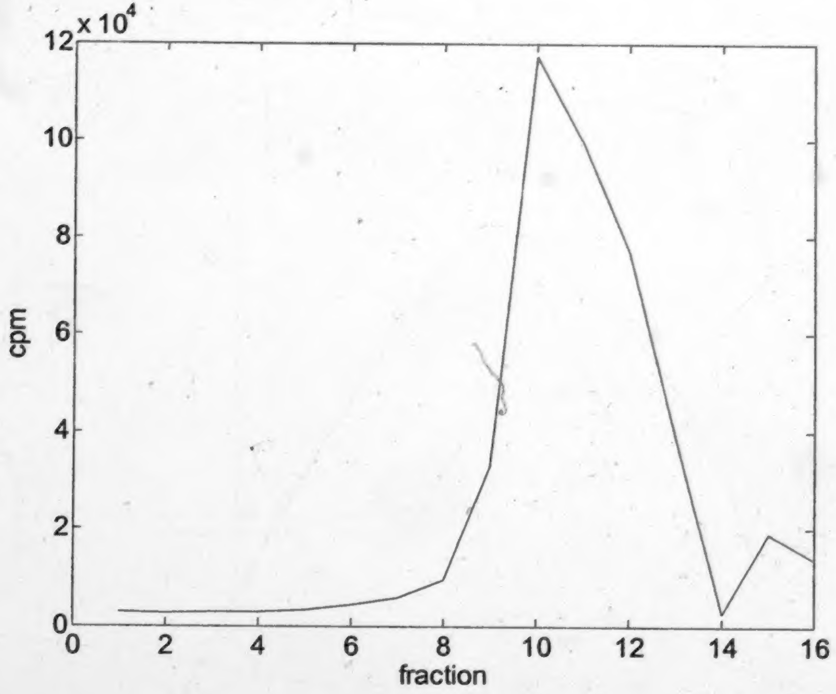

Figure 4.9: Elution profile of a liposome-free Y-90 sample. The radioactivity peaks in fraction 10 which is where a small molecule such as Y-acetate would be expected to be eluted.

Yttrium-acetate is a small molecule that should follow the tortuous route through the size exclusion column beads described previously. This is consistent with these results in which the radioactivity peaks in fraction 10. The number of variations of this labeling procedure was large, involving different volumes of reagents over a range of pH values of Na-acetate. Only selected results will be presented here that provide evidence to support our claim that we were able to develop a simple labeling procedure with excellent labeling efficiency.

To validate the hypothesis that a PD-10 column could separate labeled liposomes from free radioactivity, another sample was prepared in which 300 μL of DTPA-liposomes (Na-acetate pH 6) were incubated with 50 μL of Y-90 and no saline at room temperature for three hours. The elution profile of this sample is shown in Figure 4.10. A sample of concentrated liposomes appears cloudy to the naked eye and when it is passed down a PD-10 column, the only fractions to retain the cloudy appearance are fractions 3, 4 and 5, with fraction 4 being the cloudiest. Thus, the appearance of a large peak of radioactivity at fraction 4, spanning fractions 3 – 5 corresponded to radiolabeled liposomes. There was clear separation between the liposome peak and the free radioactivity which peaks at fraction 10 as it did in Figure 4.9. This is important because an injectable radiopharmaceutical preparation must be virtually free of unbound radioactivity.

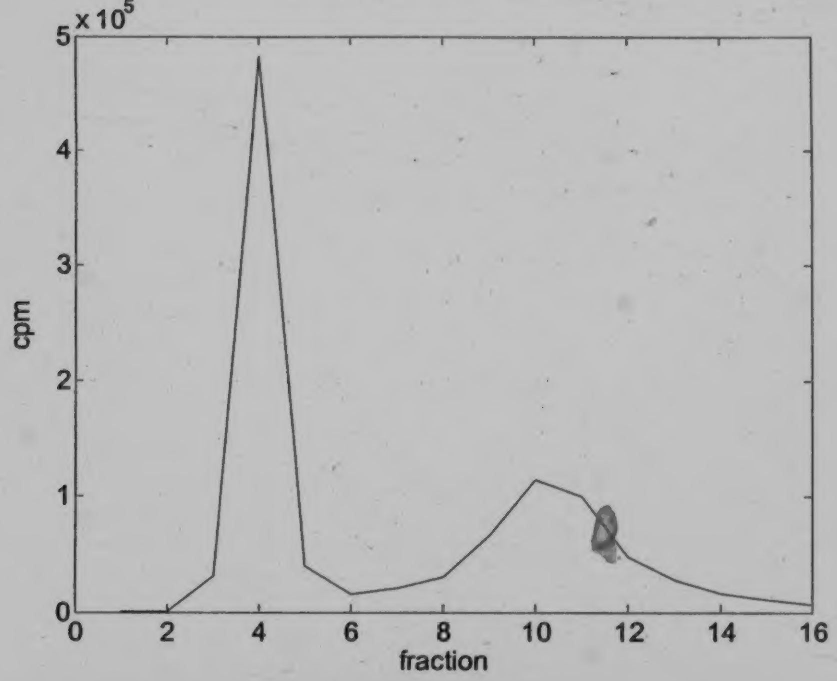

Figure 4.10: Elution profile of a sample with incomplete labeling of Y-90 to DTPA-liposomes. The radioactivity associated with the liposomes peaks in fraction 4 and can be clearly differentiated from the free radioactivity that peaks in fraction 10 as it did when no liposomes were used.

A significant improvement in labeling efficiency was observed when saline was introduced into the reaction mixture. Figure 4.11 shows the elution profile from a sample prepared when 200 μL of liposomes (pH 6), 200 μL of saline and 50 μL of Y-90 were incubated for 3 hours at room temperature. All of the radioactivity associated with this sample was found between fractions 3 and 5. Most importantly, there was no free yttrium tail observed at fraction 10 suggesting that virtually all of the yttrium was bound to the liposomes.

A final variation examined a change in the relative proportion of the reaction components and the total reaction volume. A total of 10 μL of liposomes (pH 6), 10 μL of saline and 10 μL of Y-90 were incubated at room temperature for 3 hours. The elution profile of this sample was the same as that in Figure 4.11 with all of the radioactivity being eluted between fractions 3 and 5 with no free yttrium tail (data not shown).

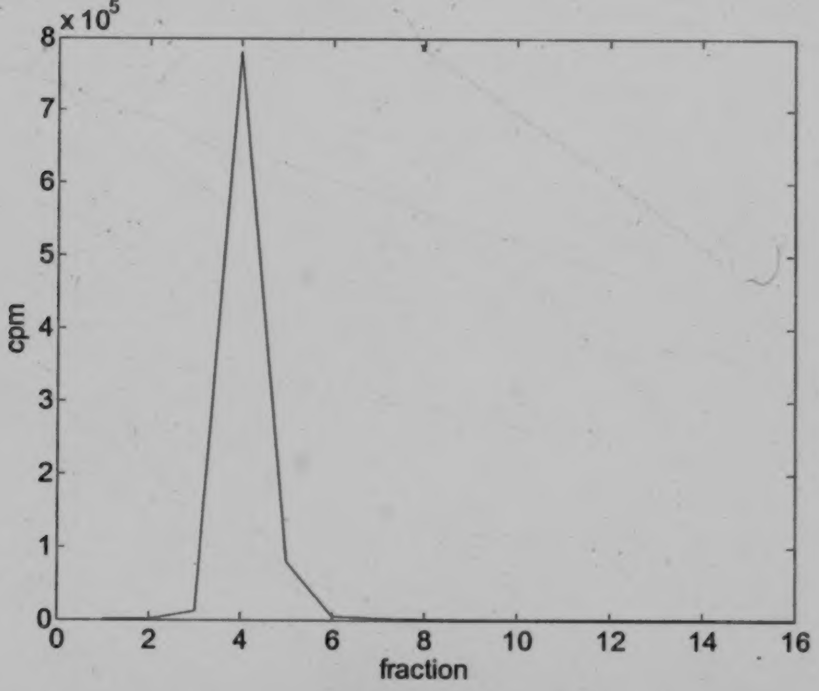

Figure 4.11: Elution profile of sample prepared by incubating 200 μL of liposomes (pH 6), 200μL of saline and 50 μL of Y-90 at room temperature for 3 hours. No free yttrium tail is observed at fraction 10 suggesting that all of the radioactivity was labeled to the liposomes.

The effect of the incubation time was investigated by preparing four identical samples containing 10 μL of liposomes (pH 6), 10 μL of saline and 10 μL of Y-90. Samples were incubated for 1, 2, 3 or 6 hours and then passed down a PD-10 column. The percentage of radioactivity labeled to the liposomes was determined by taking the ratio of the counts in the liposome peak of the elution profile to the total number of counts loaded on the column. Figure 4.12 reveals how the labeling efficiency changed as a function of incubation time.

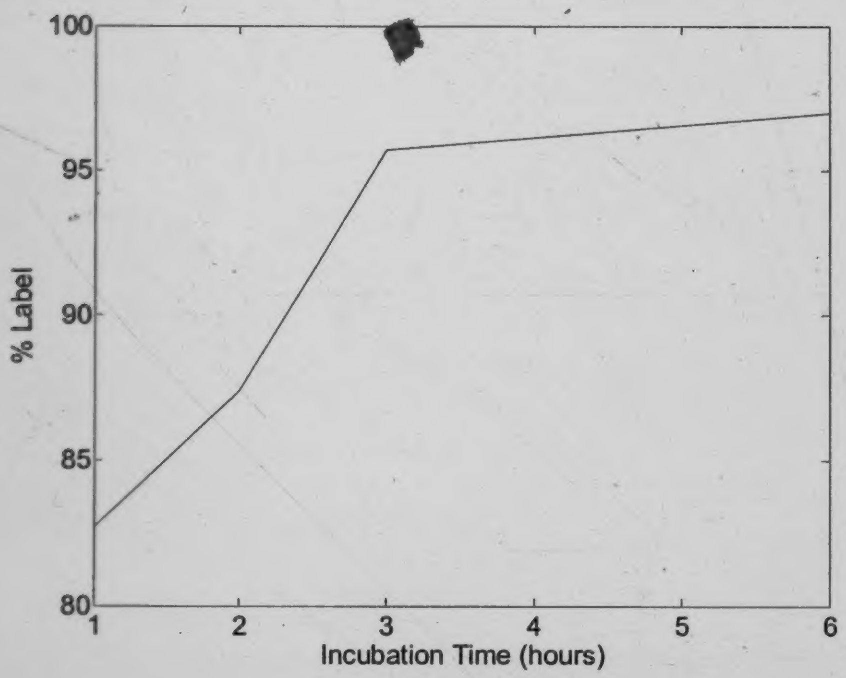

Figure 4.12: Labeling efficiency as a function of incubation time. After three hours of incubation at room temperature, the reaction mixture consisting of 10 μL of liposomes (pH 6), 10 μL of saline and 10 μL of Y-90 produced almost complete labeling of the liposomes.

After three hours of incubation, the labeling efficiency reached 96% and improved only slightly after a six hour incubation. In both the three and six hour incubations, no free yttrium tail was observed in the elution profile and a small amount of radioactivity was retained on the PD-10 columns, suggesting that the labeling efficiency might actually be closer to 100%. It was not possible to determine the labeling status of the yttrium trapped on the column, so this remains a speculative statement.

To investigate the effect of liposome concentration in the reaction mixture, an experiment was performed in which four samples were labeled. The first sample, designated as the stock, was prepared with 4 mg of DSPC in 2 mL of saline along with the other lipid components in the molar ratios given in section 4.4. The other three samples were 10, 100 and 1000 fold dilutions of the stock solution. Each reaction mixture consisted of 10 μL of liposomes (pH 6), 10 μL of saline and 10 μL of Y-90. The elution profiles of all of the samples are shown in Figure 4.13.

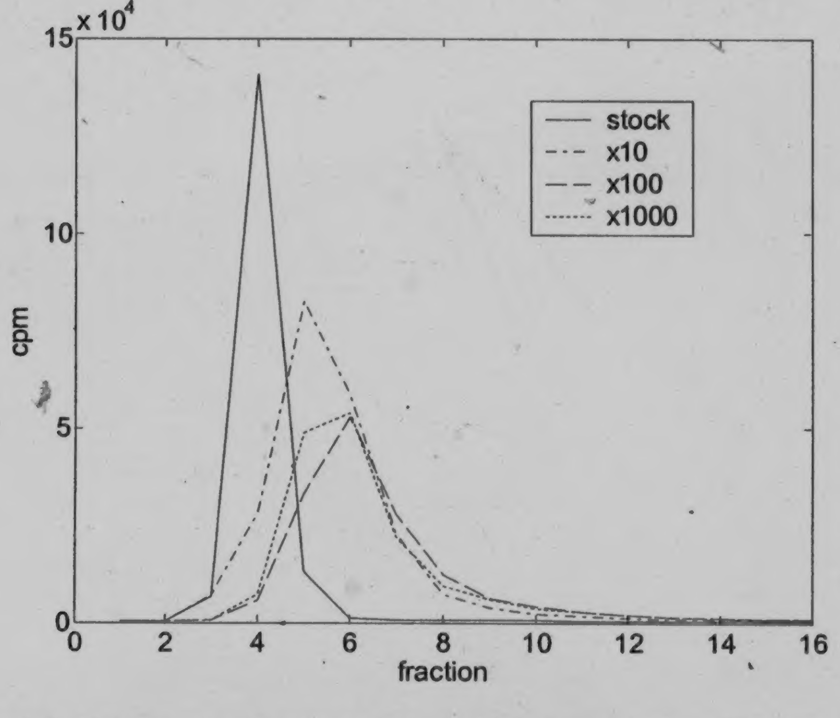

Figure 4.13: Elution profiles of samples labeled with different concentrations of liposomes. Samples were prepared with the stock solution of liposomes as well as dilution factors of 10, 100 and 1000. Dilute samples show a peak broadening effect and shift to the right.

As the concentration of the liposomes was decreased, the liposome peak in the elution profile broadened and shifted to the right so that the largest number of counts appeared in fraction 5 or 6. To verify that this was in fact still a liposome peak, another experiment was carried out in which a larger amount of radioactivity (20 μCi) was labeled to a 1000 fold dilution of the liposome stock solution. The reaction mixture was the same as that of the previous experiment and the elution profile is shown in Figure 4.14.

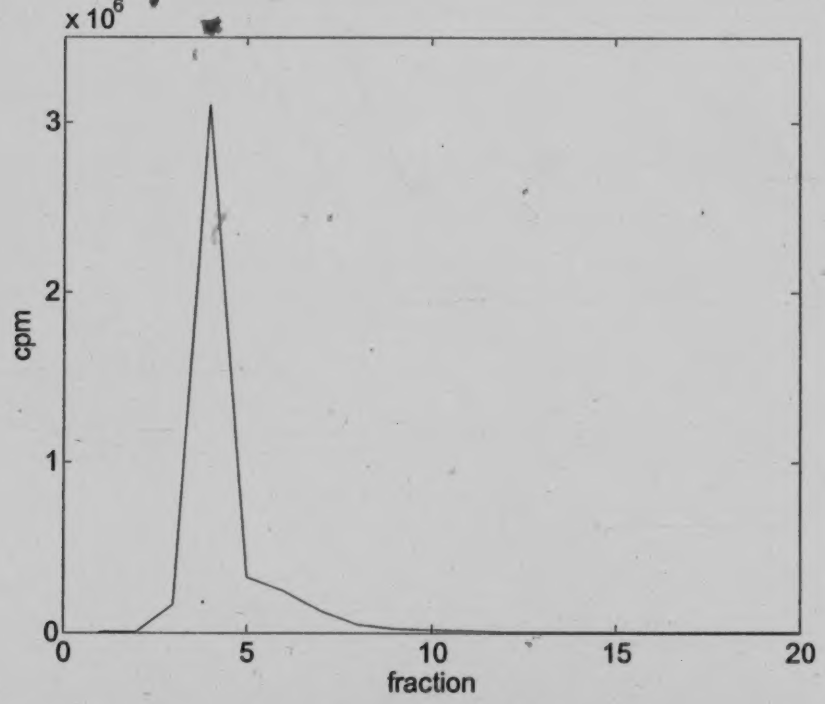

Figure 4.14: Elution profile of dilute liposomes labeled with Y-90. The dilute nature of the sample produced a broadening of the liposome peak, a phenomenon known to occur in size exclusion chromatography.

In this profile, the peak appears in fraction 4 but the tail extends out to fraction 9 or 10. To verify that the counts in the tail were still labeled liposomes, the contents of fraction 8 were passed down another PD-10 column. The hypothesis of this experiment was that if fraction 8 contained liposomes, the new elution profile should shift to the left. This proved to be the case as shown in Figure 4.15. Although the maximum number of counts is observed in fraction 6, the tail of this profile extends beyond fraction 10, suggesting that there could be an unbound yttrium component to this sample.

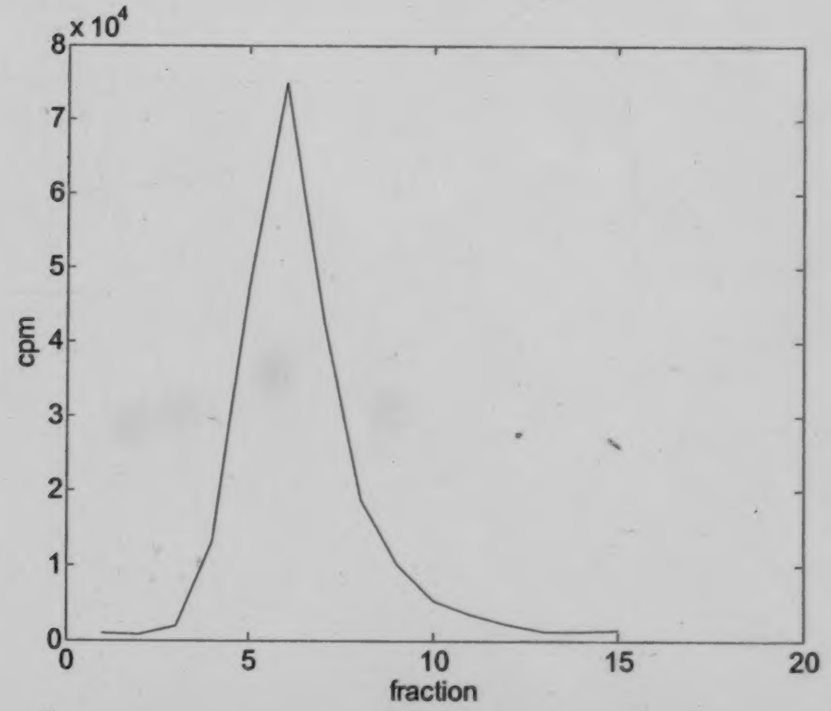

Figure 4.15: Elution profile produced when fraction 8 from Figure 4.14 was passed down a second PD-10 column. The peak in this case appears in fraction 6 suggesting that the counts in the tail of the peak in Figure 4.14 are still primarily liposome counts. The fact that this profile extends beyond fraction 10 suggests that there could be an unbound yttrium component present.

The stability of the labeled liposome preparation was also of interest. A sample was prepared from 10 μL of stock liposomes (pH 6), 10 μL saline and 10 μL Y-90 and incubated for 3 hours at room temperature. The sample was then passed down a PD-10 column. Fraction 4 contained the majority of the counts and there was no free yttrium tail. Fraction 4 was kept at room temperature for several days. Every 24 hours, an aliquot was taken from fraction 4 and passed down a PD-10 column. The ratio of the counts in the liposome peak to the counts loaded on the column was taken as the percentage still labeled to the liposomes. The stability profile of the liposomes is shown in Figure 4.16. The amount of radioactivity that remained attached to the liposomes decreased over time, reaching approximately 79% after 24 hours and 62% after 72 hours.

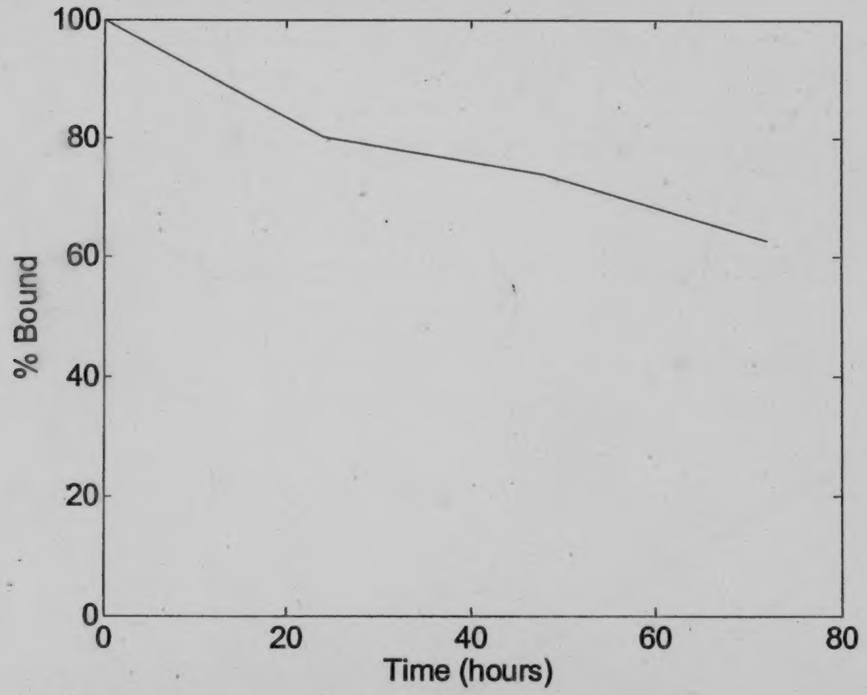

Figure 4.16: Stability profile of Y-90-labeled liposomes. Liposomes were kept at room temperature for 72 hours after labeling. Every 24 hours, an aliquot of liposomes was passed down a PD-10 column. The ratio of counts in the liposome peak to the total number of counts loaded on the column was used to determine the percentage of radioactivity still bound to the liposomes.

4.6 Conclusion

The two major objectives of liposome design were successfully met. The biotinylated liposomes created for this project were shown by laser scanning confocal microscopy to target CA-125-expressing cells via a bsMAb that recognized both CA-125 and biotin. Furthermore, the liposomes did not target a second cell line that did not express CA-125. The liposomes were also successfully labeled with Y-90. A simple labeling procedure was developed and optimized in terms of reaction components, volumes and incubation time. Purification of samples using the optimized conditions revealed labeling efficiencies close to 100% over four orders of magnitude of liposome concentration. The stability study showed that yttrium was released from the liposomes over time. The retained fraction decreased to 79% after 24 hours and 62% after 72 hours.

References

Alberts B, Bray D, Lewis J, Raff M, Roberts K and Watson J 1994 Molecular Biology Of The Cell. 3rd Edition. Garland Publishing Inc. New York. p 478.

Allen T M, Hansen C and Rutledge J. 1989 Liposomes With Prolonged Circulation Times: Factors Affecting Uptake By Reticuloendothelial And Other Tissues. *Biochim. Biophys. Acta.* **981** 27 – 35.

Allen T M, Hansen C B and Stuart D D. 1998b Targeted Sterically Stablized Liposomal Drug Delivery. Chapter 4.6 in Medical Applications Of Liposomes (Lasic and Papahadjopoulos editors). Elseveir Science

Allen T, Lopez de Menezes D, Hansen C and Moase E. 1998a Stealth Liposomes For The Targeting Of Drugs In Cancer Therapy. pp 61 – 71 in Targeting of Drugs 6: Strategies For Stealth Therapeutic Systems (Gregoriadis and McCormack editors). Plenum Press, New York.

Allen T M and Stuart D D. 1999 Liposome Pharmacokinetics: Classical, Sterically Stabilized, Cationic Liposomes And Immunoliposomes. Chapter 3 in Liposomes: Rational Design (Janoff A S editor), pp 63-87. Marcel Dekkar, New York.

Delrieu P and Ding L. 1999 United States Patent #1061: Stablized Liposomes.

Frezard F. 1999 Liposomes: From Biophysics To The Design Of Peptide Vaccines. Braz. J. Med. Biol. Res. **32** 181 – 189.

Froidevaux S and Eberle A N. 2002 Somatostatin Analogs And Radiopeptides In Cancer Therapy. *Biopolymers.* **66** 161 – 183.

Froidevaux S, Heppeler A, Eberle A N, Meier A-M, Hausler M, Beglinger C, Behe M, Powell P and Macke H R. 2000 Preclinical Comparison In AR4-2J Tumor-Bearing Mice Of Four Radiolabeled 1,4,7,10-Tetraazacyclododecane-1-4-7-10-Tetraacetic Acid-Somatostatin Analogs For Tumor Diagnosis And Internal Radiotherapy. Endocrinology **141** 3304 – 3312.

Krenning E P, de Jong, M, Kooij P P M, Breeman W A P, Bakker W H, de Herder W W, van Eijck C H J, Kwekkeboom D J, Jamar F, Pauwels S and Valkema R. 1999 Radiolabelled Somatostatin Analogue(s) For Peptide Receptor Scintigraphy And Radionuclide Therapy. *Ann. Oncol.* **10** (suppl 2) S23 – S29.

Kwekkeboom D J, Kooij P P, Bakker W H, Macke H R, Krenning E P. 1999 Comparison Of ^{111}In-DOTA-Tyr^{3}-Octreotide And ^{111}In-DTPA-Octreotide In The Same Patients: Biodistribution, Kinetics, Organ And Tumor Uptake. *J. Nucl. Med.* **40** 762 – 767.

Lasic D D and Papahadjopoulos D. 1995 Liposomes Revisited. *Science.* **267** 1275 – 1276.

McQuarrie SA, Xiao Z, Miller GG, Mercer JR and Suresh MR 2001 Modern Trends In Radioimmunotherapy Of Cancer: Pretargeting Strategies For The Treatment Of Ovarian Cancer. *Quart. J. Nucl. Med.* **45** 160-166.

Otte A, Herrmann R, Heppeler A, Behe M, Jermann E, Powell P, Maecke H R and Muller J. 1999 Yttrium-90 DOTATOC: First Clinical Results. *Eur. J. Nucl. Med.* **26** 1439 – 1447.

Pandey U, Mukherjee A, Sarma H D, Das T, Pillai M R A and Venkatesh M. 2002 Evaluation Of ^{90}Y-DTPA and ^{90}Y-DOTA For Potential Application In Intra-Vascular Radionuclide Therapy. *Appl. Radiat. Isotopes.* **57** 313 – 318.

Papahadjopoulos D, Allen T M, Gabizon A, Mayhew E, Matthay K, Huang S K, Lee K D, Woodle M C, Lasic D D, Redemann C and Martin F J. 1991 Sterically Stablized Liposomes: Improvements In Pharmacokinetics And Antitumor Therapeutic Efficacy. *Proc. Natl. Acad. Sci. USA.* **88** 11460 – 11464.

Safavy A, Smith Jr. D C, Bazooband A and Buchsbaum D J. 2002 De Novo Synthesis Of A New Diethylenetriaminepentaacetic Acid (DTPA) Bifunctional Chelating Agent. *Bioconjugate Chem.* **13** 317 – 326.

Smith-Jones P M, Stolz B, Alberta R, Ruser G, Briner U, Macke H R and Bruns C. 1998 Synthesis And Characterisation Of [^{90}Y]-Bz-DTPA-oct: A Yttrium-90-Labelled Octreotide Analogue For Radiotherapy Of Somatostatin Receptor-Positive Tumours. *Nuc. Med. Biol.* **25** 181 – 188.

van Gog F, Visser G, Stroomer J, Roos J, Snow G and van Dongen G 1997 High Dose Rhenium-186-Labeling Of Monoclonal Antibodies For Clinical Application: Pitfalls And Solutions. *Cancer Supplement* **80** 2360-2370.

Vander A, Sherman J and Luciano D. 1994 Human Physiology, 6th Edition. McGraw-Hill Inc., New York

Xiao Z, McQuarrie S A, Suresh M R, Mercer J R, Gupta S and Miller G G. 2002 A Three-Step Strategy For Targeting Drug Carriers To Human Ovarian Carcinoma Cells *In Vitro*. *J. Biotechnol.* **94** 171 – 184.

Chapter 5

Dose-Rate Profiles In Microscopic Spherical Tumours

5.1 Introduction

This work was inspired by a novel, targeted approach to i.p. radionuclide therapy that is currently being investigated at the University of Alberta (Xiao *et al.* 2002, McQuarrie *et al.* 2001). Long-circulating immunoliposomes are being used as the delivery vehicle for the radioactive cargo. These are lipid vesicles that have bs-MAbs incorporated into their formulation to facilitate tissue targeting. The liposomes used in this project have a mean diameter of 150nm and the radioactive cargo is bound to the outer surface of the vesicles. The large size of the liposomes compared to antibodies provides two potential benefits: an enhanced radioactive cargo and decreased escape from the peritoneal cavity.

Although larger than antibodies, the immunoliposomes used in this work are sufficiently small that they can be modeled as point sources.

In addition to retarding the progression of macroscopic disease established on the surfaces of the cavity, i.p. therapy can also slow the creation of additional secondary tumours by attacking the microscopic disease that diffuses through the peritoneal fluid. This chapter focuses on the dosimetry of these free-floating micrometastases. Although the MIRD (Loevinger *et al.* 1988) formalism is capable of dealing with non-uniform activity distributions (Bolch *et al.* 1999), it is often employed with a simplifying assumption of a uniform distribution of radioactivity. Numerous authors have published absorbed fractions for different radionuclides and tumour sizes with uniform activity distribution (Goddu *et al.* 1994, Sarfaraz *et al.* 1999, Humm 1986 and Bardies *et al.* 1994). Studies on multicell spheroids have shown, however, that radiolabeled whole antibodies will localize mainly on the tumour surface with penetration to three cell layers (Sutherland *et al.* 1987). Smaller antibody fragments are able to reach a depth of eight to ten cell layers (Sutherland *et al.* 1987). For this application, the size of the liposomes (150 nm) suggests that the assumption of no tumour penetration is reasonable. Bardiès *et al.* (1990) showed that in this case, an average tumour dose is not sufficient to fully describe the tumour dosimetry because the same average dose can be achieved with significantly different dose-rate profiles through the tumour.

Radionuclide therapy in the peritoneal cavity provides an interesting study in dosimetry. At the time of administration, all of the injected activity is localized to the same compartment as the tumour tissue being treated. In this particular model, we assume surface binding with no penetration of tumour tissue due to the size of the liposomes. Furthermore, binding will only take place if the tumour tissue is in contact with the radioactive bath. Therefore, tumour dosimetry must involve the simultaneous consideration of both of these source geometries (Roeske *et al.* 1993, Rotmensch *et al.* 1990). These assumptions are significantly different from many previously published radioimmunotherapy dose calculations. Nahum (1996) and O'Donoghue *et al.* (1995) both examined the relationship between tumour size and curability for different radionuclides with uniform tumour activity distribution with no dose contribution from radioactivity outside the tumour. Both demonstrated that lower energy emitters offer an advantage over high energy emitters for sufficiently small tumours. Nahum (1996) found that a higher specific cumulated activity is required to produce a tumour control probability (TCP) of 0.5 for radionuclides such as Re-188 and Y-90 than it is for Cu-67 and I-131 when the tumour radius is less than 0.05cm. At radii greater than 0.1cm, the advantage lies with the high energy emitters. O'Donoghue (1995), on the other hand, found a relationship between probability of cure and tumour radius. For Cu-67 and I-131 optimal tumour radii were 0.1cm and 0.17cm respectively and for Re-188 and Y-90 the radii were 1.3cm and 1.7cm respectively. Jungerman *et al.* (1984) investigated absorbed dose at the cellular level for a number of very low energy emitters as well as Cu-67 and I-131. Their work clearly showed the importance of proper radionuclide selection in radionuclide therapy. For example, they found that the extremely short range of Sb-119 would render this radionuclide ineffective unless it could be transported into the cell. Kwok *et al.* (1985) considered three different non-uniform activity distributions for a tumour with a radius of 6.6mm. The beta-emitters evaluated in the study were P-32 and I-131. For each of the source distributions, the higher energy emitter P-32 produced higher dose-rates throughout the tumour. Buchsbaum *et al.* (1993) and Roberson *et al.* (1992) used autoradiography to report non-uniform activity distributions within tumours after the intraperitoneal administration of radiolabeled antibodies. Buchsbaum *et al.* (1993) also compared the efficacies of I-131 and Y-90-labeled antibodies. They found that antibodies labeled with I-131 produced better results in terms of animal toxicity and tumour growth delay. They attributed these findings to the greater absorbed fraction of the lower energy emitter. The tumour model used in that work involved the subcutaneous injection of human colon cancer cells. As such, their conclusions are not necessarily applicable to the peritoneal micrometastases considered here due to the significant differences in tumour size and source geometries.

This chapter presents the calculated radial dose-rate profiles for small, spherical tumours of various radii, both from unbound activity outside the tumours and from activity bound to the surface of these tumours. Calculations were made for six radionuclides of potential therapeutic application. Section 5.2 describes the dose-rate profiles of tumours submerged in a radioactive bath whose dimensions are much larger than the range of the beta particles. Section 5.3 illustrates dose-rate profiles through tumours arising from the surface-bound radioactivity.

In the following sections, the function $\dot{C}(r)$ is used to denote the dose-rate at a distance r from a point source of activity. The values of this function were taken from calculations by Cross *et al.* (1992) who used Monte Carlo simulations based on the ETRAN code to follow monoenergetic electrons through water. Dose-rates for different radionuclides were calculated by averaging the results of monoenergetic electrons over the appropriate beta spectra. The published data provide dose-rates at relatively small distance intervals, however, the work in this chapter required a finer resolution. Interpolation of the Cross data was performed using Matlab's piecewise cubic hermite interpolating polynomials (pchip). For distances larger than those published by Cross, dose-rates were interpolated by adding one more data point to the set; the point at which the dose-rate is 0. Prestwich *et al.* (1989) reported that previous Monte Carlo calculations suggested that energy loss straggling allowed for energy deposition out to a distance of 1.2

times the Continuous Slowing Down Approximation (CSDA) range. For this work the dose-rate at 1.2 times the CSDA range was set to 0. Figure 5.1 plots the dose-rate versus distance for point sources of a number of radionuclides to show the results of the interpolation of the Cross data. Table 5.1 contains relevant physical data about the six radionuclides used in this work: ^{188}Re, ^{186}Re, ^{32}P, ^{90}Y, ^{67}Cu, and ^{131}I.

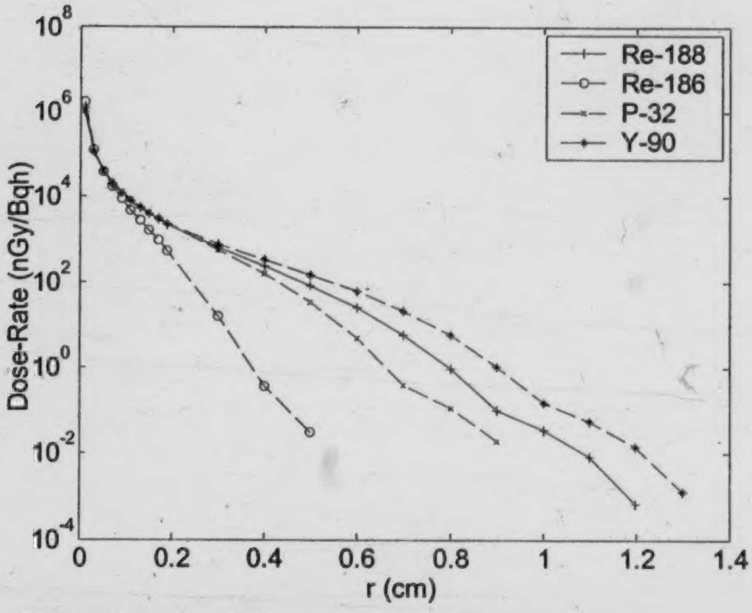

Figure 5.1: Interpolated dose point kernels for four radionuclides. Data from Cross et al. (1992) was interpolated using Matlab's piecewise cubic hermite interpolating polynomials (pchip)

5.2 Radioactive Bath

Activity attached to the liposomes that do not bind to the tumour surface can still contribute to the tumour dose. To model this, we considered a small spherical tumour immersed in a radioactive bath. It was assumed that the

Table 5.1: Physical Properties of Radionuclides

Property	^{188}Re	^{186}Re	^{90}Y	^{32}P	^{67}Cu	^{131}I
$T_{1/2}$ (days)*	0.71	3.78	2.67	14.29	2.58	8.04
E_{max} (MeV)†	2.12	1.072	2.286	1.708	0.577	0.807
E_{ave} (MeV)‡	0.795	0.329	0.935	0.695	0.141	0.181
CSDA range (g/cm^2)†	1.046	0.483	1.13	0.831	0.215	0.337
Equilibrium Dose Rate (nGy/h)/(Bq/mL)§	447	198	539	400	89	109

*From ICRP Publication 38

†From Prestwich *et al.* (1989)

‡From Srivastava and Dadachova (2001)

§Adapted from Zweit (1996)

liposomes do not penetrate into the tumour. In addition, the dimensions of the bath were much larger than the range of the beta particles emitted by the radionuclide in solution so that in the absence of the tumour the bath would be in charged particle equilibrium. The radial profile of dose-rates through a tumour in the bath was calculated by summing the contributions from each volume element of the bath. The spherical symmetry of the problem suggests that this is best accomplished by adding up the contributions of thin concentric spherical shells as illustrated in Figure 5.2.

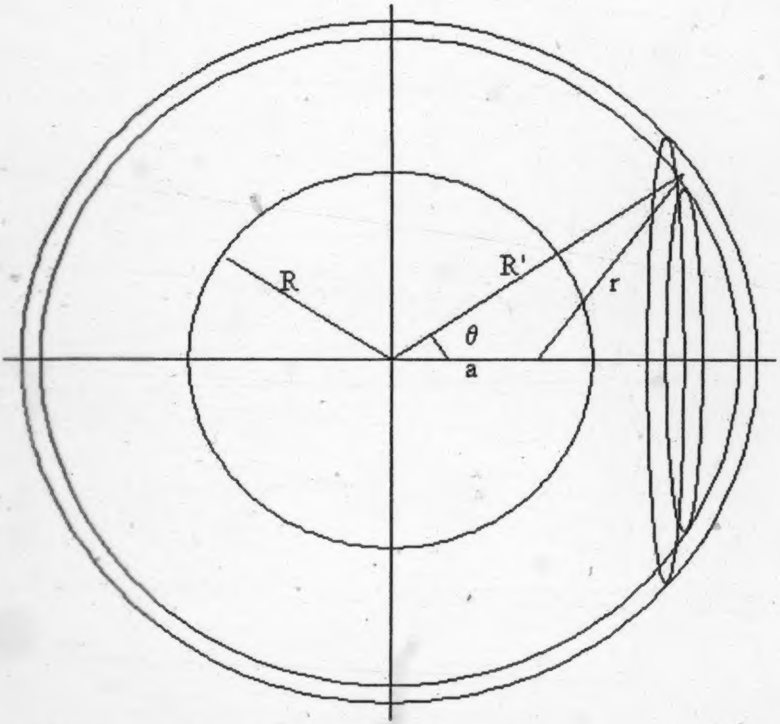

Figure 5.2: Illustration of the calculation of dose-rate at a distance *a* from the center of a tumor submerged in a radioactive bath. Contributions from thin spherical shells are summed over all volumes capable of contributing to the dose at point *a*. R = tumor radius; R' = radius of spherical shell; r = distance from all source elements defined by angle θ to point at distance a.

The dose-rate, $\dot{D}_b(a)$, at a distance *a* from the centre of a tumour of radius *R* is given by:

$$\dot{D}_b(a) = \int \dot{C}(r) A_{Db} dV \qquad (5.1)$$

The subscript *b* denotes calculations for the bath of radioactivity and A_{Db} represents the activity density of the bath in Bq/mL. Within a spherical shell of radius *R'*, all volume elements described by a particular value of θ will make an equal contribution to the dose at point *a* because they all lie at the same distance *r* from the point *a*. Exploiting this azimuthal symmetry, this expression becomes:

$$\dot{D}_b(a) = A_{Db} 2\pi \int_0^{\pi} \int_R^{\infty} \dot{C}(r) R'^2 \sin\theta dR' d\theta \qquad (5.2)$$

The upper bound of the inner integral in reality corresponds to the largest distance from which a point source could deposit energy at the point a. The distance r is itself a function of R' and θ given by:

$$r^2 = R'^2 + a^2 - 2aR'\cos\theta \qquad (5.3)$$

For the purposes of numerical evaluation, the integrals were replaced by summations and dR' and $d\theta$ were replaced with $\Delta R'$ and $\Delta\theta$. To investigate the sensitivity of the calculations to the value of $\Delta R'$, the code was also run to calculate only the dose-rate to the centre of a tumour using smaller values of $\Delta R'$. For a 0.001cm radius tumour with $\Delta R' = 10^{-5}$cm, the dose-rate to the centre of the tumour from Cu-67 was 3.5% lower than the dose-rate produced by the profile code with $\Delta R' = 10^{-3}$ cm. For all other radionuclides and tumour sizes, the results agreed to within approximately 1% of those for which $\Delta R' = 10^{-3}$cm.

5.3 Surface-Bound Radioactivity

Cancer cells that uniquely-express or over-express a surface antigen relative to healthy tissue can be targeted by radiolabeled molecules such as immunoliposomes. In the case of intraperitoneal administration, immunoliposomes would have significant difficulty penetrating to any significant depth into a tumour due to their size and the presence of the surface antigen. Thus, for the purposes of our dose-rate calculations we made the assumption that the carriers would reside entirely on the surface of the micrometastases. The dose-rate, $\dot{D}_s(a)$, at a distance a from the centre of the tumour is calculated by summing the contributions from each element of surface area, dA:

$$\dot{D}_s(a) = \int \dot{C}(r) A_{Ds} dA \qquad (5.4)$$

Here, the subscript *s* refers to the surface and A_{Ds} is the surface activity density in Bq/cm^2. Implicit in these calculations is the assumption that the activity is uniformly distributed over the surface of the tumour. This leads to the expression:

$$\dot{D}_s(a) = A_{Ds} 2\pi \int_0^{\pi} \dot{C}(r) r^2 \sin\theta d\theta \tag{5.5}$$

Figure 5.3 illustrates this geometry.

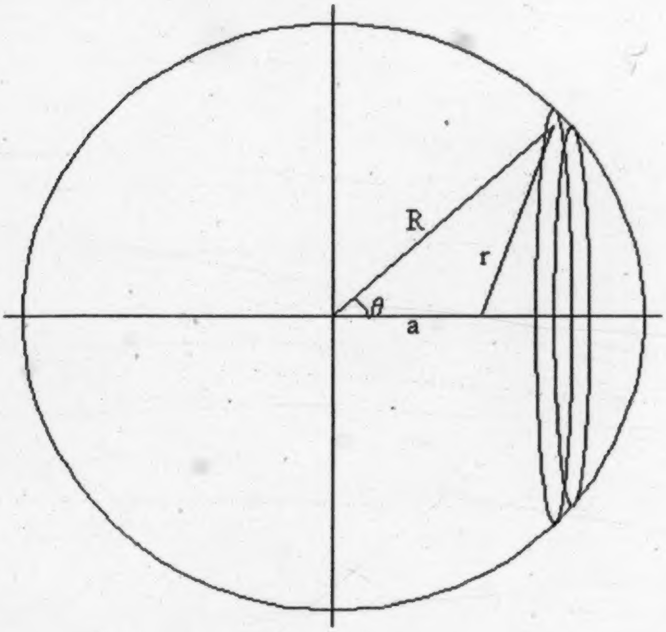

Figure 5.3: Illustration of the calculation of dose-rate at a distance *a* from the center of a tumor with uniform activity distributed over its surface. All elements of surface area described by a particular value of θ will make an equal contribution to the dose-rate at point *a* because they are all located a distance r from that point. R = tumor radius.

Once again, *r* is a function of θ as given by Eq (5.3). The only difference is that R' is now replaced by *R*, the radius of the tumour. The sensitivity of these calculations to the value of $\Delta\theta$ was also investigated. The only differences between the calculations with $\Delta\theta = 10^{-3}$ radians and $\Delta\theta = 10^{-4}$ radians occurred at points close to the outer edge of the tumour where the dose-rate changes very rapidly. Even near the tumour surface, the agreement was to better than 1%, so a value of $\Delta\theta = 10^{-3}$ radians was used due to the savings of computational resources.

5.4 Results

5.4.1 Radioactive Bath

The range of dose-rates produced in a tumour depends on the radius of the tumour and the energy of the beta particles. To illustrate the differences between a high energy emitter and a lower energy emitter, Figure 5.4 is a plot of the dose-rate profiles through tumours of various radii for Re-188 and Cu-67. Rhenium-188 is a high energy emitter with a maximum beta energy of 2.12 MeV and Cu-67 is a lower energy emitter with a maximum energy of 0.577 MeV (Prestwich *et al.* 1989). The abscissa is a dimensionless, scaled radial distance, a / R. Sufficiently small tumours provide only the slightest perturbation to charged particle equilibrium and this is evidenced by flat dose-rate profiles with values approximately equal to the equilibrium dose-rate constant. In Figure 5.4 (b), the dose-rate near the periphery of a 0.001cm tumour exceeds the equilibrium dose-rate given for Cu-67 in Table 5.1. There are two possible explanations for this discrepancy. The problem likely results from the fact that the dose point kernels change extremely rapidly at very small distances from the point source, resulting in a slight overestimation of the dose-rate at the tumour periphery. This problem would be more pronounced in lower energy emitters where the radioacitivity close to the tumour surface represents a greater relative contribution to the total tumour dose-rate than it does for a higher energy emitter due to the longer range of high energy emitters. A second possibility is that the dose point kernels produced by Cross were based on slightly different spectral shapes than those of Zweit (1996). Since the equilibrium dose-rate is based on the mean energy emitted, differences in the spectral shape would produce different values of the equilibrium dose-rate. The first explanation seems to be the most reasonable.

Figure 5.5 is a plot of the dose-rate at the centre of tumours of different radii as a percentage of the equilibrium dose-rate (Zweit, 1996) for several radionuclides. As expected, the rate at which the dose-rate deviates from the equilibrium dose-rate is dependent on the energy of the beta emitter. Higher energy emitters such as Re-188 are able to maintain dose-rates close to the equilibrium dose-rate in larger tumours compared to lower energy emitters like Cu-67 or I-131.

For all tumour sizes, the dose-rates produced by high energy emitters are significantly greater than those of low energy emitters. Re-188 produces dose-rates that are 5 and 264 times greater than that of Cu-67 at the centre of tumours of radii 0.001 cm and 0.1 cm, respectively. Our calculations of the Y-90 dose-rate profiles for 0.05 and 0.1 cm radius tumours appear to agree with those of Humm (1986) who calculated dose-rate profiles across "cold regions" of tumours by assuming that the spherical cold regions are surrounded by uniformly distributed radioactivity; a geometry similar to our "radioactive bath". Appendix 1 contains tables with dose-rate distributions for six different nuclides and five different tumour sizes.

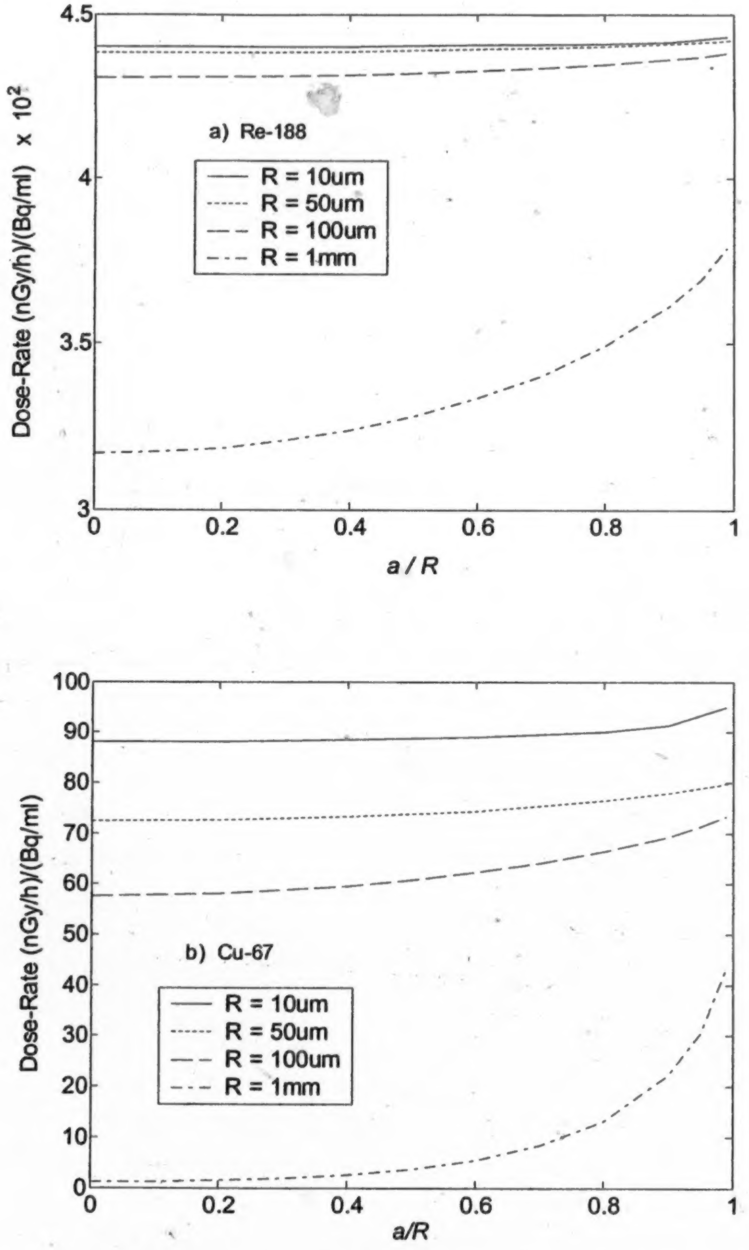

Figure 5.4: Radial dose-rate profiles through tumors submerged in a bath of (a) Re-188 and (b) Cu-67. This is the type of dose distribution produced by a nontargeted therapy. For small tumors the profiles are virtually flat (especially for the high-energy beta emitter Re-188) with dose-rates approximately equal to the equilibrium dose-rates.

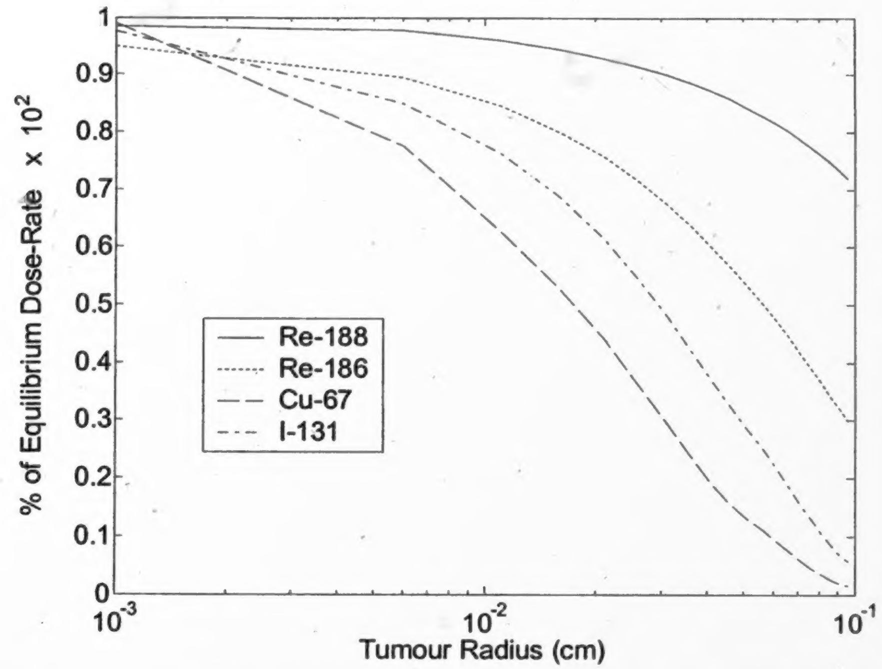

Figure 5.5: Dose-rate at the center of the tumor as a percentage of the equilibrium dose-rate. Charged particle equilibrium is preserved only for very small tumors with all nuclides; however, divergence from equilibrium is significantly quicker with low-energy beta emitters such as Cu-67 or I-131.

5.4.2 Surface-Bound Radioactivity

The profiles produced by surface-bound radionuclides show a much greater range of dose-rates than the non-targeted profiles. This can be seen in Figure 5.6, which shows the dose-rate profiles for Re-188 and Cu-67 for several different tumour sizes. Copper-67 produces a dose-rate that is approximately 2 times that of Re-188 at the centre of a 0.001cm radius tumour. This is because at these energies, the stopping power of water decreases with increasing energy. For a tumour of radius 0.1cm, Re-188 produces a dose-rate that is approximately 20 times higher than that of Cu-67.

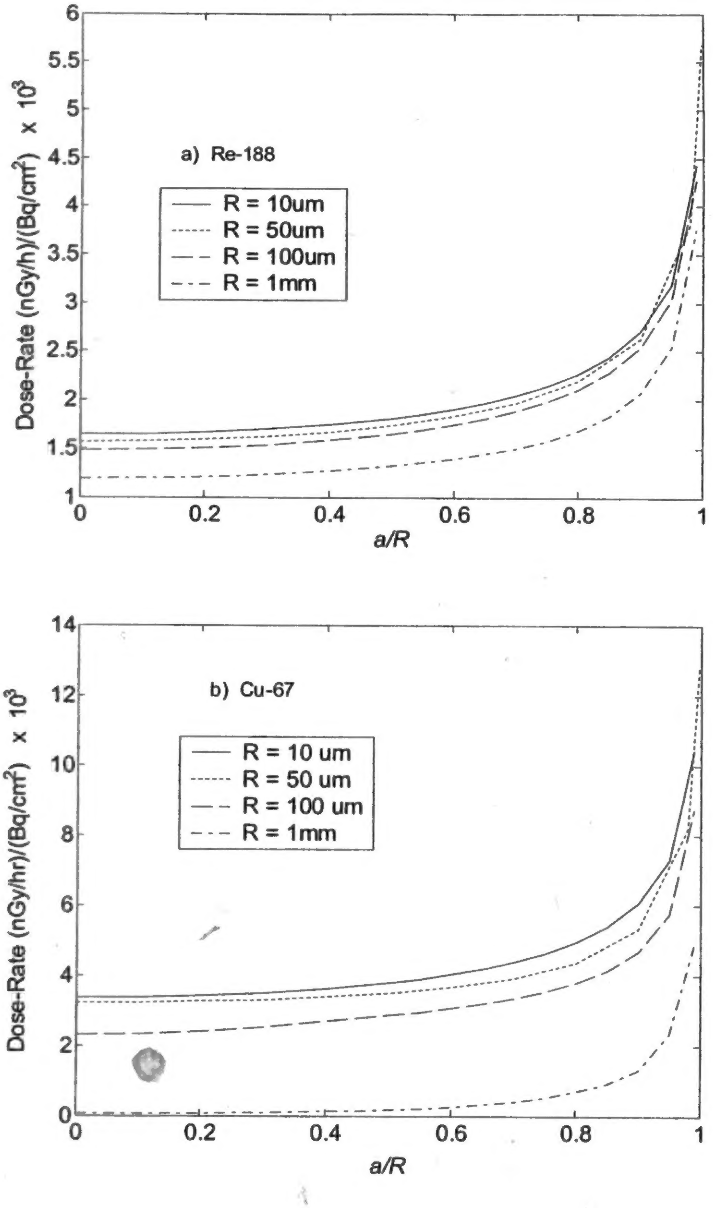

Figure 5.6: Radial dose-rate profiles through tumors with uniform surface distributions of (a) Re-188 and (b) Cu-67. The lower-energy beta emitter, Cu-67, produces significantly higher dose-rates than the high-energy bea emitter, Re-188, in smaller tumors (R = 10 μm, R = 50 μm). By the time the tumor reaches a radius of 1 mm, however, the short range of the Cu-67 betas renders this nuclide ineffective whereas the Re-188 betas are still able to penetrate to the center of the tumor.

Figure 5.7 is a plot of the interpolated dose-rate to the centre of a tumour as a function of tumour radius for both Re-188 and Cu-67 for surface-bound radionuclides. From this data, at a radius of approximately 0.025cm, the two radionuclides produce the same dose-rate at the tumour centre. For tumours larger than this, the ability of the low energy betas to penetrate to the tumour centre is compromised to a larger extent than for high energy betas. Appendix 2 contains tables of dose-rate distributions for six different radionuclides and five different tumour sizes.

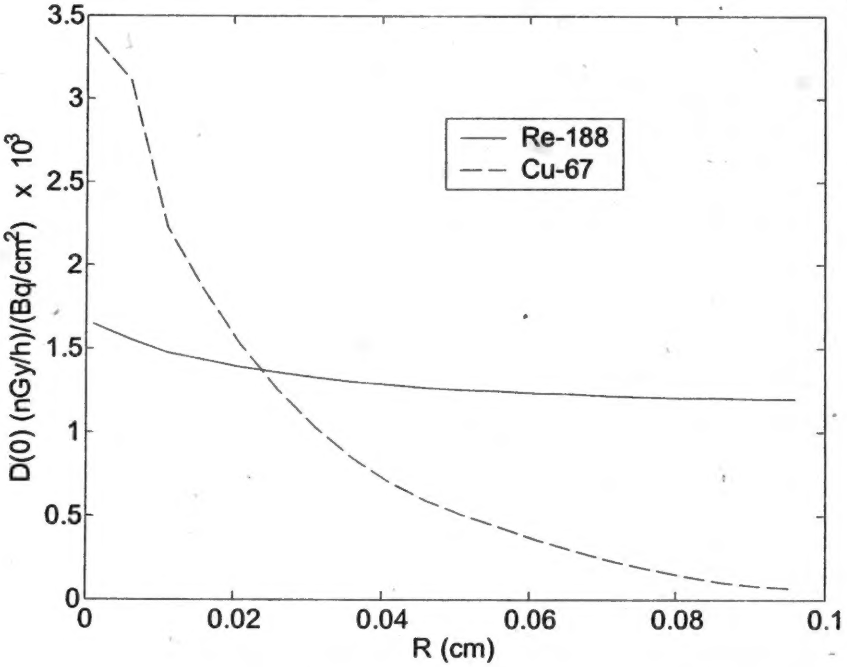

Figure 5.7: Dose-rate to the center of a tumor as a function of tumor radius for surface-bound Re-188 and Cu-67. The low-energy emitter Cu-67 produces higher dose-rates than the high-energy emitter Re-188 for very small tumors. Once the radius of the tumor exceeds approximately 0.025 cm, the high-energy emitter produces higher dose-rates.

We can compare our calculations to those of other investigators. Sarfaraz *et al.* (1999) calculated dose-rate profiles through a 0.05 cm radius tumour in which I-131 had penetrated to varying degrees. Our calculated dose-rate at the centre of the tumour appears to agree well with the case of 0.005 cm penetration. As expected, near the periphery of the tumour, our dose-rate profile changes more quickly than theirs since the penetration mediates the rapid decrease in dose rate predicted for surface-bound radioactivity. Bardiès *et al.* (1990) calculated the dose-rate profiles for surface-bound Y-90 and Cu-67 on a 0.05 cm radius tumour. At the centre of the tumour, our dose-rates appear to be slightly lower than theirs. Since all source elements are assumed to be equidistant from the centre in both models, differences in dose-rates can likely be attributed to the different dose point kernels used for the calculations. Calculations of other groups are not directly relevant here due to differences in assumptions about tumour size and radionuclide penetration (Nahum 1996, O'Donoghue *et al.* 1995, Kwok *et al.* 1985, Werner *et al.* 1988, Werner *et al.* 1991). Langmuir *et al.* (1992) measured the dose profile through 0.1cm diameter multicell spheroids using mini TLDs to provide some experimental validation for calculations based on dose point kernels. Although they were able to observe differences between regions of high and low dose, they concluded that there were significant uncertainties in the measurements. It is difficult to directly compare our results to theirs because they observed some penetration of radioactivity into the tumour tissue and they do not show the full measured dose profile.

5.5 Discussion

Knowledge of the dose-rate distribution within a tumour is necessary to calculate a tumour control probability (TCP). It is particularly important when the dose is delivered by beta particles whose range in tissue is quite small. The highly non-uniform distributions presented here for the larger of the "microscopic" tumours illustrates that an estimate of TCP based on an average tumour dose would likely be inaccurate. Furthermore, the ability of a particular radionuclide to eradicate a tumour is dependent on its ability to deliver a lethal dose to all viable parts of the tumour. This has important implications for radionuclide selection. A study on multicell spheroids by Ballangrud *et al.* (1999) showed that as the cluster grows, the most actively proliferating cells are located in a shell at the outer edge of the cluster. Spheroids with a diameter of 0.04cm contained a core of nonproliferating cells and at a diameter of 0.06cm a necrotic core could be observed. As mentioned previously, studies have shown that, for sufficiently small tumours, a uniform distribution of a low energy emitter within a tumour will be more effective than a high energy emitter because of its greater absorbed fraction (Nahum 1996, O'Donoghue *et al.* 1995). In the case of intraperitoneal injection, however, uniform uptake within a tumour is not likely. Furthermore, while this study has focused on the dosimetry of free-floating micrometastases in the peritoneal fluid, this treatment modality would also aim to treat the cancerous nodules seeded on the walls of the peritoneal cavity that remain after surgery. Very low energy emitters, Auger emitters and alpha emitters whose range in tissue is only a few cell diameters have been omitted from this study because, in this model, with no tumour penetration, these radionuclides would be ineffective in the treatment of all but the smallest micrometastases.

Targeted radionuclide therapy approaches to i.p. therapy clearly offer a tumouricidal advantage. Following the injection of the therapeutic agent into the cavity, the treatment initially provides the same bath of radioactivity that a non-targeted approach does, but offers a potential boost in the dose to the tumour via targeted binding on the tumour surface. The dose-rate profiles shown in Figure 5.6 reveal that the boost offered by this targeted approach can be highly non-uniform within the tumour. This is a consequence of the source geometry and the short range of the beta particles in tissue.

The work presented in this chapter is specific to the case of free floating micrometastases in a bath of radioactivity – a geometry that would be encountered in an i.p. radionuclide therapy technique. Roeske *et al.* (1993) and Rotmensch *et al.* (1990) have investigated the dosimetry for tumours seeded on the wall of the peritoneal cavity and have presented dose profiles along the tumour axis and isodose curves for different tumour geometries. They made assumptions about the amount of bound activity and different tumour sizes were used to illustrate the dose profiles for different radionuclides. This work provides a direct comparison of different radionuclides for given tumour sizes. Understanding the dosimetry of both of these components of cancer in the peritoneal cavity is important for assessing potential treatment protocols.

It should be noted, however, that targeted therapies are in general expensive and may not always offer a significant benefit. For example, the expression of the ovarian cancer surface antigen CA-125 is known to exhibit significant interpatient variability (Harlozinska *et al.* 1997, Molina *et al.* 1998). For patients with very low concentrations of antigen on cell surfaces, therapeutic effects will be largely produced by the bath and not the surface-bound radioactivity. As such, a less expensive, non-targeted preparation may produce a similar clinical outcome. With this dose-rate information, it might be possible to identify an antigen density threshold, below which a targeted approach might not offer a significant advantage.

To illustrate the effect of surface bound activity, consider the following example. If 2 GBq of P-32 in 1 litre of fluid were injected, the activity density of the bath, A_{Db}, would be $2\text{x}10^6$ Bq/mL. From Table A2, the dose-rate per unit activity density at the centre of a 50μm (0.005cm) radius tumour would be 392.7 (nGy/h)/(Bq/mL) giving a total dose-rate of 0.785 Gy/h. If surface-bound activity were able to boost this dose-rate by 5%, this would provide an additional 0.039Gy/h for a total of 0.824 Gy/h. Table A7 shows that the dose-rate to the centre of this tumour from surface-bound activity would be 1314 (nGy/h)/(Bq/cm^2). The required calculated surface activity density would then be 3×10^4 Bq/cm^2. The surface area of a 0.005 cm radius spherical tumour is 3.14×10^{-4} cm^2, resulting in a required activity of 9.4 Bq (1.68×10^7 atoms of ^{32}P). Based on size, composition and labeling technique arguments, we estimate that a single 150 nm diameter liposome should be able to carry on the order of 10^2 to 10^3 atoms of a radionuclide. Using a conservative value of 100 ^{32}P atoms per liposome, this suggests that 1.68×10^5 liposomes must bind to the surface. This translates into a liposome density of 5.35×10^8 cm^{-2}. Assuming the cells have a diameter of 0.001cm, the minimum required antigen number would be approximately 1.7×10^3 per cell (assuming that the density of antigen on the tumour surface is representative of the density on cell surfaces). A similar calculation can be performed for the administration of 2 GBq of a lower energy emitter such as I-131. In this case, the surface antigen concentration would have to be approximately a factor of 5.5 higher in order to produce the same total dose-rate (0.824 Gy/h). This example, based on a highly simplified calculation, is intended to illustrate the utility of this approach. A more rigorous, patient-specific calculation could be based on *in-vitro* measurements of antigen density and binding kinetics to help assess the potential benefit from a targeted therapy compared to a non-targeted therapy.

The lack of tumour penetration by the liposomes, the contribution of the radioactive bath to the tumour dose and the requirement of treating tumour nodules on the surfaces of the peritoneal cavity suggest that an immunoliposome-based approach to intraperitoneal radioimmunotherapy should involve a high energy component. The higher dose-rates produced close to the source of a lower energy emitter might support a cocktail approach, particularly for dealing with proliferative regions near the surface of non-vascularized micrometastases.

5.6 Conclusion

The radial dose-rate profiles for five tumour sizes have been calculated for six different radionuclides of potential use in liposome-based i.p. radionuclide therapy. For each tumour size, two different profiles were calculated. The first represents the dose-rates produced when the tumour is submerged in a uniform radioactive bath. The second represents the profile that results from a uniform distribution of radioactivity targeted to the surface of the tumour. The combination of these two profiles represents the geometry expected for a radionuclide therapy approach to i.p. treatment. The dose-rate profiles produced by the bath of radioactivity showed less variability with high energy emitters (i.e. Y-90 and Re-188) than they did with lower energy emitters (i.e. I-131 and Cu-67). For tumours with a radius of less than 0.01cm, the high energy profiles were virtually uniform and the dose-rate was approximately equal to the equilibrium dose-rate. For low energy emitters, this was only true for radii smaller than 0.005cm. For surface-bound radioactivity the profiles were significantly more non-uniform. Lower energy emitters produce higher dose-rates than high energy emitters for sufficiently small tumours. The results suggest that this particular treatment modality would benefit from the inclusion of a high energy emitter, perhaps as part of a cocktail of radionuclides. This data should be of clinical value because it provides information necessary for tumour control probability estimations and has the potential to help determine the advantage offered by a targeted approach on a patient-specific basis.

References

Ballangrud A M, Yang W H, Dnistrian A, Lampen N M and Sgouros G. 1999 Growth And Characterization Of LNCaP Prostate Cancer Cell Spheroids. *Clin. Cancer Res.* **5** 3171s – 3176s.

Bardies M and Chatal J. 1994 Absorbed Doses For Internal Radiotherapy From 22 Beta-Emitting Radionuclides: Beta Dosimetry Of Small Spheres. *Phys. Med. Biol.* **39** 961 – 981.

Bardiès M, Lamé J, Myers M J and Simoen J P. 1990 A Simplified Approach To Beta Dosimetry For Small Spheres Labelled On The Surface. *Phys. Med. Biol.* **35** 1039 – 1050.

Bolch W E, Bouchet L G, Robertson J S, Wessels B W, Siegel A, Howell R W, Erdi A K, Aydogan B, Costes S and Watson E E. 1999 MIRD Pamphlet No. 17: The Dosimetry Of Nonuniform Activity Distributions—Radionuclide S Values At The Voxel Level. Medical Internal Radiation Dose Committee. *J. Nucl. Med.* **40** 11S – 36S.

Buchsbaum D J, Lawrence T S, Roberson P L, Heidorn D B, Ten Haken R K, Steplewski Z. 1993 Comparison Of 131I- And 90Y-Labeled Monoclonal Antibody 17-1A For Treatment Of Human Colon Cancer Xenografts. *Int. J. Radiat. Oncol. Biol. Phys.* **25** 629 – 638.

Cross W, Freedman N and Wong P. 1992 Tables of Beta-Ray Dose Distributions in Water. *Atomic Energy of Canada Limited publication*: AECL-10521.

Goddu S, Rao D and Howell R. 1994 Multicellular Dosimetry For Micrometastases: Dependence Of Self-Dose Versus Cross-Dose To Cell Nuclei On Type And Energy Of Radiation And Subcellular Distribution Of Radionuclides. *J. Nucl. Med.* **35** 521 – 530.

Harlozinska A, Sedlaczek P, Van Dalen A, Rozdolski K, Einarsson R. 1997 TPS and CA 125 Levels In Serum, Cyst Fluid And Ascites Of Patients With Epithelial Ovarian Neoplasms. *Anticancer Res.* **17** 4473 – 4478.

Humm, J. 1986 Dosimetric Aspects Of Radiolabeled Antibodies For Tumor Therapy. *J. Nucl. Med.* **27** 1490 – 1497.

ICRP Publication 38. 1983 Radionuclide Transformations, Energy and Intensity of Emissions. Pergamon Press, Oxford.

Jungerman J A, Yu K P and Zanelli C I. 1984 Radiation Absorbed Dose Estimates At The Cellular Level For Some Electron-Emitting Radionuclides For Radioimmunotherapy. *Int. J. Appl. Radiat. Isot.* **35** 883 – 888.

Kwok C, Prestwich W and Wilson B. 1985 Calculation Of Radiation Doses For Nonuniformly Distributed β and γ Radionuclides In Soft Tissue. *Med. Phys.* **12** 405 – 412.

Langmuir V K, Wessels B W, Mendonca H, Yorke E D and Montilla L. 1992 Comparisons Of Sectioned Micro-TLD Dose Measurements With Predicted Dose From ^{131}I-Labeled Antibody. *Med. Phys.* **19** 1213 – 1218.

Loevinger R, Budinger T and Watson E. 1988 MIRD Primer For Absorbed Dose Calculations. The Society of Nuclear Medicine, New York.

McQuarrie SA, Xiao Z, Miller GG, Mercer JR and Suresh MR 2001 Modern Trends In Radioimmunotherapy Of Cancer: Pretargeting Strategies For The Treatment Of Ovarian Cancer. *Quart. J. Nucl. Med.* **45** 160-166.

Molina R, Filella X, Jo J, Agusti C and Ballesta AM. 1998 CA 125 in biological fluids. *Int. J. Biol. Markers.* **4** 224 – 230.

Nahum A. 1996 Microdosimetry And Radiocurability: Modelling Targeted Therapy With β-Emitters. *Phys. Med. Biol.* **41** 1957 – 1972.

O'Donoghue J A, Bardies M and Wheldon T E. 1995 Relationships Between Tumor Size And Curability For Uniformly Targeted Therapy With Beta-Emitting Radionuclides. *J. Nucl. Med.* **36** 1902 – 1909.

Prestwich W, Nunes J and Kwok C. 1989 Beta Dose Point Kernels for Radionuclides of Potential Use in Radioimmunotherapy. *J. Nucl. Med.* **30** 1036 – 1046.

Roberson P L, Buchsbaum D J, Heidorn D B and Ten Haken R K. 1992 Three-Dimensional Tumor Dosimetry For Radioimmunotherapy Using Serial Autoradiography. *Int. J. Radiat. Oncol. Biol. Phys.* **24** 329 – 334.

Roeske J, Chen G and Brill A. 1993 Dosimetry Of Intraperitoneally Administered Radiolabeled Antibodies. *Med. Phys.* **20** 593 – 600.

Rotmensch J, Roeske J, Chen G, Pelizzari C, Montag A, Weichselbaum R, Herbst A L. 1990 Estimates Of Dose To Intraperitoneal Micrometastases From Alpha And Beta Emitters In Radioimmunotherapy. *Gynecol. Oncol.* **38** 478 – 485.

Sarfaraz M and Wessels B. 1995 Validation Of An Analytical Expression For The Absorbed Dose From A Spherical β Source Geometry And Its Application To Micrometastatic Radionuclide Therapy. *Clin. Cancer Res.* **5** 3020s – 3023s.

Srivastava S and Dadachova E. 2001 Recent Advances in Radionuclide Therapy. *Semin. Nucl. Med.* **XXXI** 330 – 341.

Sutherland R, Buchegger F, Schreyer M, Vacca A, and Mach J P. 1987 Penetration And Binding Of Radiolabeled Anti-Carcinoembryonic Antigen Monoclonal Antibodies And Their Antigen Biding Fragments In Human Colon Multicellular Tumor Spheroids. *Cancer Res.* **47** 1627 – 1633.

Werner B, Kwok C and Das I. 1988 Dose Distributions In Regions Containing Beta Sources: Large Spherical Source Regions In A Homogeneous Medium. *Med. Phys.* **15** 358 – 363.

Werner B L, Rahman M, Salk W N and Kwok C S. 1991 Dose Distributions In Regions Containing Beta Sources: Uniform Spherical Source Regions In Homogeneous Media. *Med. Phys.* **18** 1181 – 1191.

Xiao Z, McQuarrie S A, Suresh M R, Mercer J R, Gupta S and Miller G G. 2002 A Three-Step Strategy For Targeting Drug Carriers To Human Ovarian Carcinoma Cells *In Vitro*. *J. Biotechnol.* **94** 171 – 184.

Zweit J. 1996 Radionuclides and Carrier Molecules For Therapy. *Phys. Med. Biol.* **41** 1905 – 1914.

Appendix 1: Dose-Rate Profiles (Radioactive Bath)

The following tables contain dose-rate distributions for 5 different tumour sizes and six different radionuclides. The quantity *a* represents the distance from the centre of the tumour. The tumours are assumed to be submerged in a bath of uniformly distributed radioactivity; a simplified representation of a non-targeted approach to treating micrometastases in the peritoneal cavity. Data in these tables are in the form of absolute dose-rates. Scaling the dose-rates by appropriate equilibrium dose-rates would allow the reader to compare the ability of different radionuclides to preserve uniformity throughout the tumour.

Table A1: Non-Targeted Dose-Rate Profile: Tumour Radius = 0.001cm

	Dose-Rate (nGy/h)/(Bq/mL)					
***a* ($\times10^{-3}$) cm**	**Re-188**	**Re-186**	**P-32**	**Y-90**	**Cu-67**	**I-131**
0	440.1	188.1	402.8	534.0	88.1	106.4
0.2	440.1	188.1	402.8	534.0	88.1	106.5
0.4	440.2	188.3	402.9	534.1	88.4	106.7
0.6	440.5	188.7	403.1	534.3	89.0	107.1
0.8	440.9	189.4	403.5	534.7	90.1	108.0
0.9	441.4	190.1	403.9	535.1	91.3	108.9
0.99	442.9	192.4	405.1	536.3	95.0	112.0

Table A2: Non-Targeted Dose-Rate Profile: Tumour Radius = 0.005cm

	Dose-rate (nGy/h)/(Bq/mL)					
***a* (x10^{-2})cm**	**Re-188**	**Re-186**	**P-32**	**Y-90**	**Cu-67**	**I-131**
0	438.1	179.5	392.7	529.4	72.4	94.9
0.1	438.3	179.7	392.8	529.4	72.6	95.1
0.2	438.6	180.2	393.1	529.7	73.3	95.6
0.3	439.2	181.1	393.6	530.2	74.4	96.5
0.4	440.2	182.6	394.4	531.0	76.4	98.2
0.45	440.9	183.7	395.0	531.5	77.8	99.4
0.49	441.7	184.9	395.6	532.2	79.5	100.8
0.499	441.9	185.3	395.8	532.3	80.0	101.2

Table A3: Non-Targeted Dose-Rate Profile: Tumour Radius = 0.01cm

	Dose-rate (nGy/h)/(Bq/mL)					
***a* (x10^{-2})cm**	**Re-188**	**Re-186**	**P-32**	**Y-90**	**Cu-67**	**I-131**
0	430.5	169.2	386.1	523.1	57.6	84.8
0.2	430.7	169.5	386.3	523.3	58.1	85.1
0.4	431.4	170.3	386.9	523.8	59.6	86.0
0.5	431.9	171.0	387.3	524.2	60.8	86.7
0.6	432.6	171.9	387.9	524.7	62.3	87.6
0.7	433.4	173.1	388.6	525.4	64.1	88.8
0.8	434.5	174.6	389.5	526.3	66.4	90.4
0.9	436.0	176.7	390.7	527.4	69.3	92.6
0.95	436.9	178.2	391.4	528.2	71.3	94.2
0.99	437.9	179.6	392.3	529.0	73.3	95.8

Table A4: Non-Targeted Dose-Rate Profile: Tumour Radius = 0.05cm

	Dose-rate (nGy/h)/(Bq/mL)					
a ($\times10^{-1}$)cm	Re-188	Re-186	P-32	Y-90	Cu-67	I-131
0	378.1	107.2	333.0	473.5	12.1	32.1
0.1	379.0	108.2	333.9	474.3	12.8	32.9
0.2	381.6	111.3	336.7	476.9	15.0	35.8
0.3	386.5	117.0	341.7	481.6	19.5	41.1
0.4	394.6	127.4	349.9	489.2	28.1	50.4
0.45	401.0	135.8	356.0	494.9	36.2	58.1
0.49	409.0	146.6	363.2	501.8	48.7	68.4

Table A5: Non-Targeted Dose-Rate Profile: Tumour Radius = 0.1cm

	Dose-rate (nGy/h)/(Bq/mL)					
a ($\times10^{-1}$)cm	Re-188	Re-186	P-32	Y-90	Cu-67	I-131
0	316.8	56.1	267.7	412.8	1.2	5.7
0.1	317.3	56.5	268.2	413.2	1.2	5.9
0.2	318.5	57.7	269.5	414.5	1.5	6.6
0.3	320.7	59.8	271.9	416.6	1.9	7.7
0.4	323.8	62.9	275.2	419.6	2.5	9.5
0.5	328.0	67.0	279.7	423.7	3.6	12.1
0.6	333.4	72.4	285.4	428.9	5.4	15.7
0.7	340.2	79.5	292.7	435.6	8.3	20.6
0.8	349.0	88.8	301.9	444.2	13.2	27.8
0.9	361.0	102.6	314.3	455.6	22.1	38.8
0.95	369.3	112.8	322.4	463.2	30.4	47.4
0.99	378.8	125.1	331.4	471.6	43.2	58.5

Appendix 2: Dose-rate Profiles (Surface-bound radioactivity)

The following tables contain dose-rate profiles for spherical tumours with uniformly distributed activity on their surfaces. More data points are included in these tables because the dose-rates show significantly greater variation through the tumour than they do with the non-targeted approach.

Table A6: Dose-Rate Profile From Surface-Bound Activity: Tumour Radius = 0.001cm

	Dose-rate (x 10^3) (nGy/h)/(Bq/cm^2)					
***a* (x10^{-3})cm**	**Re-188**	**Re-186**	**P-32**	**Y-90**	**Cu-67**	**I-131**
0	1.645	2.484	1.331	1.297	3.362	2.827
0.1	1.651	2.493	1.335	1.301	3.376	2.838
0.2	1.668	2.518	1.349	1.315	3.421	2.872
0.3	1.698	2.563	1.373	1.338	3.500	2.932
0.4	1.743	2.632	1.410	1.374	3.617	3.023
0.5	1.809	2.730	1.463	1.426	3.786	3.154
0.55	1.852	2.795	1.497	1.459	3.895	3.240
0.6	1.903	2.872	1.538	1.500	4.026	3.344
0.65	1.966	2.965	1.589	1.549	4.185	3.469
0.7	2.043	3.081	1.650	1.609	4.381	3.624
0.75	2.140	3.226	1.728	1.685	4.627	3.820
0.8	2.266	3.416	1.830	1.785	4.948	4.075
0.85	2.440	3.676	1.970	1.921	5.389	4.426
0.9	2.703	4.071	2.181	2.128	6.054	4.957
0.95	3.189	4.800	2.572	2.510	7.285	5.939
0.99	4.430	6.659	3.568	3.484	10.420	8.443

Table A7: Dose-Rate Profile From Surface-Bound Activity: Tumour Radius = 0.005cm

	Dose-rate (x 10^3) (nGy/h)/(Bq/cm^2)					
a **(x10^{-2})cm**	**Re-188**	**Re-186**	**P-32**	**Y-90**	**Cu-67**	**I-131**
0	1.571	2.151	1.314	1.263	3.223	2.158
0.05	1.577	2.163	1.319	1.268	3.233	2.165
0.1	1.594	2.201	1.332	1.281	3.260	2.192
0.15	1.624	2.265	1.357	1.305	3.307	2.248
0.2	1.669	2.352	1.393	1.341	3.383	2.348
0.25	1.735	2.467	1.446	1.393	3.496	2.498
0.3	1.829	2.621	1.522	1.467	3.664	2.711
0.35	1.969	2.842	1.634	1.577	3.925	2.992
0.4	2.192	3.188	1.814	1.752	4.366	3.405
0.45	2.629	3.854	2.165	2.096	5.319	4.200
0.49	3.808	5.630	3.112	3.022	8.176	6.497
0.499	5.674	8.429	4.612	4.487	12.864	10.246

Table A8: Dose-Rate Profile From Surface-Bound Activity: Tumour Radius = 0.01cm

	Dose-rate (x 10^3) (nGy/h)/(Bq/cm^2)					
a **(x10^{-2})cm**	**Re-188**	**Re-186**	**P-32**	**Y-90**	**Cu-67**	**I-131**
0	1.484	2.055	1.317	1.250	2.310	1.895
0.1	1.490	2.062	1.321	1.254	2.337	1.904
0.2	1.507	2.085	1.335	1.267	2.415	1.929
0.3	1.537	2.123	1.358	1.290	2.539	1.973
0.4	1.583	2.177	1.394	1.325	2.692	2.041
0.5	1.649	2.261	1.446	1.376	2.865	2.140
0.55	1.691	2.323	1.480	1.409	2.962	2.204
0.6	1.743	2.404	1.521	1.449	3.070	2.282
0.65	1.806	2.505	1.570	1.498	3.196	2.381
0.7	1.883	2.631	1.632	1.558	3.348	2.516
0.75	1.980	2.787	1.709	1.634	3.538	2.700
0.8	2.106	2.987	1.810	1.733	3.786	2.950
0.85	2.280	3.259	1.950	1.869	4.132	3.283
0.9	2.543	3.663	2.161	2.076	4.667	3.762
0.95	3.030	4.402	2.551	2.458	5.732	4.642
0.99	4.270	6.270	3.547	3.432	8.724	7.045

Table A9: Dose-Rate Profile From Surface-Bound Activity: Tumour Radius = 0.05cm

	Dose-rate (x 10^3) (nGy/h)/(Bq/cm^2)					
***a* (x10^{-2})cm**	**Re-188**	**Re-186**	**P-32**	**Y-90**	**Cu-67**	**I-131**
0	1.254	1.245	1.328	1.230	0.520	0.891
0.05	1.259	1.251	1.332	1.234	0.528	0.898
0.1	1.272	1.268	1.346	1.247	0.551	0.918
0.15	1.295	1.298	1.370	1.270	0.593	0.954
0.2	1.331	1.345	1.406	1.304	0.659	1.010
0.25	1.384	1.420	1.458	1.353	0.756	1.092
0.3	1.465	1.546	1.532	1.424	0.896	1.210
0.35	1.591	1.750	1.642	1.529	1.102	1.390
0.4	1.802	2.083	1.817	1.698	1.451	1.687
0.45	2.228	2.672	2.160	2.028	2.455	2.290
0.49	3.399	4.455	3.097	2.942	4.885	4.274
0.499	5.263	7.267	4.594	4.404	9.229	7.774

Table A10: Dose-Rate Profile From Surface-Bound Activity: Tumour Radius = 0.1cm

	Dose-rate (x 10^3) (nGy/h)/(Bq/cm^2)					
a **(x10^{-1})cm**	**Re-188**	**Re-186**	**P-32**	**Y-90**	**Cu-67**	**I-131**
0	1.192	0.810	1.272	1.195	0.058	0.235
0.1	1.196	0.816	1.276	1.199	0.062	0.242
0.15	1.202	0.824	1.282	1.204	0.066	0.251
0.2	1.210	0.834	1.290	1.212	0.072	0.264
0.25	1.220	0.848	1.300	1.222	0.080	0.281
0.3	1.233	0.866	1.314	1.234	0.091	0.303
0.35	1.249	0.888	1.331	1.250	0.106	0.329
0.4	1.269	0.914	1.351	1.268	0.124	0.359
0.45	1.292	0.946	1.374	1.291	0.148	0.396
0.5	1.320	0.984	1.403	1.318	0.179	0.438
0.55	1.353	1.029	1.437	1.350	0.217	0.489
0.6	1.392	1.083	1.478	1.388	0.267	0.549
0.65	1.441	1.148	1.527	1.435	0.331	0.622
0.7	1.501	1.228	1.588	1.493	0.416	0.713
0.75	1.577	1.334	1.665	1.566	0.532	0.830
0.8	1.681	1.488	1.766	1.661	0.692	0.984
0.85	1.832	1.721	1.903	1.791	0.921	1.202
0.9	2.071	2.090	2.110	1.989	1.299	1.542
0.95	2.535	2.736	2.492	2.357	2.332	2.202
0.99	3.758	4.591	3.478	3.316	4.842	4.257

Chapter 6

Dosimetric Model For Liposomal Radionuclide Therapy Of Micrometastases In The Peritoneal Cavity

6.1 Introduction

Intraperitoneal radiation therapy is intended to attack tumours seeded on the walls of the peritoneal cavity as well as the clusters of cells (micrometastases) suspended in the peritoneal fluid. The radioactive preparation is generally administered in a large volume of fluid to ensure good distribution within the cavity (Buijs *et al.*, 1998, Alvarez *et al.*, 1997, Kolstad *et al.*, 1977). As such, the dose to tumour tissue will come from two sources: the free liposomes in solution and the liposomes bound to the surface of tumour cells.

Rotmensch *et al.* (1990) and Roeske *et al.* (1993) investigated the dosimetry of tumours seeded on the wall of the peritoneal cavity. They considered the contributions from both surface-bound radioactivity and the free radioactivity in solution in the peritoneal cavity during the treatment. They produced dose profiles along tumour axes as well as isodose curves for different tumour geometries. The work presented in this chapter expands on the idea of two sources contributing to tumour dosimetry by incorporating the ideas of binding kinetics and tumour control probabilities (TCPs). Watson *et al.* (1989) developed a model to investigate the dosimetry of healthy tissues as a result of radioactivity in the peritoneal cavity. They presented specific absorbed fractions for photon doses and also examined the dose resulting from the electron-irradiation of the peritoneal cavity wall.

The model presented in this chapter investigates the processes affecting the dosimetry of the free-floating micrometastases in the peritoneal fluid during targeted liposomal radionuclide therapy. The ultimate goal is to describe the TCP for micrometastases of various sizes in terms of the biological parameters that govern the binding kinetics between liposomes and tumour tissue. This is accomplished by first developing a set of coupled differential equations, the solution to which provides the time-dependent number of liposomes bound to the surface of a tumour as well as the total number of liposomes in the peritoneal cavity. Secondly, with this information, the calculated dose-rate distributions from chapter 5 are adapted to calculate the integrated dose to different parts of the tumour. Time-dependent TCPs are then calculated via a simple radiation biology model that relates absorbed dose to the surviving fraction. For the purposes of illustration, TCP calculations are performed with Re-188 as the therapeutic radionuclide. Calculations investigating the relative contributions of surface-bound radioactivity and free radioactivity are shown for both Y-90 and Cu-67 as examples of high and lower energy emitters respectively.

6.2 Model Development

In order to calculate the dose to a tumour, one must first identify the dynamic processes that take place within the system. In reality, because it is not feasible to incorporate all possible interactions into this model, only those processes that are considered to be of greatest importance are outlined below:

Liposome interaction with CA-125. This represents a chemical kinetics problem in which free liposomes can bind to CA-125 molecules and liposome-CA-125 complexes can dissociate.

$$C + L \underset{k_2}{\overset{k_1}{\Leftrightarrow}} CL \tag{6.1}$$

In this reaction diagram, L represents the free liposomes in solution, C represents the free CA-125 on the tumour surface and CL represents the population of liposome-CA-125 complexes. With conventional antibody binding kinetics, the equilibrium rate constant, $K_{eq} = k_1/k_2$, would have a value on the order of 10^9 to 10^{12} for a tightly bound system (Larsson, 1988).

CA-125 on cell surfaces is shed and regenerated. Ovarian cancer cells undergo a continual turnover of CA-125 on their surfaces. The antigen that is shed could come from either of the populations C or CL defined above. A key assumption in this model is that the total population of CA-125 (i.e. the sum of the populations C and CL) remains constant over the time period studied.

Liposomes do not penetrate into tumour tissue. The presence of the CA-125 antigen on the surface of ovarian cancer cells suggests that the immunoliposomes will be unable to penetrate significantly beyond the surface of any tumour tissue (Sutherland *et al.*, 1987). This model assumes all bound liposomes reside on the surface of a tumour.

Liposomes can escape from the peritoneal cavity. Previous studies have shown that antibodies and colloids injected into the peritoneal cavity are capable of escaping the cavity resulting in uptake by other organs (Buijs *et al.* 1998, Alvarez *et al.* 1997, Bakri *et al.* 1984). Other studies have shown that larger preparations such as microspheres exhibit better peritoneal retention (Vergote *et al.*, 1992a, Vergote *et al.*, 1992b). The size of liposomes lies between antibodies and microspheres and their ability to escape the cavity has been incorporated into the model.

System of Equations

The system of ordinary differential equations given below describes the time-rate of change of the populations *C*, *L* and *CL* as governed by the processes described above:

$$\frac{d[C]}{dt} = -k_1[L][C] + k_2[CL] \tag{6.2}$$

$$\frac{d[L]}{dt} = -k_3[L] \tag{6.3}$$

$$\frac{d[CL]}{dt} = k_1[L][C] - k_2[CL] \tag{6.4}$$

We have assumed that $[L] >> [C]$ so that the binding of liposomes to tumour tissue does not affect the concentration of liposomes in the fluid. The constant k_1 is used to describe the rate at which liposomes associate with CA-125 on the surface of a tumour. The constant k_2 represents the effective rate at which liposomes are released from the surface of the tumour. The aforementioned conservation of total CA-125 on a tumour surface requires that k_2 incorporates both the dissociation of liposome-CA-125 complexes and the shed of liposome-CA-125 complexes from the surface of the tumour. Finally, k_3 represents the rate at which liposomes escape from the peritoneal cavity. All of the constants are positive-valued. If we define a vector:

$$\bar{x} = ([C]\ ,\ [CL]\ ,\ [L]) \tag{6.5}$$

the problem is non-linear due to the coupling terms involving [C] and [L]. The concentration of free liposomes in the peritoneal cavity is assumed to be independent of the other populations, and can be solved for independently:

$$L(t) = L_o e^{-k_3 t} \tag{6.6}$$

The term L_o represents the initial concentration of liposomes. The reduced two-dimensional system of equations has effective exchange coefficients that are time-dependent and the system is given by:

$$\frac{d\bar{y}}{dt} = A(t) \cdot \bar{y} \tag{6.7}$$

where:

$$\bar{y} = ([C]\ ,\ [CL]) \tag{6.8}$$

and the matrix *A(t)* is given by:

$$A(t) = \begin{pmatrix} -k_1 L_o e^{-k_3 t} & k_2 \\ k_1 L_o e^{-k_3 t} & -k_2 \end{pmatrix} \tag{6.9}$$

The time-dependent exchange coefficients suggest that this system is best studied numerically (Barrington-Leigh, 2004).

6.3 Dose Calculations

The dose to a small, spherical cluster of ovarian cancer cells in the peritoneal cavity will come from two sources: immunoliposomes bound to the surface of the cluster (D_s), and free immunoliposomes suspended in the fluid in which the cluster is located (D_b). If the surface-bound activity is uniformly distributed, the symmetry of the problem suggests that the dose distribution within the tumour will only exhibit a radial dependence. The details of the calculations of radial dose-rate profiles were described in chapter 5 for static source geometries. A summary is provided here with appropriate changes to reflect the dynamic source distributions in this application. To calculate the dose-rate, $\dot{D}_s(a,t)$, to a point in the tumour at a distance a from the centre, one must integrate the contributions from all radioactive source elements. For bound immunoliposomes that are uniformly distributed over the surface of the tumour, this is expressed as follows:

$$\begin{aligned}\dot{D}_s(a,t) &= \int \dot{C}(r) A_{Ds}(t) dA \\ &= A_{Ds}(t) 2\pi \int_0^{\pi} \dot{C}(r) R^2 \sin\theta d\theta\end{aligned} \tag{6.16}$$

where A_{Ds} is the surface activity density, R is the tumour radius and the function $\dot{C}(r)$ corresponds to the beta dose-rate at a distance r from a point source of activity. Various authors have described analytic expressions for this function (Leichner *et al.* 1993). However this work is based on the numerical results of Monte Carlo simulations performed by Cross *et al.* (1992) for a large number of radionuclides. The surface activity density, $A_{Ds}(t)$, is a time-dependent quantity subject to the binding kinetics described above and the physical properties of the radionuclide. It is related to the biological parameters discussed previously through the quantity [CL]*(t)* in the following way:

$$A_{Ds}(t) = \frac{A_o e^{-\lambda_r t} [CL](t) C_o N_A V}{4\pi R^2} \tag{6.17}$$

where A_0 is the activity per liposome, λ_r is the physical decay constant of the radionuclide, R is the tumour radius, N_A is Avagadro's number and V is the volume of fluid in the peritoneal cavity. This leads to:

$$\dot{D}_s(a,t) = \frac{A_0 e^{-\lambda_r t} [CL](t) C_o N_A V}{2R^2} \int_0^{\pi} \dot{C}(r) R^2 \sin\theta d\theta \tag{6.18}$$

For a given value of θ, the distance, r, from the surface to the point a is given by:

$$r^2 = a^2 + R^2 - 2aR\cos\theta \tag{6.19}$$

The dose-rate, $\dot{D}_b(a,t)$, that results from the uniformly distributed bath of activity is calculated in a similar manner, integrating the contributions from elemental volumes, *dV*:

$$\begin{aligned}\dot{D}_b(a,t) &= \int \dot{C}(r) A_{Db}(t) dV \\ &= A_{Db}(t) 2\pi \int_0^\pi \int_R^\infty \dot{C}(r) R'^2 \sin\theta dR' d\theta\end{aligned} \tag{6.20}$$

The activity density, $A_{Db}(t)$, is given by:

$$A_{Db}(t) = A_o L_o e^{-k_3 t} N_A e^{-\lambda_r t} \tag{6.21}$$

The integrated dose at a time *t* after the injection of liposomes is given by:

$$D(a,t) = \int_0^t \dot{D}_s(a,t) dt + \int_0^t \dot{D}_b(a,t) dt \tag{6.22}$$

6.4 Tumour Control Probability

With an understanding of the dynamic behaviour of the system as developed above, it is possible to translate integrated dose calculations into time-dependent tumour control probabilities (TCPs). The inhomogeneity of dose distributions in radioimmunotherapy techniques has been well documented (Nahum 1996, Hui *et al.* 1992, Langmuir *et al.* 1988). The short range of the beta particles in tissue and the difficulty achieving uniform source distributions within a tumour are primarily responsible. Consequently, calculation of average tumour dose is not necessarily an effective predictor of therapeutic success. A more rigorous calculation of TCP must incorporate this dose inhomogeneity into its formulation.

For the source geometries investigated in this work, the dose distribution within the tumour will exhibit radial dependence only. Tumourlets are defined as isodose volumes within a tumour and they can be used to facilitate TCP calculations. They will be constructed as thin spherical shells, where the volume of a shell of radius *r* is given by:

$$V = 4\pi r^2 dr \tag{6.23}$$

If the density of cells, ρ, is constant, the number of cells in the tumourlet is:

$$N = 4\pi\rho r^2 dr \tag{6.24}$$

Borrowing the notation of Goitein *et al.* (1995), the number of cells still alive in the tumourlet after a dose, *D*, is given by:

$$\overline{N} = N \cdot SF(D) \tag{6.25}$$

Where *SF(D)* represents the surviving fraction of cells exposed to dose D. The TCP is given by the probability of killing all clonogens, which, according to Poisson statistics is:

$$TCP = e^{-N \cdot SF(D)} \tag{6.26}$$

For a tumour consisting of *M* tumourlets, the total TCP is given by:

$$\begin{aligned} TCP &= e^{-\sum_{i=1}^{M} N_i SF(D_i)} \\ &= \prod_{i=1}^{M} e^{-N_i \cdot SF(D_i)} \end{aligned} \tag{6.27}$$

The total TCP is thus expressed as the product of the TCPs of the individual tumourlets. The function that describes the surviving fraction in terms of dose, *SF(D)*, can be taken from any radiobiological model that fits appropriate data. The term "appropriate data" is used because this treatment modality represents a low dose-rate approach and the majority of published data is based on high dose-rate irradiations. For this work, it was assumed that all cell killing results from lethal lesions produced by a single ionization.

$$SF(D) = e^{-\alpha D} \tag{6.28}$$

This has been referred to as the low dose-rate approximation of the linear quadratic model with the assumption that β equals zero (Atthey *et al.* 2000).

Implicit in the model is the assumption that each tumourlet has identical radiosensitivity. In addition, the effects of tumour growth are neglected. The dependence of the surviving fraction on dose allows us to trace the TCP back to the biological parameters discussed in Eqs (6.2), (6.3) and (6.4). The significance of this result is that it allows for the possibility of patient-specific treatment optimization based on parameters that could be measured on cells harvested from a peritoneal lavage.

6.5 Results

The model was applied to small tumours ranging in size from a radius of 0.005 cm to 0.1 cm. This is intended to encompass the range of cell clusters that could be found in the clinic. The system was solved with values of k_1 ranging from $10^3 - 5 \times 10^7$ $M^{-1}s^{-1}$, values of k_2 ranging from $10^{-2} - 10^{-6}$ s^{-1} (based on work by Schwesinger *et al.*, 2000) and values of k_3 ranging from $0 - 3.85 \times 10^{-5}$ s^{-1}. These values of k_3 describe biological half lives in the peritoneal cavity that range from infinite to 5 hours respectively. The system of differential equations was evaluated numerically using Matlab's ode45 function.

6.5.1 Binding Kinetics

The number of liposomes bound to the surface of a tumour at a time *t* after injection is strongly dependent on the rate constants given in equations (2), (3) and (4). Figure 6.1 is a plot of the number of liposomes bound to a 0.05cm radius tumour as a function of time. In this case, the initial concentration of CA-125, C_o, corresponds to a tumour surface antigen density of 10^8 cm^{-2} (roughly 3×10^6 per cell). L_o has a value of 5.463×10^{-12} M, which would correspond to an injected activity of 37.2 GBq in a 1 litre preparation (with 10^3 Re-188 atoms per liposome). Data is plotted for a number of parameter sets to illustrate how the different rate constants affect the time-dependent surface concentration. In Set 1, the parameters used are: $k_1 = 10^5$ M^{-1}s^{-1}, $k_2 = 10^{-5}$ s^{-1} and $k_3 = 0$. In Set 2, the parameters are: $k_1 = 10^5$ M^{-1}s^{-1}, $k_2 = 10^{-5}$ s^{-1} and $k_3 = 8.022\text{x}10^{-6}$ s^{-1}. This value of k_3 is used to illustrate the case for which liposomes are removed from the peritoneal cavity with a half-life of 24 hours.

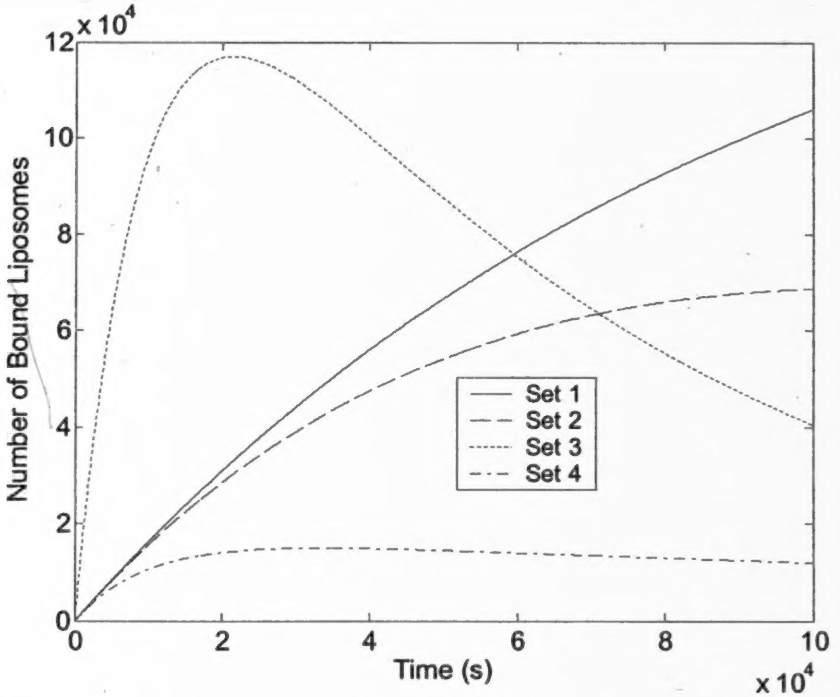

Figure 6.1: Number of liposomes bound to the surface of a 0.05 cm radius tumour as a function of time. Four different parameter sets are shown to illustrate the importance of the binding kinetics in an intraperitoneal immunotherapy. The parameter sets used are: Set 1: $k_1 = 10^5$ M^{-1}s^{-1}, $k_2 = 10^{-5}$ s^{-1} and $k_3 = 0$. Set 2: $k_1 = 10^5$ M^{-1}s^{-1}, $k_2 = 10^{-5}$ s^{-1} and $k_3 = 8.022\text{x}10^{-6}$ s^{-1}. Set 3: $k_1 = 10^6$ M^{-1}s^{-1}, $k_2 = 10^{-4}$ s^{-1} and $k_3 = 1.6044\text{x}10^{-5}$ s^{-1}. Set 4: $k_1 = 10^5$ M^{-1}s^{-1}, $k_2 = 10^{-4}$ s^{-1} and $k_3 = 4.011\text{x}10^{-6}$ s^{-1}

The effect of this removal is a decrease in the number of liposomes available for binding with free CA-125 on the tumour surface. Consequently, as the number of liposomes in the peritoneal cavity decreases in Set 2, the difference in the number of bound liposomes between Set 1 and Set 2 increases. In Set 3, $k_1 = 10^6$ M^{-1}s^{-1},

$k_2 = 10^{-4}$ s^{-1} and $k_3 = 1.6044 \times 10^{-5}$ s^{-1} ($T_{1/2}$ = 12 hours). In this case, the maximum number of bound liposomes is reached earlier than any of the other sets due to the larger value of k_1. After this maximum number has been reached, however, the larger values of k_2 and k_3 result in a more rapid clearance of liposomes from the tumour surface. Finally, in Set 4, $k_1 = 10^5 M^{-1}s^{-1}$, $k_2 = 10^{-4}$ s^{-1} and $k_3 = 4.011 \times 10^{-6}$ s^{-1} ($T_{1/2}$ = 48 hours). Compared to Set 3, k_1 is an order of magnitude smaller and this explains the significantly smaller maximum number of bound liposomes.

6.5.2 Tumour Control Probabilities

The data presented in this section were based on liposomes labeled with Re-188. The calculations assumed that each liposome carried 10^3 Re-188 atoms. The value of α was taken as 0.3 Gy^{-1}. The density of cells, ρ, in the micrometastases was 5×10^8 cm^{-3} and a volume of 1 litre was assumed. Tumourlets were constructed as concentric spherical shells of thickness 10^{-3}cm. The beta dose-rates in each tumourlet were interpolated from the dose-rate profiles given in chapter 5, using MatLab's piecewise cubic hermite interpolating polynomials (pchip). The integrated dose to each tumourlet from surface-bound liposomes was calculated numerically using Simpson's method by evaluating the surface activity density using [CL]*(t)* at time intervals of 10 seconds. The integrated dose from the free liposomes in solution was evaluated analytically at time intervals of 10 seconds and the sum of these two quantities provided the total integrated dose to each tumourlet at each time point. Figure 6.2 is a plot of several TCP curves as a function of time for a 0.05cm radius tumour. The parameter sets used are the same as those used in Figure 6.1.

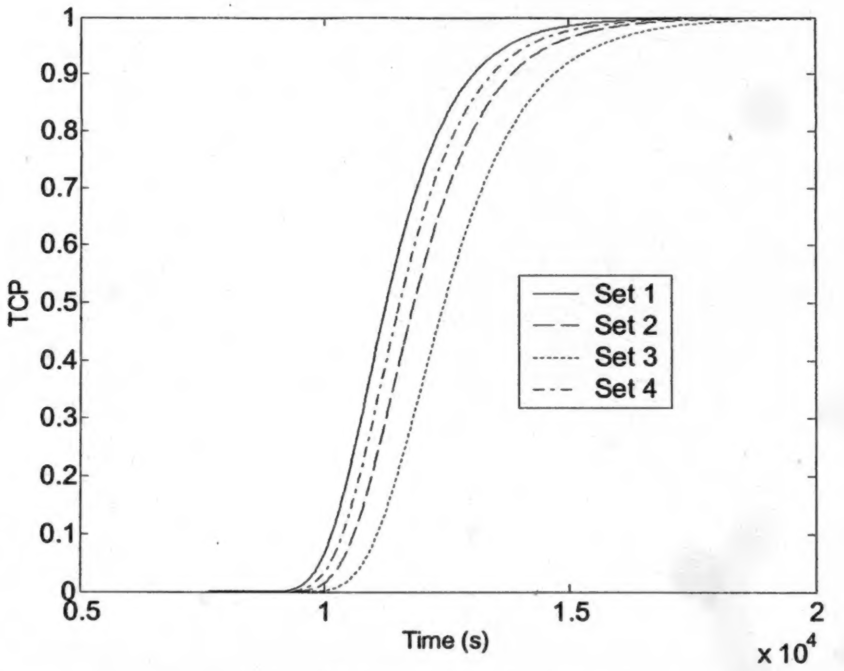

Figure 6.2: Tumour Control Probability (TCP) as a function of time for a 0.05 cm radius tumour. The parameter sets used are: Set 1: $k_1 = 10^5$ $M^{-1}s^{-1}$, $k_2 = 10^{-5}$ s^{-1} and $k_3 = 0$. Set 2: $k_1 = 10^5$ $M^{-1}s^{-1}$, $k_2 = 10^{-5}$ s^{-1} and $k_3 = 8.022\text{x}10^{-6}$ s^{-1}. Set 3: $k_1 = 10^6$ $M^{-1}s^{-1}$, $k_2 = 10^{-4}$ s^{-1} and $k_3 = 1.6044\text{x}10^{-5}$ s^{-1}. Set 4: $k_1 = 10^5$ $M^{-1}s^{-1}$, $k_2 = 10^{-4}$ s^{-1} and $k_3 = 4.011\text{x}10^{-6}$ s^{-1}. The biological processes play an important role in determining how quickly a tumour will be killed. For these particular data sets, the biological elimination constant, k_3, appears to be the dominant factor since the TCP curves appear in order of increasing k_3 from left to right.

It would not be feasible to show these plots for all of the variations of the parameter sets that were evaluated. Instead, the importance of the various parameters is evaluated indirectly by choosing an arbitrary therapeutic goal. In this case, the time required to achieve a TCP of 95% ($TTCP_{95}$) was selected. By doing this, the results of a large number of parameter sets can be incorporated into a single figure. Often, TCP is expressed as a function of dose. In this application, however, the dose distribution throughout the micrometastases can be highly non-uniform. Furthermore, with intraperitoneal administration of radioactivity, the possibility exists of performing a peritoneal lavage after an incubation period to try to remove as much unbound radioactivity as possible. This is an attractive idea because of the possible reduction in healthy tissue dose. By expressing the TCP of the micrometastases as a function of time, one might be able to use this information to assist with therapy by optimizing the time of peritoneal lavage. Figure 6.3 contains surface plots of $TTCP_{95}$ as a function of both the binding rate constant k_1 and the surface antigen density C_o. The data presented is for a tumour of radius 0.05cm with $k_2 = 10^{-5}\ s^{-1}$ and $k_3 = 8.022\times10^{-6}\ s^{-1}(T_{1/2} = 24$ hours). In part A) the injected activity is 37 GBq in 1 litre of fluid and in part B) it is 9 GBq in 1 litre of fluid.

One feature that is common to both parts of Figure 6.3 is the approach to a plateau as k_1 and C_o decrease. Once this plateau has been reached, the tumour dose delivered by surface-bound liposomes is negligible and the tumouricidal effects of the treatment are mediated entirely by the liposomes in solution. Plots of this type for different tumour sizes and injected activities have a very similar appearance and are not shown here. The most important difference between these plots is the value of $TTCP_{95}$ at the plateau. The plateau value of $TTCP_{95}$ as a function of the injected activity is plotted in Figure 6.4 for tumours of radii 0.005cm, 0.01cm, 0.05cm and 0.1cm. In this case, $k_3 = 8.022\times10^{-6}\ s^{-1}$ ($T_{1/2} = 24$ hours). Once the plateau has been reached, the ability of the therapy to kill the micrometastases is the same as it would be if the liposomes were prepared without the antibodies for targeting.

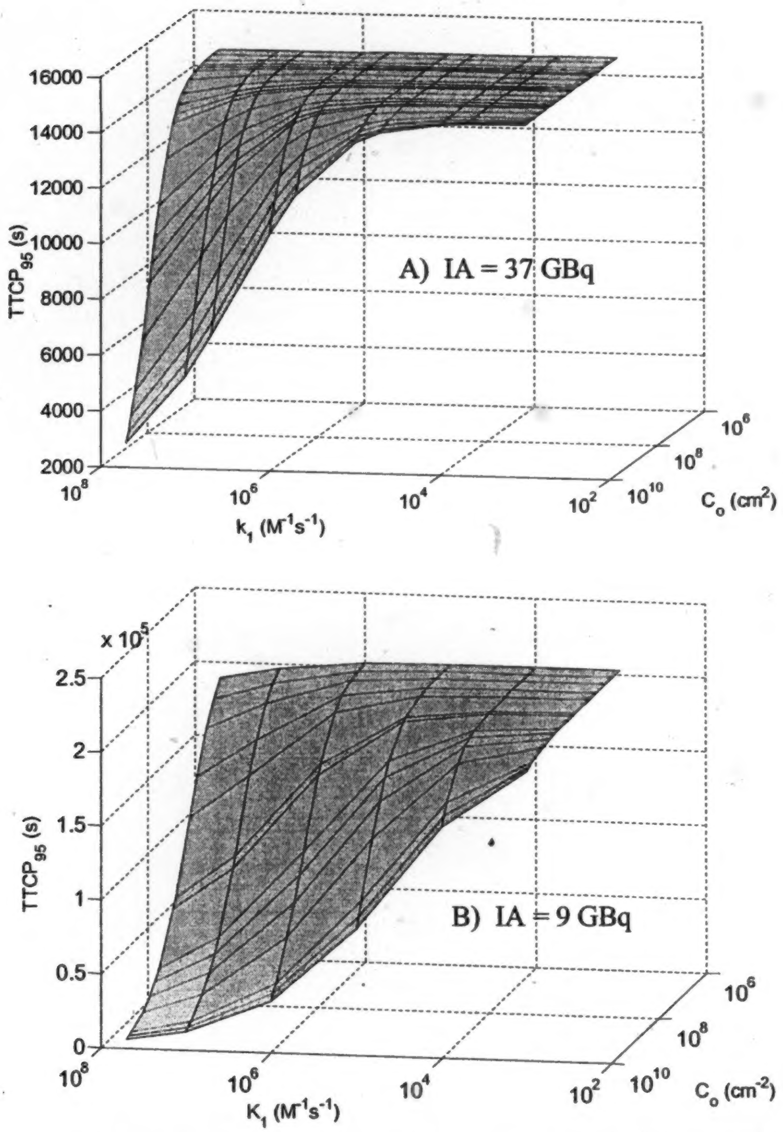

Figure 6.3: Surface plot of the time required to produce a TCP of 95% ($TTCP_{95}$) as a function of the binding rate constant, k_1, and antigen surface density, C_o, for a 0.05cm radius tumour. In part A), the injected activity is 37 GBq in 1 litre of fluid and in part B) it is 9 GBq in 1 litre of fluid. For both parts, $k_2 = 10^{-5}\ s^{-1}$ and $k_3 = 8.022 \times 10^{-6}\ s^{-1}$. As k_1 and Co decrease, the surfaces eventually reach a plateau. The value of TTCP95 at the plateau is the same as it would be if a non-targeted approach were used (i.e. if there were no liposomes bound to the surface of the tumour).

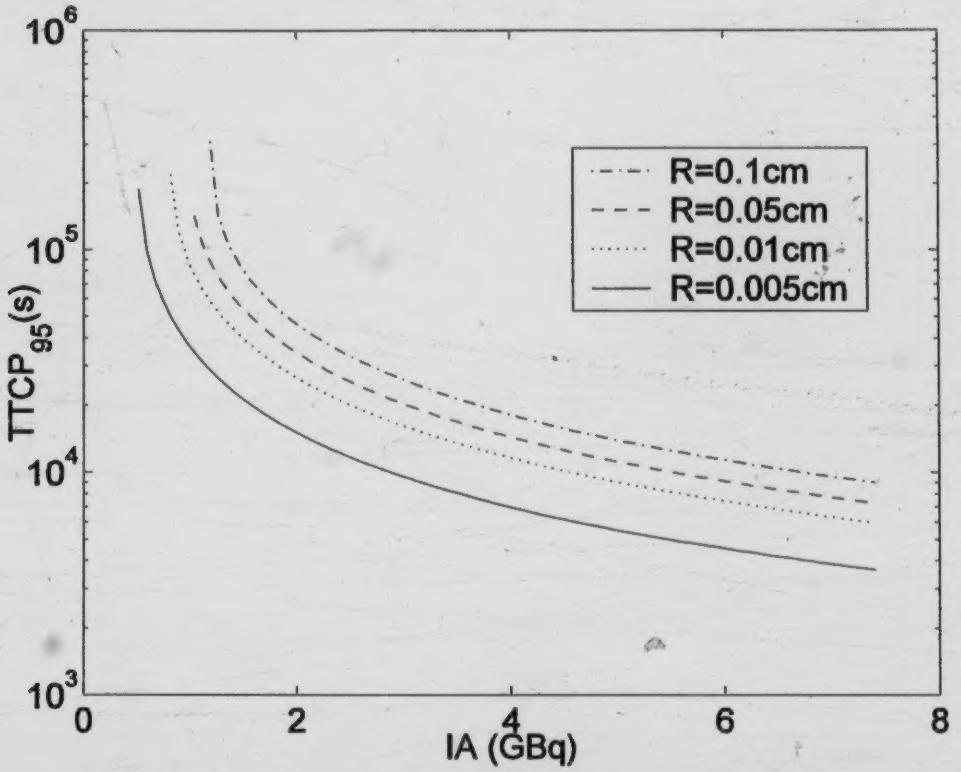

Figure 6.4. TTCP$_{95}$ as a function of injected activity (IA) for a non-targeted approach. These curves assume that there is no radioactivity bound to the surface of the tumour so that the lethal effects of the treatment are mediated entirely by the radioactivity in solution. Any binding of radioactive material to the surface would boost the dose to the tumour and reduce TTCP$_{95}$ (as shown in Figure 6.3), however very weak or slow binding cannot increase TTCP$_{95}$ beyond the values shown in this figure. The values of TTCP$_{95}$ in this figure would correspond to the plateau values of surface plots such as those shown in Figure 6.3.

The relative importance of surface-bound liposomes is increased as the injected activity is decreased due to a decrease in dose from the free liposomes in the peritoneal cavity. This is a logical result because the dose delivered by the bath of activity is independent of the binding kinetics. As such, decreasing the injected activity enhances the effect of the surface-bound liposomes. This is verified by the data in that the values of k_1 and C_o at which $TTCP_{95}$ deviates from its plateau are lower for the case where the injected activity is 9 GBq compared to an injected activity of 37 GBq as shown in Figure 6.3.

It is of interest to investigate the conditions that are required for a targeted approach to offer an advantage over a non-targeted approach. In particular, in this model, one can identify the antigen density, C_o, required to produce an arbitrary improvement in the treatment. For example, Figure 6.5 (parts A, B, C and D) are surface plots of the antigen density required to decrease $TTCP_{95}$ from a non-targeted approach by 5% for tumours of radii 0.005cm, 0.01cm, 0.05cm and 0.1cm respectively. The required antigen density is expressed as a function of the dissociation rate constant, k_2, and the biological elimination constant, k_3. In all cases, the value of k_1 was taken as 10^5 $M^{-1}s^{-1}$ and the injected activity was 18 GBq.

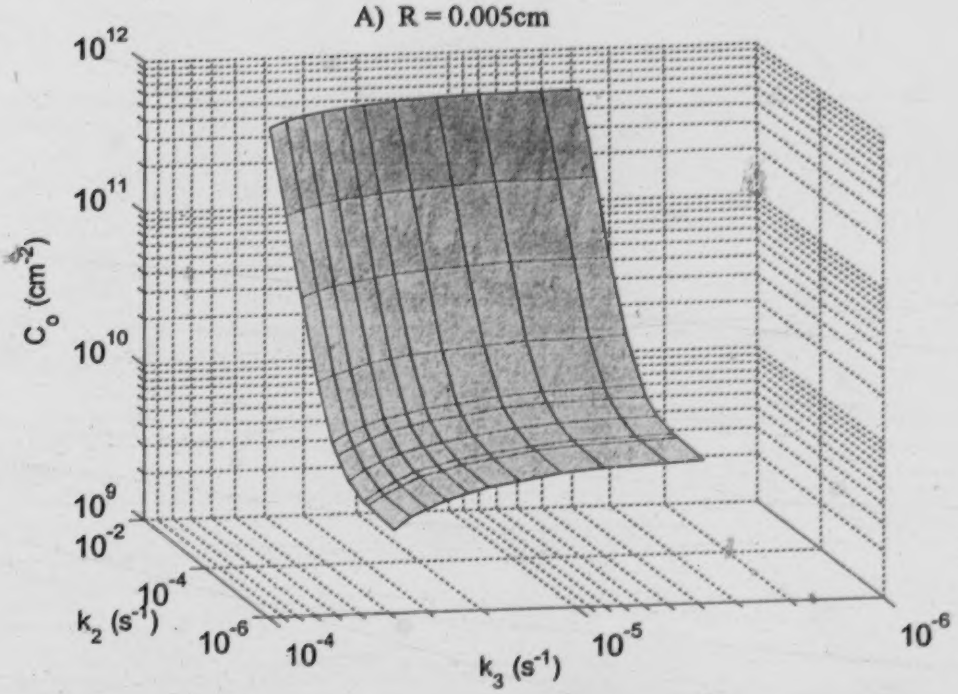

Figure 6.5. Antigen density required to produce a 5% improvement in $TTCP_{95}$ over that from a non-targeted approach for tumours of various radii: A) 0.005cm, B) 0.01cm, C) 0.05 cm and D) 0.1cm. This requirement is expressed as a function of both the dissociation rate constant, k_2, and the biological elimination constant, k_3. The value of k_1 was taken as 10^5 M^{-1}s^{-1} and the injected activity was 18 GBq. The required antigen density increases as the value of k_2 increases and the value of k_3 decreases.

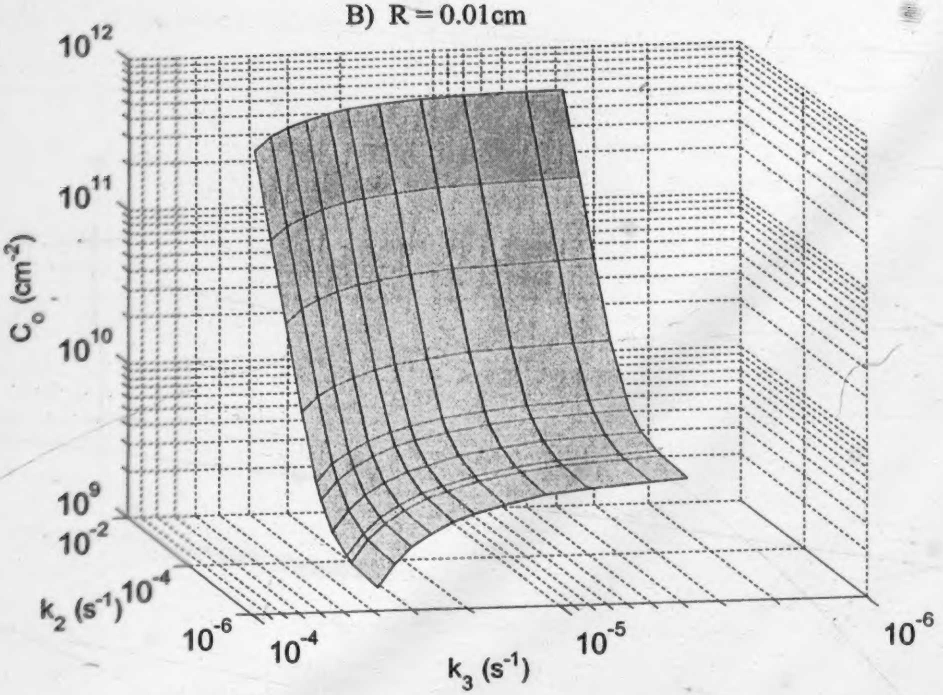

Figure 6.5 B. Antigen density required to produce a 5% improvement in $TTCP_{95}$ over that from a non-targeted approach for tumour of radius 0.01cm. This requirement is expressed as a function of both the dissociation rate constant, k_2, and the biological elimination constant, k_3. The value of k_1 was taken as 10^5 $M^{-1}s^{-1}$ and the injected activity was 18 GBq. The required antigen density increases as the value of k_2 increases and the value of k_3 decreases.

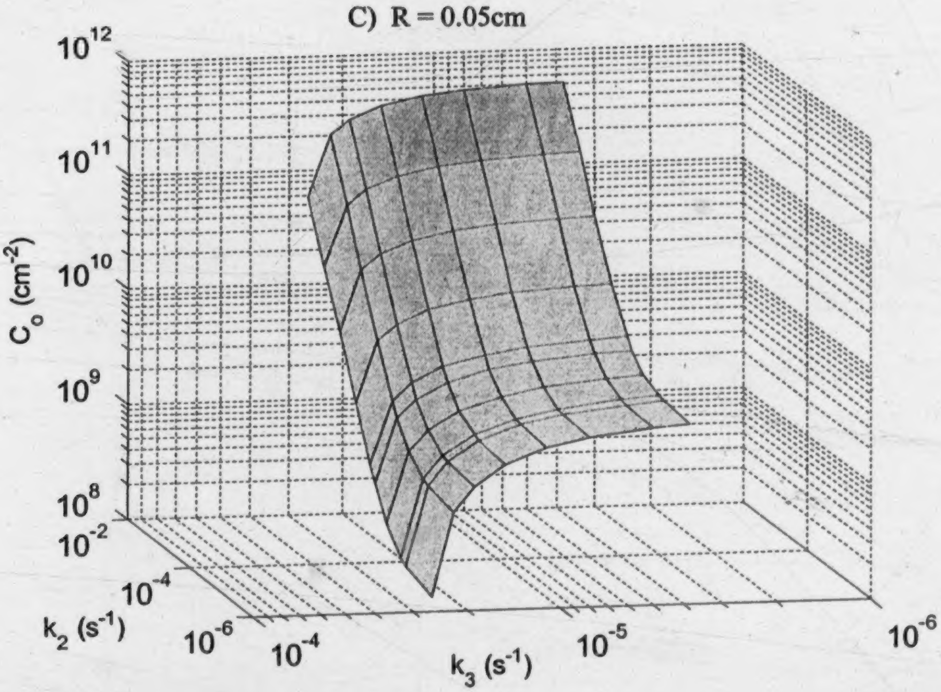

Figure 6.5 C. Antigen density required to produce a 5% improvement in $TTCP_{95}$ over that from a non-targeted approach for tumour of radius 0.05 cm. This requirement is expressed as a function of both the dissociation rate constant, k_2, and the biological elimination constant, k_3. The value of k_1 was taken as 10^5 $M^{-1}s^{-1}$ and the injected activity was 18 GBq. The required antigen density increases as the value of k_2 increases and the value of k_3 decreases.

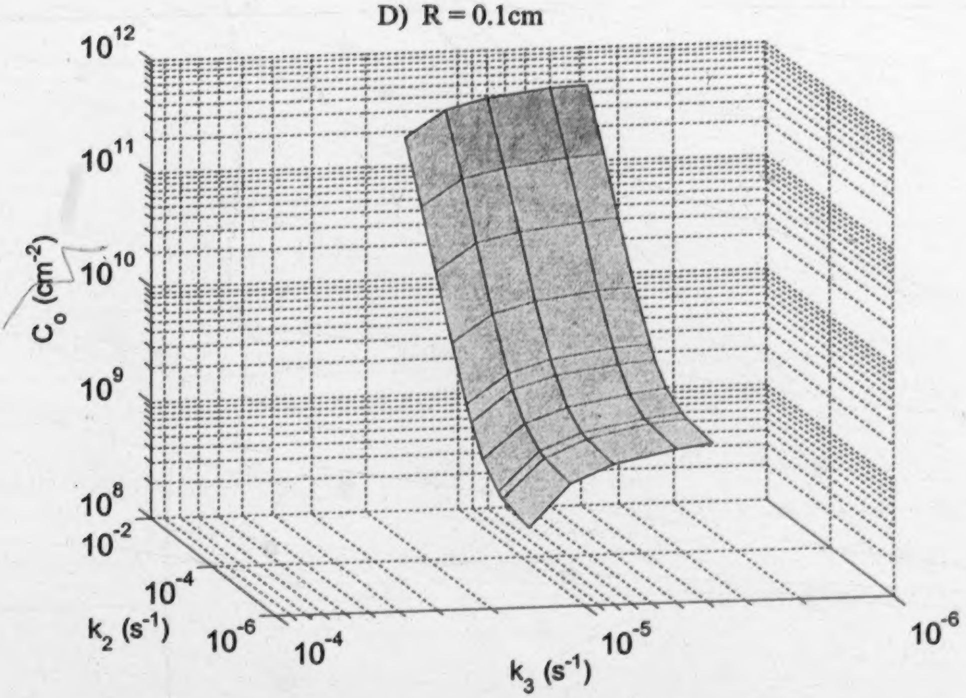

Figure 6.5 D. Antigen density required to produce a 5% improvement in $TTCP_{95}$ over that from a non-targeted approach for tumours of radius 0.1cm. This requirement is expressed as a function of both the dissociation rate constant, k_2, and the biological elimination constant, k_3. The value of k_1 was taken as 10^5 $M^{-1}s^{-1}$ and the injected activity was 18 GBq. The required antigen density increases as the value of k_2 increases and the value of k_3 decreases.

As the value of k_2 increases, liposomes are more readily removed from the surface of the tumour and consequently, the antigen density must increase to compensate for this. On the other hand, as the value of k_3 increases, liposomes are removed from the peritoneal cavity at a greater rate. This increases the rate at which the dose-rate from the free liposomes decreases, which in turn, increases the time required for the liposomes in solution to deliver a lethal dose to the tumour. As mentioned previously, this allows more time for liposomes to bind to the surface of the tumours. Consequently, for a given value of k_2, an increase in the value of k_3 translates into a decrease in the surface antigen density required to produce the 5% decrease in $TTCP_{95}$. The size of the tumour is also important. Smaller tumours have fewer cells to kill and exhibit smaller variations in dose-rate throughout the tumour. This means that they will be killed more quickly and hence require greater surface antigen density if the surface-bound radioactivity is to play a significant role in killing the tumour.

To investigate the relative contribution of surface-bound radioactivity for high and lower energy emitters, the model was applied to liposomes labeled with 1000 atoms of Y-90 or Cu-67. These two radionuclides were chosen because they have similar physical half-lives (2.67 and 2.58 days respectively). This essentially eliminates variations in dose-rate over the course of a treatment as a variable in the comparison. The comparison then focuses on the different energies of the emitters. The ratio of the dose contributed by surface-bound liposomes to the total dose was calculated as a function of the depth within the tumour and treatment time for a 0.01 cm radius tumour. Two parameters were investigated: k_1 and k_3. Two values of k_3 were chosen to represent an infinite half life of liposomes in the cavity and a half life of 12 hours. The two values of k_1 were 10^5 and 10^6. The remaining parameters were fixed at: $k_2 = 10^{-5}$, $C_o = 10^8$ and the injected activity was 1.85 GBq. The results of the calculations are shown in Figures 6.6 and 6.7.

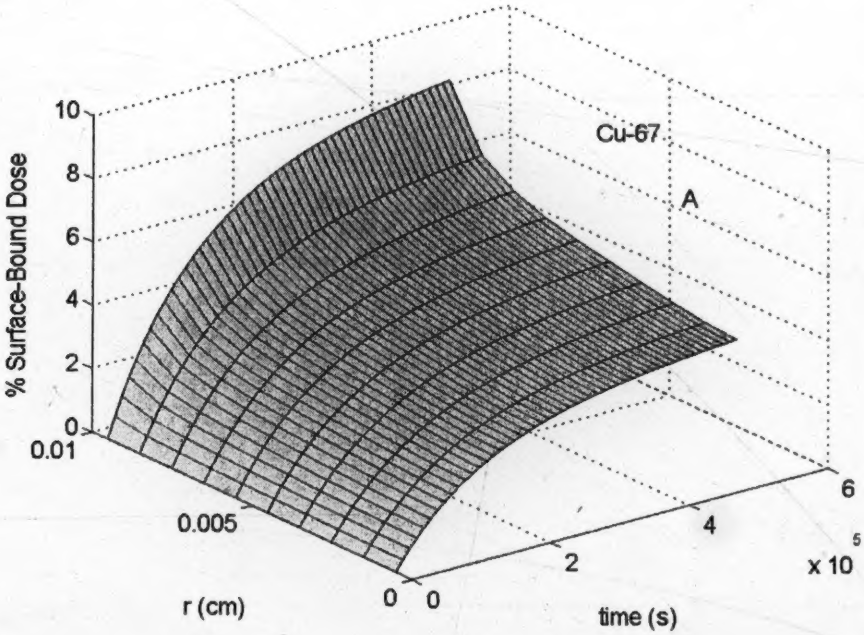

Figure 6.6: The percent of the total dose contributed by the surface-bound radioactivity is shown as a function of both the time of the treatment and the depth within the tumour, r, for Cu-67. In panel A, the parameter values are: $k_1 = 10^5$ and $k_3 = 0$. In panel B, the values are: $k_1 = 10^5$ and $k_3 = 1.6 \times 10^{-5}$. In panel C, the parameter values are: $k_1 = 10^6$ and $k_3 = 0$. In panel D, the values are: $k_1 = 10^6$ and $k_3 = 1.6 \times 10^{-5}$. The injected activity was 1.85 GBq and the values of k_2 and C_o were 10^{-5} and 10^8 respectively.

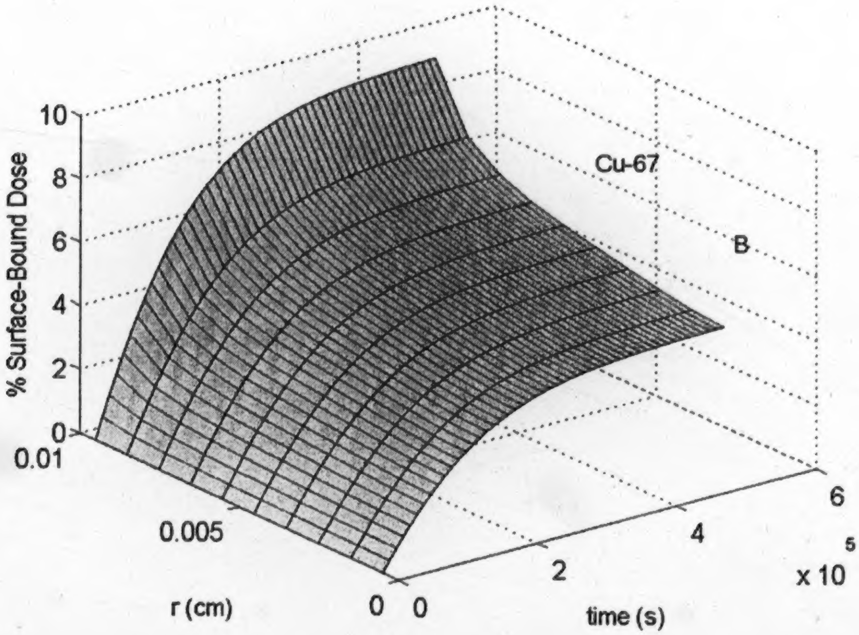

Figure 6.6 B: The percent of the total dose contributed by the surface-bound radioactivity as a function of both the time of the treatment and the depth within the tumour, r, for Cu-67. Parameter values are: $k_1 = 10^5$ and $k_3 = 1.6 \times 10^{-5}$. The injected activity was 1.85 GBq and the values of k_2 and C_o are 10^{-5} and 10^8 respectively.

Regardless of the parameter value combination, the lower energy emitter, Cu-67, produced a greater relative contribution from the radioactivity bound to the surface of the tumour than the high energy emitter, Y-90. For both radionuclides, increasing the value of k_3 increased the relative contribution of the surface-bound liposomes. Increasing the value of k_2 from 10^5 to 10^6 significantly increased the number of liposomes that bind to the tumour and, consequently, increased the dose contribution from the surface-bound population.

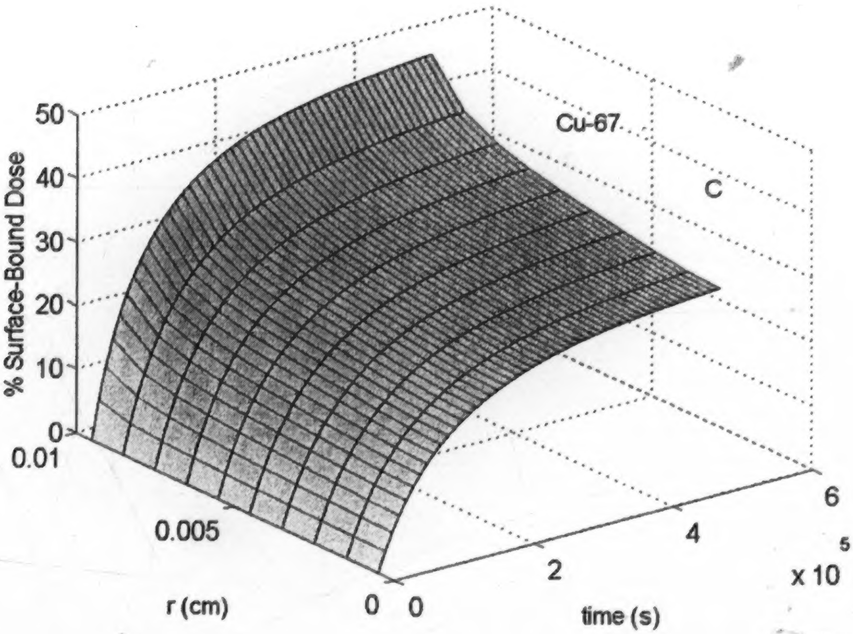

Figure 6.6 C: The percent of the total dose contributed by the surface-bound radioactivity as a function of both the time of the treatment and the depth within the tumour, r, for Cu-67. Parameter values are: $k_1 = 10^6$ and $k_3 = 0$. The injected activity was 1.85 GBq and the values of k_2 and C_o are 10^{-5} and 10^8 respectively.

The inhomogeneity of the surface-bound dose-rate profiles is evidenced in the surface plots. The contribution of the surface-bound liposomes was greatest at the outer edge of the tumour. In panels A and B, one can see that the targeting of liposomes to the surface of the tumour played a greater role in dose deposition for the lower energy emitter. In these panels, the contribution from the high energy emitter, Y-90 was very low. When the value of k_1 was increased in panels C and D, the contribution of the surface-bound liposomes increased significantly.

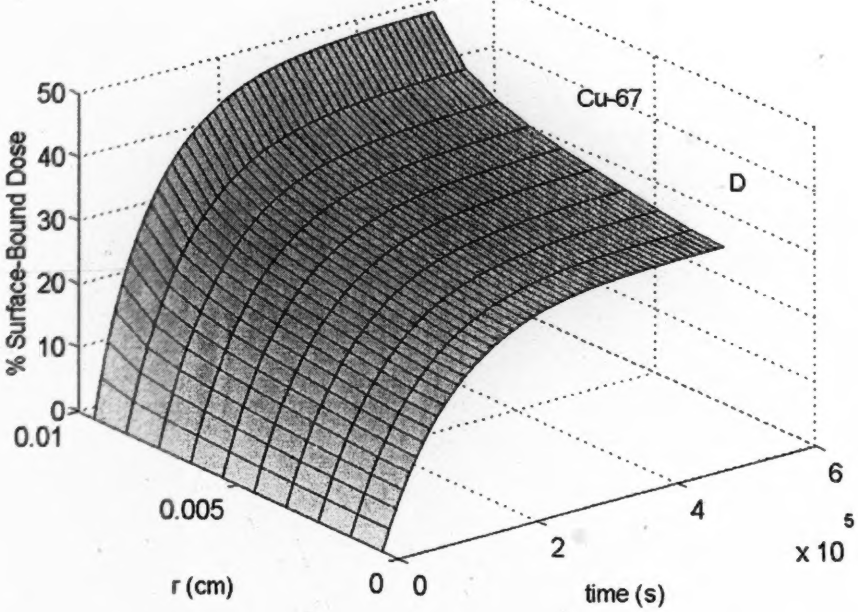

Figure 6.6 D: The percent of the total dose contributed by the surface-bound radioactivity as a function of both the time of the treatment and the depth within the tumour, r, for Cu-67. Parameter values are: $k_1 = 10^6$ and $k_3 = 1.6 \times 10^{-5}$. The injected activity was 1.85 GBq and the values of k_2 and C_o are 10^{-5} and 10^8 respectively.

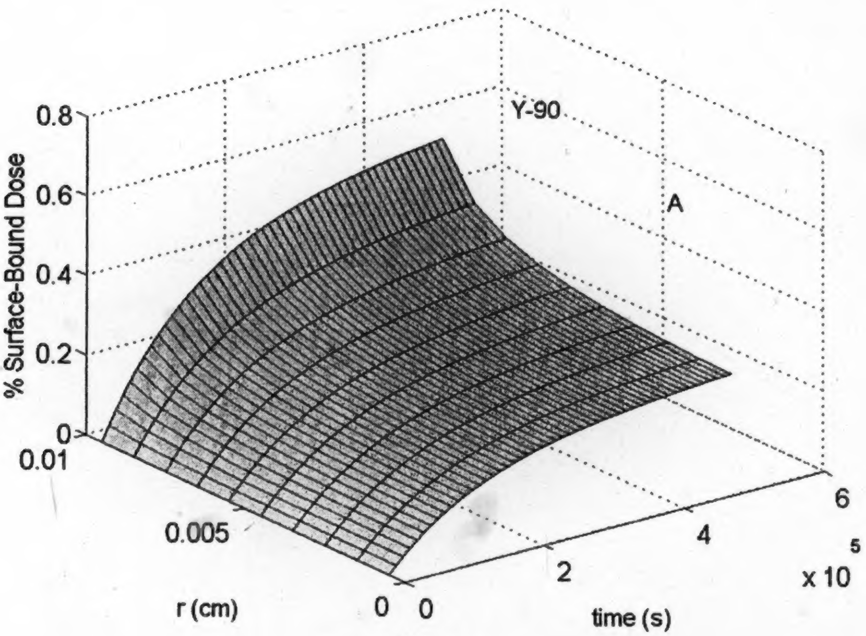

Figure 6.7: The percent of the total dose contributed by the surface-bound radioactivity is shown as a function of both the time of the treatment and the depth within the tumour, r, for Y-90. In panel A, the parameter values are: $k_1 = 10^5$ and $k_3 = 0$. In panel B, the values are: $k_1 = 10^5$ and $k_3 = 1.6 \times 10^{-5}$. In panel C, the parameter values are: $k_1 = 10^6$ and $k_3 = 0$. In panel D, the values are: $k_1 = 10^6$ and $k_3 = 1.6 \times 10^{-5}$. The injected activity was 1.85 GBq and the values of k_2 and C_o were 10^{-5} and 10^8 respectively.

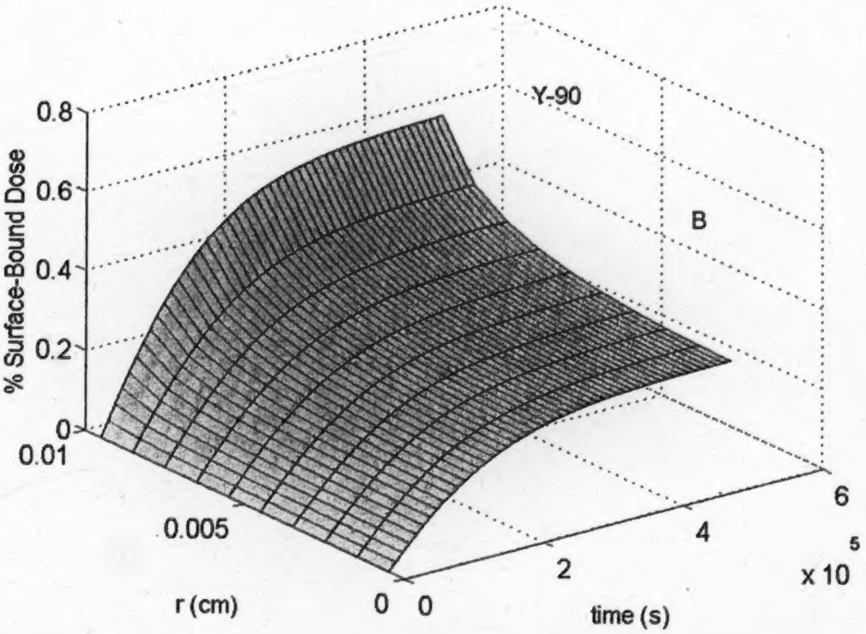

Figure 6.7 B: The percent of the total dose contributed by the surface-bound radioactivity as a function of both the time of the treatment and the depth within the tumour, r, for Y-90. Parameter values are: $k_1 = 10^5$ and $k_3 = 1.6 \times 10^{-5}$. The injected activity was 1.85 GBq and the values of k_2 and C_o are 10^{-5} and 10^8 respectively.

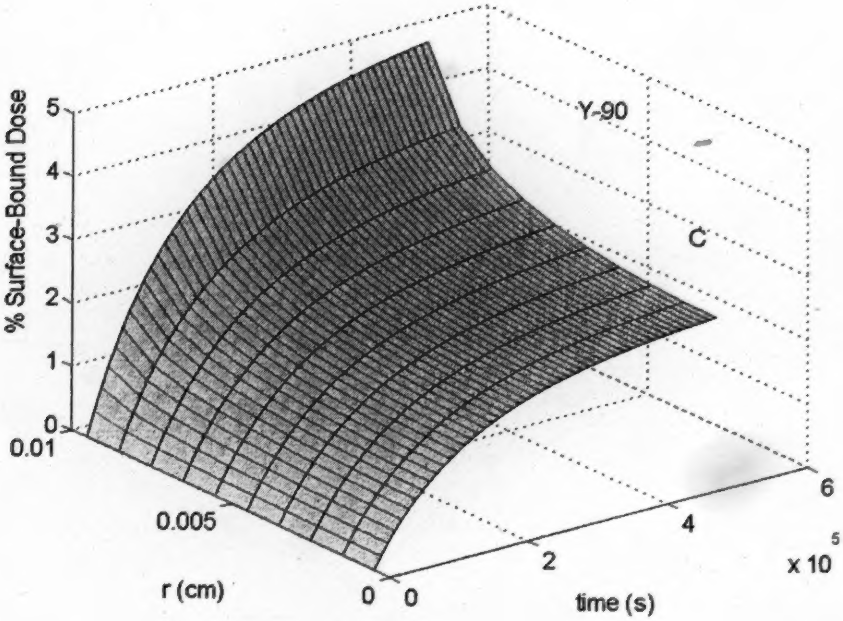

Figure 6.7 C: The percent of the total dose contributed by the surface-bound radioactivity as a function of both the time of the treatment and the depth within the tumour, r, for Y-90. Parameter values are: $k_1 = 10^6$ and $k_3 = 0$. The injected activity was 1.85 GBq and the values of k_2 and C_o are 10^{-5} and 10^8 respectively.

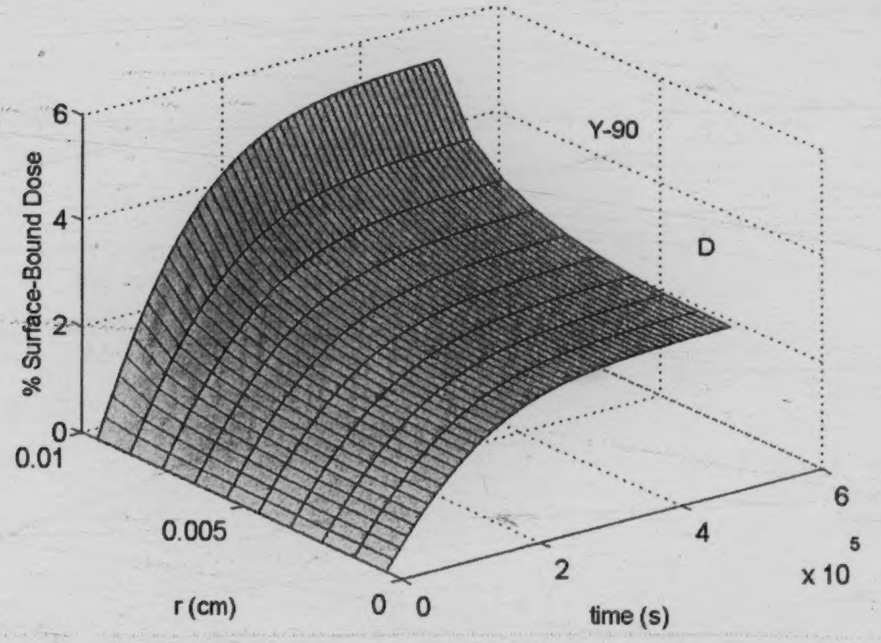

Figure 6.7 D: The percent of the total dose contributed by the surface-bound radioactivity as a function of both the time of the treatment and the depth within the tumour, r, for Y-90. Parameter values are: $k_1 = 10^6$ and $k_3 = 1.6 \times 10^{-5}$. The injected activity was 1.85 GBq and the values of k_2 and C_o are 10^{-5} and 10^8 respectively.

6.6 Discussion

Intraperitoneal radionuclide therapy for late stage ovarian cancer has produced some positive clinical outcomes in human trials. It has also produced some serious complications (Kolstad *et al.*, 1977, Kairemo, 1996). The use of radiolabelled immunoliposomes represents a novel variation on the theme with the potential to retain the targeting capabilities of traditional radioimmunotherapies while increasing the dose-rate to the tumour tissue. Intraperitoneal radiation therapy also allows for the possibility of patient-specific treatment planning. The work presented in this chapter is intended to illustrate some of the factors that might affect the outcome of the treatment. This is of interest because many if not all of the parameters used in this model can be estimated with a combination of *in-vivo* and *in-vitro* work. The biodistribution of the therapeutic agent can be estimated by administering a lower activity of ^{188}Re that can be monitored via its 155 keV photon emission with a 15% abundance (ICRP 1983). From this, an estimate of the biological elimination constant k_3 is possible. *In-vitro* studies can be performed on ovarian cancer cells harvested from the peritoneal fluid to assess CA-125 concentrations. These cells can also be used to study the binding kinetics to provide estimates of the parameters k_1 and k_2 as well as the radiation sensitivity of the cells. Together, this information could be used to estimate an optimal injected activity and provide an estimate of when a second peritoneal lavage could be performed to remove as much unbound radioactivity as possible, thereby reducing the healthy tissue dose.

The motivation for this work was to investigate how dynamic processes such as liposome binding and antigen shedding would affect tumour dose, and ultimately tumour control probability. For simplicity, several aspects of radiation biology have been left out of the analysis. A very simple cell survival model was used to avoid complicating the analysis with additional parameters. An i.p. administration of radioactivity would likely yield treatment protocols of several days. As such, a more detailed approach would require the use of a model that incorporates the effects of the cell cycle, including repopulation (Zaider *et al*, 2000, Howell *et al.*, 1998, Dale, 1996, Omura *et al*, 1998). Furthermore, the radiation sensitivity of cells within micrometastases would show variability, particularly in spheroids large enough to produce hypoxic centers. Dale (1996) described in detail how the linear quadratic model can be adapted to account for the effects of dose-rate during a treatment. The model suggests that the dose-rate-dependent βD^2 term must be modified by a function that reduces its effective contribution. This is because of the cellular capacity for sublethal damage repair if the treatment is not delivered instantaneously. The model is further complicated when a continuously changing dose rate is incorporated along with the potential for tumour cell repopulation as would be necessary for a radionuclide therapy.

Howell *et al.* (1994, 1998) expanded on this when they investigated the pharmacokinetics of antibody based therapies with radionuclides of different physical half-lives. They defined a relative advantage factor to describe the factor by which a longer-lived radionuclide is more likely to sterilize a tumour than a shorter-lived radionuclide when both radionuclides must meet an identical prescribed biologically effective dose to a critical organ. They found that a longer lived radionuclide such as P-32 can achieve a relative advantage factor greater than 2 over Y-90. Finally, in order to study the effects of this treatment on a population of patients, one would have to consider the interpatient variability of the parameters employed. Jones *et al.* (2000) modeled this phenomenon to show that if some of these parameters (i.e. cellular radiosensitivity and tumour doubling time) can be quantified prior to treatment, one could optimize the treatment protocol accordingly.

One of the assumptions made in this model is that [L]>>[C]. This seems reasonable for the case of a single tumour. A 15 GBq injection with 10^3 Re-188 atoms per liposome contains 1.3×10^{12} liposomes. A tumour of radius 0.05 cm with an antigen density of 10^{10} cm^{-2} has a total of 3.1×10^8 antigen. Attaching a liposome to every one of those antigen molecules would decrease the initial number of liposomes in the peritoneal cavity by 0.02%. In reality, though the antigen density may be lower and the number of free CA-125 molecules greater than zero, the number of micrometastases would be much larger than one. It is hoped, however, that a peritoneal lavage performed prior to the administration of the liposomes would remove a significant number of micrometastases.

6.7 Conclusion

A model was been developed to describe the time-dependent tumour control probabilities of micrometastases in the peritoneal cavity during intraperitoneal radionuclide therapy using radiolabeled immunoliposomes. Tumour dose was delivered by two sources: liposomes bound to the surface of the tumour, and the liposomes in solution in the peritoneal cavity that form a radioactive bath. Ultimately the dose was expressed in terms of a number of biological parameters that described the dynamic behaviour of the system. These included the tumour surface density of the antigen CA-125, the rate at which liposomes bind to, and unbind from, the tumour and the rate at which liposomes are removed from the peritoneal cavity. The amount of CA-125 on the surface of the cancer cells was critically important for the realization of a benefit from using a targeted approach. If insufficient CA-125 was present, the vast majority of the tumour dose came from the liposomes in solution. The expression of TCP as a function of these parameters is important because it allows for the possibility of patient-specific treatment planning since these parameters can be estimated for each patient based on *in vivo* and *in vitro* studies.

References

Alvarez RD, Partridge EE, Khazaeli MB, Plott G, Austin M, Kilgore L, Russell CD, Liu T, Grizzle WE, Schlom J, LoBuglio AF and Meredith RF 1997 Intraperitoneal Radioimmunotherapy Of Ovarian Cancer With ^{177}Lu-CC49: A Phase I/II Study. *Gynecol. Oncol.* **65** 94-101.

Atthey M, Nahum AE, Flower MA and McCready VR 2000 Effects Of Cellular Repair And Proliferation On Targeted Radionuclide Therapy: A Modelling Study. *Phys. Med. Biol.* **45** N15-N20.

Bakri YN, Given FT 1984 Radioactivity In Blood And Urine Following Intraperitoneal Instillation Of Chromic Phosphate In Patients With And Without Ascites. *Am. J. Obstet. Gynecol.* **150** 184-188.

Barrington-Leigh R. Personal Communication, 2004.

Buijs WC, Tibben JG, Boerman OC, Molthoff CF, Massuger LF, Koenders EB, Schijf CP, Siegel JA and Corstens FH 1998 Dosimetric Analysis Of Chimeric Monoclonal Antibody cMOv18 IgG In Ovarian Carcinoma Patients After Intraperitoneal And Intravenous Administration. *Eur. J. Nucl. Med.* **25** 1552-1561.

Cross WG, Freedman NO and Wong PY 1992 Tables Of Beta-Ray Dose Distributions In Water. Chalk River, Ontario: Atomic Energy Of Canada Ltd., Chalk River Laboratories. AECL-10521

Dale RG 1996 Dose-Rate Effects In Targeted Radiotherapy. *Phys. Med. Biol.* **41** 1871-1884.

Goitein M, Niemierko A and Okunieff P 1995 The Probability Of Controlling An Inhomogeneously Irradiated Tumour: A Stratagem For Improving Tumour Control Through Partial Tumour Boosting. Proceedings Of The 19th L H Gray Conference: Quantitative Imaging In Oncology. Chapter 2. Techniques For Tumour Volume Definition. pp 25-39

Howell RW, Goddu SM and Rao DV 1994 Application Of The Linear-Quadratic Model To Radioimmunotherapy: Further Support For The Advantage Of Longer-Lived Radionuclides. *J. Nucl. Med.* **35** 1861 – 1869.

Howell RW, Goddu SM and Rao DV 1998 Proliferation And The Advantage Of Longer-Lived Radionuclides In Radioimmunotherapy. *Med. Phys.* **25** 37-42.

Hui T, Fisher D, Press O, Eary J, Weinstein J, Badger C and Bernstein I 1992 Localized beta Dosimetry Of ^{131}I-Labeled Antibodies In Follicular Lymphoma. *Med. Phys.* **19** 97-104.

ICRP Publication 38 1983 Radionuclide Transormations. Energy And Intensity Of Emissions. Pergamon Press, Oxford.

Jones B and Dale RG 2000 Radiobiological Modeling And Clinical Trials. *Int. J. Radiat. Oncol. Biol. Phys.* **48** 259 – 265.

Kairemo KJ 1996 Radioimmunotherapy Of Solid Cancers: A Review. *Acta Oncol.* **35** 343-355.

Kolstad P, Davy M and Hoeg K 1977 Individualized Treatment Of Ovarian Cancer. *Am. J. Obstet. Gynecol.* **128** 617 – 625.

Langmuir V and Sutherland R 1988 Dosimetry Models For Radioimmunotherapy. *Med. Phys* **15** 867-873.

Larsson L 1988 Immunocytochemistry: Theory and Practice. CRC Press Inc. Boca Raton. pp 1 – 2.

Leichner P and Kwok C 1993 Tumor Dosimetry In Radioimmunotherapy: Methods Of Calculation For Beta Particles. *Med. Phys.* **20** Pt. 2 529-534.

Nahum A 1996 Microdosimetry And Radiocurability: Modelling Targeted Therapy With β-Emitters. *Phys. Med. Biol.* **41** 1957-1972.

Omura M, Torigoe S, Kurihara H, Matsubara S and Kubota N 1998 Comparison Between Fractionated High Dose Rate Irradiation And Continuous Low Dose Rate Irradiation In Spheroids. *Acta Oncol.* **37** 681-686.

Roeske J, Chen G and Brill A. 1993 Dosimetry Of Intraperitoneally Administered Radiolabeled Antibodies. *Med. Phys.* **20** 593 – 600.

Rotmensch J, Roeske J, Chen G, Pelizzari C, Montag A, Weichselbaum R, Herbst A L. 1990 Estimates Of Dose To Intraperitoneal Micrometastases From Alpha And Beta Emitters In Radioimmunotherapy. *Gynecol. Oncol.* **38** 478 – 485.

Schwesinger F, Ros R, Strunz T, Anselmetti D, Guntherodt H-J, Honegger A., Jermutus L, Tiefenauer L and Pluckthun A 2000 Unbinding Forces Of Single Antibody-Antigen Complexes Correlate With Their Theraml Dissociation Rates. *Proc. Natl. Acad. Sci. USA.* **97** 9972-9977.

Sutherland R, Buchegger F, Schreyer M, Vacca A and Mach J-P 1987 Penetration And Binding Of Radiolabeled Anti-Carcinoembryonic Antigen Monoclonal Antibodies And Their Antigen Binding Fragments In Human Colon Multicellular Tumor Spheroids. *Cancer Res.* **47** 1627-1633.

Vergote I, Larsen RH, De Vos L, Nesland JM, Bruland O, Bjorgum J, Alstad J, Trope C and Nustad K 1992b Therapeutic Efficacy Of The α-Emitter ^{211}At Bound On Microspheres Compared With ^{90}Y and ^{32}P Colloids In A Murine Intraperitoneal Tumour Model. *Gynecol. Oncol.* **47** 366-372.

Vergote I, Larsen RH, De Vos L, Winderen M, Ellingsen T, Bjorgum J, Hoff P, Aas M, Trope C and Nustad K 1992a Distribution Of Intraperintoneally Injected Microspheres Labeled With The Alpha-Emitter Astatine (211At) Compared With Phosphorus (32P) And Yttrium (90Y) Colloids In Mice. *Gynecol. Oncol.* **47** 358-65.

Watson EE, Stabin MG, Davis JL and Eckerman KF 1989 A Model Of The Peritoneal Cavity For Use In Internal Dosimetry. *J. Nucl. Med.* **30** 2002-2011.

Zaider M and Minerbo GN 2000 Tumour Control Probability: A Formulation Applicable To Any Temporal Protocol Of Dose Delivery. *Phys. Med. Biol.* **45** 279-293.

Chapter 7

Microdosimetry of Single Cells During Intraperitoneal Radionuclide Therapy

7.1 Introduction

Intraperitoneal radionuclide therapy is a treatment modality employed to slow the progress of cancers that have metastasized to the peritoneal cavity. This technique has evolved over time to produce treatments that are better able to minimize normal tissue complications and offer greater tumour selectivity. These developments have been facilitated by research into radionuclide selection and delivery vehicles. Currently there is interest in both alpha and beta emitters used in both targeted and non-targeted delivery systems (Bakri *et al.* 1984, Vergote *et al.* 1992a, Vergote *et al.* 1992b, Alvarez *et al.* 1997, Buijs *et al.* 1998, McQuarrie *et al.* 2001). The high LET and short range of alpha emitters make them attractive candidates for the treatment of single cells or small clusters of cells suspended in the peritoneal fluid, however, the treatment of any macroscopic tumours seeded on the walls of the peritoneal cavity could be problematic if adequate source distribution within the tumour is not possible. The longer range of beta emitters suggests that they will produce improved dose homogeneity relative to alpha emitters in larger tumours at a cost of decreased dose to single cells or small clusters of cells per particle traversal. Delivery systems have been designed to improve some of the shortcomings of original work involving radiolabeled colloids (Barki *et al.* 1984, Vergote *et al.* 1992b). Greater peritoneal retention has been achieved using larger preparations such as microspheres (Vergote *et al.* 1992a, Vergote *et al.* 1992b), while tumour selectivity has been enhanced with targeting moieties such as monoclonal antibodies (Alvarez *et al.* 1997, Buijs *et al.* 1998). For the remainder of this work, such therapies will be discussed in the context of beta emitting radionuclides.

Typically, an intraperitoneal radionuclide therapy involves the administration of the radioactive preparation and a significant volume of saline to ensure uniform distribution of radioactivity throughout the peritoneal cavity (Buijs *et al.* 1998, Alvarez *et al.* 1997, Kolstad *et al.* 1977). Non-targeted therapies will thus provide tumour dose from all source elements that lie within a distance that is less than the maximum range of the beta emitter. Targeted therapies also produce this source geometry but the tumour dose is enhanced by the binding of the targeting moiety to the surface of the cells (Rotmensch *et al.* 1990, Roeske *et al.* 1993). With targeted therapies, there also exists the possibility of cross-fire, in which radionuclides bound to one cell can produce an energy deposition event in another cell.

For macroscopic tumour volumes, beta dosimetry calculations generally involve the use of the MIRD formalism (Loevinger *et al.* 1988, Bolch *et al.* 1999) or dose point kernels. Dose point kernels are functions that describe the dose rate as a function of distance from a point source of radioactivity (Cross *et al.* 1992). If the spatial distribution of radioactivity within the tumour is known, the corresponding dose distribution can often be determined via convolution with the appropriate dose point kernel (Kwok *et al.* 1985). For microscopic target volumes involving potentially few particle traversals with a range of path lengths and initial energies incident on the volumes, it seems reasonable to expect a significant variability in the absorbed dose to the volumes. Microdosimetry is the tool used to investigate the stochastic nature of energy deposition in small volumes. The quantity called specific energy, denoted by z, is the microdosimetric equivalent of absorbed dose and has the same units (Gy). The distribution of z produced by the traversal of the target volume by individual particles is called the single event spectrum and is denoted by $f_1(z)$ (ICRU 36 1983). Monte Carlo simulation allows for the determination of $f_1(z)$ by tracking many individual electrons through the target volume and scoring the energy deposited in the volume.

The work presented here is an investigation of the microdosimetry of single cells suspended in the peritoneal fluid during intraperitoneal radionuclide therapy. The Monte Carlo code system used for this purpose was EGSnrc. This system has a limitation of a low energy cutoff of 10 keV for electrons, below which energy is assumed to be deposited locally. Two monoenergetic single event spectra calculated with EGSnrc are compared to those produced by two other codes in previously published work. The specific energy single event spectra for five beta emitting radionuclides (Lu-177, Cu-67, Re-186, Re-188, Y-90) are presented for two source geometries: radioactivity bound to the surface of the cells and free radioactivity in the peritoneal fluid. The effect of cross-fire in this treatment modality is not considered in this work.

7.2 Monte Carlo Simulations

EGSnrc is the latest in the family of EGS Monte Carlo codes. This software simulates the coupled transport of both charged particles and photons (Kawrakow *et al.* 2002, Kawrakow 2000). In general it applies a condensed history technique to the charged particle transport where the cumulative effects of individual interactions are condensed into single discrete steps as primary and secondary particles are followed. Improvements over its predecessor, EGS4, in areas such as the multiple scattering and boundary crossing algorithms made this code attractive for the investigation of microdosimetry problems. In particular, the ability to track particles in single scatter mode, whereby the particle histories are no longer condensed, was exploited for this investigation. As mentioned previously, EGSnrc retains the 10 keV cutoff for electron transport which could be problematic in certain microdosimetric applications since a 10 keV electron still has a range of approximately 2.5 μm (Bolch *et al.* 1994).

For all simulations both the target and the surrounding medium were assumed to be water equivalent. The cellular target was modeled as a sphere with a radius of 10 μm. For each electron history, the particle (and any secondary electrons, Auger electrons, bremsstrahlung photons, characteristic x-rays etc.) was tracked in single scatter mode whenever its coordinates were within 100 mean free paths of the target boundary. Energy deposition was scored in 50 eV bins. For both source geometries it was assumed that the spectrum of the beta particle energy distribution could be described by a series of steps with a constant value over a 1 keV interval. Single event spectra were obtained for electrons with initial energies between 11 keV and 2500 keV. The endpoint of 2500 keV extends beyond the energy range of those radionuclides considered in this work (see Table 7.4). The sampling frequencies are shown in Table 7.1.

Table 7.1: Sampling frequency for "monoenergetic" single event spectra

Energy Range (keV)	Sampling Frequency (keV)
11 - 99	1
100 - 600	10
700 - 1000	100
1250 - 2500	250

The energies listed in Table 7.1 represent the midpoint of a 1 keV range of energies that was used to create the "monoenergetic" single event spectra. For example, the spectrum for 36 keV electrons for surface bound radioactivity was obtained by uniformly sampling 2 x 10^6 initial electron energies between 35.5 and 36.5 keV. This allowed us to sample the entire beta spectrum for each radionuclide below 100 keV where the single event spectra change most rapidly. Spectra generated with this technique were indistinguishable from truly monoenergetic spectra at high energies (i.e. 1 MeV) since the spectra change much more slowly at these energies. Due to the 10 keV cutoff of EGSnrc, spectra for electrons with energies below 10 keV were modeled instead of simulated. Although this introduced uncertainties into the calculations, the spectra seemed reasonable given the trends of the spectra for energies in the vicinity of 10 keV and the short range of these electrons compared to the target diameter. The contributions of Auger electrons and internal conversion electrons were also included in the spectra.

7.2.1 Surface-Bound Radioactivity

To simulate surface-bound radioactivity an isotropically-emitting point source was positioned on the surface of the target volume. At each energy, 2 x

10^6 histories were collected. The "monoenergetic" single event spectra were then appropriately weighted by a radionuclide's beta spectrum to produce the composite radionuclide beta single event spectrum. The beta spectra for the radionuclides used in this study were taken from the online radiation dose assessment resource (RADAR) (www.doseinfo-radar.com) and are shown in Figure 7.1.

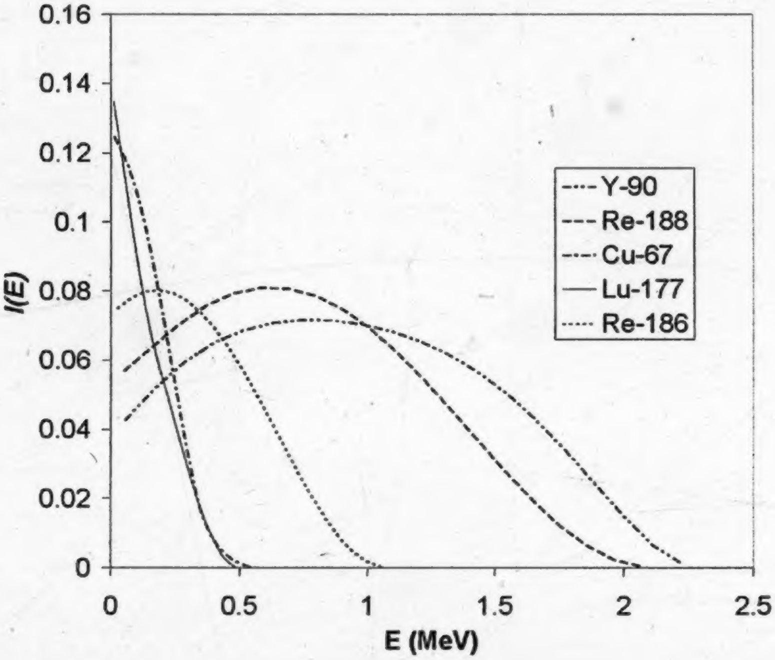

Figure 7.1: Beta spectra of the radionuclides used in this work. *I(E)* denotes the relative intensity of beta emissions of energy E. Spectra have not been normalized.

In addition to the beta spectrum for each radionuclide, contributions from Auger electrons and internal conversion electrons emitted by the radionuclide were also considered. The criteria for inclusion were energies greater than 1 keV and a branching ratio greater than 10^{-3}. Yttrium-90 does not emit any particles that meet these criteria, but the emissions used for these simulations from the other radionuclides are given in Table 7.2. Data for this table were taken from the DEXRAX program distributed by the ORNL Center for Biokinetic and Dosimetric Research (http://ordose.ornl.gov/). This program provides a detailed listing of the emissions from a large number of radionuclides.

Table 7.2: Auger electron (ae) and internal conversion electron (ic) emissions from Cu-67, Re-186, Lu-177 and Re-188. Inclusion creiteria were energy greater than 1 keV and branching ratio greater than 10^{-3}.

Cu-67			**Re-186**		
E (keV)	Branching Ratio	Type	E (keV)	Branching Ratio	Type
9.5	1.51E-03	ae	11.8	1.28E-03	ae
8.5	6.89E-03	ae	10.3	2.16E-03	ae
8.5	3.82E-03	ae	10.1	8.09E-03	ae
8.4	4.58E-03	ae	10.0	1.64E-03	ae
7.6	4.69E-03	ae	9.7	1.95E-03	ae
7.5	3.00E-02	ae	9.5	5.82E-03	ae
7.5	2.04E-03	ae	8.6	1.30E-02	ae
7.4	3.82E-03	ae	8.1	1.19E-02	ae
7.4	9.86E-03	ae	8.0	2.31E-03	ae
7.2	3.45E-03	ae	8.0	1.31E-02	ae
1.1	1.99E-03	ae	7.5	9.59E-03	ae
1.0	6.37E-03	ae	6.5	2.08E-02	ae
1.0	1.02E-02	ae	6.1	1.92E-02	ae
174.9	9.46E-03	ic	2.2	1.34E-01	ae
93.2	2.18E-03	ic	2.1	1.15E-01	ae
92.3	2.45E-03	ic	137.2	4.23E-03	ic
92.3	1.68E-03	ic	134.7	1.40E-02	ic
92.1	1.07E-02	ic	126.3	2.23E-02	ic
83.7	1.21E-01	ic	124.8	2.87E-02	ic
81.6	5.10E-03	ic	124.2	4.26E-03	ic
			122.7	1.20E-03	ic
			120.4	4.09E-03	ic
			112.5	6.89E-03	ic
			111.2	8.27E-03	ic
			110.6	1.12E-03	ic
			63.3	3.80E-02	ic
			53.2	1.06E-02	ic

Lu-177			Re-188		
E (keV)	Branching Ratio	Type	E (keV)	Branching Ratio	Type
10.3	1.86E-03	ae	11.80	1.39E-03	ae
9.4	1.14E-03	ae	10.3	2.41E-03	ae
9.1	3.30E-03	ae	10.1	8.78E-03	ae
8.8	1.15E-02	ae	8.6	1.46E-02	ae
7.7	2.00E-02	ae	8.0	1.43E-02	ae
7.5	1.61E-03	ae	6.5	2.32E-02	ae
7.0	1.90E-02	ae	2.2	1.48E-01	ae
5.8	3.24E-02	ae	155.0	4.20E-03	ic
1.9	1.93E-01	ae	152.6	1.40E-02	ic
143.0	5.96E-03	ic	144.2	2.11E-02	ic
113.0	4.99E-03	ic	142.7	2.86E-02	ic
110.8	1.74E-02	ic	142.1	5.52E-03	ic
103.4	3.02E-02	ic	81.2	4.88E-02	ic
102.2	3.43E-02	ic			
101.7	5.54E-03	ic			
47.6	5.25E-02	ic			
6.3	1.11E-03	ic			

7.2.2 Free Radioactivity

The problem of the free radioactivity was slightly more complicated. High energy beta emitters such as Y-90 have a range in water in excess of 1 cm. For target volumes that represent single cells it would be too inefficient to calculate the single event spectrum by randomly sampling position, energy and trajectory for each beta emission. Instead, some assumptions about the spectrum of electrons "seen" by the target volume were made and then the single event spectrum was determined by tracking electrons that, by definition, cross the target volume. The CSDA spectrum for each radionuclide was calculated in the manner described by Johns *et al.* (1983). If the bath of radioactivity is sufficiently large that charged particle equilibrium exists, then the amount of energy emitted by any small volume in the bath must equal the amount of energy absorbed in the same volume. The spectrum of energies emitted by the volume is given by the radionuclide's beta spectrum, denoted by $I(E)$. To determine the relative intensity of betas of energy E in the CSDA spectrum, $C(E)$, one must evaluate the following integral:

$$C(E)=\frac{1}{S_{tot}(E)}\int_{E}^{E_{\beta max}} I(E')dE' \qquad (7.1)$$

where $S_{tot}(E)$ is the total stopping power of the medium and $E_{\beta max}$ is the maximum beta energy for the radioisotope. The spectra produced by the Auger electrons and internal conversion electrons were calculated in a similar manner and then added to the function $C(E)$ after being weighted by the appropriate branching ratio as given in Table 7.2. The CSDA spectra for the radionuclides used in this study are shown in Figure 7.2. In the case of the free radioactivity it was assumed that the electrons follow random trajectories through the target. To facilitate this, the initial trajectory direction cosines for each electron track was provided as input to the EGSnrc code. All subsequent interactions and directions were determined by the Monte Carlo process. The initial trajectory direction cosines were calculated based on vectors connecting two points on the surface of the target sphere.

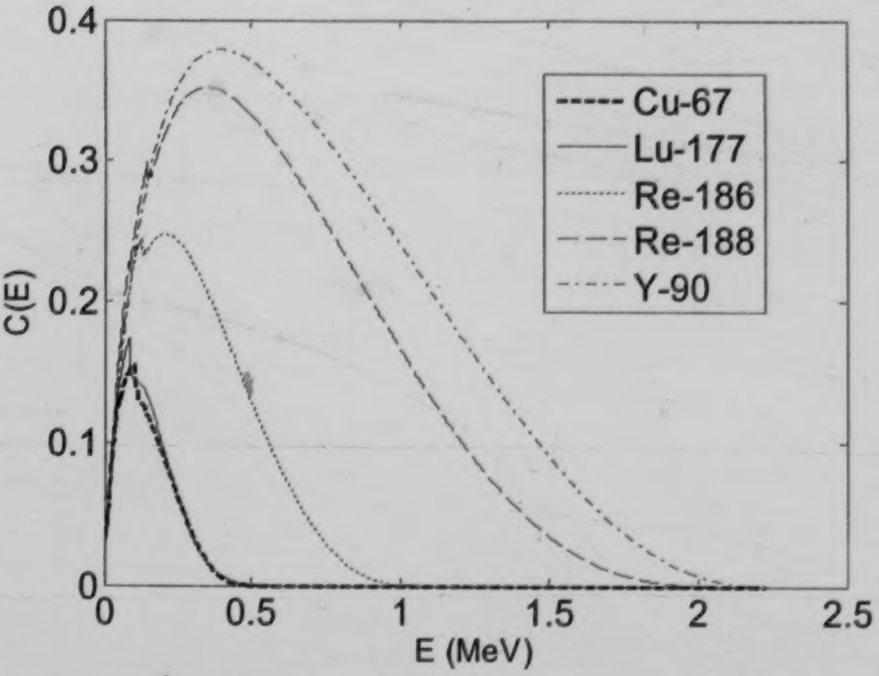

Figure 7.2: CSDA spectra for the radionuclides used in this work. *C(E)* denotes the relative intensity of electrons of energy E at any point in the medium.

The points on the sphere were sampled in a uniform, random manner. For comparison purposes, when those trajectories were extrapolated as linear paths through the sphere, the distribution of path lengths was identical to that of a convex body exposed to a uniform isotropic fluence of infinite straight lines. This type of randomness is referred to as isotropic uniform randomness in the work of Kellerer (1984).

7.3 Results

The single event spectra for low energy electrons (i.e. below approximately 50 keV) were characterized by the presence of a peak at a specific energy that corresponded to the initial energy of these electrons. A number of low energy electron single event spectra are shown in Figures 7.3 and 7.4 for surface bound and free radioactivity respectively.

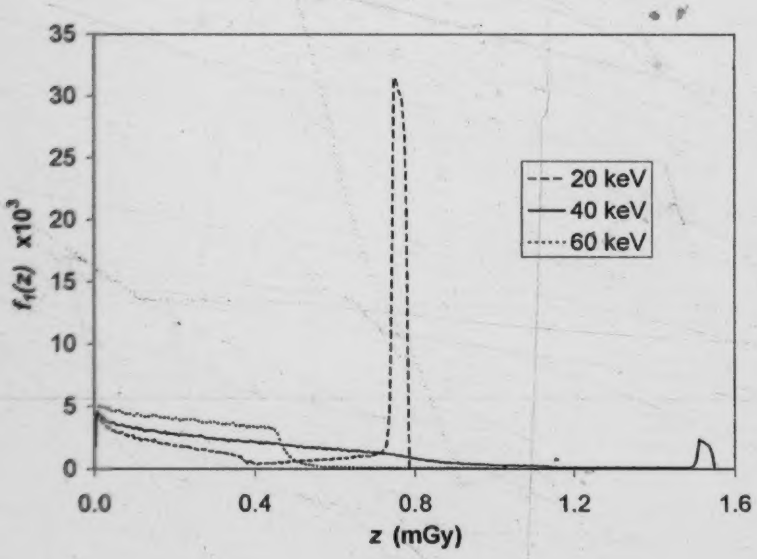

Figure 7.3: Single event spectra for surface-bound low energy electrons. Below 50 keV the spectra show a peak at a value of z corresponding to the initial energy of the electrons. At these energies the spectra change rapidly with energy.

The presence of the peak was observed in both source geometries and resulted from the fact that at these energies the diameter of the target volume was sufficiently large that it either exceeded the range of the electrons or allowed for a non-negligible possibility that the tortuous path followed by these electrons would result in the deposition of the entire electron energy within the target. The spectra for electrons with initial energies below 10 keV were modeled after the spectrum

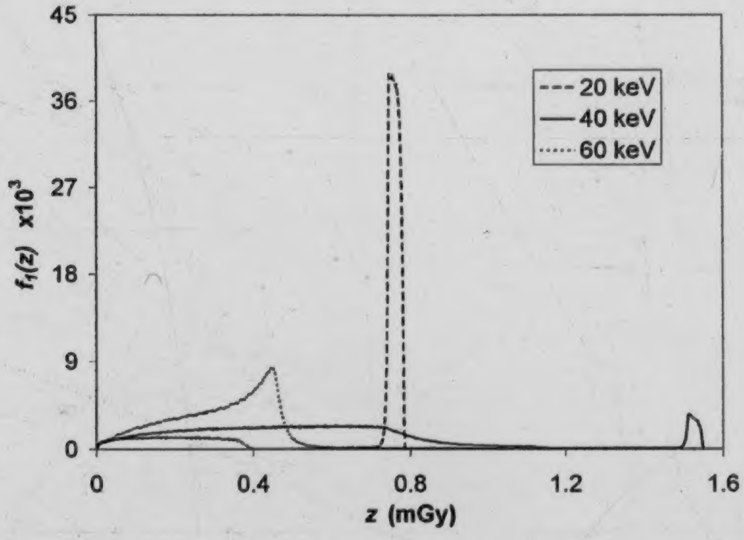

Figure 7.4: Single event spectra for low energy electrons in the free radioactivity source geometry.

for electrons with an initial energy of 11 keV. At this energy, the spectrum was comprised of a large peak centered at approximately 0.42 mGy and a small, low z tail. The size of the low z tail decreased rapidly between 15 keV and 11 keV so for simplicity, the spectra for electrons below 10 keV were represented by a single peak at the appropriate value of z with the same size as the peak in the 11 keV spectra.

The surface-bound single event spectra for Auger electrons were modeled in a similar manner, however, they were based on the spectrum produced by a truly monoenergetic 11 keV electron. The contributions of a higher energy internal conversion electron was based on the closest pseudo-monoenergetic single event spectrum. It is difficult to quantify the uncertainty associated with these spectra using this approach, however, it should be reasonably low since the spectra are dominated by a single feature. High energy electrons crossing the target deposited less energy than low energy electrons due to the decreased stopping power. Single event spectra for a number of high energy electrons are shown in Figures 7.5 and 7.6 for surface bound and free radioactivity respectively.

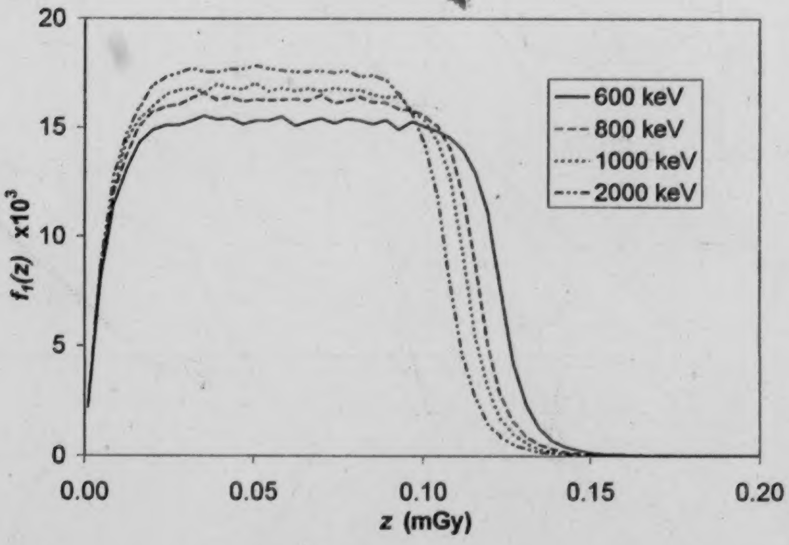

Figure 7.5: Single event spectra for surface-bound high energy electrons. The spectra change much more slowly at these energies. The peaks appear noisy due to the 50 eV bins used to score energy deposition.

The surface bound spectra were almost symmetric about the midpoint of the distributions while the spectra for the free radioactivity were peaked toward the higher z range of the distribution. The differences in the spectra between surface bound and free radioactivity at all energies stemmed from the differences in the path length distributions that described the electron trajectories.

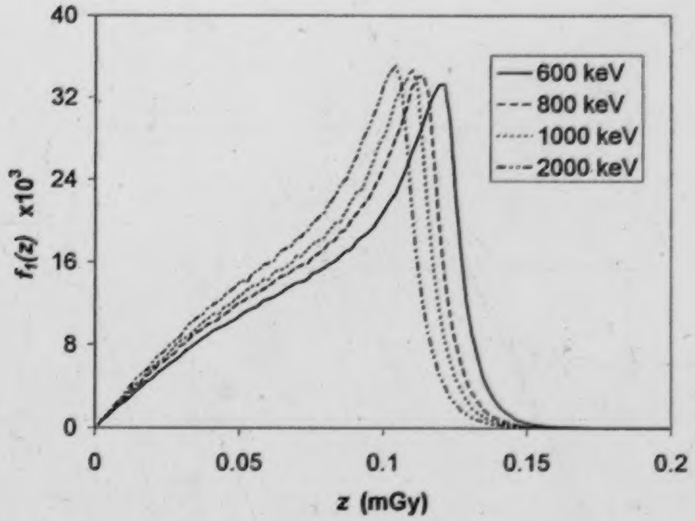

Figure 7.6: Single event spectra for high energy electrons in the free radioactivity source geometry. The peaks are shifted to higher values of z relative to the surface bound geometry due to larger mean path lengths through the target.

For simplicity, consider the trajectories through the target to be straight lines. To determine the path length distribution for an isotropically-emitting point source, one must uniformly sample the surface of a hypothetical sphere centered on the point source. The surface area element in spherical coordinates is given by:

$$dA = r^2 \sin\theta d\phi d\theta \tag{7.2}$$

In terms of the path lengths, the azimuthal angle, ϕ, does not affect the distribution because of the symmetry of the problem. Cumulative inverse sampling of the polar angle, θ, takes the following form:

$$\frac{\int_0^{\theta} \sin\theta' \, d\theta'}{\int_0^{\pi/2} \sin\theta \, d\theta} = R \qquad (7.3)$$

In this expression, R is a random number between 0 and 1 and the polar angle is allowed to take values between 0 and $\pi/2$ because this range of angles produces emissions that intersect the target sphere as shown in Figure 7.7.

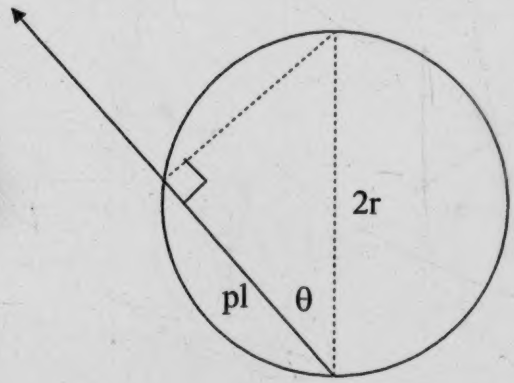

Figure 7.7: Illustration of a sample path length through a spherical target volume from a radionuclide bound to the surface of the target.

In the Monte Carlo process, an individual value of θ is found by solving Eq 7.4:

$$\theta = \cos^{-1}(1 - 2R) \qquad (7.4)$$

For a given value of θ, the path length, pl, through the target is given by:

$$pl = 2r\cos\theta \qquad (7.5)$$

Using the expression for θ from equation 7.4, it is clear that the path length distribution for this source geometry is flat; any path length is as probable as any other over the range of 0 to 2r, where r is the radius of the target sphere. The random path lengths chosen for the free radioactivity follow a distribution given by:

$$P(pl) = \frac{pl}{2r^2} \tag{7.6}$$

Where *P(pl)* denotes the probability distribution of *pl*. This function increases linearly from 0 at a path length of 0 to a maximum at 2r. The expectation value of this distribution is given by (4/3)r, where r is the target radius (Kellerer, 1984).

We compared results obtained using EGSnrc to two other Monte Carlo codes by repeating the calculations of other investigators for two beta energies in the surface bound source geometry. Bolch *et al.* (1994) presented single event spectra for 100 keV and 1 MeV electrons bound to the surface of a 10 μm diameter cell as determined with the OREC Monte Carlo Code. Stewart *et al.* (2002) repeated this work with the PENELOPE code system. The OREC code system tracks electrons in water event by event, down to a cutoff energy of 7.4 eV (Kim *et al.* 1996). The PENELOPE system implements a mixed simulation algorithm. Hard electron interactions, events in which polar scattering angle or energy loss exceed previously selected values (Baró *et al.* 1995), are simulated in a "detailed" way while multiple scattering theory is applied to soft interactions (Stewart *et al.* 2002). Table 7.3 contains the values of $\bar{z}_f$ from all three code systems.

There was very good agreement between EGSnrc and OREC for the 1 MeV electrons. At 100 keV, EGSnrc produced a value of $\bar{z}_f$ that was 7.4% lower than that of OREC and 2.4% greater than that of PENELOPE. The shapes of the 100 keV spectra were similar though not identical and it was unclear if this resulted from differences in the transport physics, the nature of the user codes or was a potential artifact related to the 10 keV cutoff energy.

Table 7.3: Comparison of EGSnrc with the OREC and PENELOPE Monte Carlo systems. Values of $\bar{z}_f$ were calculated for a sphere with a radius of 5 μm. Agreement between EGSnrc and OREC is very good at 1000 keV but shows a 7.3% discrepancy at 100 keV. PENELOPE also shows reasonable agreement with EGSnrc.

	$\bar{z}_f$ (mGy)	
Monte Carlo System	100 keV	1000 keV
EGSnrc	0.63	0.27
OREC	0.68	0.26
PENELOPE	0.615	Within 6% of OREC

To investigate the effects of the cutoff energy, single event spectra for 20, 50, 100, 500 and 1000 keV electrons in the surface-bound geometry were generated with different cutoff energies. Each spectrum was generated with 10^6 electron histories. For the 100, 500 and 1000 keV spectra the cutoff ranged from 10 keV to 40 keV. At 500 and 1000 keV the spectra with a cutoff of 40 keV were indistinguishable from those with the 10 keV cutoff (data no shown). At 100 keV the broad principal peak was indistinguishable over this range of cutoff energies and only a very small difference in the high z tail was visible at a cutoff energy of 40 keV (data not shown). This suggested that for the majority of the electron energies relevant to the beta emitters considered in this work, the 10 keV cutoff energy would not adversely affect the results. The effects of the cutoff were apparent at electron energies of 20 and 50 keV. For these energies, the cutoffs ranged from 10 to 15 keV and 10 to 20 keV respectively. Figure 7.8 shows two single event spectra for 50 keV electrons with cutoff energies of 10 keV and 20 keV.

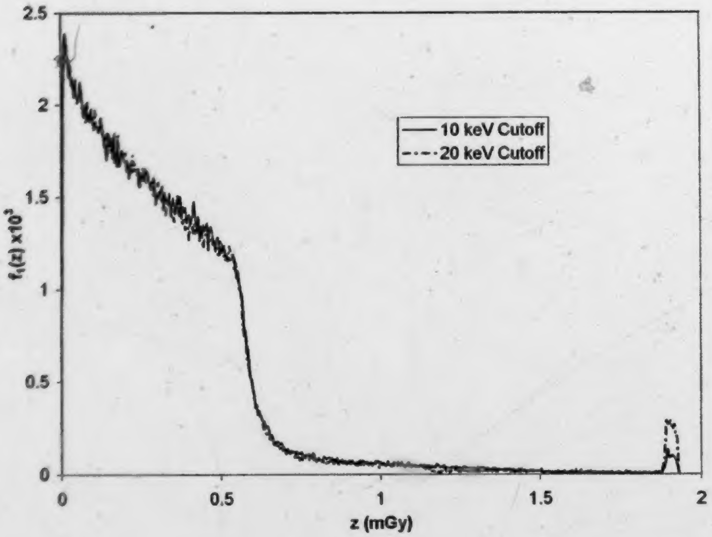

Figure 7.8: Single event spectra for surface-bound 50 keV electrons with cutoff energies of 10 keV and 20 keV. The higher cutoff energy results in an increased number of events that deposit the entire electron energy in the target volume.

Although the spectra were noisy due to the small bin width, it is apparent that the effect of the higher cutoff energy was to increase the number of events that resulted in the deposition of the entire electron energy in the target volume. To compensate for the larger peak at 1.9 mGy, the remainder of the spectrum with the 20 keV cutoff energy was slightly lower than that with the 10 keV cutoff energy. In Figure 7.9, the number of events in the 1.9 mGy peak was plotted as a function of the cutoff energy.

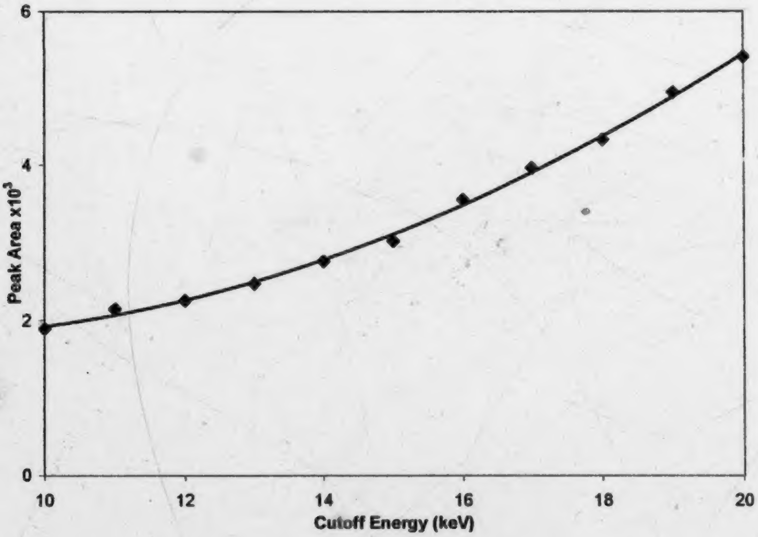

Figure 7.9: Peak area as a function of cutoff energy for surface-bound 50 keV electrons. The curve has not completely leveled off at a cutoff energy of 10 keV suggesting that EGSnrc is slightly overestimating the number of events in the 1.9 mGy peak shown in Figure 7.8.

As the cutoff energy decreased to 10 keV the area of the peak was still decreasing but at a diminishing rate. This suggested that EGSnrc would slightly overestimate the true number of electrons depositing their entire energy within the target volume. Figure 7.10 shows two single event spectra for 20 keV electrons with cutoff energies of 10 keV and 15 keV.

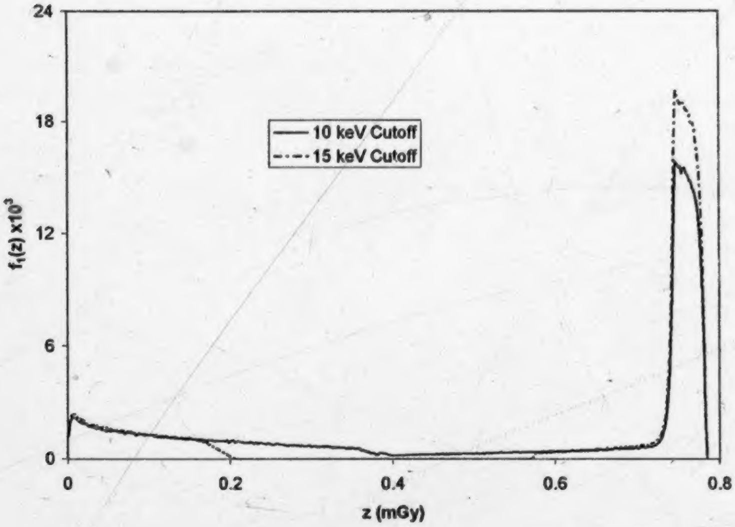

Figure 7.10: Single event spectra for surface-bound 20 keV electrons with cutoff energies of 10 keV and 15 keV. The higher cutoff energy results in an increased number of events that deposit the entire electron energy in the target volume

As with the 50 keV electrons, the higher cutoff energy resulted in an increased number of events depositing the entire electron energy within the target volume. With the cutoff energy set to 15 keV, the spectrum contained no events with values of *z* between approximately 0.2 and 0.57 mGy. This served to illustrate the scenario in which the histories of electrons whose energies and trajectories were sufficient to take them outside of the target volume were prematurely terminated resulting in an overestimation of the amount of energy deposited inside the target. As the cutoff energy was decreased this gap was filled in with the number of events in the 0.75 mGy peak decreasing to compensate. The area of the 0.75 mGy peak as a function of cutoff energy is shown in Figure 7.11.

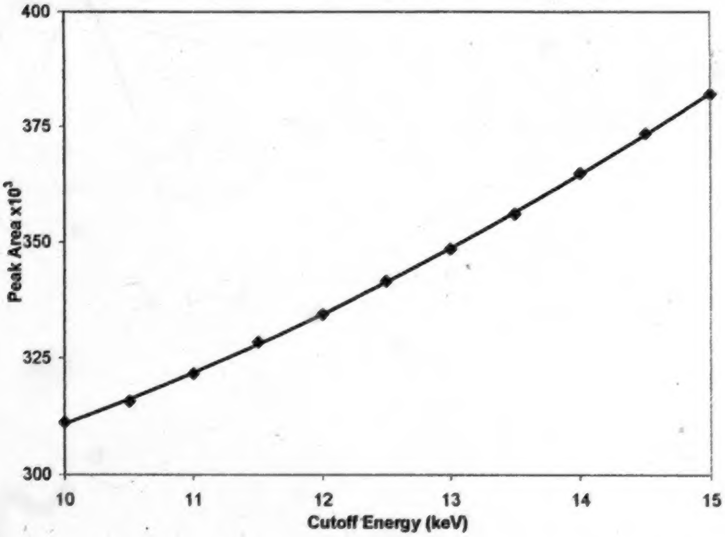

Figure 7.11: Peak area as a function of cutoff energy for surface-bound 20 keV electrons. The effects of the cutoff energy are more pronounced at lower electron energies. As the cutoff energy decreases to 10 keV, the area of the 0.75 mGy peak is still decreasing, suggesting that the cutoff energy of 10 keV results in an overestimate of the true peak size.

As the cutoff energy decreased to 10 keV, the curve had started to level off. These results indicated that the effects of the cutoff became more pronounced as the electron energy decreased. Once again, these data suggest that EGSnrc will overestimate the true number of events in the 0.75 mGy peak.

Each radionuclide beta single event spectrum was obtained by summing the "monoenergetic" single event spectra that were weighted by the appropriate beta or CSDA spectrum as described with Figure 7.12 and Eqs (7.7) and (7.8).

$$f_r(z) = \sum_{i=1}^{N} f_1(z, E_{si}) w_i \tag{7.7}$$

$$w_i = \frac{\int_{E_i}^{E_{i+1}} I(E)dE}{\int_0^{E_{\beta\max}} I(E)dE} \tag{7.8}$$

In Eq (7.7), $f_r(z)$ represents the single event spectrum for the radionuclide, while $f_1(z,E_{si})$ represents the "monoenergetic" single event spectrum for electrons of energy E_{si}, and w_i is the weighting factor for that spectrum as determined by the radionuclide beta spectrum. The spectra $f_1(z,E_{si})$ are used to represent the single event distributions for electrons with energies between E_i and E_{i+1}. Since the "monoenergetic" single event spectra at E_{si} were obtained with electrons whose initial energies were uniformly distributed over a 1 keV range centred on E_{si}, we have actually sampled the entire beta or CSDA spectrum for energies below 100 keV within the limitation of the assumption of a constant value of the spectrum over a 1 keV interval. This complete sampling is particularly important in this range since these are the energies at which the "monoenergetic" single event spectra change most rapidly. The radionuclide single event spectra for surface bound and free radioactivity are shown in Figures 7.13 and 7.14 respectively. Figure 7.13 shows only the contributions from the beta emissions. Auger electrons and internal conversion electrons are considered separately due to the complicating factor of the coupled emission of beta particles with Auger electrons and internal conversion electrons. The monoenergetic emissions are included in Figure 7.14 due to the difference in source geometry.

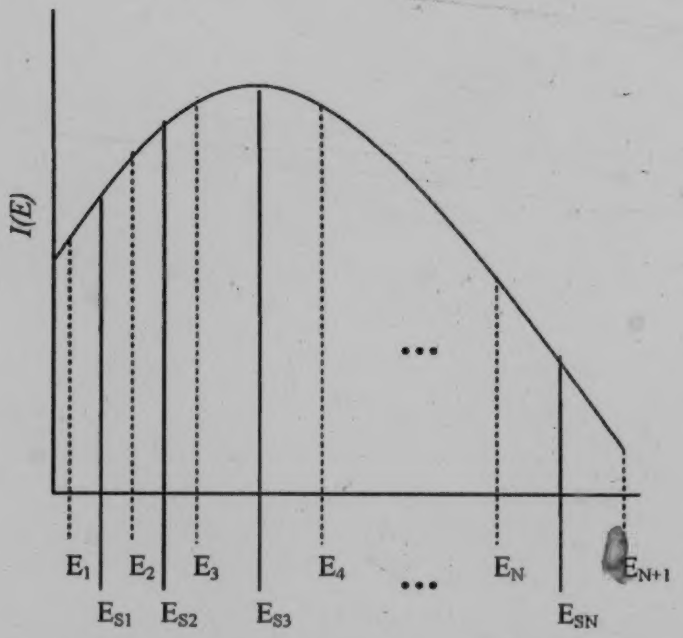

Figure 7.12: Illustration of weighting system used to calculate radionuclide single event spectra. Monoenergetic single event spectra were calculated at all energies E_{si}. The spectrum at E_{si} is used to represent all electron spectra between energies E_i and E_{i+1}.

The expectation value of the spectrum is known as the frequency-mean specific energy per event and is denoted by $\bar{z}_f$ (ICRU 36, 1983). Table 7.4 lists the values of $\bar{z}_f$ and their standard deviations for the radionuclides studied in this work. As expected, the value of $\bar{z}_f$ increased as the energy of the beta emitter decreased.

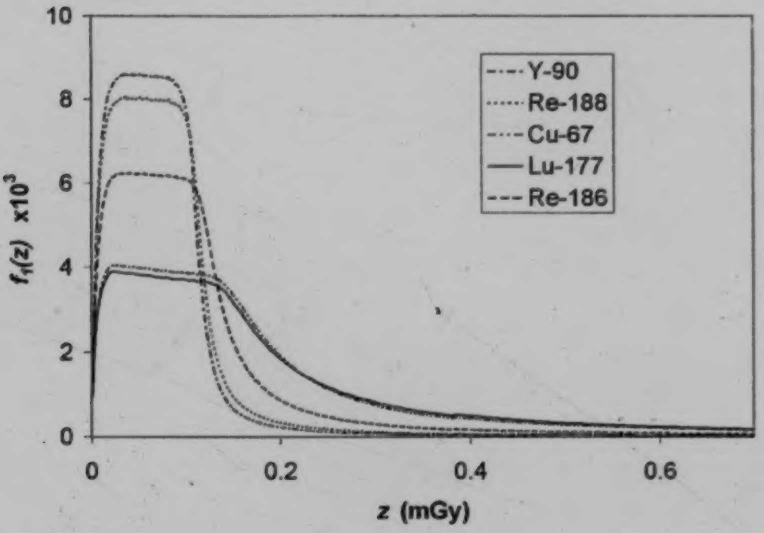

Figure 7.13: Radionuclide single event spectra for surface bound Cu-67, Re-188 and Y-90. Lower energy emitters have a larger frequency mean specific energy per event, $\bar{z}_f$, than high energy emitters due to the more pronounced high z tail.

The value of $\bar{z}_f$ for Lu-177 was 2.75 times higher than it was for the high energy emitter Y-90 for the surface bound radioactivity and 2.18 times higher for the free radioactivity. The contribution of those electrons capable of depositing all of their energy in the target was enhanced in lower energy emitters relative to high energy emitters. This fact was responsible for the high *z* tail that was significantly more pronounced in the Cu-67 and Lu-177 spectra than it was in the Y-90 and Re-188 spectra. It was the relative importance of the high *z* tail that increased the standard deviations in the values of $\bar{z}_f$ for the lower energy emitters.

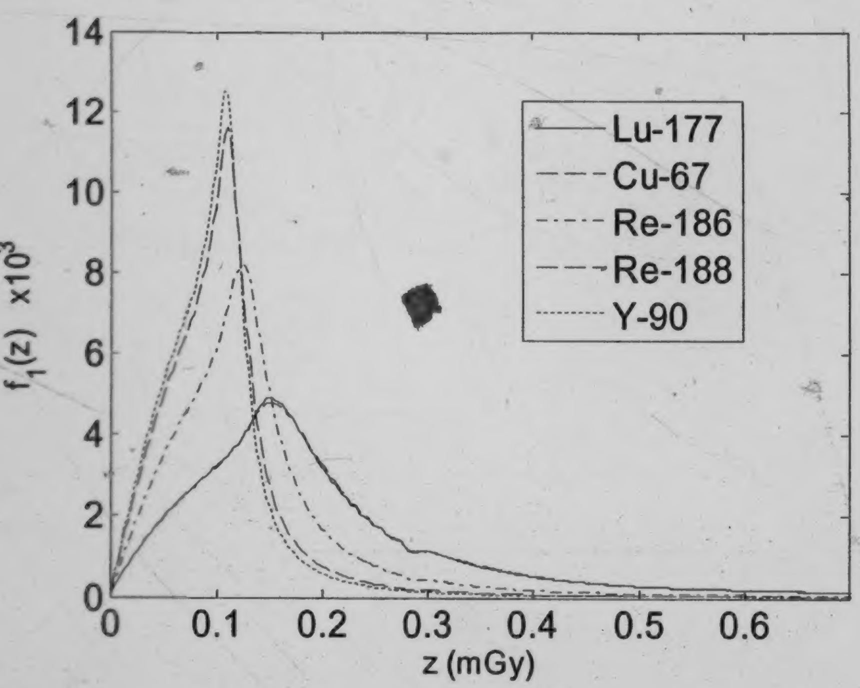

Figure 7.14: Radionuclide single event spectra for free radioactivity. The value of $\bar{z}_f$ in this geometry is larger than the corresponding value for the surface-bound radioactivity for each radionuclide because of the longer mean path length through the target for this source geometry.

In all cases, the value of the standard deviation in $\bar{z}_f$ was similar to the value of $\bar{z}_f$ itself. This showed that the range of path lengths through the target and initial energies of electrons incident on the target were sufficient to produce a significant variability in the amount of energy deposited per particle traversal. The value of $\bar{z}_f$ was larger for the free radioactivity than it was for the surface-bound radioactivity for all of the radionuclides. The longer mean path length through the target was primarily responsible for this for all of the radionuclides.

Table 7.4: Frequency mean specific energy per event, $\bar{z}_f$, and their standard deviations for both surface-bound radioactivity and free radioactivity in the peritoneal fluid. As the energy of the beta emitter increases, the value of $\bar{z}_f$ decreases.

		Surface-bound Radioactivity		Free Radioactivity	
Radionuclide	$E_{\beta max}$ (MeV)	$\bar{z}_f$ (mGy)	$\sigma\ \bar{z}_f$ (mGy)	$\bar{z}_f$ (mGy)	$\sigma\ \bar{z}_f$ (mGy)
Lu-177	0.498	0.22	0.24	0.24	0.22
Cu-67	0.577	0.20	0.23	0.24	0.22
Re-186	1.072	0.13	0.16	0.15	0.15
Re-188	2.120	0.09	0.11	0.12	0.11
Y-90	2.286	0.08	0.10	0.11	0.10

For the surface bound geometry, special consideration must be given to the Auger electron (ae) and internal conversion (ic) electron emissions. This results from the fact that the emission of ae and ic are coupled to the emission of a beta particle during the decay process. As such, after a decay in which an ae or ic is emitted, there exist four possible scenarios: 1. both particles miss the target, 2. only the ae/ic hits the target, 3. only the beta particle hits the target and 4. both the beta particle and the ae/ic hit the target. Since at least one hit is required by definition for the single event spectrum, scenario 1 will not contribute to the spectrum. To facilitate the calculations, one needs to know the probability, p, that an emitted particle will interact in the target. One might expect that the value of p should be 0.5 based on geometrical considerations. In fact, the value of p is an energy-dependent quantity. According to the simulations performed using EGSnrc, the value of p is greater than 0.5 for electrons with initial energies less than approximately 83 keV and less than 0.5 for electrons with initial energies greater than 83 keV. These data are shown in Figure 7.15. The probabilities of large angle scattering increase with decreasing energy. As such, a low energy electron whose initial trajectory is almost tangential to the target but away from the target has a reasonable probability of scattering into the target. These events increase the value of p above 0.5 for low energy electrons. For high energy electrons whose initial trajectory is almost tangential to the target but into the target, there exists the possibility that the electron will not undergo a hard interaction before it leaves the target. These events produce values of p below 0.5 for high energy electrons.

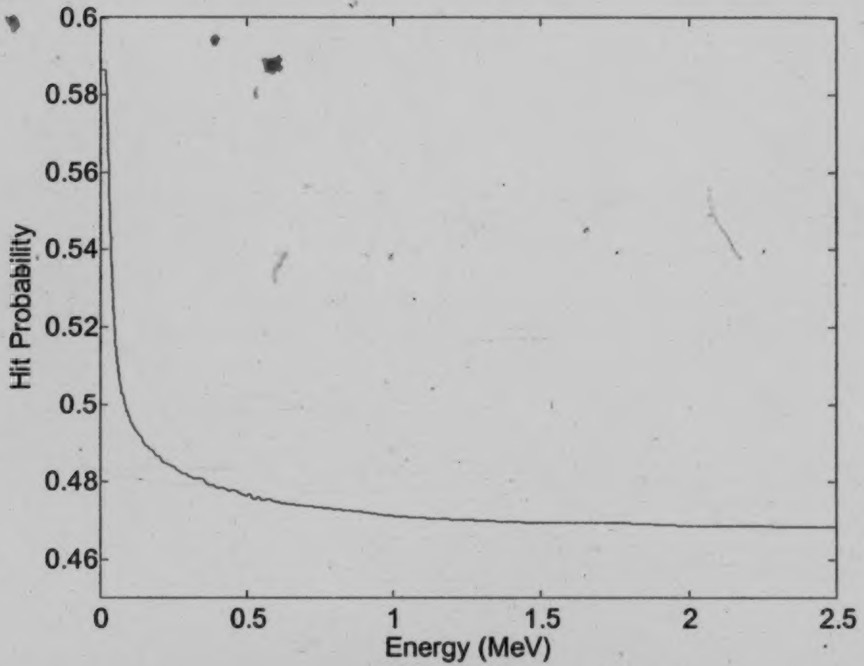

Figure 7.15: Energy-dependent probability that an electron emitted from the surface of a cell will undergo at least one hard interaction in the cell volume.

The average value of p, given by p_r, for the beta spectrum of a radionuclide is calculated by weighting the beta spectrum by the hit probability curve given in Figure 7.15. The values for the radionuclides used in this study are given in Table 7.5.

Table 7.5: Radionuclide-specific p values

Radionuclide	p_r
Lu-177	0.5102
Cu-67	0.5066
Re-186	0.4883
Re-188	0.4780
Y-90	0.4758

The event spectrum that describes the probability density of the specific energy per decay for a radionuclide is then constructed by appropriately weighting the beta spectrum contribution and the ae/ic contributions. The weight given to the beta spectrum contribution comes from two parts. First is the fraction of decays that do not result in the emission of any ae/ic electrons. The second contribution is from those decays in which an ae/ic is emitted but only the beta particle enters the target. If the radionuclide has a total of N ae/ic emissions and the ith emission has a branching ratio, y_i, then the weight of the beta spectrum contribution, w_{beta}, is given by

$$w_{beta} = 1 - \sum_{i=1}^{N} y_i + \sum_{i=1}^{N} y_i \frac{p_r(1-p_i)}{p_r(1-p_i) + p_i(1-p_r) + p_i p_r} \tag{7.9}$$

In Eq(7.9), p_i denotes the probability that the ith ae/ic emission will interact in the target. In a similar manner, the probability, w_{ei}, that only the ae/ic will hit the target is given by:

$$w_{ei} = y_i \frac{p_i(1-p_r)}{p_r(1-p_i) + p_i(1-p_r) + p_i p_r} \tag{7.10}$$

Finally, the probability, w_{bi}, that both particles hit the target is given by

$$w_{bi} = y_i \frac{p_i p_r}{p_r(1-p_i) + p_i(1-p_r) + p_i p_r} \tag{7.11}$$

The case of both particles hitting the target requires the calculation of a new spectrum to describe the probability density of z. The spectrum $f_{bi}(z)$ represents the distribution of z when the ith ae/ic hits the target along with the beta particle and is given by

$$f_{bi}(z) = f_{1beta}(z) * f_{1ei}(z) \tag{7.12}$$

Here the symbol * is used to denote a convolution operation. The total spectrum, $f_{r1}(z)$, describing the distribution of z per decay of the radionuclide is then constructed according to the following

$$f_{r1}(z) = w_{beta} f_{1beta}(z) + \sum_{i=1}^{N} w_{ei} f_{1ei}(z) + \sum_{i=1}^{N} w_{bi} f_{bi}(z) \tag{7.13}$$

These spectra are shown in Figure 7.16 a and b and the mean values and standard deviations are shown in Table 7.6.

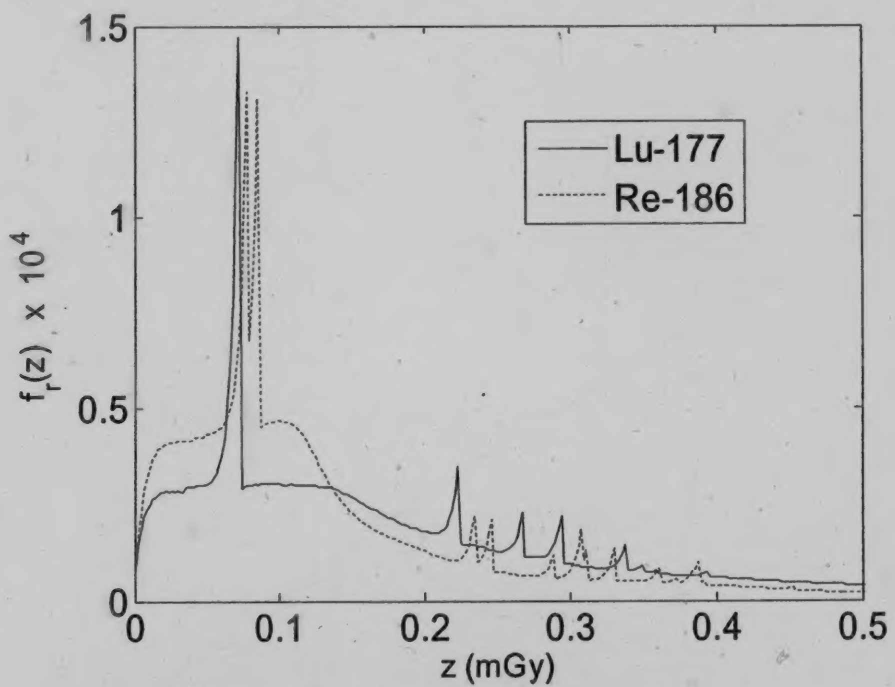

Figure 7.16 a: Specific energy distributions per decay for Lu-177 and Re-186. The low energy Auger electrons are responsible for the sharp peaks in the distributions.

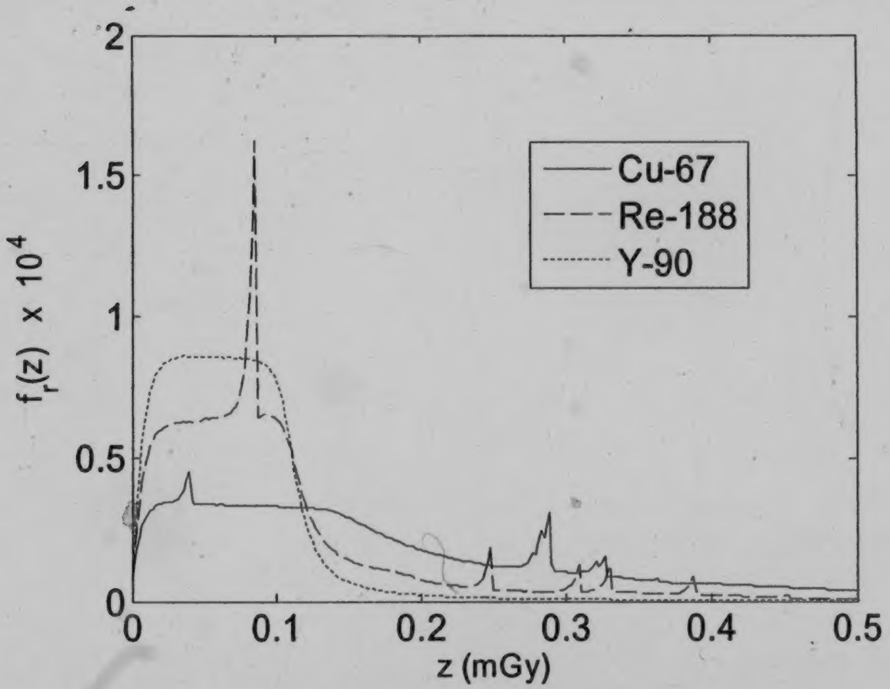

Figure 7.16 b: Specific energy distributions per decay for Cu-67, Re-188 and Y-90. The Auger peaks are not as pronounced in these radionuclides as they are in Lu-177 and Re-186.

Table 7.6: Mean specific energy per event per decay

Radionuclide	$E_{\beta max}$ (MeV)	$\bar{z}_{fr}$ (mGy)	σ $\bar{z}_{fr}$ (mGy)
Lu-177	0.498	0.24	0.25
Cu-67	0.577	0.24	0.25
Re-186	1.072	0.16	0.17
Re-188	2.120	0.11	0.13
Y-90	2.286	0.08	0.10

In all cases, the combined effect of the Auger electrons and internal conversion electrons was to raise the average amount of energy deposited in the cell per decay.

It is also of interest to investigate the patterns of energy deposition for targeted delivery systems capable of carrying different numbers of radioactive atoms. The probability of a certain number of hits per carrier can be obtained from the binomial distribution:

$$P_p(n|N) = \frac{N!}{n!(N-n)!} p^n (1-p)^{N-n} \tag{7.14}$$

This expression gives the probability of getting n hits from a carrier after N radioactive decays when the probability of a hit per decay is p.

The hit probabilities were calculated by summing up the possible decay scenarios and weighting them appropriately according to the various branching ratios. The values for the radionuclides are shown in Table 7.7.

Table 7.7: Radionuclide-specific p values including Auger and internal conversion electrons

Radionuclide	p
Lu-177	0.6292
Cu-67	0.5699
Re-186	0.6328
Re-188	0.5745
Y-90	0.4759

The radionuclide event spectra provide the necessary information for the determination of the distribution of energy deposition events for any number of hits. Using the technique described in section 3.3, the distribution of specific energies in the target after n hits is given by:

$$f_{rn}(z) = f_{r1}(z) * f_{rn-1}(z) \tag{7.15}$$

With the assumption that all of the radioactive atoms decay on the surface on the target sphere, one can calculate the distribution of specific energies on a "per carrier" basis. If the carrier holds a total of N atoms, the distribution of specific energy is given by:

$$f(z,N)=\sum_{n=0}^{N}P_p(n|N)f_n(z) \qquad (7.16)$$

where $P_p(n|N)$ is the binomial coefficient given in Eq 7.14. The results of these calculations are now illustrated with several figures. A number of the spectra, $f_n(z)$, are shown in Figure 7.17 for Y-90. In this and subsequent figures, the abscissa is a dimensionless, scaled specific energy on a logarithmic scale. The energies have been normalized to the expectation value of the spectrum $f_1(z)$. The y-axis is scaled by this normalized specific energy.

As n increased, the spectra shifted to higher values of z and eventually assumed an approximately Gaussian shape. The expectation values of the spectra, $f_n(z)$, scaled as $n\,\bar{z}_f$ but the relative spreads of the spectra varied in a non-linear manner with n. The relative spread is given by:

$$\lambda_n=\frac{\sqrt{\overline{z_n^2}-\bar{z}_n^{\,2}}}{\bar{z}_n} \qquad (7.17)$$

Where:

$$\overline{z_n^i}=\frac{\int_0^\infty z_n^i f_n(z)\,dz}{\int_0^\infty f_n(z)\,dz} \qquad (7.18)$$

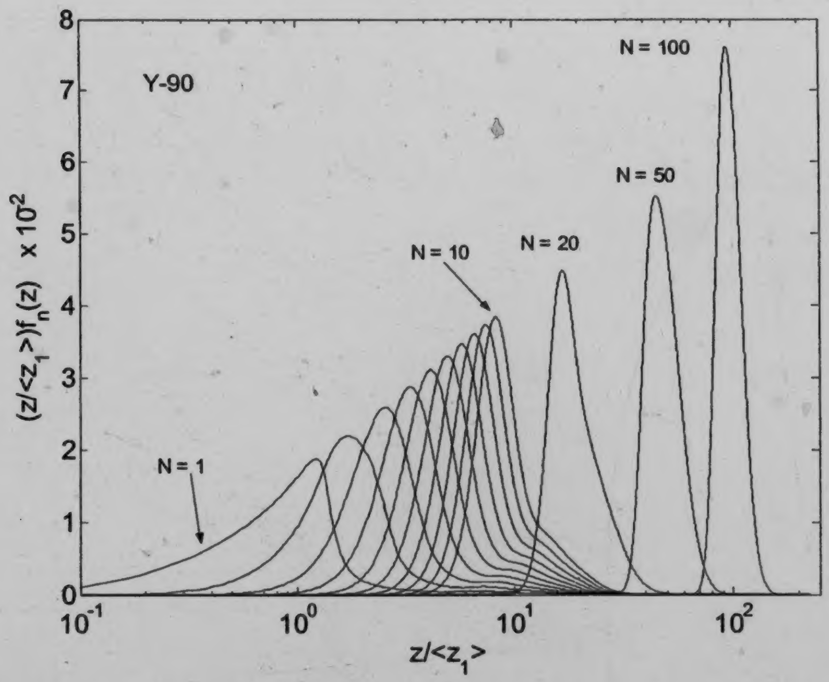

Figure 7.17: Specific energy distributions, $f_n(z)$, for Y-90. The mean value of the distributions is given by $n\bar{z}_1$. The x-axis is on a logarithmic scale and has been normalized to the expectation value of $f_1(z)$. The y-axis has been scaled by this normalized energy.

The relative spread for values of n between 1 and 100 are shown in Figure 7.18. Initially, the value of λ_n decreased rapidly with increasing n. This rate of change decreased as n increased. The value of λ_n decreased from 123% to 88% as n increased from 1 to 2, and it decreased from 16.3% to 12.6% as n increased from 60 to 100.

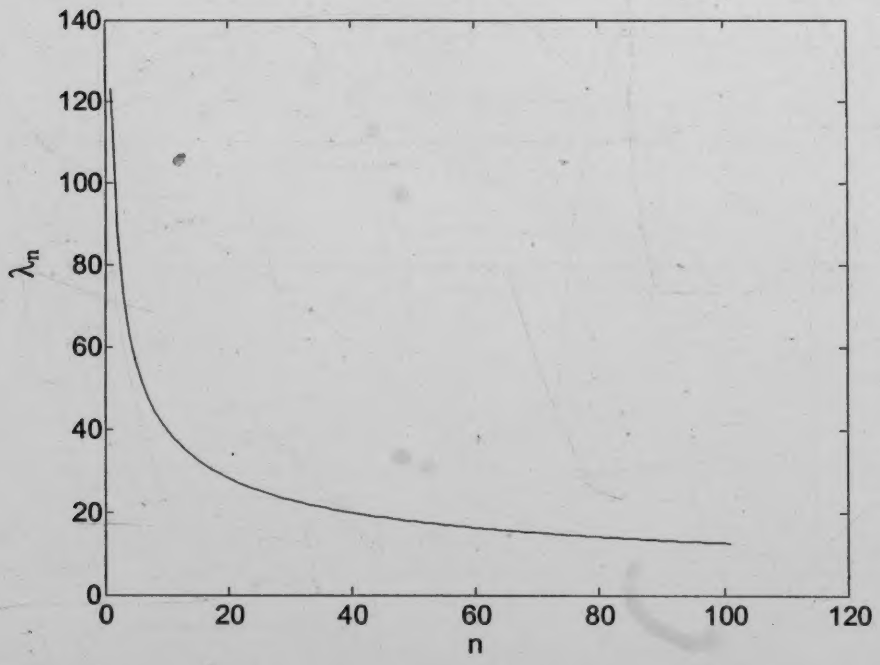

Figure 7.18: Relative spread of specific energy distributions, $f_n(z)$, as a function of n. The relative spread decreases rapidly with increasing n at low n but is decreasing slowly at n = 100.

The spectra, $f(z,N)$, were generated by summing together the binomially-weighted spectra, $f_{rn}(z)$, with n taking all values between 1 and N. The relative importance of the spectra, $f_{rn}(z)$, increased as the value of n approached the mean value of the binomial distribution (np) from above and below. Figures 7.19 – 7.23 show these spectra for the five radionuclides being considered here. Plotted on the same axes for each radionuclide are the spectra for the following values of N: 1 – 10, 20, 50 and 100.

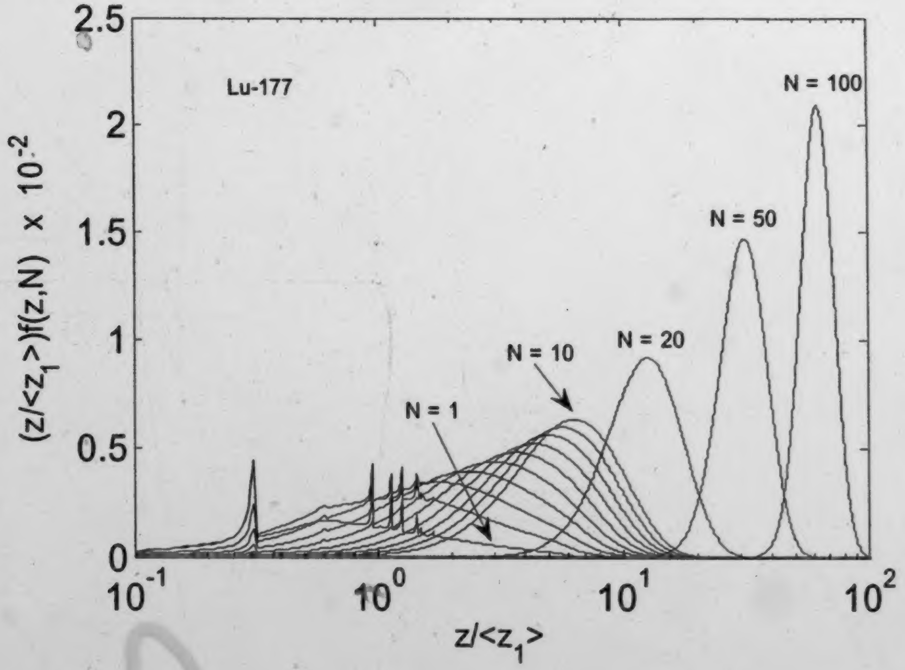

Figure 7.19: Weighted event spectra for Lu-177. Spectra are shown for N = 1 – 10, 20, 50 and100. N is the number of radioactive atoms per carrier. As N increases, the spectra shift to higher values of $z/<z_1>$ and the relative spread decreases. The spectra are scaled such that the expectation value of $z/<z_1>$ for N = 1 is 1.

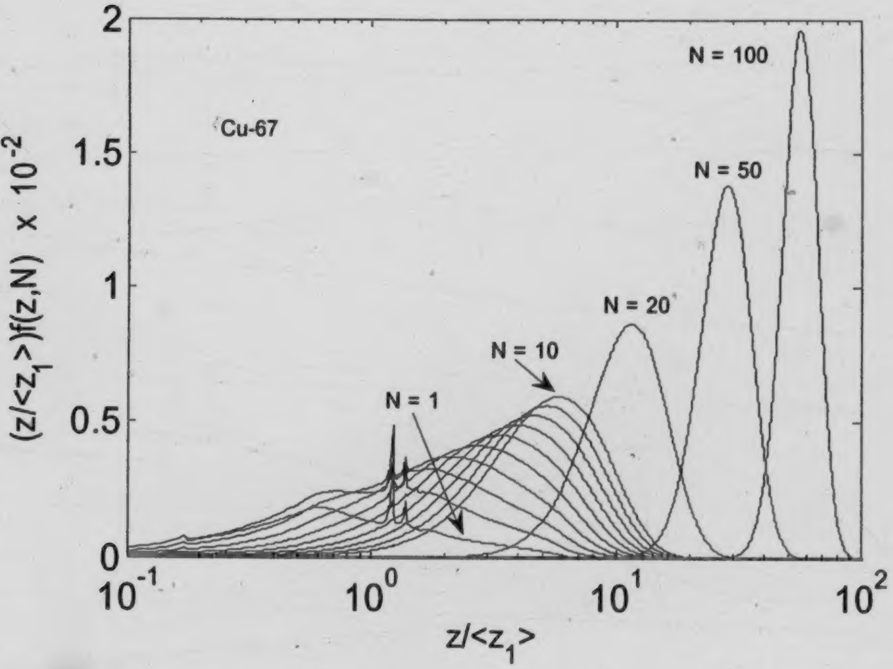

Figure 7.20: Weighted event spectra for Cu-67.

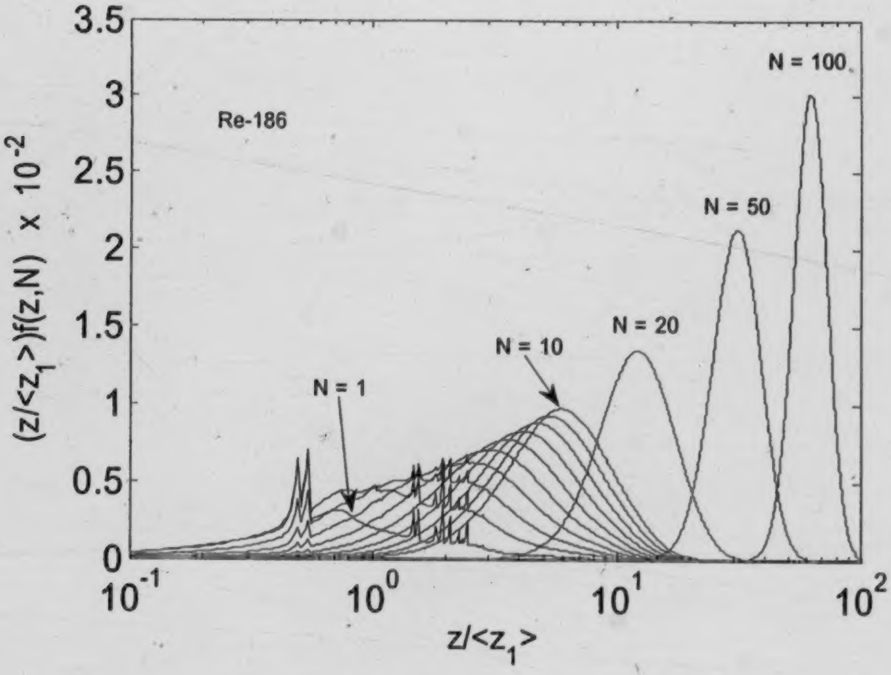

Figure 7.21: Weighted event spectra for Re-186.

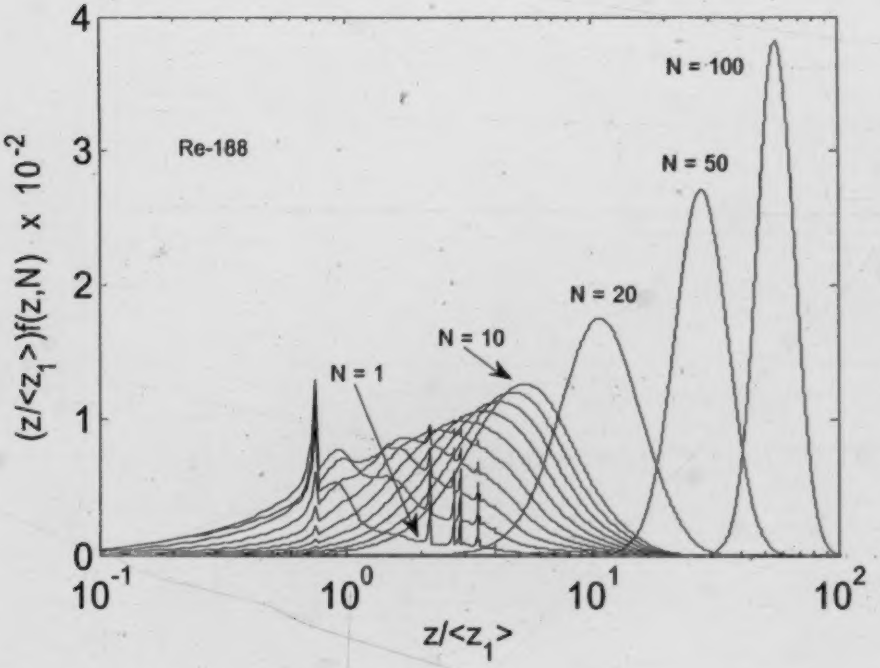

Figure 7.22: Weighted event spectra for Re-188.

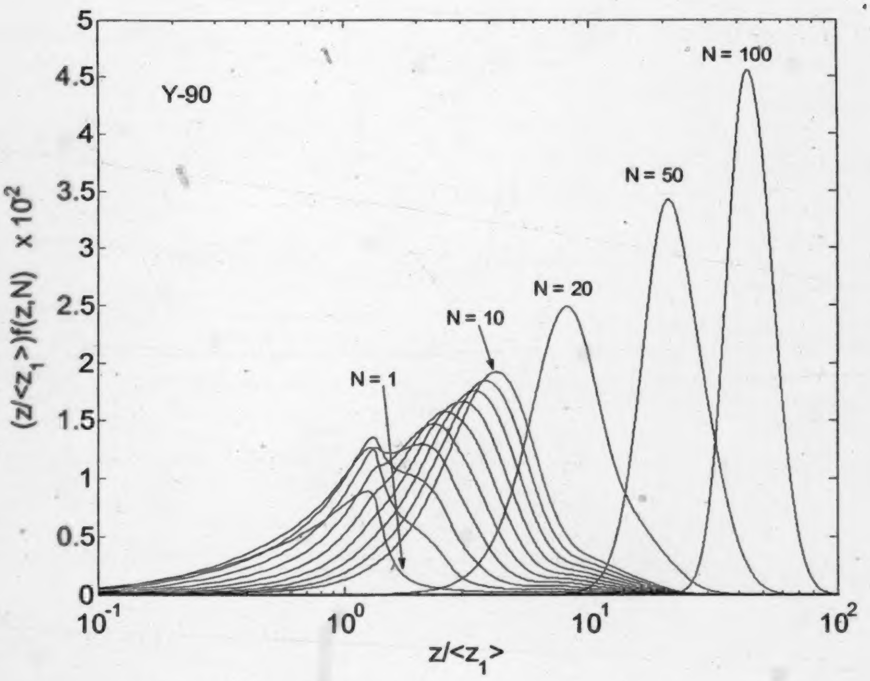

Figure 7.23: Weighted event spectra for Y-90.

The differences in energy deposition patterns between the different radionuclides becomes apparent when the mean values of the spectra, *f(z,N)*, are plotted on the same set of axes. This is shown in Figure 7.24. Clearly the lower energy emitters deposit significantly more energy per carrier than the higher energy emitters.

7.4 Discussion

Comparison of beta emitters for a particular radionuclide therapy is a complicated problem. Meaningful conclusions are difficult to draw due to differences in things like labeling efficiency, compound stability, dose-rates and *in-vivo* biodistribution kinetics. Determination of the single event spectra for radionuclides is a useful start in this respect because it differentiates the

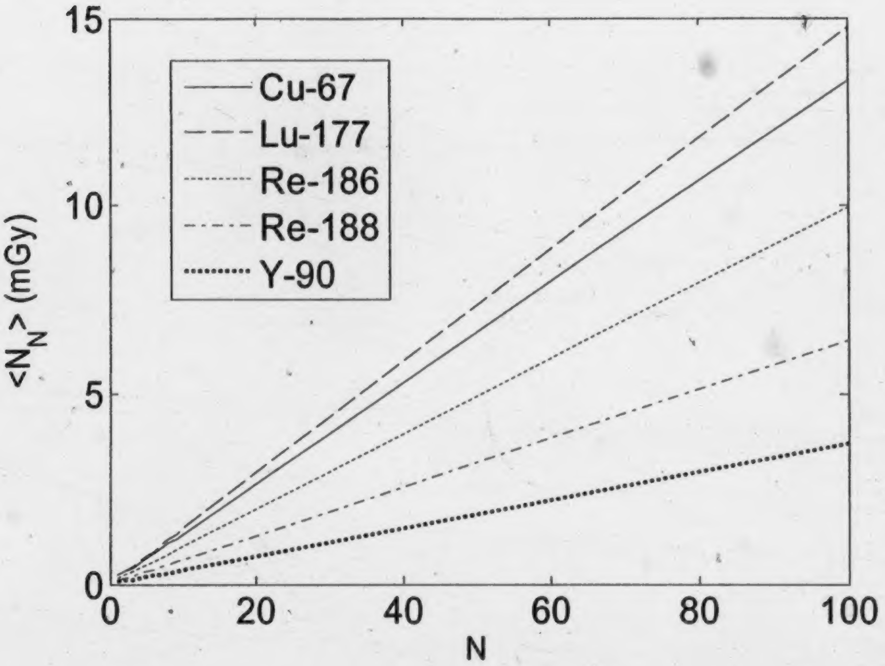

Figure 7.24: Mean values of *f(z,N)* for different radionuclides. The lower energy emitters (Lu-177, Cu-67) clearly deposit significantly more energy per carrier than the high energy emitters (Re-188, Y-90).

radionuclides in terms of the physical process of energy deposition. This information could be used in conjunction with the aforementioned variables to assist in the radionuclide selection procedure for a therapy; particularly if the pathology of the disease to be treated is known.

The CSDA spectra used to describe the energy distribution of electrons incident on the target for the free radioactivity source geometry should be a reasonable approximation of the true spectra. It is likely, however, that the lower energy range of the spectra are under-represented since, by definition, the continuous slowing down approximation does not consider the production of secondary electrons in collision processes.

Since the focus of this investigation was on beta-emitters whose endpoint energies are orders of magnitude greater than the 10 keV cutoff of EGSnrc, the effects of the cutoff on the overall radionuclide beta single event spectra should be small. The 0.75 mGy peak discussed previously in the context of the 20 keV electrons contributed to the radionuclide spectra well into the high z tail where the probability densities were already quite low. Ultimately, the cutoff might have resulted in a small overestimation of the values of $\bar{z}_f$ and their standard deviations. Larger uncertainties will be associated with the spectra corresponding to the Auger emitters since the ones included in this study were virtually all below 10 keV. Nonetheless, the general behaviour of the system should be well represented by this approach.

It should be noted that the "per decay" event spectra represent a simplification of the true process of the radioactive decay of these radionuclides. Implicit in their construction is the assumption that only one Auger electron or internal conversion electron is emitted in any given decay. In reality, there would likely be decays in which more than one emission accompanied the beta particle. Such processes would significantly complicate the calculation of the spectra, if one were to include all combinations of hits and misses by the particles involved. It is believed that the spectra presented in this chapter are sufficient to illustrate the effects of the Auger electrons and internal conversion electrons on the overall process of energy deposition by a radionuclide bound to the surface of a cell.

This investigation focused on the contribution of electrons to single cell dose. Photon emissions were not included in the calculations. Simulation of photon transport through the cell with energies as low as 20 keV showed very few interactions per traversal. The emission of very soft x-rays might contribute to the spectra but they have not been included here.

One of the interesting results of these calculations was the higher $\bar{z}_f$ values for the free radioactivity compared to the surface bound radioactivity. It would not be valid to interpret this to mean that a targeted therapy would not offer an advantage over a non-targeted approach. A non-targeted approach produces one source geometry – the free radioactivity. A targeted approach also produces this geometry but enhances the tumour dose by bringing additional radioactivity into contact with the surface of the cells. Furthermore, an intraperitoneal radionuclide therapy must treat multicellular clusters and macroscopic tumour nodules on the peritoneal surfaces in addition to the single cells suspended in the peritoneal fluid. For multicellular clusters, the model presented in chapter 6 suggested that the relative importance of the surface bound radioactivity increased as the size of the cluster increased.

The figures in section 7.3 that contain the spectra $f(z,N)$ illustrated the effects of multiple independent beta particles irradiating a single cell. They were presented in the context of "per carrier" distributions. In reality it is unlikely that all of the radioactive atoms bound to a carrier would decay while the carrier was bound to the target, particularly if the half-life of the radionuclide were very short or very long, or if the number of radioactive atoms per carrier was very large. With the assumption that every carrier produces the same source-target geometry, the number of radioactive decays, N, could be shared between any number of carriers, and the distributions would not change. In a sense, the distributions merely facilitate comparison between different radionuclides on the basis of energy deposition patterns.

7.5 Conclusion

The specific energy single event spectra for single cells from five beta emitting radionuclides were calculated for the two source geometries. The first represented an isotropically-emitting point source bound to the surface of the cell and the second represented a bath of free radioactivity in which a single cell was submerged. The two geometries together represented a targeted i.p. radionuclide therapy. As expected, the value of $\bar{z}_f$ decreased with increasing beta energy. The contribution of Auger electrons in the surface-bound geometry produced sharp peaks in the distributions. The electrons incident on the target from the free radioactivity source geometry had a greater mean path length through the target than those from the surface-bound geometry and consequently the value of $\bar{z}_f$ was greater for this geometry than for the surface-bound geometry. This work attempted to quantify the patterns of energy deposition in cellular targets for different radionuclides. This information could be of potential use in assisting in radionuclide selection processes for this type of therapy.

References

Alvarez RD, Partridge EE, Khazaeli MB, Plott G, Austin M, Kilgore L, Russell CD, Liu T, Grizzle WE, Schlom J, LoBuglio AF and Meredith RF 1997 Intraperitoneal Radioimmunotherapy Of Ovarian Cancer With ^{177}Lu-CC49: A Phase I/II Study. *Gynecol. Oncol.* **65** 94-101.

Bakri YN, Given FT 1984 Radioactivity In Blood And Urine Following Intraperitoneal Instillation Of Chromic Phosphate In Patients With And Without Ascites. *Am. J. Obstet. Gynecol.* **150** 184-188.

Baró J, Sempau J, Fernandez-Varea JM and Salvat F 1995 PENELOPE: An Algorithm For Monte Carlo Simulation Of The Penetration And Energy Loss Of Electrons And Positrons In Matter. Nucl. *Intsr. And Meth. In Phys. Res. B* **100** 31-46.

Bolch WE, Bouchet LG, Robertson JS, Wessels BW, Siegel JA, Howell RW, Erdi AK, Aydogan B, Costes S and Watson EE 1999 MIRD Pamphlet No. 17: The Dosimetry Of Nonuniform Activity Distributions—Radionuclide S Values At The Voxel Level. Medical Internal Radiation Dose Committee. *J. Nucl. Med.* **40** 11S-36S.

Bolch WE and Kim E-H 1994 Calculations Of Electron Single Event Distributions For Use In Internal Beta Microdosimtery. *Radiat. Prot. Dosim.* **52** 77-80.

Buijs WC, Tibben JG, Boerman OC, Molthoff CF, Massuger LF, Koenders EB, Schijf CP, Siegel JA and Corstens FH 1998 Dosimetric Analysis Of Chimeric Monoclonal Antibody cMOv18 IgG In Ovarian Carcinoma Patients After Intraperitoneal And Intravenous Administration. *Eur. J. Nucl. Med.* **25** 1552-1561.

Cross W, Freedman N and Wong P 1992 Tables of Beta-Ray Dose Distributions in Water. *Atomic Energy of Canada Limited publication*: AECL-10521

ICRU Report 36 1983 Microdosimetry. Washington D.C. ICRU

Johns HE and Cunningham JR 1983 The Physics Of Radiology. Fourth Edition. Charles C Thomas, Springfield. pp. 204-208

Kawrakow I 2000 Accurate Condensed History Monte Carlo Simulation Of Electron Transport I. EGSnrc, The New EGS4 Version. *Med. Phys.* **27** 485-498

Kawrakow I, Rogers DWO 2002 The EGSnrc Code System: Monte Carlo Simulation of Electron And Photon Transport. NRCC Report PIRS-701

Kellerer AM 1984 Chord-Length Distributions And Related Quantities For Spheroids. *Radiat. Res.* **98** 425-437.

Kim EH, Bolch WE, Reece WD and Poston JW 1996 A Microdosimetric Algorithm For Electron Point Kernel Data: 1. Monoenergetic Electron Sources. *Radiat. Prot. Dosim.* **63** 245 – 252.

Kolstad P, Davy M and Hoeg K 1977 Individualized Treatment Of Ovarian Cancer. *Am. J. Obstet. Gynecol.* **128** 617 – 625.

Kwok CS, Prestwich, WV and Wilson BC 1985 Calculation Of Radiation Doses For Nonuniformly Distributed β and γ Radionuclides In Soft Tissue. *Med. Phys.* **12** 405-412.

Loevinger R, Budinger T and Watson E 1988 MIRD Primer For Absorbed Dose Calculations. New York. The Society of Nuclear Medicine

McQuarrie SA, Xiao Z, Miller GG, Mercer JR and Suresh MR 2001 Modern Trends in Radioimmunotherapy of Cancer: Pretargeting Strategies for the Treatment of Ovarian Cancer. *Quart. J. Nucl. Med.* **45** 160 – 166.

Nahum A 1996 Microdosimetry And Radiocurability: Modelling Targeted Therapy With β-Emitters. *Phys. Med. Biol.* **41** 1957-1972.

Roeske J Chen G Brill A 1993 Dosimetry Of Intraperitoneally Administered Radiolabeled Antibodies. *Med. Phys.* **20** 593-600.

Rotmensch J Roeske J Chen G Pelizzari C Montag A Weichselbaum R Herbst AL 1990 Estimates Of Dose To Intraperitoneal Micrometastases From Alpha And Beta Emitters In Radioimmunotherapy. *Gynecol. Oncol.* **38** 478-485.

Stewart RD, Wilson WE, McDonald JC and Strom DJ 2002 Microdosimetric Properties Of Ionizing Electrons In Water: A Test Of The PENELOPE Code System. *Phys. Med. Biol.* **47** 79-88.

Vergote I, Larsen RH, De Vos L, Nesland JM, Bruland O, Bjorgum J, Alstad J, Trope C and Nustad K 1992b Therapeutic Efficacy Of The α-Emitter ^{211}At Bound On Microspheres Compared With ^{90}Y and ^{32}P Colloids In A Murine Intraperitoneal Tumour Model. *Gynecol. Oncol.* **47** 366-372.

Vergote I, Larsen RH, De Vos L, Winderen M, Ellingsen T, Bjorgum J, Hoff P, Aas M, Trope C and Nustad K 1992a Distribution Of Intraperintoneally Injected Microspheres Labeled With The Alpha-Emitter Astatine (211At) Compared With Phosphorus (32P) And Yttrium (90Y) Colloids In Mice. *Gynecol. Oncol.* **47** 358-65.

Chapter 8

Concluding Remarks and Future Directions

Late stage ovarian cancer will likely remain a disease to be treated as opposed to cured for the foreseeable future. The treatment of metastases has proven to be an exceptionally difficult obstacle to overcome. The ability to target a therapeutic agent to cancer cells is certainly a valuable asset, however, until that agent can be rendered truly inert until it has reached its target, normal tissue toxicity will continue to limit permissible doses of cancer therapies. With respect to ovarian cancer, the tremendous survival rate for early stage cancer explains why there is intense interest in finding a reliable screening tool. The fact that such a tool does not currently exist explains why there is also interest in arresting the development of the disease inside the peritoneal cavity. Numerous radionuclide therapies have been developed for this purpose, based on a number of different radionuclides and carriers. Differences in the physical, chemical and biological properties associated with these therapies render direct comparisons difficult. For this reason, modeling of a therapy is a useful exercise. Within the limitations of the accuracy of the model itself and the choice of parameter values, one can use a model to investigate the differences between radionuclides. Instead of trying to answer a general and oversimplified question such as 'what is the optimal radionuclide for this therapy?', one can instead attempt to address a question such as, 'under what conditions would the use of this particular radionuclide be optimal?'.

The particular therapy that inspired the majority of the work in this thesis was based on the use of liposomes to selectively deliver radioactivity to ovarian cancer cells in the peritoneal cavity that express the antigen CA-125. A liposome formulation was developed that was capable of carrying significantly more radioactivity per carrier than a conventional targeting moiety such as a monoclonal antibody. The chelating agent DTPA was used to bind atoms of Y-90 to the outer surface of the liposomes. Laser scanning confocal microscopy was used to validate the hypothesis that these liposomes could be selectively bound to cells expressing CA-125. A bispecific antibody was used to tether the liposomes to the cell surface. The microscopy revealed that there was uptake by cells expressing CA-125 and no uptake by cells that did not express CA-125, suggesting that the binding was specific.

To model the dosimetry associated with radiolabeled liposomes, dose-rate profiles through spherical tumours of various radii were calculated based on dose point kernels. Two source geometries were considered. The first was radioactivity uniformly distributed on the surface of the tumour and the second was a radioactive bath in which the tumour was submerged. Together these represented an intraperitoneal radionuclide therapy. The dose-rate profiles produced by the bath of radioactivity showed less variability with high energy emitters (i.e. ^{90}Y and ^{188}Re) than they did with lower energy emitters (i.e. ^{131}I and

^{67}Cu). For tumours with a radius of less than 0.01cm, the high energy profiles were virtually uniform and the dose-rate was approximately equal to the equilibrium dose-rate. For low energy emitters, this was only true for radii smaller than 0.005cm. For surface-bound radioactivity the profiles were significantly more non-uniform. Lower energy emitters produce higher dose-rates than high energy emitters for sufficiently small tumours. The results suggest that this particular treatment modality would benefit from the inclusion of a high energy emitter, perhaps as part of a cocktail of radionuclides.

Once the dose-rate profiles were calculated, they were incorporated into a model developed to describe the time-dependent tumour control probabilities of micrometastes in the peritoneal cavity during intraperitoneal radionuclide therapy. Ultimately the dose was expressed in terms of a number of biological parameters that describe the dynamic behaviour of the system. These included the tumour surface density of the antigen CA-125, the rate at which liposomes bind to, and unbind from, the tumour and the rate at which liposomes are removed from the peritoneal cavity. The amount of CA-125 on the surface of the cancer cells was critically important for the realization of a benefit from using a targeted approach. If insufficient CA-125 was present, the vast majority of the tumour dose came from the liposomes in solution. The rate at which liposomes escaped the peritoneal cavity was also important. Radioactivity that escaped the cavity decreased the dose rate to the metastases in the cavity and increases the dose to critical tissues such as bone marrow. This work suggests that it might be possible to optimize treatment on a patient-specific basis as a number of the parameters used in the model could possibly be measured using in-vitro assays from cells harvested from a patient's ascites fluid.

The dosimetry of single cells in the peritoneal cavity was given special consideration due to the small size of the target volume. A microdosimetric approach was taken in which the single event spectra for a number of different radionuclides were calculated for both of the source geometries mentioned previously. Radionuclide spectra were calculated by weighting monoenergetic single event spectra according to an appropriate radionuclide spectrum for each geometry. In the surface-bound geometry the spectra were the radionuclide beta decay spectra. For the free radioactivity CSDA spectra were calculated based on the assumption that the bath of radioactivity was sufficiently large to produce charged particle equilibrium. In both cases, Auger electrons and internal conversion electrons were included in the calculations. The Auger electrons produced sharp peaks in the event distributions. The frequency-mean specific energy per event, $\bar{z}_f$, decreased as the energy of the beta emitter increased due to the inverse relationship between stopping power and energy over this energy range. For a given radionuclide, the free radioactivity produced a larger frequency-mean specific energy per event than the surface-bound geometry due to the longer mean path length through the target volume. For multiple events, the mean value of the specific energy distribution scaled linearly with $\bar{z}_f$ and the relative spread decreased continuously though in a non-linear manner.

An expansion of the dosimetry associated with this radionuclide therapy would benefit greatly from biodistribution studies in animals. Normal tissue dosimetry is of particular concern given that bone marrow toxicity is usually the dose-limiting factor for i.p. therapies. Serial serum and organ uptake data would allow for integrated organ dose estimates. It would also be beneficial to investigate the labeling of liposomes with other radionuclides. Since the pharmacokinetics of the liposomes should be independent of the radionuclide, this would allow for low-dose diagnostic procedures prior to therapy for the purpose of predictive dosimetry. To compliment the theoretical determination of radionuclide single event spectra, an experimental evaluation would also be of interest. This would be possible for the surface-bound geometry with the use of a

Rossi chamber – a specialized spherical ionization chamber operated at low gas pressures to allow macroscopic volumes to accurately simulate the response of microscopic volumes.

Cancer therapy will continue to evolve to exploit developments in the fields of physics, chemistry, biology and biochemistry. Metastatic disease highlights the importance of sophisticated, targeted approaches to therapy for the purpose of killing tumour tissue with minimal consequences for the surrounding healthy tissue.

Bibliography

**Numbers in parentheses are page references for the citations

Alberts B, Bray D, Lewis J, Raff M, Roberts K and Watson J 1994 Molecular Biology Of The Cell. 3rd Edition. Garland Publishing Inc. New York. p 478. (59)

Allen T M, Hansen C and Rutledge J. 1989 Liposomes With Prolonged Circulation Times: Factors Affecting Uptake By Reticuloendothelial And Other Tissues. *Biochim. Biophys. Acta.* **981** 27 – 35. (49)

Allen T M, Hansen C B and Stuart D D. 1998b Targeted Sterically Stablized Liposomal Drug Delivery. Chapter 4.6 in Medical Applications Of Liposomes (Lasic and Papahadjopoulos editors). Elseveir Science (49, 50, 51)

Allen T, Lopez de Menezes D, Hansen C and Moase E. 1998a Stealth Liposomes For The Targeting Of Drugs In Cancer Therapy. pp 61 – 71 in Targeting of Drugs 6: Strategies For Stealth Therapeutic Systems (Gregoriadis and McCormack editors). Plenum Press, New York. (48, 49, 50)

Allen T M and Stuart D D. 1999 Liposome Pharmacokinetics: Classical, Sterically Stabilized, Cationic Liposomes And Immunoliposomes. Chapter 3 in Liposomes: Rational Design (Janoff A S editor), pp 63-87. Marcel Dekkar, New York. (48)

Alvarez RD, Partridge EE, Khazaeli MB, Plott G, Austin M, Kilgore L, Russell CD, Liu T, Grizzle WE, Schlom J, LoBuglio AF and Meredith RF 1997 Intraperitoneal Radioimmunotherapy Of Ovarian Cancer With ^{177}Lu-CC49: A Phase I/II Study. *Gynecol. Oncol.* **65** 94-101. (15, 109, 112, 144, 145)

Anderiesz C and Quinn M A. 2003 Screening for Ovarian Cancer. *Med. J. Australia.* **178** 655 – 656. (9)

Atthey M, Nahum AE, Flower MA and McCready VR 2000 Effects Of Cellular Repair And Proliferation On Targeted Radionuclide Therapy: A Modelling Study. *Phys. Med. Biol.* **45** N15-N20. (116)

Aubineau-Laniece I, Pihet P, Winkler R, Hofmann W and Charlton D E. 2002 Monte Carlo Code For Microdosimetry Of Inhaled Alpha Emitters. *Radiat. Protec. Dosim.* **99** 463 – 468. (38)

Aurlien E, Larsen R H, Akabani G, Olsen D R, Zalutsky M R and Bruland O S. 2000 Exposure Of Human Osteosarcoma And Bone Marrow Cells To Tumour-Targeted Alpha-Particles And Gamma-Irradiation: Analysis Of Cell Survival And Microdosimetry. *Int. J. Radiat. Biol.* **76** 1129 – 1141. (37)

Austin A L, Ellender M, Haines J W, Harrison J D and Lord B I. 1999 Temporal Change In Microdosimetry To Bone Marrow And Stromal Progenitor Cells From Alpha-Particle-Emitting Radionuclides Incorporated In Bone. *Radiat. Res.* **152(6 Suppl)** S38 – S42. (37)

Baker V V. 2003 Salvage Therapy For Recurrent Epithelial Ovarian Cancer. *Hematol. Oncol. Clin. N.* **17** 977 – 988. (13)

Bakri YN, Given FT 1984 Radioactivity In Blood And Urine Following Intraperitoneal Instillation Of Chromic Phosphate In Patients With And Without Ascites. *Am. J. Obstet. Gynecol.* **150** 184-188. (15, 112, 144)

Ballangrud A M, Yang W H, Dnistrian A, Lampen N M and Sgouros G. 1999 Growth And Characterization Of LNCaP Prostate Cancer Cell Spheroids. *Clin. Cancer Res.* **5** 3171s – 3176s. (94)

Bardies M and Chatal J. 1994 Absorbed Doses For Internal Radiotherapy From 22 Beta-Emitting Radionuclides: Beta Dosimetry Of Small Spheres. *Phys. Med. Biol.* **39** 961 – 981. (79)

Bardiès M, Lamé J, Myers M J and Simoen J P. 1990 A Simplified Approach To Beta Dosimetry For Small Spheres Labelled On The Surface. *Phys. Med. Biol.* **35** 1039 – 1050. (79, 93)

Baró J, Sempau J, Fernandez-Varea JM and Salvat F 1995 PENELOPE: An Algorithm For Monte Carlo Simulation Of The Penetration And Energy Loss Of Electrons And Positrons In Matter. Nucl. *Intsr. And Meth. In Phys. Res. B* **100** 31-46. (159)

Berek J S, Dembo A and Ozols R F. 1993 Cancer Medicine, 3rd Edition (Holland, Frei, Bast *et al.* eds). Section XXXI-5, pp1659 – 1690. Lea & Febiger, Philadelphia. (6, 7, 8, 10)

Berek J S, Dorigo O, Schultes B and Nicodemus C. 2003 Specific Keynote: Immunological Therapy For Ovarian Cancer. *Gynecol. Oncol.* **88** S105 – S109. (8)

Berek J S, Thomas G M and Ozols R F. 1997 Cancer Medicine, 4th Edition (Holland, Bast, Morton *et al.* eds). Chapter 133, pp 2289 – 2326. Williams and Wilkins, Baltimore. (7, 13)

Berger M J. 1971 MIRD Pamphlet No. 7: Distribution Of Absorbed Dose Around A Point Beta Source Of Electrons And Beta Particles In Water And Other Media. Medical Internal Radiation Dose Committee. *J. Nucl. Med.* **12** 5S – 24S. (34)

Berger M J. 1973 Improved Point Kernels For Electron And Beta Ray Dosimetry. *National Bureau Of Standards Report*: NBSIR-73-107. (34)

Bloomer W D, McLaughlin W H, Lambrecht R M, Atcher R W, Mirzadeh S, Madara J L, Milius R A, Zalutsky M R, Adelstein S J and Wolf A P. 1984 ^{211}At Radiocolloid Therapy: Further Observations And Comparison With Radiocolloids Of ^{32}P, ^{165}Dy and ^{90}Y. *Int. J. Radiat. Oncol. Biol. Phys.* **10** 341 – 348. (15)

Bolch W E, Bouchet L G, Robertson J S, Wessels B W, Siegel A, Howell R W, Erdi A K, Aydogan B, Costes S and Watson E E. 1999 MIRD Pamphlet No. 17: The Dosimetry Of Nonuniform Activity Distributions—Radionuclide S Values At The Voxel Level. Medical Internal Radiation Dose Committee. *J. Nucl. Med.* **40** 11S – 36S. (79, 145)

Bolch WE and Kim E-H 1994 Calculations Of Electron Single Event Distributions For Use In Internal Beta Microdosimtery. *Radiat. Prot. Dosim.* **52** 77-80. (147, 159)

Buchsbaum D J, Lawrence T S, Roberson P L, Heidorn D B, Ten Haken R K, Steplewski Z. 1993 Comparison Of 131I- And 90Y-Labeled Monoclonal Antibody 17-1A For Treatment Of Human Colon Cancer Xenografts. *Int. J. Radiat. Oncol. Biol. Phys.* **25** 629 – 638. (80)

Buijs WC, Tibben JG, Boerman OC, Molthoff CF, Massuger LF, Koenders EB, Schijf CP, Siegel JA and Corstens FH 1998 Dosimetric Analysis Of Chimeric Monoclonal Antibody cMOv18 IgG In Ovarian Carcinoma Patients After Intraperitoneal And Intravenous Administration. *Eur. J. Nucl. Med.* **25** 1552-1561. (15, 19, 109, 112, 144, 145)

Cramer D W, Welch E R, Scully R E and Wojciechowski C A. 1982 Ovarian Cancer and Talc: A Case Control Study. *Cancer* **50** 372 – 376. (7)

Croll M N and Brady L W. 1979 Intracavitary Uses Of Colloids. *Semin. Nucl. Med.* **IX** 108 – 113. (13, 21)

Cross W G. 1967a Tables Of Beta Dose Distributions. *Atomic Energy of Canada Limited Publication*: AECL-2793. (34)

Cross W G. 1967b The Distribution Of Absorbed Energy From A Point Beta Source. *Can. J. Phys.* **45** 2021 – 2040. (34)

Cross W G. 1969 Distribution Of Absorbed Beta Energy in Solid Media. *Can J. Phys.* **47** 75 – 83. (34)

Cross W G, Freedman N O and Wong P Y. 1992 Tables of Beta-Ray Dose Distributions in Water. *Atomic Energy of Canada Limited publication*: AECL-10521. (33, 33, 37, 81, 82, 114, 146)

Dale RG 1996 Dose-Rate Effects In Targeted Radiotherapy. *Phys. Med. Biol.* **41** 1871-1884. (138)

del Regato J A, Spjut H J and Cox J D. 1985 Ackerman and del Regato's Cancer. Chapter 16, pp 749 – 776. The C. V. Mosby Company, St. Louis. (6, 9, 11, 12, 13)

Delrieu P and Ding L. 1999 United States Patent #1061: Stablized Liposomes. (46)

Epenetos A A, Munro A J, Stewart S, Rampling R, Lambert H E, McKenzie C G, Soutter P, Rahemtulla A, Hooker G, Sivolapenko G B, Snook D, Courtenay-Luck N, Dhokia B, Krausz T, Taylor-Papadimitriou J, Durbin H and Bodmer W F. 1987 Antibody-Guided Irradiation Of Advanced Ovarian Cancer With Intraperitoneally Administered Radiolabeled Monoclonal Antibodies. *J. Clin. Oncol.* **5** 1890 – 1899. (23)

Freeman, G R. 1987 Ionization And Charge Separation In Irradiated Materials. Chapter 2 in Kinetics Of Non-Homogeneous Processes, A Practical Introduction For Chemists, Biologists, Physicists, and Materials Scientists (Freeman, G R. editor). John Wiley & Sons, New York. (33)

Frezard F. 1999 Liposomes: From Biophysics To The Design Of Peptide Vaccines. Braz. J. Med. Biol. Res. **32** 181 – 189. (46)

Froidevaux S and Eberle A N. 2002 Somatostatin Analogs And Radiopeptides In Cancer Therapy. *Biopolymers.* **66** 161 – 183. (51)

Froidevaux S, Heppeler A, Eberle A N, Meier A-M, Hausler M, Beglinger C, Behe M, Powell P and Macke H R. 2000 Preclinical Comparison In AR4-2J Tumor-Bearing Mice Of Four Radiolabeled 1,4,7,10-Tetraazacyclododecane-1-4-7-10-Tetraacetic Acid-Somatostatin Analogs For Tumor Diagnosis And Internal Radiotherapy. Endocrinology **141** 3304 – 3312. (55, 56)

Goddu S, Rao D and Howell R. 1994 Multicellular Dosimetry For Micrometastases: Dependence Of Self-Dose Versus Cross-Dose To Cell Nuclei On Type And Energy Of Radiation And Subcellular Distribution Of Radionuclides. *J. Nucl. Med.* **35** 521 – 530. (79)

Goitein M, Niemierko A and Okunieff P 1995 The Probability Of Controlling An Inhomogeneously Irradiated Tumour: A Stratagem For Improving Tumour Control Through Partial Tumour Boosting. Proceedings Of The 19th L H Gray Conference: Quantitative Imaging In Oncology. Chapter 2. Techniques For Tumour Volume Definition. pp 25-39 (116)

Gray H. 2000 *Anatomy of the Human Body.* Lea & Febiger, Philadelphia. Bartleby.com. www.bartleby.com/107/. (5)

Hall E J. 1994 Radiobiology For The Radiologist, 4th Edition. Lippincott, Philadelphia. (29)

Hang C L, Fu M, Hsieh B B, Leung S W, Wu C J, Yip H K and Ting G. 2003 Intracoronary Beta-Irradiation With Liquid Rhenium-188: Results Of The Taiwan Radiation In Prevention Of Post-Pure Balloon Angioplasty Restenosis Study. *Chest.* **124** 1284 – 1293. (21)

Harlozinska A, Sedlaczek P, Van Dalen A, Rozdolski K, Einarsson R. 1997 TPS and CA 125 Levels In Serum, Cyst Fluid And Ascites Of Patients With Epithelial Ovarian Neoplasms. *Anticancer Res.* **17** 4473 – 4478. (95)

Heintz A P M, Odicino F, Maisonneuve P, Beller U, Benedet J L, Creasman W T, Ngan H Y S, Sideri M and Pecorelli S. 2001 Carcinoma of the Ovary. *J. Epidemiol. Biostat.* **6** 107 – 138. (9, 11)

Howell RW, Goddu SM and Rao DV 1994 Application Of The Linear-Quadratic Model To Radioimmunotherapy: Further Support For The Advantage Of Longer-Lived Radionuclides. *J. Nucl. Med.* **35** 1861 – 1869. (139)

Howell RW, Goddu SM and Rao DV 1998 Proliferation And The Advantage Of Longer-Lived Radionuclides In Radioimmunotherapy. *Med. Phys.* **25** 37-42. (138, 139)

Hui T, Fisher D, Press O, Eary J, Weinstein J, Badger C and Bernstein I 1992 Localized beta Dosimetry Of ^{131}I-Labeled Antibodies In Follicular Lymphoma. *Med. Phys.* **19** 97-104. (115)

Humm, J. 1986 Dosimetric Aspects Of Radiolabeled Antibodies For Tumor Therapy. *J. Nucl. Med.* **27** 1490 – 1497. (79, 88)

Humm J L and Cobb L M. 1990 Nonuniformity Of Tumor Dose In Radioimmunotherapy. *J. Nucl. Med.* **31** 75 – 83. (18)

ICRP Publication 38 1983 Radionuclide Transormations. Energy And Intensity Of Emissions. Pergamon Press, Oxford. (83, 138)

ICRU 1983 Microdosimetry. International Commission on Radiation Units and Measurements Report **36.** ICRU, Bethesda. (30, 38, 39, 40, 146, 160)

Imam S. 2001 Advancements In Cancer Therapy With Alpha-Emitters: A Review. *Int. J. Radiat. Oncol. Biol. Phys.* **51** 271 – 278. (17)

Jacobs A J, Fer M, Su F M, Breitz H, Thompson J, Goodgold H, Cain J, Heaps J and Weiden P. 1993 A Phase I Trial Of A Rhenium 186-Labeled Monoclonal Antibody Administered Intraperitoneally In Ovarian Carcinoma: Toxicity And Clinical Response. *Obstet. Gynecol.* **82** 586 – 593. (20)

Jain R K and Baxter L T. 1988 Mechanisms Of Heterogeneous Distribution Of Monoclonal Antibodies And Other Macromolecules In Tumors: Significance Of Elevated Interstitial Pressure. *Cancer Res.* **48** 7022 – 7032. (18)

Johns H E and Cunningham J R. 1983 The Physics Of Radiology, 4th Edition. Charles C Thomas, Springfield. (31, 32, 151)

Jones B and Dale RG 2000 Radiobiological Modeling And Clinical Trials. *Int. J. Radiat. Oncol. Biol. Phys.* **48** 259 – 265. (139)

Jungerman J A, Yu K P and Zanelli C I. 1984 Radiation Absorbed Dose Estimates At The Cellular Level For Some Electron-Emitting Radionuclides For Radioimmunotherapy. *Int. J. Appl. Radiat. Isot.* **35** 883 – 888. (80)

Kairemo KJ 1996 Radioimmunotherapy Of Solid Cancers: A Review. *Acta Oncol.* **35** 343-355. (137)

Karlan B Y. 1997 The Status Of Ultrasound And Color Doppler Imaging For The Early Detection Of Ovarian Carcinoma. *Cancer Invest.* **15** 265 – 269. (9)

Kawrakow I 2000 Accurate Condensed History Monte Carlo Simulation Of Electron Transport I. EGSnrc, The New EGS4 Version. *Med. Phys.* **27** 485-498 (147)

Kawrakow I, Rogers DWO 2002 The EGSnrc Code System: Monte Carlo Simulation of Electron And Photon Transport. NRCC Report PIRS-701 (147)

Kellerer AM 1984 Chord-Length Distributions And Related Quantities For Spheroids. *Radiat. Res.* **98** 425-437. (153, 159)

Kellerer A M. 1985 Fundamentals Of Microdosimetry. Chapter 2 in The Dosimetry Of Ionizing Radiation, Volume 1 (Kase K R, Bjarngard B E and Attix F H. editors). Academic Press, Inc. Orlando. pp 77 – 162. (37, 38)

Kellerer A M and Chmelevsky D. 1975a Concepts Of Microdosimetry I. Quantities. *Rad. Environm. Biophys.* **12** 61 – 69. (38)

Kellerer A M and Chmelevsky D. 1975b Concepts Of Microdosimetry II. Probability Distributions Of The Microdosimetric Variables. *Rad. Environm. Biophys.* **12** 205 – 216. (38)

Kellerer A M and Chmelevsky D. 1975c Concepts Of Microdosimetry III. Mean Values Of The Microdosimetric Distributions. *Rad. Environm. Biophys.* **12** 321 – 335. (38)

Kim EH, Bolch WE, Reece WD and Poston JW 1996 A Microdosimetric Algorithm For Electron Point Kernel Data: 1. Monoenergetic Electron Sources. *Radiat. Prot. Dosim.* **63** 245 – 252. (159)

Kolstad P, Davy M and Hoeg K. 1977 Individualized Treatment Of Ovarian Cancer. *Am. J. Obstet. Gynecol.* **128** 617 – 625. (14, 15, 109, 137, 145)

Krenning E P, de Jong, M, Kooij P P M, Breeman W A P, Bakker W H, de Herder W W, van Eijck C H J, Kwekkeboom D J, Jamar F, Pauwels S and Valkema R. 1999 Radiolabelled Somatostatin Analogue(s) For Peptide Receptor Scintigraphy And Radionuclide Therapy. *Ann. Oncol.* **10** (suppl 2) S23 – S29. (55)

Kwekkeboom D J, Kooij P P, Bakker W H, Macke H R, Krenning E P. 1999 Comparison Of ^{111}In-DOTA-Tyr^{3}-Octreotide And ^{111}In-DTPA-Octreotide In The Same Patients: Biodistribution, Kinetics, Organ And Tumor Uptake. *J. Nucl. Med.* **40** 762 – 767. (56)

Kwok C, Prestwich W and Wilson B. 1985 Calculation Of Radiation Doses For Nonuniformly Distributed β and γ Radionuclides In Soft Tissue. *Med. Phys.* **12** 405 – 412. (34, 80, 93, 146)

Langmuir V and Sutherland R 1988 Dosimetry Models For Radioimmunotherapy. *Med. Phys* **15** 867-873. (115)

Langmuir V K, Wessels B W, Mendonca H, Yorke E D and Montilla L. 1992 Comparisons Of Sectioned Micro-TLD Dose Measurements With Predicted Dose From ^{131}I-Labeled Antibody. *Med. Phys.* **19** 1213 – 1218. (93)

Larsson L 1988 Immunocytochemistry: Theory and Practice. CRC Press Inc. Boca Raton. pp 1 – 2. (111)

Lasic D D and Papahadjopoulos D. 1995 Liposomes Revisited. *Science.* **267** 1275 – 1276. (45)

Leichner P and Kwok C 1993 Tumor Dosimetry In Radioimmunotherapy: Methods Of Calculation For Beta Particles. *Med. Phys.* **20** Pt. 2 529-534. (114)

Loevinger R, Budinger T and Watson E. 1988 MIRD Primer For Absorbed Dose Calculations. The Society of Nuclear Medicine, New York. (79, 145)

Macey D J and Meredith R F. 1999 A Strategy To Reduce Red Marrow Dose For Intraperitoneal Radioimmunotherapy. *Clin. Cancer Res.* **5** 3044s – 3047s. (22)

MacGibbon A, Bucci J, MacLeod C, Solomon J, Dalrymple C, Firth I and Carter J. 1999 Whole Abdominal Radiotherapy Following Second-Look Laparotomy For Ovarian Carcinoma. *Gynecol. Oncol.* **75** 62 – 67. (13)

Maraveyas A, Snook D, Hird V, Kosmas C, Meares C, Lambert H and Epenetos A A. 1994 Pharmacokinetics And Toxicity Of An Yttrium-90-CITC-DTPA-HMFG1 Radioimmunoconjugate For Intraperitoneal Radioimmunotherapy Of Ovarian Cancer. *Cancer* **73** 1067 – 1075. (20)

Mattes M J. 2002 Radionuclide-Antibody Conjugates For Single-Cell Cytotoxicity. *Cancer.* **94** 1215 – 1223. (17)

McDevitt M, Sgouros G, Finn R D, Humm J L, Jurcic J G, Larson S M and Scheinberg D A. 1998 Radioimmunotherapy With Alph-Emitting Nuclides. *Eur. J. Nucl. Med.* **25** 1341 – 1351. (17)

McDevitt M R, Finn R D, Ma D, Larson S M and Scheinberg D A. 1999 Preparation Of Alpha-Emitting 213-Bi-Labeled Antibody Constructs For Clinical Use. *J. Nucl. Med.* **40** 1722 – 1727. (17)

McQuarrie SA, Xiao Z, Miller GG, Mercer JR and Suresh MR 2001 Modern Trends In Radioimmunotherapy Of Cancer: Pretargeting Strategies For The Treatment Of Ovarian Cancer. *Quart. J. Nucl. Med.* **45** 160-166. (53, 78, 144)

Meredith R F, Partridge E E, Alvarez R D, Khazaeli M B, Plott G, Russell C D, Wheeler R H, Liu T, Grizzle W E, Schlom J and LoBuglio A F. 1996 Intraperitoneal Radioimmunotherapy Of Ovarian Cancer. *J. Nucl. Med.* **37** 1491 – 1496. (21)

Molina R, Filella X, Jo J, Agusti C and Ballesta AM. 1998 CA 125 in biological fluids. *Int. J. Biol. Markers.* **4** 224 – 230. (95)

Nahum A. 1996 Microdosimetry And Radiocurability: Modelling Targeted Therapy With β-Emitters. *Phys. Med. Biol.* **41** 1957 – 1972. (80, 93, 94, 115)

National Cancer Institute of Canada 2004 Canadian Cancer Statistics 2004. p. 18. Toronto. (6)

O'Brien T J, Tanimoto H, Konishi I and Gee M. 1998 More Than 15 Years Of CA 125: What Is Known About The Antigen, Its Sturcture And Its Function. *Int. J. Biol. Markers.* **13** 188 – 195. (8)

O'Donoghue J A, Bardies M and Wheldon T E. 1995 Relationships Between Tumor Size And Curability For Uniformly Targeted Therapy With Beta-Emitting Radionuclides. *J. Nucl. Med.* **36** 1902 – 1909. (80, 93, 94)

Omura M, Torigoe S, Kurihara H, Matsubara S and Kubota N 1998 Comparison Between Fractionated High Dose Rate Irradiation And Continuous Low Dose Rate Irradiation In Spheroids. *Acta Oncol.* **37** 681-686. (138)

Otte A, Herrmann R, Heppeler A, Behe M, Jermann E, Powell P, Maecke H R and Muller J. 1999 Yttrium-90 DOTATOC: First Clinical Results. *Eur. J. Nucl. Med.* **26** 1439 – 1447. (56)

Pandey U, Mukherjee A, Sarma H D, Das T, Pillai M R A and Venkatesh M. 2002 Evaluation Of ^{90}Y-DTPA and ^{90}Y-DOTA For Potential Application In Intra-Vascular Radionuclide Therapy. *Appl. Radiat. Isotopes.* **57** 313 – 318. (65)

Papahadjopoulos D, Allen T M, Gabizon A, Mayhew E, Matthay K, Huang S K, Lee K D, Woodle M C, Lasic D D, Redemann C and Martin F J. 1991 Sterically Stablized Liposomes: Improvements In Pharmacokinetics And Antitumor Therapeutic Efficacy. *Proc. Natl. Acad. Sci. USA.* **88** 11460 – 11464. (49)

Paretzke H G. 1987 Radiation Track Structure Theory. Chapter 3 in Kinetics Of Non-Homogeneous Processes, A Practical Introduction For Chemists, Biologists, Physicists, and Materials Scientists (Freeman, G R. editor). John Wiley & Sons, New York. (33)

Paretzke H G and Berger M. 1978 Stopping Power And Energy Degradation For Electrons In Water Vapor. pp 749 - 758 in Sixth Symposium On Microdosimetry (Booz J and Ebert H G. editors), Report EUR 6064. Harwood Academic Publishers, London. (33)

Perkins G L, Slater E D, Sanders G K and Prichard J G. 2003 Serum Tumor Markers. *Am. Fam. Physician.* **68** 1075 – 1082. (9)

Prestwich W, Nunes J and Kwok C. 1989 Beta Dose Point Kernels for Radionuclides of Potential Use in Radioimmunotherapy. *J. Nucl. Med.* **30** 1036 – 1046. (34, 81, 83, 87)

Roberson P L, Buchsbaum D J, Heidorn D B and Ten Haken R K. 1992 Three-Dimensional Tumor Dosimetry For Radioimmunotherapy Using Serial Autoradiography. *Int. J. Radiat. Oncol. Biol. Phys.* **24** 329 – 334. (18, 80)

Roeske J, Chen G and Brill A. 1993 Dosimetry Of Intraperitoneally Administered Radiolabeled Antibodies. *Med. Phys.* **20** 593 – 600. (38, 80, 95, 109, 145)

Rosenshein N B. 1983 Radioisotopes In The Treatment Of Ovarian Cancer. *Clin. Obstet. Gynecol.* **10** 279 – 295. (14)

Rotmensch J, Roeske J, Chen G, Pelizzari C, Montag A, Weichselbaum R, Herbst A L. 1990 Estimates Of Dose To Intraperitoneal Micrometastases From Alpha And Beta Emitters In Radioimmunotherapy. *Gynecol. Oncol.* **38** 478 – 485. (80, 95, 109, 145)

Rotmensch J, Whitlock J L, Schwartz J L, Hines J J, Reba R C and Harper P V. 1997 *In vitro* And *In vivo* Studies On The Development Of The α-Emitting Radionuclide Bismuth 212 For Intraperitoneal Use Against Microscopic Ovarian Carcinoma. *Am. J. Obstet. Gynecol.* **176** 833 – 840. (15)

Safavy A, Smith Jr. D C, Bazooband A and Buchsbaum D J. 2002 De Novo Synthesis Of A New Diethylenetriaminepentaacetic Acid (DTPA) Bifunctional Chelating Agent. *Bioconjugate Chem.* **13** 317 – 326. (55)

Sarfaraz M and Wessels B. 1995 Validation Of An Analytical Expression For The Absorbed Dose From A Spherical β Source Geometry And Its Application To Micrometastatic Radionuclide Therapy. *Clin. Cancer Res.* **5** 3020s – 3023s. (79, 93)

Schwesinger F, Ros R, Strunz T, Anselmetti D, Guntherodt H-J, Honegger A., Jermutus L, Tiefenauer L and Pluckthun A 2000 Unbinding Forces Of Single Antibody-Antigen Complexes Correlate With Their Theraml Dissociation Rates. *Proc. Natl. Acad. Sci. USA.* **97** 9972-9977. (117)

Sgouros G. 1993 Bone Marrow Dosimetry For Radioimmunotherapy: Theoretical Considerations. *J. Nucl. Med.* **34** 689 – 694. (22)

Smith-Jones P M, Stolz B, Alberta R, Ruser G, Briner U, Macke H R and Bruns C. 1998 Synthesis And Characterisation Of [^{90}Y]-Bz-DTPA-oct: A Yttrium-90-Labelled Octreotide Analogue For Radiotherapy Of Somatostatin Receptor-Positive Tumours. *Nuc. Med. Biol.* **25** 181 – 188. (56)

Spencer L V. 1955 Theory Of Electron Penetration. *Phys. Rev.* **98** 1597 – 1615. (34)

Srivastava S and Dadachova E. 2001 Recent Advances in Radionuclide Therapy. *Semin. Nucl. Med.* **XXXI** 330-341. (15, 19, 83)

Stewart J S W, Hird V, Snook D, Sullivan M, Hooker G, Courtenay-Luck N, Sivolapenko G, Griffiths M, Myers M J, Lambert H E, Munro A J and Epenetos A A. 1989 Intraperitoneal Radioimmunotherapy For Ovarian Cancer: Pharmacokinetics, Toxicity , And Efficacy Of I-131 Labeled Monoclonal Antibodies. *Int. J. Radiat. Oncol. Biol. Phys.* **16** 405 – 413. (23)

Stewart RD, Wilson WE, McDonald JC and Strom DJ 2002 Microdosimetric Properties Of Ionizing Electrons In Water: A Test Of The PENELOPE Code System. *Phys. Med. Biol.* **47** 79-88. (159)

Stinchcomb T G and Roeske J C. 1999 Values Of "S", $<z_1>$ and $<z_1^2>$ For Dosimetry Using Alpha-Particle Emitters. *Med. Phys.* **26** 1960 – 1971. (38)

Sutherland R, Buchegger F, Schreyer M, Vacca A, and Mach J P. 1987 Penetration And Binding Of Radiolabeled Anti-Carcinoembryonic Antigen Monoclonal Antibodies And Their Antigen Biding Fragments In Human Colon Multicellular Tumor Spheroids. *Cancer Res.* **47** 1627 – 1633. (79, 111)

Syme A M, Kirkby C, Riauka T A, Fallone B G and McQuarrie S A. 2004 Monte Carlo investigation of single cell beta dosimetry for intraperitoneal radionuclide therapy. *Phys. Med. Biol.* **49** 1959 – 1972. (4)

Syme A M, McQuarrie S A and Fallone B G. 2003a Beta Dose-Rate Distributions In Microscopic Spherical Tumours For Intraperitoneal Radioimmunotherapy. *Int. J. Radiat. Oncol. Biol. Phys.* **56** 1495 – 1506. (4)

Syme A M, McQuarrie S A, Middleton J W and Fallone BG. 2003b Dosimetric Model For Intraperitoneal Targeted Liposomal Radioimmunotherapy Of Ovarian Cancer Micrometastases. *Phys. Med. Biol.* **48** 1305 – 1320. (4)

Tailor A, Bourne T H, Campbell S, Okokon E, Dew T and Collins W P. 2003 Results From An Ultrasound-Based Familial Ovarian Cancer Screening Clinic: a 10-Year Observational Study. *Ultrasound Obst. Gyn.* **21** 378 – 385. (9)

Trimble E, Berry D, Gore M, Kavanagh J, Cohen C, Pecorelli S, Creasman W, Mason P and Heinz P. 2003 Discussion: Current Issues In The Design Of Ovarian Cancer Treatment Trials. *Gynecol. Oncol.* **88** S122 – S123. (12)

Turner J E. 1995 Atoms, Radiation And Radiation Protection, 2nd Edition. John Wiley and Sons, New York. (30)

Urban N, McIntosh M W, Andersen M R and Karlan B Y. 2003 Ovarian Cancer Screening. *Hematol. Oncol. Clin. N.* **17** 989 – 1005. (8, 9)

van Gog F, Visser G, Stroomer J, Roos J, Snow G and van Dongen G 1997 High Dose Rhenium-186-Labeling Of Monoclonal Antibodies For Clinical Application: Pitfalls And Solutions. *Cancer Supplement* **80** 2360-2370. (59)

Vander A, Sherman J and Luciano D. 1994 Human Physiology, 6th Edition. McGraw-Hill Inc., New York. (50)

Vergote I, Larsen RH, De Vos L, Winderen M, Ellingsen T, Bjorgum J, Hoff P, Aas M, Trope C and Nustad K. 1992b Distribution Of Intraperintoneally Injected Microspheres Labeled With The Alpha-Emitter Astatine (211At) Compared With Phosphorus (32P) And Yttrium (90Y) Colloids In Mice. *Gynecol. Oncol.* **47** 358-65. (15, 112, 144, 145)

Vergote I, Larsen RH, De Vos L, Nesland JM, Bruland O, Bjorgum J, Alstad J, Trope C and Nustad K. 1992c Therapeutic Efficacy Of The α-Emitter ^{211}At Bound On Microspheres Compared With ^{90}Y and ^{32}P Colloids In A Murine Intraperitoneal Tumour Model. *Gynecol. Oncol.* **47** 366-72. (15)

Vergote I B, Vergote-De Vos L N, Abeler V M, Aas M, Lindegaard M W, Kjorstad K E, and Trope C G. 1992a Randomized Trial Comparing Cisplatin With Radioactive Phosphorus Or Whole Abdomen Irradiation As Adjuvant Treatment In Ovarian Cancer. *Cancer.* **69** 741 – 749. (14, 112, 144, 145)

Wang S J, Lin W Y, Chen M N, Chen J T, Ho W L, Hsieh B T, Huang H, Shen L H, Ting G and Knapp FF Jr. 2001 Histologic Study Of Effects Of Radiation Synovectomy With Rhenium-188 Microsphere. *Nucl. Med. Biol.* **28** 727 – 732. (21)

Ward B, Mather S, Shepherd J, Crowther M, Hawkins L, Britton K and Slevin M L. 1988 The Treatment Of Intraperitoneal Malignant Disease With Monoclonal Antibody Guided ^{131}I Radiotherapy. *Br. J. Cancer.* **58** 658 – 662. (23)

Watson EE, Stabin MG, Davis JL and Eckerman KF 1989 A Model Of The Peritoneal Cavity For Use In Internal Dosimetry. *J. Nucl. Med.* **30** 2002-2011. (110)

Werner B, Kwok C and Das I. 1988 Dose Distributions In Regions Containing Beta Sources: Large Spherical Source Regions In A Homogeneous Medium. *Med. Phys.* **15** 358 – 363. (93)

Werner B L, Rahman M, Salk W N and Kwok C S. 1991 Dose Distributions In Regions Containing Beta Sources: Uniform Spherical Source Regions In Homogeneous Media. *Med. Phys.* **18** 1181 – 1191. (93)

Whitehouse C and Solomon E. 2003 Current Status Of The Molecular Characterization Of The Ovarian Cancer Antigen CA125 And Implications For Its Use In Clinical Screening. *Gynecol. Oncol.* **88** S152 – S157. (6, 8, 11)

Wong N A, Broadbent M R, Paterson-Brown S and al-Nafussi A. 2002 Gastrointestinal Stromal Tumor in Ascitic Fluid. A Case Report. *Acta Cytol.* **46** 723 – 727. (10)

Xiao Z, McQuarrie S A, Suresh M R, Mercer J R, Gupta S and Miller G G. 2002 A Three-Step Strategy For Targeting Drug Carriers To Human Ovarian Carcinoma Cells *In Vitro*. *J. Biotechnol.* **94** 171 – 184. (53, 78)

Yanoh K, Takeshima N, Hirai Y, Minami A, Tsuzuku M, Toyoda N and Hasumi K. 1999 Morphologic Analyses Of Positive Peritoneal Cytology In Endometrial Carcinoma. *Acta Cytol.* **43** 814 – 819. (10)

Young R C, Brady M F, Nieberg R K, Long H J, Mayer A R, Lentz S S, Hurteau J and Alberts D S. 2003 Adjuvant Treatment For Early Ovarian Cancer: A Randomized Phase III Trial Of Intraperitoneal 32P Or Intravenous Cyclophosphamide And Cisplatin – A Gynecologic Oncology Group Study. *J. Clin. Oncol.* **21** 4350 – 4355. (14)

Zaider M and Minerbo GN 2000 Tumour Control Probability: A Formulation Applicable To Any Temporal Protocol Of Dose Delivery. *Phys. Med. Biol.* **45** 279-293. (138)

Zweit J. 1996 Radionuclides and Carrier Molecules For Therapy. *Phys. Med. Biol.* **41** 1905 – 1914. (83, 88)